Fatigue Crack Growth of Filled Elastomers

Christian H. H. RATSIMBA

Department of Materials
Queen Mary and Westfield College
University of London

A thesis submitted for the degree of Doctor of Philosophy

June 2000

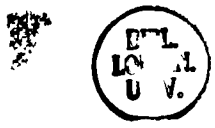

ABSTRACT

In the past, the use of a fracture mechanics approach to describe crack growth in elastomers has been shown to work well for specimens of simple test geometry, simply loaded. This has been the case because elastic strain energy density (*e.s.e.d.*) functions could reliably be used to calculate both the magnitude of elastic stored energy available to drive a crack and the magnitude of the rate of release of such energy as the crack grows.

The aim of this thesis was to investigate the applicability of such a methodology to situations of more complex loading. To this end two novel test-piece geometries were developed. The first consisted of a pure shear geometry with the sample having been pre-strained in the longitudinal direction to varying extents, hence introducing a type of bi-axial deformation. The second consisted of a pure shear geometry test-piece inclined at 30° to the horizontal and loaded in the vertical direction, hence inducing simultaneously pure shear and simple shear loading. Both types of test-piece were used to study the validity of the particular *e.s.e.d.* functions, the energetics and mechanics of crack growth and crack growth geometries on a macro and micro scale.

The constants in particular *e.s.e.d.* functions were determined by uniaxially deforming in pure shear each of the carbon black reinforced materials used in this study. The resulting functions became progressively less good at predicting the elastic strain energy in the novel geometry test-pieces as the deformation modes became more complex. Anisotropy induced by deforming specimens in one direction was not easily removed even by an imposed large deformation in another direction. Nevertheless, the functions were successfully used to predict crack growth directions in the 30° inclined test-piece. However in the pre-strain pure shear test-pieces the functions significantly underestimated the elastic strain energy. Hence the real energies had to be determined from the forces and extensions measured during cyclic crack growth tests. In these tests crack growth rates for a given tearing energy (elastic energy release rate) increased as the magnitude of the pre-strain increased. This significant weakening was associated with the development of a strain induced molecular and carbon black anisotropy.

ACKNOWLEDGEMENTS

I would like to express my sincere gratitude and appreciation to my supervisors, Dr. James Busfield, Pr. Craig Davies and Pr. Alan Thomas for their guidance, their inspirational comments, encouragement throughout this work and last but not least their kindness.

I am obliged to BTR (AVS) and Queen Mary and Westfield College for funding this project.

A long term undertaking such as this inevitably involves assistance from a wide range of people:

Bill Hoskins, Colin Langdown and Kevin Sonnet for their help in manufacturing and testing of materials and the technicians for having made the mechanical testing area and the other labs a more friendly place to work in.

All the past and present colleagues from rooms 105 and 104 with a special mention to Chudej Deeprasertkul with whom I shared many experimental problems and Katsuhiko Tsunoda who brought my fracture mechanics knowledge to new heights.

Also to all these friends who live, lived, danced, and partied in this house behind a cemetery (22 Moody Street) and helped me to enjoy all this time.

Finally, I would like to thank my parents, my sister and my brother for their support and encouragement without which none of these would have been possible.

TABLE OF CONTENTS

LIST OF SYMBOLS

Symbols	Dimension (SI Units)	Name
A	$F.L^{-2}$ (Pa)	Constant from the Davies *et al* elastic strain energy density function
a	L^2 (m^2)	Area of the new surface created during fracture
A_t	L^2F^{-1} ($m^3J^{-1}cycle^{-1}$)	Constant in the crack growth empirical relationship for region 2
a_T	No dimension	Shift factor in the WLF relationship
α	No dimension (degrees or radians)	Angle between the clamps of the angle test-piece
α_i	No dimension	Extension ratio in the direction *i*
b	L^{-1}(m)	Arbitrary constant in the expression of the change in configurational entropy
B_t	S.I units	Constant in the exponential crack growth relationship
β	No dimension	Constant in the exponential crack growth relationship
c	L (m)	Crack length
c'	L (m)	Crack length referred to the deformed state (pre-strained)
c_1 *and* c_2	L (m)	Crack length upper and lower boundaries in integration for fatigue life determination
C_1	No dimension	Characteristic coefficient in the WLF equation
C_2	T (K)	Characteristic coefficient in the WLF equation

C	No dimension	Constant from the Davies et al elastic strain energy function.
C_{ijkl} or C_{ij}	$F.L^{-2}$ (Pa)	Coefficients of the energy of deformation per unit volume or elastic strain energy function.
d	L (m)	Diameter of the crack tip
δ	L (m)	Vertical displacement
E_c	$F.L^{-2}$ (Pa)	Compression modulus
E_s	$F.L^{-2}$ (Pa)	Shear modulus
e_0	No dimension	Tensile strain corresponding to T_0
e_c	No dimension	Compression strain
f_s, f_n and f_t	F (N)	The shear force, normal force and the total force on the 30° inclined test-piece
F_n	F (N)	Component of the nodal force normal to the crack plane in the Virtual Crack Closure Technique
F_t	F (N)	Tensile forces in the simultaneous extension, inflation and torsion of a cylindrical annulus
F_A, F_B	F (N)	Forces applied in region A and B for the split test-piece
f	F (N)	Applied tearing force in trouser test or angle test-piece
ΔF	$F.L^{-2}$ (Pa)	Helmoltz free energy per unit volume
$f(n)$	No dimension	Mathematical function representing the stress-softening phenomenon
Φ	No dimension	Volume fraction of carbon black
ϕ	No dimension (radians or degrees)	Angle representing the extent of shear

φ	No dimensions	Constant from the Davies et al elastic strain energy function.
G	$F.L^{-1}$ ($J.m^{-2}$)	Energy release rate (with respect to the crack length)
Γ		Contour around the crack tip along which the *J*-integral is calculated
γ	No dimension	Shear strain
h	L (m)	Height of a single, double cress-section shear springs or of circular cylindrical tube
η_n	No dimension	Constants from the Odgen elastic strain energy function
I_1, I_2 *and* I_3	No dimensions	Strain invariants
I_m	No dimension	Limiting value of I_1 corresponding to the fully stretched network
J	$F.L^{-1}$ ($J.m^{-2}$)	*J*-integral
K	$F.L^{-3/2}$ ($Pa.m^{1/2}$)	Stress intensity factor
K_c	$F.L^{-3/2}$ ($Pa.m^{1/2}$)	Fracture toughness
K	No dimension	Numerical constant allowing for the calculation of the actual cross-link density in filled elastomers
k	$F.L.T^{-1}$ ($Joule.K^{-1}$)	Boltzmann constant ($=1.38\times10^{-23}$)
k_t	No dimension	Constant in the expression of the tearing energy in simple extension
κ	No dimension	Elastomer/solvent interaction parameter
L_0	L (m)	Unstrained height in a pure shear test-piece
L_0'	L (m)	Initial height of a pre-strained pure shear in the deformed state

l	L (m)	Length of a single statistical link
Λ	$F.L^{-2}$ (Pa)	Constant from the Davies *et al* elastic strain energy function
λ	No dimension	Extension ratio in the direction of the stretching in a uniaxial test or in the extension ratio in the legs of a trouser test (principal directions)
λ_1, λ_2 *and* λ_3 or λ_i	No dimensions	Principal extension ratios in direction *i*
λ_A and λ_B	No dimensions	Extension ratios in regions A and B for the split test-piece
m	$F.L.T^{-1}$ (Joule.K^{-1})	Arbitrary constant in the configurational entropy in a single chain
M	F.L (J)	Torsion couple
M_c	M.$mole^{-1}$ (kg.$mole^{-1}$)	Number average molar mass between cross-links
M_0	M (kg)	Mass of the elastomer specimen
M_m	M (kg)	Mass of elastomer hydrocarbon
M_t	M (kg)	Total mass of mix formulation
M_c	M (kg)	Average molecular mass between cross-links
μ_n	$F.L^{-2}$ (Pa)	Constants from the Odgen elastic strain energy function
F_t	F (N)	Tensile forces to the ends of the circular tube
N_v	L^{-3} (m^{-3})	Number of elastomers chains per unit volume
N	No dimension	Fatigue life or number of cycles to failure

N_A	No dimension	Avogadro constant or number of molecules per mole (6.023×10^{23})
n	No dimension	Number of cycles
n_j	No dimension	The outward normal vector to
υ	No dimension	Frequency of the cyclic deformations
P	No dimension	Number of possible configurations that molecule can adopt at a given extension
q	No dimension	Number of statistical links of length l
θ	No dimension	Angle of inclination of the pure shear test-piece in the inclined geometry
Θ	T (K or °C))	Temperature
Θ_s	T (K)	Reference temperature in the WLF equation
R	$F.L.T^{-1}.mol^{-1}$	Universal molar gas constant (8.31 $J.K^{-1}.mol^{-1}$)
R_v	$F.L^{-2}$ (Pa)	Force per unit deformed acting normally to the inner surface of the tube
R_q	L (m)	Root mean square of the heights from the central line average on a fracture profile
dc/dt	$L.t^{-1}$ ($m.s^{-1}$)	Rate of tearing
r	No dimension or L (m)	Radial co-ordinate in cylindrical co-ordinate
r_0	L ($m.cycle^{-1}$)	Crack growth per cycle uniquely due to the ozone scission
ρ	$M.L^{-3}$ (kg.m-3)	Density of the elastomer
ρ_{RH}	ML^{-3} ($kg.m^{-3}$)	Density of elastomer hydrocarbon

S_p	No dimension	Shape factor
S_t	$F.L^{-1}$ ($J.m^{-2}$)	Surface free-energy (or surface tension)
S *or* ΔS	$F.L^{-2}.T^{-1}$ ($Joule.K^{-1}.m^{-3}$)	Entropy or variation of entropy of deformation per unit volume
s *or* Δs	$F.L.T^{-1}$ ($Joule.K^{-1}$)	Configurational entropy (chain entropy) or variation of configurational entropy
σ	$F.L^{-2}$ (Pa)	Engineering stress or force per unit underformed cross sectional area.
σ_i	$F.L^{-2}$ (Pa)	Engineering stress or force per unit underformed cross sectional area in the principal direction *i*
σ_{ij}	$F.L^{-2}$ (Pa)	Component of the stress tensor
ς	L^{-1} (m^{-1})	Angle of torsion per unit deformed height of the circular tube
T	$F.L^{-1}$ ($J.m^{-2}$)	Tearing energy
T_{min}	$F.L^{-1}$ ($J.m^{-2}$)	Minimum tearing energy during a cycle
$\boldsymbol{T}$	F (N)	Traction vector
T_0	$F.L^{-1}$ ($J.m^{-2}$)	Fatigue limit or minimum tearing energy to initiate mechanical crack growth
T_i	$F.L^{-1}$ ($J.m^{-2}$)	Initial tearing energy from the initial crack
T_c	$F.L^{-1}$ ($J.m^{-2}$)	Tearing energy higher limit (region 3) before catastrophical tearing
T_Z	$F.L^{-1}$ ($J.m^{-2}$)	Threshold tearing energy for the occurrence of crack growth due to ozone under fixed load
T_r	$F.L^{-1}$ ($J.m^{-2}$)	Tearing energy higher limit for region 2 of the crack growth characteristics

t	L (m)	Thickness
t_1 ,t_2 *and* t_3, or t_i	$F.L^{-2}$ (Pa)	Principal true stresses
t_z	No dimension	Time fraction of each cycle for which the sample is under stress
τ	$F.L^{-2}$ (Pa)	Shear stress
Θ	T (K)	Absolute temperature or temperature (°C)
U *or* ΔU	FL^{-2} (Pa)	Internal energy per unit volume
U_r	F.L (J)	Energy released due to a crack of length c
$\boldsymbol{u}$	L (m)	Displacement vector
u	F.L (J)	Energy stored or elastic strain energy
u_n	L (m)	Normal displacement of the node directly behind the crack tip
V	L^3 (m^3)	Volume of elastomer
V_m	L^3 (m^3)	Volume of the elastomer network
V_s	L^3 (m^3)	Volume of solvent absorbed
V_0	L^3 (m^3)	Molar volume of the solvent
v_r	No dimension	Volume fraction of elastomer
$[X]_{act}$	$M^{-1}(kg^{-1})$	Actual cross-link density
$[X]_{phy}$	$M^{-1}(kg^{-1})$	Physical and chemical cross-links
x, y *and* z	No dimensions or L (m)	(Values of the) three Cartesian co-ordinates in the initial undeformed state
x', y' *and* z'	No dimensions or L (m)	(Values of the) three cartesian coordinate in the deformed state

x and x_p	L (m)	Correction factor in tearing energy of pure shear and pre-strained pure shear
y_m	L (m)	is the average height in profile measurement
ψ	No dimension (degrees or radians)	Angle of splitting in the split test-piece
W	$F.L^{-2}$ (Pa)	Work of deformation per unit volume or elastic strain energy density function or elastic strain energy density (*e.s.e.d.*) function
W_n	$F.L^{-2}$ (Joule.m^{-3})	Elastic strain energy density after n cycles
W_b	$F.L^{-2}$ (Pa)	Work to break per unit volume
W_S	$F.L^{-2}$ (Joule.m^{-3})	Elastic strain energy density due to the cyclic deformations
w	L (m)	Width of the legs in trouser test specimen or pure shear test-piece
w'	L (m)	Width of the pure shear test-piece in the deformed state (pre-strained)

LIST OF ABBREVIATIONS

Abbreviations	Name
e.s.e.d. function	Elastic strain energy density function
FEA	Finite Element Analysis
VCE	Virtual Crack Extension
VCCT	Virtual Crack Closure Technique
NR	Natural Rubber, cis 1,4 poly-isoprene
SBR	Styrene Butadiene Rubber
SEM	Scanning electron microscopy
pphr	Parts per hundred rubber in weight
WLF	William, Landel and Ferry equation
CIIR	Chlorobutyl
cpm	Number of cycle per minute
HAF	High Abrasion furnace carbon black (or N330)
MT	Medium thermal carbon black (or N990)
EV	Efficient Vulcanising system
G.T. function	Elastic strain energy function proposed by Gent and Thomas
PS	Pre-strain
PC	Pre-conditioning

LIST OF FIGURES

CHAPTER 2

CHAPTER 3

CHAPTER 4

CHAPTER 5

CHAPTER 6

LIST OF TABLES

CHAPTER 3

CHAPTER 4

CHAPTER 5

1

Introduction

Elastomers are frequently used as anti-vibration devices, such as mounts or bushes, in the automobile industry. These components are often geometrically complex, are loaded in a complex manner and are subject to additional cyclic loading during vehicle running. Component life prediction has become an increasingly important design parameter as warranty times for components have been continuously extended. Cyclic crack growth in components frequently leads to failure and it is this process of crack growth that is the concern of this thesis.

The work to drive crack growth is supplied by the release of elastic stored energy (tearing energy in elastomers) in a loaded component as a crack grows. This fracture mechanics approach works well for highly elastic simple elastomers, loaded in a simple manner (tensile, simple shear, pure shear) as although high strains are involved the materials are essentially brittle (i.e. little or no plastic strain). It has been shown that for a given elastomeric material a characteristic tearing energy was needed to drive a crack at a given rate in a variety of simply loaded test piece geometries even in cases where non irreversible, non elastic, dissipation of energy occurred in the region of the crack tip[1]. It is hence clear that at least in these simple test geometries the crack tip profile and associated internal molecular fracture processes are a material characteristic. In these circumstances it is only necessary to know the magnitude of the elastic strain energy that would be released as a crack grows in a test piece to be able to predict the crack growth rate. In a simple test piece, simply loaded, this strain energy release rate can be determined by experimentation or using finite element analysis (FEA) with an appropriate elastic strain energy (*e.s.e.d.*) function. The *e.s.e.d.* function must describe accurately the stress-strain behaviour of the elastomeric material in any simple stressing mode whatever its loading path. Such functions exist for simple unfilled elastomers and here the modelling process works

well and it is possible to predict crack growth rates for a given test geometry. The situation for components of complex geometry loaded in a complex manner, manufactured from carbon black filled elastomers is much more difficult to analyse. Here the elastic strain energy distributions in a component can only be modelled using FEA. For this it is necessary to have an *e.s.e.d.* function for the material applicable in all stressing modes. For carbon black filled elastomers this would appear to be possible for the first loading cycle. However, on unloading and relaxing the second stress-strain curve is significantly different from the first[2, 3] and hence would need to be represented by an *e.s.e.d.* function containing numerically different constants, at least. This variation continues for each subsequent loading cycle although the magnitude of the cyclic variation continuously diminishes. For a complex component, of course, different points go through different loading cycles and in theory would require different *e.s.e.d.* functions to represent this behaviour. This would make it very difficult to even determine which direction a crack should grow in, let alone to determine the magnitude of the strain energy release rate necessary to drive such a crack. The loading history dependent stress-strain behaviour described above is represented within the material by the development of orientation of the carbon black and of the molecular network. This orientation would clearly lead to anisotropic stress-strain behaviour further complicating the picture. At moderate strains, as in the bulk of a component, the anisotropic energy release rate would probably determine the macroscopic direction of crack growth at a given time. At high strains, at the crack tip, the local anisotropy would determine, in part, the magnitude of the energy release rate necessary to drive a crack and would determine the crack path on a microscopic scale. The energy release rate (tearing energy) necessary to drive a crack would hence be dependent in a complex manner on the components detailed loading history. This, combined with an inability to accurately calculate the elastic energy stored in a component means that currently only very empirical unreliable methods are used in an attempt to predict the life of a component. While it is clearly not possible to jump from life prediction of simply loaded test pieces to that of complex components loaded in a complex manner it should be possible to investigate in non simply loaded components the effect of the most important variables on crack growth rates. Therefore in this thesis systems of

gradually increasing complexity are investigated in an attempt to derive general rules which describe crack growth in complex components. Suitable *e.s.e.d.* functions are examined, for a range of unfilled and carbon black filled elastomers and with a particular focus on the effect of a simple preloading history on the stress-strain behaviour. Cyclic crack growth are studied in bi-axially loaded specimens and tearing energy/ crack growth rate relationship are determined. This includes a determination of the energy release rates (tearing energy) by both experimental means and by FEA using suitable *e.s.e.d.* functions. Fracture surfaces are examined in an attempt to study local crack paths and the relationship with the material anisotropy. The effects are studied in both strain crystallising/ non-strain crystallising elastomers and in elastomers containing different carbon black contents in an attempt to determine the role of these materials variables on crack growth.

REFERENCES

[1] Rivlin R. S. and Thomas A. G., *J. Polym. Sci.*, **10**, 291 (1953).

[2] Mullins L., *J. Rubber Res.*, **16**, 275 (1947).

[3] Mullins L., *J. Phys. Colloid Chem.*, **54**, 239 (1950).

2

Review of the relevant literature

2.1 Introduction

As can be seen from the introduction to this thesis it is necessary here to review aspects of the stress-strain behaviour of filled and unfilled elastomers together with the application of fracture mechanics to crack growth. Hence, section 2.2 deals with the simple statistical theory of rubber like elasticity together with phenomenological models used to describe the stress-strain behaviour (elastic strain energy density function or *e.s.e.d.* function) of filled and unfilled elastomers. At the end of this section, the effect of limited viscous behaviour superimposed on the elastic behaviour is considered. Section 2.3 reviews the application of fracture mechanics to elastomers. It introduces the concepts of strength and tearing energy and discusses material parameters which control crack growth. In section 2.4, crack growth in cyclically loaded elastomers (fatigue crack growth) is reviewed and the effect of test variables on life prediction is discussed. Section 2.5 reviews the methodologies that have been utilised to both test and analyse crack growth in non-simply loaded components. Finally, aspects of the review most important to the work proposed here are summarised and a proposed programme of study is presented.

2.2 Stress-strain behaviour/ *e.s.e.d.* functions

2.2.2 The statistical-thermodynamic theory of a molecular network

The application of the statistical theory to the problem of long-chain molecules corresponding to a vulcanised or cross-linked elastomer starts from the concept of the entropy of a single chain. Extension of the chain is associated with a reduction of the configurational entropy, and *vice versa*. The configurational entropy

is given by the Boltzmann equation:

$$S = k \ln P \tag{2.2-1}$$

where P is a function which represents the number of possible configurations that molecules can adopt at a given extension, and k is the Boltzmann constant. It is hence this change in P which determines the force required to extend a specimen. P is usually expressed, whatever the statistical form used, as a function of the molecular end-to-end length r. r in turn can be expressed in terms of the number of statistical links q of length l which make up a molecule of fully extended length, ql.

From single chain statistics, if one end of the chain is fixed at the origin of a Cartesian co-ordinate system, the probability that the other end is situated within a volume $dxdydz$ can be shown to be defined by the Gaussian probability function:

$$P(x,y,z)\mathrm{d}x\mathrm{d}y\mathrm{d}z = (b^2/\pi^{3/2})\exp\left[-(b^2(x^2+y^2+z^2)\right]\mathrm{d}x\mathrm{d}y\mathrm{d}z \tag{2.2-2}$$

where $\frac{1}{b^2} = \frac{2ql^2}{3}$. The probability of a given distance r between the ends of the chains, regardless of direction, is given by a different function $P(r)$:

$$\mathrm{P}(r)\mathrm{d}r = \left(\frac{b^3}{\pi^{3/2}}\right)4\pi r^2\exp(-b^2r^2)\mathrm{d}r \tag{2.2-3}$$

In this equation the most probable end to end length is given by $r = 1/b$ which gives the maximum of $P(r)$. The root mean square end-to-end distance for a free chain, obtained from Equation 2.2-3, is:

$$\left(\overline{r^2}\right)^{1/2} = \left(3/2b^2\right)^{1/2} = lq^{1/2} \tag{2.2-4}$$

and is proportional to the square root of the number of links in the chain. The Gaussian statistical treatment involves an approximation which is equivalent to the assumption that the number of links is large and that

$$r \langle\langle ql \tag{2.2-5}$$

This implies that the end-to-end distance is very much less than the fully extended length of the chain.

From Equation 2.2-1 it is possible to calculate the configurational entropy for a single chain:

$$s = m - kb^2 r^2 \tag{2.2-6}$$

where m is a constant which includes the arbitrary volume element $dxdydz$.

The extension of this calculation to a network was initially introduced by Kuhn[1] whose theory was subsequently modified by Treloar[2]. Two assumptions are necessary to generalise this calculation to a network. The first one is that the x, y, and z components change on deformation in the same ratio as the corresponding dimensions of the bulk elastomer. It is called the affine deformation assumption. The second assumption is that the material deforms without a change of volume. On the basis of these assumptions, the most general type of pure homogeneous deformation, that is a strain not involving rotation of the principal axes, may be defined by the three extension ratios (or principal semi-axes of the strain ellipsoid) $\lambda_1, \lambda_2, \lambda_3$, such that:

$$x' = \lambda_1 x, \quad y' = \lambda_2 y, \quad z' = \lambda_3 z \tag{2.2-7}$$

where (x, y, z) is a particular material position in a rectangular Cartesian co-ordinate system initially, and (x', y', z') is the position in the deformed state. The directions of the axes (x, y, z) are called the principal directions. The incompressibility assumption leads to:

$$\lambda_1 \lambda_2 \lambda_3 = 1 \tag{2.2-8}$$

The change of configurational entropy on deformation of an individual chain is therefore from Equation 2.2-6:

$$\Delta s = -kb^2\left[(\lambda_1^2 - 1)x^2 + (\lambda_2^2 - 1)y^2 + (\lambda_3^2 - 1)z^2\right] \qquad (2.2\text{-}9)$$

This expression summed over the assembly of N_v chains contained in unit volume of the network to get the entropy of deformation ΔS has been shown to have the form:

$$\Delta S = -\frac{1}{2}N_v k(\lambda_1^2 + \lambda_2^2 + \lambda_3^2 - 3) \qquad (2.2\text{-}10)$$

The basic assumption of the kinetic theory is that all states of deformation have the same internal energy ($\Delta U = 0$) and the same non-configurational entropy. Hence, the change in the Helmoltz free energy ΔF, which for an isothermal reversible process is equal to the work W done by the applied forces becomes:

$$\Delta F = \Delta U - T\Delta S = -T\Delta S \qquad (2.2\text{-}11)$$

The work of deformation per unit volume is then:

$$W = \frac{1}{2}N_v kT(\lambda_1^2 + \lambda_2^2 + \lambda_3^2 - 3) \qquad (2.2\text{-}12)$$

For simple tensile extension (Figure 2.2-1), which may be defined in terms of a single extension ratio λ, and two equal contractions in the transverse directions combined with an incompressibility condition then:

$$\lambda_2 = \lambda, \quad \lambda_1 = \lambda_3 = \lambda^{-1/2} \qquad (2.2\text{-}13)$$

and Equation 2.2-11 becomes :

$$W = \frac{1}{2} N_v kT(\lambda^2 + \frac{2}{\lambda} - 3) \qquad (2.2\text{-}14)$$

and the force per unit undeformed cross sectional area or engineering stress σ required to deform the network is given by[3]:

$$\sigma = \frac{dW}{d\lambda} = N_v kT(\lambda - \frac{1}{\lambda^2}) \qquad (2.2\text{-}15)$$

For a simple shear strain in the (x, y) plane (Figure 2.2-2) the principal axes of strain are defined by the extension ratios:

$$\lambda_1 = \lambda, \quad \lambda_2 = 1/\lambda, \quad \lambda_3 = 1 \qquad (2.2\text{-}16)$$

and the corresponding shear strain γ is[4]:

$$\gamma = \lambda - 1/\lambda \qquad (2.2\text{-}17)$$

The work of deformation, Equation 2.2-11 thus becomes:

$$W = \frac{1}{2} N_v kT(\lambda^2 - 2 + 1/\lambda^2) = \frac{1}{2} N_v kT\gamma^2 \qquad (2.2\text{-}18)$$

The only work performed is that done by the shear stress τ, having the following expression:

$$\tau = \mathrm{d}W/\mathrm{d}\gamma = N_v kT\gamma \qquad (2.2\text{-}19)$$

It appears from this expression that $N_v kT$ is equivalent to the shear modulus, subsequently designated E_s. The number of chains per unit volume N_v is given by $N_v = (\rho/M_c)N_A$ where N_A is the Avogadro constant, M_c is the number average molar mass between cross-links and ρ is the density of the elastomer. Thus,

$$E_s = N_v kT = \rho RT / M_c \qquad (2.2\text{-}20)$$

where R is the gas constant per mole. This theory predicts a simple relationship between the stress and the strain. In simple shear, the shear stress is linearly related to the shear strain by the shear modulus E_s. The form of the relationships are similar for all elastomers being only scaled by the magnitude of the distance between cross-links. This theory is subject to all the limitations imposed by the assumption of the Gaussian chain behaviour and in addition to the assumption of affine deformation. It however predicts the initial elastic modulus at small strains well, but breaks down as the chain extension approaches strains of 50% for an unfilled elastomer. The high strain behaviour caused by the effects of a finite extensibility are of course not predicted and neither is the marked non-linearity at moderate strains (Figure 2.2-4). The phenomenological theories, to be discussed next, are not restricted by any particular physical interpretation and concentrate largely on trying to represent the high strain behaviour of unfilled elastomers with attempts to extend these ideas to represent the behaviour of filled elastomers.

2.2.3 Phenomenological theories

2.2.3.1 General Rivlin theory of large deformations for incompressible materials

Rivlin[5] showed, from the concept of an ideal elastic solid, (one in which energy cannot be dissipated) that its mechanical behaviour may be describe by means of an *e.s.e.d.* function or Helmoltz free energy of deformation per unit volume of material referred to the undeformed state, which is a single-valued function of the state of deformation. In the case of an isothermal pure homogeneous deformation, because the deformation is completely described by the principal extension ratios $(\lambda_1, \lambda_2, \lambda_3)$, the *e.s.e.d.* function W is a function of λ_1, λ_2 and λ_3 only. Symmetry considerations, conservation of the *e.s.e.d.* function in a rotation of the body through 180^0 about one of the co-ordinate axis and the isotropy of the material lead to the

conclusion that W must be expressible as a single valued function of any three independent symmetric functions of λ_1^2, λ_2^2 and λ_3^2. Specifically, we may choose as these functions the strain invariants I_1, I_2 and I_3, and we then have:

$$W = W(I_1, I_2, I_3) \tag{2.2-21}$$

where:

$$I_1 = \lambda_1^2 + \lambda_2^2 + \lambda_3^2 \tag{2.2-22}$$

$$I_2 = \lambda_1^2\lambda_2^2 + \lambda_2^2\lambda_3^2 + \lambda_3^2\lambda_1^2 \tag{2.2-23}$$

$$I_3 = (\lambda_1\lambda_2\lambda_3)^2 \tag{2.2-24}$$

When the material is unstrained, I_1, I_2 and I_3 take the values 3, 3 and 1 respectively. It can be shown that if the linear stress-strain relations of classical elasticity are to apply for a sufficiently small deformation of the material, W can be approximated with any desired degree of accuracy by a power series in $I_1 - 3$, $I_2 - 3$ and $I_3 - 1$. Thus, we may write:

$$W = \sum_{i+j+k=1}^{\infty} C_{ijk}(I_1 - 3)^i (I_2 - 3)^j (I_3 - 1)^k \tag{2.2-25}$$

Under suitable conditions, an elastomer may be considered as an incompressible material and therefore $I_3 = 1$. The coefficient $C_{00} = 0$ since the undeformed state is considered to be that in which the strain energy is zero. The *e.s.e.d.* function is then simplified to:

$$W = \sum_{i+j=1}^{\infty} C_{ij}(I_1 - 3)^i (I_2 - 3)^j \tag{2.2-26}$$

Then by considering the pure homogeneous deformation of a unit volume of elastomer, Rivlin[5] showed that a set of relationships exist between the principal true stresses, t_1, t_2 and t_3, the principal extension ratios λ_1, λ_2 and λ_3, and the partial derivatives of W with respect to the invariants I_1 and I_2:

$$\frac{t_1 - t_2}{\lambda_1^2 - \lambda_2^2} = \frac{2}{\lambda_1\lambda_2\lambda_3}\left\{\frac{\partial W}{\partial I_1} + \lambda_3^2\frac{\partial W}{\partial I_2}\right\} \tag{2.2-27}$$

$$\frac{t_1 - t_3}{\lambda_1^2 - \lambda_3^2} = \frac{2}{\lambda_1\lambda_2\lambda_3}\left\{\frac{\partial W}{\partial I_1} + \lambda_2^2\frac{\partial W}{\partial I_2}\right\} \tag{2.2-28}$$

$$\frac{t_2 - t_3}{\lambda_2^2 - \lambda_3^2} = \frac{2}{\lambda_1\lambda_2\lambda_3}\left\{\frac{\partial W}{\partial I_1} + \lambda_1^2\frac{\partial W}{\partial I_2}\right\} \tag{2.2-29}$$

The left-hand side terms of Equations 2.2-27 to 2.2-29 are called the reduced stresses. Stress-strain relations for simple homogeneous deformation modes can be easily derived from these equations. Specifically, for incompressible materials subjected to uniaxial tension (or compression), Rivlin[6] derived the relationship:

$$\frac{\sigma}{(\lambda - \lambda^{-2})} = 2\left\{\frac{\partial W}{\partial I_1} + \frac{1}{\lambda}\frac{\partial W}{\partial I_2}\right\} \tag{2.2-30}$$

where σ is the engineering stress (referred to the undeformed state; we then have $t_i = \sigma_i\lambda_i$) and $\lambda_1 = \lambda_3 = 1/\sqrt{\lambda}$ and $\lambda_2 = \lambda$ (Figure 2.2-1). In simple shear, we have:

$$\frac{\tau}{\gamma} = 2\left\{\frac{\partial W}{\partial I_1} + \frac{\partial W}{\partial I_2}\right\} \tag{2.2-31}$$

where τ is the engineering shear stress and γ is the shear strain given by $\gamma = \lambda - 1/\lambda$ with $\lambda = \lambda_1$ (Figure 2.2-2). For pure shear, the relationship is:

$$\frac{\sigma}{(\lambda-\lambda^{-3})}=2\left\{\frac{\partial W}{\partial I_1}+\frac{\partial W}{\partial I_2}\right\} \qquad (2.2\text{-}32)$$

where $\lambda=\lambda_1$ and $\lambda_3=1/\lambda$ (Figure 2.2-3).

Rivlin[7] also derived the analytical expressions relating the stresses and the partial derivatives of W with respect to I_1 and I_2 for more complex loading. These deformations include torsion, shear, flexure and certain combinations of these deformations. One of them, which will be of interest in this study, is the calculation of the forces to maintain simultaneous extension, inflation and torsion in a uniform circular cylindrical tube of highly elastic material. The details of the analytical solution are shown in Appendix 1.

Though the phenomenological theory is not bound to any molecular or physical phenomena, in case of unfilled elastomers, $\partial W/\partial I_1$ and $\partial W/\partial I_2$ has been usually related to respectively the intrinsic elastic properties of the network and the deviations to the statistical theory. The deviations from the statistical theory are attributed to the following molecular phenomena[3]:

(1) non-Gaussian chain or network statistics: the distribution of the end-to-end distance of the chains follows a Gaussian statistic as the q links of equal length l of a chain can take any directions in space. When a chain reaches its finite extensibility, the possible configurations of this chain are restricted and can not be considered as a Gaussian distribution.

(2) interaction between chains[8, 9].

(3) chain entanglements[10, 11].

(4) irreversible effects: Gent and Rivlin[12] observed a relation between the magnitude of $\partial W/\partial I_2$ and the magnitude of the hysteresis.

(5) non-random packing effects: there are dependencies between the configuration of neighbouring chains because of the competition of the chains for space[13].

These relationships can be used either to predict the stress-strain behaviour from a knowledge of W as a function of I_1 and I_2 or inversely to derive W from a knowledge of the stress-strain behaviour from one or several different modes of

deformation. In the literature, the various tests used to either generate input data for FEA or to check the quality of the material model are in general uniaxial tests like tension, simple shear or pure shear and biaxial or equi-biaxial tests. Data can be gathered from these independent tests so that the *e.s.e.d.* function coefficients can be determined by regression from several sets of data. The usual method to test the general applicability of a particular *e.s.e.d.* function derived from a given mode of deformation is to use it to predict the behaviour in another loading mode. The next section examines proposed models for the strain energy function particularly for filled elastomers and examines their applicability.

2.2.3.2 Models for filled materials

Mooney[14] developed the first phenomenological theory in 1940 prior to the development of statistical theory, to account for the large elastic deformation of elastomers. In fact, this model corresponds to the first order expression of the most general Rivlin function given in Equation 2.2-26 and is of the form:

$$W = C_{10}(I_1 - 3) + C_{01}(I_2 - 3) \tag{2.2-33}$$

In simple extension, Equation 2.2-33 yields:

$$\frac{\sigma}{\left[\lambda - \lambda^{-2}\right]} = 2\left[C_{10} + C_{01}\lambda^{-1}\right] \tag{2.2-34}$$

A plot of the reduced stress term on the left-hand side of this equation versus λ^{-1} should give a straight line of slope $2C_{01}$ and an intercept of $2C_{10}$. A typical plot for an unfilled elastomer is as shown in Figure 2.2-5. It shows an upturn, that may correspond to the onset of finite extensibility, at a relatively large extension (λ=2.5 or λ^{-1}=0.4) and a substantial part of the curve approximates to a straight line. But Yeoh[15] showed that only a small strain range could be fitted as a straight line using this type of plot for a carbon black filled elastomer. The Mooney expression appears to be unsuitable for modelling the behaviour of filled elastomers. It has also been pointed

out[16] that the Mooney constants determined from tensile data are inadequate for predicting the behaviour in other modes of deformation.

Tschoegl[17] suggested that the failure of the Mooney-Rivlin equations arises from not taking enough terms of the Rivlin series Equation 2.2-26. James and Green[18] fitted test data for highly carbon black filled elastomers with various high order expansions of the Rivlin series. They reported that a third order deformation expansion with 5 terms, Equation 2.2-35, gave better predictions beyond the range of the input data than expansion of higher order or of a higher number of terms:

$$W = C_{10}(I_1 - 3) + C_{01}(I_1 - 3) + C_{20}(I_1 - 3)^2 + C_{11}(I_1 - 3)(I_2 - 3) + C_{30}(I_1 - 3)^3 \qquad (2.2\text{-}35)$$

Gregory[19] noted that a simple relationship existed between stress/strain data obtained in uniaxial tension, uniaxial compression and simple shear. He showed for filled elastomers that a plot of the reduced stress, the left-hand terms in Equations 2.2-27 to 2.2-29 ($\sigma/(\lambda - \lambda^{-2})$ in uniaxial tension or compression, and τ/γ in simple shear) against the invariant $I_1 - 3$ gave a single curve for data in these three deformation modes. This is possible when the two following conditions are satisfied:
(a) W is a function of I_1 and not a significant function of I_2. This can be alternatively expressed by saying that $\partial W/\partial I_1$ is much larger than $\partial W/\partial I_2$.
(b) $\partial W/\partial I_1$ is independent of I_2.

These two conditions are not generally satisfied for unfilled elastomers as both $\partial W/\partial I_1$ and $\partial W/\partial I_2$ vary appreciably with I_1 and I_2 at small strains.[20] But at larger strains $\partial W/\partial I_1$ becomes relatively larger than $\partial W/\partial I_2$. In practice, $\partial W/\partial I_2$ for filled elastomers is not only smaller than $\partial W/\partial I_1$, as it would be expected from the strain-amplification effect[31], but is also numerically close to zero[20, 21, 22]. Taken together, the above suggests that assumptions (a) and (b) may well prove valid enough in practice, with the exception of low strains, to allow the use of a strain energy function which depends only on I_1. This idea has been further developed at Queen Mary and Westfield College by Davies *et al*[23], to produce a simple function, which predicts the behaviour of carbon black filled elastomers from small strains to at least 100% strain.

They argued that if assumptions (a) and (b) were true for strains up to 100% in shear, and as the reduced stress in simple shear was equal to τ/γ and E_S was the chord shear modulus, then

$$\frac{\tau}{\gamma} = 2\ \partial W/\partial I_1 \tag{2.2-36}$$

$$\text{or } E_s = 2\ \partial W/\partial I_1 \tag{2.2-37}$$

with $(I_1 - 3) = \gamma^2$. From close examination of published results of the MRPRA Natural Rubber engineering data sheets[24], it appears that the chord modulus strain dependence could, to a fair approximation, be represented, over the published strain range (1-100 %), by a power law. This was also observed by Stacer *et al*[25] from results on highly filled materials over a more restricted range. Thus,

$$E_s = A\gamma^{-\varphi} \tag{2.2-38}$$

where A and φ are constants for a given elastomer formulation. Combining Equations 2.2-37 and 2.2-38 and then integrating the results produced:

$$W = \frac{A}{2(1-\varphi/2)}(I_1 - 3)^{(1-\varphi/2)}. \tag{2.2-39}$$

This is a simple two constant strain energy function, which while derived for simple shear should be generally applicable. It could characterise the stress-strain behaviour of most filled elastomers in the strain range of 1-100 %, the range of interest for most engineering applications. But in order to represent the data for all carbon black contents over the whole of the strain range studied (up to 100 %) and to retain the assumption that W is a function of I_1 only, an additive term $A(I_1 - 3)^2$ was included in Equation 2.2-39. If a fitting of the very small strain behaviour was desired, one extra term C could be incorporated into Equation 2.2-39 to yield:

$$W = \frac{A}{2(1-\varphi/2)}(I_1 - 3 + C^2)^{(1-\varphi/2)} + \Lambda(I_1 - 3)^2 \qquad (2.2\text{-}40)$$

giving:

$$dW/dI_1 = \frac{A}{2}(I_1 - 3 + C^2)^{-\varphi/2} + 2\Lambda(I_1 - 3). \qquad (2.2\text{-}41)$$

C gave a finite value of the modulus at zero strain which is necessary for use in finite element programmes. C was related to the small strain modulus by:

$$\left(\frac{\tau}{\gamma}\right)_{\gamma \to 0} = AC^{-\varphi} \qquad (2.2\text{-}42)$$

It has been demonstrated[23] that this function (Equation 2.2-40) works well in predicting stress-strain behaviour in tension, simple shear, pure shear and compression. Figure 2.2-6 shows firstly the validity of the assumptions (a) and (b) as the values of the reduced stresses for four different deformation modes sit almost on the same curve when plotted as a function of $I_1 - 3$, which is a measure of the strain in the specimen. Secondly, Figure 2.2-6 shows that the function represented by Equation 2.2-40 fits all data over the whole strain range.

2.2.3.2 Alternative forms of representation

Other empirical relationships for W have been reported[26, 27, 28]. These diverge from the Rivlin type of relationship in that some discard the principle that the strain invariants I_1 and I_2 are even-powered functions of the extension ratios and some are written in terms of strains or extension ratios rather than in terms of strain invariants.

For incompressible elastomers Ogden[27] expresses W in the form of a series:

$$W = \sum_n \frac{\mu_n}{\eta_n}\left[(\lambda_1)^{\eta_n} + (\lambda_2)^{\eta_n} + (\lambda_3)^{\eta_n} - 3\right] \qquad (2.2\text{-}43)$$

in which the μ_n are constants and the η_n are not necessarily integers, and may be either positive or negative. This representation includes the statistical theory ($\eta_1 = 2$) and the Mooney equation ($\eta_1 = 2, \eta_2 = -2$), as special cases. Ogden[27] showed that a three-term expression is required to represent tension, pure shear and equi-biaxial extension for an unfilled elastomer, containing six adjustable parameters.

The degree of agreement with experiment is quite satisfactory for unfilled elastomers. Ogden's formulation has the merit of mathematical simplicity, although the magnitudes of a large number of independent constants have to be determined, because all the terms in the equation are of identical form. According to Rivlin and Sawyers[29] the Ogden model is a special case of the Rivlin strain energy function and Treloar[3] affirmed that the two formulations are equivalent and that the choice was simply a question of convenience.

The choice of an *e.s.e.d.* function as input data for fracture mechanics based finite element analysis requires that the chosen function describes reasonably the whole range of strains especially the large strain behaviour with the upturn in the stress-strain behaviour due to the finite extensibility of the chains. It would give some confidence in the use of a model if the parameters had some molecular/physical significance. In this respect, Gent[30] for example, suggested a new *e.s.e.d.* function which may be written as:

$$W = -C_{10}(I_m - 3)\ln\left[1 - \frac{(I_1 - 3)}{(I_m - 3)}\right] \qquad (2.2\text{-}44)$$

where I_m is the limiting value of I_1 corresponding to the deformation when the network is fully stretched. At small strains, this equation reduces to Equation 2.2-12 from the statistical theory where C_{10} is equal to the shear modulus E_s or $N_v kT$. At large strains, this function shows as expected the upturn in the stress-strain plot. This *e.s.e.d.* function is claimed to have the advantage that it reduces the description of the stress-strain behaviour of an elastomer to two parameters having a clear physical meaning. Unfortunately, as far as the present author is aware, this function has not been tested on filled elastomers nor in different modes of loading.

Other phenomenological models have attempted to describe the behaviour at large strains by taking a considerable number of terms in the Rivlin or Ogden power series. But this leads to unstable functions predicting physically unrealistic behaviour under conditions outside the range of the experimental data. Using the work of Gregory[19], Yeoh[15] proposed to take only the first three terms of the Rivlin series obtaining the following cubic function in $I_1 - 3$:

$$W = C_{10}(I_1 - 3) + C_{20}(I_1 - 3)^2 + C_{30}(I_1 - 3)^3 \qquad (2.2\text{-}45)$$

and reported good ability to predict multi-axial data, including comparison with the published biaxial data of James and Green[18] for filled elastomers. Conceptually, this proposed function is a model with a shear modulus varying as a second-degree polynomial in $I_1 - 3$. The variation of the shear modulus in the case of carbon black elastomers is a fall of the modulus with increasing strain and a rise at large deformations due to finite extensibility. This characteristic behaviour can be modelled if C_{20} is negative while C_{10} and C_{30} are positive. In addition to its good prediction abilities, robustness and ease of determination, this function can be input readily into commercial FEA software and make it very attractive for use in fracture mechanics analysis.

It could be concluded from this section that it is legitimate to assume for carbon black filled elastomers that the *e.s.e.d.* function is only a function of I_1. Such functions have been shown to predict uniaxial or multi-axial data with a good accuracy. This leads to great simplifications in the mathematical form of these functions and for their derivations from stress-strain experimental data. From this consideration, the review shows that there is not a unique solution. The choice of a function will depend on the particular situation. The best strain energy function for the prediction of stiffness of an engineering component will be different from the best one to be used for a fracture mechanics application. The first one will generally need to be accurate at small and moderate strains (<100%) unlike the second one which would be required to predict moderate and large strains accurately. But an example of a simple *e.s.e.d.* function for use in a finite element based fracture mechanics study appears to be the function proposed by Yeoh[15] in Equation 2.2-45.

2.2.4 Non-elastic behaviour and characterisation of filled elastomers

The previous sections have demonstrated that to an adequate approximation the mechanical behaviour of a filled elastomer can be described utilising an appropriate *e.s.e.d.* function. This is certainly true for simple modes of deformation and for first cycle loading. In reality, carbon black filled elastomers exhibit significant viscous behaviour which becomes increasingly apparent on second and subsequent cycles of loading, and as the deformation modes become more complex. This section attempts to address the effect of this behaviour on the elastic strain energy in a deformed component, particularly with respect to subsequent sections on strength and crack growth.

2.2.4.1 Description and origins of the non-elastic behaviour

In filled vulcanised elastomers, part of the applied energy spent in deforming them is dissipated in overcoming viscous resistance to motion of the molecular chains (visco-elastic behaviour) and in breaking or modifying the structure associated with the molecular or filler network. In unfilled vulcanised elastomers, the dissipation mechanisms associated with the molecular structure, mainly visco-elastic losses, are not generally significant in terms of the deviation from elastic behaviour. In the case of filled elastomers, the energy dissipations are much more significant. Carbon black causes a large increase in the viscosity due to hydrodynamic effects (displacement of large particles through the elastomer matrix). The breakdown and the reformation of carbon particle aggregates is also believed to be one of the causes of the increased energy dissipation. The latter mechanism[32] is believed to be limited to low stresses. All these energy losses are illustrated by the presence of significant deformation hysteresis where the path followed on loading and unloading are different on a stress-strain curve (Figure 2.2-7).

Similar mechanisms are believed to be involved in the well-known cyclic stress-softening effect, the Mullins' effect[31], which occurs when an elastomer is cyclically deformed. When virgin samples of carbon black-filled elastomers are strained and then allowed to retract, subsequent extensions to the same strain require

a lower force as showed in Figure 2.2-8. The greatest softening occurs during the first cycle, but the effect continues at a decreasing rate in subsequent cycles.

The hysteresis and the stress-softening phenomena have been subjected to many investigations[31, 32, 33]. As they occur in both unfilled and filled elastomers to an approximately similar extent for the same stress, Harwood *et al*[34] suggested that the two phenomena were mainly due to deformation of the elastomer phase and not directly due to carbon black. Possible sources included breaking and remaking of cross-links during extension, residual local orientation of network chains persisting after recovery and breaking of network chains. They showed that the hysteresis and the stress-softening in a filled elastomer could be related to that of the unfilled one by the use of a strain-amplification factor, which was the ratio of the average strain in the elastomer phase to the measured overall strain. This scaling factor was introduced because the presence of rigid filler particles increased dramatically the local strain in the elastomer matrix. As a conclusion, the apparent differences between the stress-strain hysteresis loops of unfilled and filled elastomers was said to be due to an increase in the effective strain in the elastomer phase resulting from the presence of the filler.

Another molecular mechanism responsible for the non-elastic behaviour, in the form of an increased high strain hysteresis is strain-induced crystallisation which occurs particularly in natural rubber. At large extensions, the elastomer chains orientate and align resulting in the formation of crystallites. This crystallisation is an additional energy dissipation process which is observed as a more pronounced upturn in the stress-strain curve at large strains when compared with that of a non-strain crystallising elastomer.

2.2.4.2 Effect of viscous behaviour on e.s.e.d. functions

On first cycle loading the viscous behaviour affects both the loading and unloading curves (Figure 2.2-7). The strain energy functions referred to earlier are usually derived by fitting the first such loading curve. This methodology almost certainly overestimates the elastic strain energy in a specimen. A number of attempts have been made to obtain an approximate solution to the problem. Kawabata *et al*[35] used an average of loading and unloading curves. Gent and Kim[36] suggested that the

area under the unloading curve should be used to calculate the elastic strain energy. Furthermore, they calculated that an overestimation ranging from 35-130% depending on the imposed strain, of the elastic strain energy occurred in carbon black filled NR and SBR elastomers if the loading curve was used. The correct solution is almost certainly to use some average of the two curves, but this averaging process will depend on both the material and the test conditions. It is hence currently best to use a particular well-defined solution, for a particular problem.

The problem described above is compounded as the hysteresis loop changes systematically on each cycle due to stress softening. Other authors[37] have attempted to solve this problem by mathematically representing the stress-softening phenomenon with a strain energy function of the following form:

$$W_n = f(n)\ W_1 \qquad (2.2\text{-}46)$$

where W_1 and W_n are the *e.s.e.d.* functions on the first and n^{th} number of cycles, and $f(n)$ is a decreasing function of n. This model developed for a constant maximum cyclic strain condition is obviously limited to this particular test condition and can not be applied as a general case. In a general situation, the strain energy function depends not only on the previous number of cycles that the specimen has endured but on the whole strain amplitude history.

Because the stress-strain curve reaches almost a steady state after a finite number of cycles, other approaches have been proposed. The strain energy function can be derived after softening the elastomer for a given number of cycles in an attempt to stabilise its stress-strain behaviour. This latter method is usually called conditioning. An example of such a method was proposed by Yeoh[15]. It consists of cycling the test piece from zero strain to a selected strain for five cycles and takes the average of the sixth to the eighth cycle as the representative stress-strain behaviour. Chow and Cundiff[38] proposed to repeat the same procedure from small deformation levels to progressively larger deformation levels. At each deformation level, the test piece was then cycled from zero strain to this deformation level for eight cycles and the average of the stress strain maxima in the sixth to the eighth loading cycle was taken. This average stress gives a single point on the stress-strain curve. Collectively,

the recorded averages of stress strain maxima at each deformation level defined a quasi-equilibrium stress versus strain curve for the material.

Such procedures will clearly work quite well for a component for which the approach represents approximately its only loading cycles. However, it clearly cannot have a general applicability for components loaded in a more complex manner. Because of these difficulties, it is clearly best during cyclic crack growth studies to attempt to measure directly the elastic stored energy released in a specimen as a crack grows.

2.2.5 Conclusions

It has been shown that the stress-strain behaviour of filled elastomers can be reasonably represented by an *e.s.e.d.* function which only depends on the strain invariant I_1. Section 2.3.3.2 proposed functions of that type, amongst them the cubic function of Yeoh[15] and the Davies *et al*[23] function. It has been shown[19, 23] that this type of function only depending on I_1 predicts well the behaviour of filled elastomers under uniaxial, equi-biaxial and in some cases in general bi-axial loading. But there is no evidence that these models would successfully predict the behaviour in still more complex situations. One of the objectives of this work will hence be to examine the applicability of the elastic strain energy approach to such situations.

The above is of course a first cycle approach and the review illustrates that few attempts and no real solutions exist to predict the elastic strain energy in a component after many loading cycles, the situation encountered for anti-vibration components and in the fatigue crack growth tests to be performed in this study. It is suggested that this is best done directly either experimentally or by modelling a test-piece or component, with or without a crack of a given length.

2.3 Strength of elastomers

The study of cyclic crack growth in filled elastomers under non-simple loading is the main concern of this thesis. In section 2.2, methods for measuring and predicting the elastic strain energy in a specimen or component were discussed as it is

this which drives crack growth. In this section the process of crack growth is discussed under conditions of constant force, or strain rate, to be followed in a subsequent section 2.4, by a discussion of cyclically loaded crack growth. In this section, fracture mechanics approaches are discussed together with the concept of tearing energy. Materials parameters which increase the tearing energy necessary to drive a crack and hence increase strength are discussed.

2.3.1 Possible approaches for the fracture mechanics of elastomers

Three fracture mechanics parameters namely the energy release rate, the stress intensity factor and the *J*-integral are utilised to describe crack growth. They are briefly described here and their relevance to crack growth in elastomers which are highly non-linear elastic materials is stated.

The first one, a critical stress theory states that when a sample with a crack in it is subjected to a stress, the material in the region of the crack tip is under a larger amplified stress. When the stress at the crack tip exceeds a certain critical value the material at the crack tip will rupture and the crack grow through the material. Analysis of the stress field in the neighbourhood of a crack was mathematically solved for ideal linear elastic materials by Westergaard[39]. The concept is based on the stress intensity factor (K), which is a measure of the relative magnitude of the elastic stress field in the crack tip region. K depends on the applied stress, the dimensions of the component and the crack length. A crack will grow if a critical stress intensity factor K_c is exceeded. In contrast to K, K_c is a purported to be a materials parameter called the fracture toughness which depends on the temperature, the rate of loading and the modes of loading. When plastic flow or visco-elastic behaviour occurs, the stress distribution in the crack tip region must be determined from non-linear relationships. The mathematical solutions are generally intractable except for very special cases. The more recent tendency is the elaboration of a fracture mechanics criterion for non-linear elastic bodies based on either the *J*-integral theory proposed by Rice[40] or an extension of the Griffith[41] energy balance approach.

Historically, the energy balance approach was the first successful attempt to relate the fracture behaviour of a solid material subjected to a far field applied stress. The basic idea in the Griffith fracture theory is that there is a driving force for crack

extension (that results from the release of potential energy in the body) working against an inherent resistance to crack growth. The resistance to crack growth, in glass at least, is in part associated with the necessity to supply surface energy for the newly formed surfaces. A crack of length c will spread by an amount dc at a certain overall deformation of the test-piece, if, and only if, the energy W stored elastically in the test-piece is thereby decreased by an amount -dW which is greater than the increase of surface free-energy required to form the new surfaces. If the area of new surface, formed by an increase in crack length dc, is da, then Griffith's criterion may be written

$$-\left(\frac{\partial W}{\partial c}\right)_l \geq S_t\left(\frac{\partial a}{\partial c}\right)_l \qquad (2.3\text{-}1)$$

where S_t is the surface free-energy per unit area of the material (or surface tension). The suffix l indicates that the differentiation is carried out under conditions of constant displacement. For a crack propagating through a thin sheet, of thickness t, the criterion becomes

$$-\left(\frac{\partial W}{\partial c}\right)_l \geq 2S_t t \qquad (2.3\text{-}2)$$

The quantity $\frac{1}{t}\left(\frac{\partial W}{\partial c}\right)_l$ is called the energy release rate and is generally named G. For elastomers, Rivlin and Thomas[42] recognised that the elastic strain energy changes given up to support the crack extension need to be transferred into forms other than the increase of surface free-energy as a significant volume of material is irreversibly relaxed. These energy changes should be proportional to the amount of crack growth and hence, they would be related to the crack tip deformation state and be independent of the shape of the test specimen and the manner in which it is loaded. The energy required for unit crack growth in a sheet of unit thickness could therefore be regarded as a characteristic of the tear process. The criterion is similar to Griffith's criterion and was written as follows:

$$-\frac{1}{t}\left(\frac{\partial W}{\partial c}\right)_l \geq T \qquad (2.3\text{-}3)$$

where the symbol T denotes the characteristic tearing energy which is not anymore interpreted as a surface free-energy. Rivlin and Thomas[42] examined a number of different types of test piece in order to verify their hypothesis. This will be described in the next section. They found that T was a material property that was independent of the choice of the particular test piece geometry used.

The J-integral theory characterises the stress and the strain field at the crack tip for 2-D non-linear elastic materials under small displacement gradient analyses. The definition of the J-integral is as follows:

$$J = \int_{\Gamma} W \mathrm{d}y - \int_{\Gamma} \boldsymbol{T}.\frac{\partial \boldsymbol{u}}{\partial x}\mathrm{d}s \qquad (2.3\text{-}4)$$

where Γ is a curve that surrounds the crack-tip, $\boldsymbol{T}$ is the traction vector defined as $T_i = \sigma_{ij} n_j$, n_j being the component of $\boldsymbol{n}$ the outward normal along Γ, $\boldsymbol{u}$ is the displacement vector, W is the *e.s.e.d.* function and y is the direction taken normal to the crack line (Figure 2.3-1). For perfectly elastic not necessarily linear elastic materials, J is path-independent . Therefore it will have the same magnitude for all choices of Γ. Rice also demonstrated that J could be interpreted in terms of energy release rate and showed that[43]:

$$J = G = -\frac{1}{t}\left(\frac{\partial W}{\partial c}\right)_l \qquad (2.3\text{-}5)$$

Subsequently, Rice's theory has been extended to large displacement gradients[44] found in highly extensible materials. Hence J and T are both defined as the energy release rate with respect to crack length:

$$J = T = -\frac{1}{t}\left(\frac{\partial W}{\partial c}\right)_l \qquad (2.3\text{-}6)$$

In conclusion, an energy release rate formulation, introduced as the tearing energy by Rivlin and Thomas[42] for highly extensible materials appears to be the most appropriate approach to study the crack growth of elastomers. Although the *J*-integral is equivalent to the tearing energy, its mathematically more complex formulation makes it more difficult to estimate unless numerical methods are used.

2.3.2 Tearing energy calculations and limitations

As explained in the previous section, the idea behind the tearing energy approach is that for highly non-linear elastic materials, the energy dissipation due to tearing (crack growth) would be dependent only on the physical properties of the material and not on the overall geometry of the test-piece. The mechanism by which this elastic strain energy is lost, by sudden relaxation of small regions of the highly-strained elastomer at the tip of the crack when tearing takes place is a very localised process. The magnitude of the energy dissipated depends on the local strain and the local physical properties of the elastomer. The tearing energy should therefore provide a true measure of the tear resistance independent of the geometry of the test-piece and of the way the forces are applied.

Rivlin and Thomas[42] used two test-pieces of different geometries which gave global deformation states known as simple extension and pure shear. These are shown in Figures 2.3-2 (a) and (b) respectively. These test-pieces enabled them to calculate the strain energy release rate directly from measured applied forces and strains. In the case of the simple-extension test-piece, commonly known as a "trouser" test-piece, its tearing energy is given by

$$T = \frac{2f\lambda}{t} - wW \qquad (2.3\text{-}7)$$

where f is the applied tearing force, λ is the extension ratio in each leg, t is the original thickness in the unstrained state, w is the total width of the test-piece and W is

the strain energy density in the legs of the test piece that are in simple extension. In the case of a pure shear test-piece, its tearing energy is given by

$$T = WL_0 \tag{2.3-8}$$

where W is the strain energy density in that region of the test piece which is in a state of pure shear, and L_0 is the unstrained distance between the two parallel clamps.

When the crack growth results were expressed in terms of tearing energies, similar values were obtained from both types of test-piece , indicating that the tearing energy gives a quantitative measure of a material property. Later investigations using other test-pieces, such as a split tear test-piece (Figure 2.3-2 (c))[45] and an angled test-piece (Figure 2.3-2 (d)) [46] have confirmed the earlier findings. For the split tear test piece, its tearing energy is given by

$$T = \frac{F_A \lambda_A \sin\psi}{t} + \frac{F_B(\lambda_A \cos\psi - \lambda_B)}{t} - w(W_A - W_B) \tag{2.3-9}$$

where ψ is the angle of splitting, λ_A, λ_B and W_A, W_B are the extension ratios and stored energy densities in regions A and B respectively, $\tan\psi = F_A/F_B$, and w is the width. In the case of the angled test-piece, its tearing energy is given by the relation

$$T = \frac{2f}{t}\sin\alpha \tag{2.3-10}$$

where f and t have the same meaning as in Equation 2.3-7 and α is the angle between the clamps.

Figure 2.3-3 shows that the four test-pieces of widely differing geometries all give similar relationships between tearing energy and tearing rate[46]. This confirmed that tearing energy gave a true quantitative measure of tear resistance. The magnitude of the tearing energies they obtained ranged from 1.0 $kJ.m^{-2}$ to 100 $kJ.m^{-2}$. These values exceed substantially the surface energy, which is about 0.1 $J.m^{-2}$ for many materials. This clearly implied that energy losses or hysteresis play a major

contribution to the tearing process of an elastomer, and are probably the major factor in determining its strength.

Thomas[47] made further progress by relating the tearing energy to the strain distribution around the tip of a crack. Based on a semi-circular crack tip model for an elastomer, he showed that the tearing energy T, is approximately related to the diameter of a crack tip, d, by the relationship below

$$T = dW \tag{2.3-11}$$

where W is the elastic stored energy per unit volume at the crack tip. If a test-piece is taken to break, the relationship becomes

$$T = dW_b \tag{2.3-12}$$

where W_b denotes the work to break per unit volume of elastomer. Thomas verified this relationship experimentally by measuring the tearing energy of test-pieces having model tips of diameter in the range of 1 mm to 3 mm. He found that the ratio T/d was substantially constant. Furthermore, it agreed well with the work to break in tensile-tests carries out independently on different elastomers of various strengths.

Lake and Thomas[48] used the Equation 2.3-11 to predict the threshold tearing energy, T_0. They defined T_0 as the minimum tearing energy at which mechanical crack growth can occur. At tearing energies less than T_0 crack growth is attributable solely to chemical attack by ozone. This is normally very much slower than tearing above T_0[49]. All elastomers whose molecular backbones contain carbon-carbon double bonds are susceptible to ozone attack and this causes cracking. Since ozone crack growth is chemical in origin, the rate of growth is independent of the applied tearing energy. Lake and Thomas[48] found that the magnitude of T_0 was more-or-less similar for a wide range of elastomers, including both crystallising and non-crystallising elastomers which differ significantly in other strength properties such as tensile strength and tear strength. The magnitude of T_0 for a range of polymers is usually about 0.05 $kJ.m^{-2}$, suggesting that it may be a basic parameter relating to the types of molecules which comprise the material. Lake and Thomas[48] calculated T_0 from the molecular structure of an elastomer and the strength of primary chemical bonds. The

value of T_0 estimated from this theory is about 25 J.m^{-2}, about half the value obtained experimentally. In view of the uncertainties in the approximations and assumptions of the theory, the agreement between theory and experiment is regarded remarkably good. To determine T_0 experimentally, the tear measurements have to be carried out using swollen elastomers at a slow rate of tearing and at high temperature to eliminate hysteresis. This is known as the threshold conditions. In the case of carbon black filled elastomers, Bhoumick *et al*[50] found T_0 to be around 200 J.m^{-2}, which indicates that, the minimum tearing energy T_0 for mechanical crack growth in carbon black-filled elastomers is about three to four times higher than that for unfilled materials. They attributed this to the increased energy dissipation due to the detachment of adhering polymer molecules from particles of carbon black at forces somewhat below those which cause main-chain fracture.

It is important to recognise that the tearing energy T is not a constant value for a particular material; it depends strongly on both the temperature and rate of tear, which can also be considered as the rate at which material is deformed to rupture at the tear tip. This dependency will be discussed later in the section about reinforcing mechanisms. Tsunoda *et al*[51] showed that the thickness of a test-piece can have an effect on the tear behaviour and thought that these effects related to the scale of behaviour at the crack tip. The roughness developed on the crack surface is of the order of a few tenths of a millimetre in scale. If the test piece thickness is also of this order, then it might be expected that the scale of the roughness, and hence the crack growth behaviour, would be influenced by the thickness. Results for SBR for two thicknesses are shown in Figure 2.3-4. In the more rapid (smooth-) tear region no effect of thickness is found, but a significant effect is seen in the rough and stick-slip regions. This is consistent with expectations, as the smooth tear region presumably results from as sharp a crack tip as possible, but the development of the full potential roughness at lower tearing energies is inhibited by the thickness limitation in the rough and stick-slip tear regions.

2.3.3 Energy dissipation processes

The dissipation of energy internally could be regarded in one sense as a serious disadvantage for elastomers. Under repeated deformation, the heat evolved

may cause rapid thermal deterioration. In another sense however energy dissipation is responsible for the improved resistance to a wide variety of fracture processes: tensile break, tearing, fatigue, and abrasion.

Energy dissipation affects the fracture process through two different mechanisms. The first corresponds to the energy dissipation in the bulk of the material and reduces the elastic energy available to drive the crack. The second mechanism corresponds to the energy dissipation in the crack tip region at large strains. Both make crack growth more difficult. The details of these energy dissipative processes are reviewed in this section and the implications of the two different mechanisms are discussed.

2.3.3.1 Viscous strengthening

It is difficult to separate the effect of viscous energy losses in either the bulk of a loaded specimen or at the crack tip on the elastic tearing energy necessary to grow a crack. The viscous behaviour in the bulk increases the applied force necessary to obtain a given elastic strain energy available to drive a crack. Viscous energy dissipation at large strains around the crack tip also increases the apparent tearing energy necessary to drive a crack. In non-crystallisable elastomers, it is both these effects which give the observed temperature and rate dependence of crack growth as illustrated in Figure 2.3-5 for an unfilled SBR. This data is seen transformed[52] using the William, Landel and Ferry[53] (WLF) relationships into a single master curve in Figure 2.3-6. The WLF relationship is:

$$\ln\ a_T = -\frac{C_1(\Theta - \Theta_s)}{C_2 + (\Theta - \Theta_s)} \qquad (2.3\text{-}13)$$

where a_T is the shift factor, Θ_s is the reference temperature to which the other isotherms are shifted and C_1 and C_2 are experimental constants. The shift factor a_T for the tearing energies was found to be similar but slightly higher than that for the measured internal viscosities. This is however good evidence that the rate and temperature dependence of the tearing energy arises principally from that for the internal viscosity.

The addition of carbon black to SBR causes a large increase in tearing energy and strength to occur. This effect is probably mostly due to crack tip effects and crack deviation is discussed in later sections. However if the deviation is prevented by using a constrained trouser test[54] then the increase in tearing energy is still present but much smaller. Furthermore the WLF equation can still be used to represent the temperature dependence[54, 55] which suggests that the effect of carbon black on the bulk visco-elastic behaviour is significant.

2.3.3.2 Energy dissipations in the crack tip region: high strain hysteresis, strain-induced crystallisation and crack tip blunting.

(a) High strain hysteresis

The high strain hysteresis is the hysteresis or energy loss associated with a strain cycle up to near the breaking point of the elastomer. Andrews[56] observed and explained the modification of the stress field around the crack tip due to this high strain hysteresis. He showed that the stress at the tip of a propagating crack is much less than the stress at the tip immediately prior to propagation, and the greater the hysteresis of the elastomer, the larger the reduction in stress. From these observations, Andrews arrived at the conclusion that the high rupture resistance of material exhibiting pronounced high strain hysteresis such as a strain-crystallising elastomer or carbon black reinforced elastomers can be attributed to a reduction of the local stress at the tip of the propagating crack.

(b) Strain induced crystallisation

Strain-crystallisation is another energy dissipation process, characteristic of some elastomers notably including NR. Strain-induced crystallinity in polymers is anisotropic and consists of fibrillar structures running in the direction of strain. This contrasts with the spherulite structure found in the absence of strain, for most crystallising polymers. With semi-crystalline polymers, as the strain increases the spherulite microstructures gradually give way to a fibrillar texture. In case of strain-crystallisable elastomers, most notably NR, the material is purely amorphous in the unstrained state. The degree of crystallinity increases[57] with increasing strain and for NR reaches a maximum value of around 30%. The source of strengthening is

substantial energy dissipation which accompanies strain-crystallisation more preferentially in the highly deformed crack tip region than in the bulk of the material. Strain-crystallising elastomers are consequently much stronger than amorphous ones resulting from the increased high strain hysteresis in the crack tip region. But as well as increasing energy dissipation, strain-crystallisation probably plays a major factor in contributing to crack deviation, the major reinforcement mechanism in elastomers.

Over wide ranges, the catastrophic tearing energy is insensitive to rate and temperature for a strain-crystallising elastomer, such as NR (Figure 2.3-7). It appears that the effects of crystallisation, which can induce very substantial hysteresis at high strains, outweigh the visco-elastic effects in such materials. This substantial hysteresis at high strains could be a probable explanation of the time-independent crack growth observed in crystallisable elastomers and would also explain the observed stick-slip and knotty behaviour (Figure 2.3-8 (b) and (c)). Upon an increment of crack growth, the drop in tearing energy is sufficient to stop further crack growth. The crack will only break ahead again when the critical tearing value is reached when the force has increased again. This behaviour is in contrast to the "steady", time dependent smooth tearing of non-crystallising elastomers.

(c) Crack tip blunting or knotty-tearing

The reinforcing mechanisms referred to previously result from two different energy dissipation processes. But the major form of reinforcement is due to the occurrence of a sufficient strength anisotropy at the crack tip resulting in crack deviation. This phenomenon also called crack tip blunting or knotty-tearing is believed to be promoted by strain-induced crystallisation or the presence of carbon black.

The form of tearing termed "knotty" tearing consists of a discontinuous stick-slip process, in which the tear develops laterally or even circles around under increasing force until a new tear breaks ahead and the tear force drops abruptly. The process then repeats itself. An example is shown in Figure 2.3-8 (c) together with the three other types of tear[58] with their respective force and tear patterns. Steady tearing results in macroscopic surface roughness, small deviations from the tear path produce stick-slip tear and longer deviations give knotty-tearing. In this mode, the tear

deviates under increasing force, until a new tear breaks ahead and the tear force drops abruptly.

The reinforcing effect is restricted to a limited range of tear rates and temperatures, being virtually absent outside this range. The region where reinforcement occurs[59, 60] depends on the particular filler and elastomer employed.

When the tear is prevented by closely spaced metal guides from deviating from a linear path (Figure 2.3-9) or is made to propagate smoothly by holding the test sheet extended in the direction of tearing[36], the tear force is much smaller, being about two or three times that for the corresponding unfilled material. This suggests that knotty-tearing appears to be the major form of tear reinforcement.

The possible processes put forward to explain the deviation of the tear from a straight path, or blunting of the tip are the following ones:

(1) The frozen stress mechanism. Andrews[61] pointed to the influence of hysteresis around an advancing crack caused by strain-crystallisation. Andrews[61] obtained direct evidence of this process by observing cracks in transparent samples during a complete extension-retraction cycle when the crack tip was viewed microscopically in polarised light. The observed optical anisotropy suggests that crack would deviate from a direct path and follow the curve of maximum stress lying off axis. The absence, under many circumstances, of time-dependent crack growth in crystallising elastomers perhaps reflects an extreme effect of the crack deviation.

(2) Anisotropic strength at the tip of the crack. Its existence and major role in strengthening[62, 63, 64] has been demonstrated recently. Anisotropic strength is caused by chain alignment as well as mechanico-chemical chain scission. Chain alignment causes anisotropy at the crack tip[65]. If sufficient chain alignment develops to form a "fibrous-type" structure with "interlaminar" weaknesses, then the crack deviates by propagating between "laminae". Contrarily, if sufficient (irreversible) chain rupture occurs (prior to reaching a critical state of alignment), then the micro-crack extends across the sample in a direction perpendicular to the load. Non-catastrophic energy dissipation in the damage zone is essential to attaining sufficient anisotropy for crack deviation. Thus, there is a competition in the damage zone, catastrophic chain scission tending to allow the crack to grow straight across the sample, and non-catastrophic energy dissipation, which increases load uniformity among the chains in the damage zone, allowing the development of high anisotropy

and which can result in crack deviation. Also according to Medalia[66] and Greensmith[67], the marked strength anisotropy can be attributed to a high degree of orientation of carbon black particles or agglomerates at the crack tip. In this case, the effect of carbon black type and concentration on knotty-tearing found by Greensmith[67] and De and Gent[60] support this hypothesis. Compounds with the more reinforcing carbon black show higher tearing energy as it is believed that a good bonding between the filler and the elastomer matrix favours the alignment of the carbon black aggregates perpendicular to the crack path. There is also a pronounced effect of cross-link concentrations which De and Gent[60] explained as follows; "When the cross-link concentration is low, the stresses set up at the tear tip may be too low to induce sufficient alignment of carbon black particles there. On the other hand, when the cross-link concentration is excessively high, breaking strains for networks of short chains may be too low to induce the degree of anisotropy necessary for knotty-tearing. It is possible that only a combination of high stress and high strain at the crack tip will produce the required degree of strength anisotropy." They also reaffirmed that strain induced crystallisation makes no additional contribution to the extent of the strength anisotropy.

(3) Hydrostatic component of the tensile stress. Another factor that may contribute to tip blunting is the hydrostatic component of the tensile stress, which may be sufficient to cause cavitation. Various microscopical observations[68] have suggested that secondary fractures can occur at some distance from the main fracture "plane". Such fractures may simply originate at nearby flaws under the high stresses involved but may reflect cavitation processes. It is known that cavitation can occur in elastomers and that the required hydrostatic tension is of the order of the Young's modulus[69]; it appears likely that the high stresses at a crack tip will be sufficient to reduce this value locally.

(4) Mechanical hysteresis. In addition to affecting tear strength through mechanical hysteresis, the visco-elastic behaviour may also have an effect through crack blunting. Comparison of the results for tearing with constrained[54] or unconstrained[55] crack tips in non-crystallising elastomers suggests (1) that the (WLF) transform proposed by Williams, Landel, and Ferry[53]can be used to interrelate rate and temperature effects for tearing provided the tip diameter remains constant (or below a certain level (about 0.1 mm)), and (2) that departures from the normal

transform occur when the tip diameter is allowed to increase. The fact that the results in the latter case can be superimposed by a different transform suggests that the tip diameter varies systematically with variations in visco-elastic behaviour.

2.4 Fatigue crack growth

The tearing energy approach, discussed in the previous section has proved to be successful in treating the fracture of elastomers. But the tearing tests presented previously only estimate the strength of an elastomer under a single loading cycle producing rapid crack growth. For the majority of elastomeric components, failure is not usually due to a large static load resulting in catastrophic failure but to much smaller cyclic fatigue loads, resulting in small-scale tearing. The study of the fatigue crack growth of a material should constitute the most appropriate approach in an attempt to predict the service life of component. A review of the work on fatigue crack growth is presented here.

2.4.1 Fatigue crack initiation

The initiation of mechanical fatigue cracks in elastomers is due to the presence of inhomogeneities, or irregularities which result in highly localised stress concentrations on loading. The origins of these inhomogeneities are diverse. Compounded elastomers contain various additives such as curatives, process aids and fillers. They therefore exhibit various degrees of inhomogeneity on a microscopic scale, probably of the order of 10 μm in size, depending on the specific additives used. An elastomer without these additives may also contain gel particles or microvoids. Another precursor to mechanical fatigue cracks are cracks initiated by ozone degradation at areas on the surface where tensile stresses are present. Improper design of elastomer compounds and abrupt change in the shape such as corners, holes, raised or indented letters on the surface can also act as stress raisers.

When examining fatigue fractured surfaces, three stages of fatigue failure[70] may be recorded: crack initiation, crack propagation, and a final rupture at a critical length of the crack. But generally, there is no sharp distinction between crack initiation and crack propagation regions. When an elastomer part without any obvious

crack is subjected to repeated stresses, a certain time passes before visible fatigue cracks appear. Whether this induction time should be part of a crack initiation process or part of a crack propagation process is often subject to debate. What matters in practice is how fast a crack of a certain size will propagate under certain loading conditions and crack initiation is a crack propagation process from an inherent flaw. With laboratory test pieces the random process of crack initiation from a natural flaw is obviated by requiring a pre-crack. This leads to a more reproducible test, since sensitivity to defects that are not inherent material properties is eliminated. This shifts the focus in fatigue analysis away from crack initiation onto fatigue crack propagation.

2.4.2 Crack growth behaviour

It was seen in the previous sections that the relationship between tearing energy and the tearing rate was a characteristic of a material independent of test-piece geometry. In case of fatigue crack growth, it is generally found that the extent of crack growth during each loading cycle is determined by the maximum tearing energy during that cycle (T). Measurement of crack growth rates under repeated loading using various test-piece geometries for an unfilled NR compound[71] showed that the crack growth rate was independent of the test-piece geometry and was dependent only on the magnitude of the applied tearing energy (Figure 2.4-1). Similar results for carbon black filled elastomers were obtained by Lake and Lindley[72]. The relationship $\mathrm{d}c/\mathrm{d}n = f(T)$, where c refers to the crack length and n to the number of cycles is hence a true strength property of the material. Figure 2.4-1 shows that over the range covered,

$$\mathrm{d}c/\mathrm{d}n = B_t T^{\beta} \qquad (2.4\text{–}1)$$

where B_t and β are constants. It is found experimentally that this approximately represents the behaviour of various elastomers over a useful, but limited, range of T values. For NR, β is often about 2, whereas for non-crystallising elastomers, such as

SBR it is typically about 4. These statements are usually true for both unfilled and filled compounds.

Figure 2.4-2 shows a plot of the measured crack growth rates for unfilled NR and SBR elastomers over a much wider range of tearing energy T[49]. It is possible to divide the plot into a number of regions characteristic of a given crack growth behaviour. The full lines represent empirical approximations to the results and are of the forms[49]:

Region 1

$$dc/dn = r_0 \qquad T<T_0 \qquad (2.4\text{-}2)$$

Region 2

$$dc/dn = A_t(T-T_0) + r_0 \qquad T_0<T<T_t \qquad (2.4\text{-}3)$$

Region 3

$$dc/dn = B_t T^{\beta} \qquad T_t<T<T_c \qquad (2.4\text{-}4)$$

Region 4

$$dc/dn = \infty \qquad T = T_c \qquad (2.4\text{-}5)$$

where r_0, A_t and B_t are growth rate constants, T_0 is the minimum tearing energy for mechanico-oxidative crack growth, T_t is a transition tearing energy at which the dependence of crack growth rate on T changes from a linear to a power law relationship, and T_c is the catastrophic tearing energy at which rupture occurs virtually instantaneously[42]. Division of the crack growth characteristic into distinct parts, 1 to 4, governed by the empirical equations 2.4-2 to 2.4-5 is however oversimplified. In practice, many materials follow more complex empirical relationships. In other cases, the power law may hold over a broad range from T_0 to T_c. However, two distinct mechanisms responsible for the growth of cracks or flaws have been identified. Below T_0, ozone scission is the prime mechanism and above, mechanico-oxidative crack growth predominates. As explained in the section dealing with tearing measurements, the physical interpretation of T_0 is the minimum tearing energy at which the stress at the tip crack reaches the breaking value for the elastomer. Experiments in *vaccuo* show that T_0 is primarily a mechanical property of a vulcanised elastomer, although its value is somewhat reduced by the presence of oxygen.

The slow (fatigue limit), intermediate (mechanico-oxidative) and rapid (high tearing energies) crack growth rate regions are examined in more details below.

(1) Mechanico-oxidative region

This region is called mechanico-oxidative because atmospheric oxygen is contributing to crack growth. It has been proposed that a stress-activated scission process leading to the breakage of the molecular chains in the neighbourhood of the crack tip contributes to crack growth[73]. The effect is akin to adding or enhancing a time dependent crack growth process. At low tearing energies this results in crack growth rates for NR being three times higher in air compared to vacuum[74] (Figure 2.4-3). However, at higher tearing energies, the effect of oxygen was seen to be frequency dependent. At high frequencies dc/dn was the same in air and vacuum as the influence of the time dependent crack growth process is minimal. At lower frequencies dc/dn was significantly higher in air as the time dependent crack growth process contributed significantly to the crack growth rate.

Gent and Hindi[75] investigated the effect of oxygen on the tear strength of various elastomers. Oxygen had a much bigger effect on SBR than on NR. At low tearing energies (T<1kJ.m^{-2}), the rate of crack growth for both elastomers was reduced by a factor of up to 10 in the absence of oxygen.

(2) High tearing energies

Figure 2.4-4[76] illustrates that the cyclic crack growth characteristics at high tearing energies are sometimes bi-functional. The behaviour can either follow what are described on Figure 2.4-4 as tensile failure or tear test. For both crystallising and non-crystallising elastomers, the transition is associated with both a change in the nature of the fracture surface and a marked increase in the rate of growth over a narrow range of tearing energies, often with very erratic behaviour in the transition region[51]. For crystallising elastomers, the transition usually coincides with the catastrophic tearing strength, as normally measured. It was explained[76] that catastrophic tear in a crystallising elastomer occurs because the rate of growth is so high that crystallisation at the tip is absent or insufficient to be effective. Consistent with this if the bulk of the elastomer becomes crystalline first, as in tensile strength

test, stable growth is observed above the normal catastrophic tearing energy (Figure 2.4-4). This stable growth is believed to be relevant to tensile failure[77].

(3) The fatigue limit and the effect of ozone

The reaction between ozone and the double bond along the backbone of this polymer chain is rapid and is believed to cause a direct cleavage of the bond and hence of the polymer chains. Under a cyclic loading, when mechanical crack growth is very slow or absent, ozone attack may be the dominant crack growth process until the cracks are large enough to permit mechanical growth to take over: that is, until T_0 is reached. The cyclic ozone crack growth closely parallels the behaviour observed for the growth of a single crack by ozone under a fixed load. In the latter case the growth is time dependent and provided the temperature is well above the glass transition temperature for the elastomer, the rate is commonly found to be proportional to the ozone concentration and independent of the tearing energy (Figure 2.4-4), provided this exceeds a threshold value, T_z say. The rate is similar for a number of polymers including NR and SBR and thus the time-dependent growth can be represented by an equation of the form

$$\frac{dc}{dt} = \alpha_z [O_3] \qquad T_z < T \tag{2.4-6}$$

where $[O_3]$ is the concentration in ozone, α_z a constant representative of the elastomer and may be influenced by the degree of cross-linking, fillers and other vulcanising ingredients, as well as elastomer type. Under cyclic conditions, Equation 2.4-6 becomes:

$$\frac{dc}{dn} = \left(\frac{t_z}{\upsilon}\right)\alpha_z [O_3] \qquad T_z < T < T_0 \tag{2.4-7}$$

where t_z is the time fraction of each cycle for which the sample is under stress and υ is the frequency. The effect of ozone under cyclic conditions can therefore be predicted from static tests. Unsaturated elastomers are normally protected by the

incorporation of waxes and anti-ozonants. Waxes are mostly effective in static applications.

The behaviour represented by Equation 2.4-6 is consistent with a simple mechanism in which the rate of crack growth is controlled mainly by the rate of impact of ozone molecules on the elastomer chains at the crack tip. At lower temperatures, in relation to the glass transition temperature, the rate may be greatly reduced and may become controlled by the visco-elastic behaviour of the elastomer.[85] It appears that the retraction of severed chains ends, after ozone scission has occurred, is the rate-limiting factor in this region. For elastomers containing no protective agents, T_z is typically only 0.1 J.m^{-2}; compared with 50 J.m^{-2} for the mechanical threshold T_0. If elastomer is unstressed or if the energy at flaws is less than T_z, ozone attack does occur but is much less apparent, since it is restricted to a very slow, uniform erosion of the surface with no visible cracks.

The existence of T_0 means that if this value of the tearing energy is not exceeded during cyclic fatigue then the fatigue life of the article will be virtually infinite. Thus elastomers can, like other materials such as metals, exhibit a fatigue limit. The tensile strain e_0 corresponding to T_0 is called the mechanical fatigue limit for a particular elastomer. e_0 for NR and most of the synthetic elastomers examined to date lies within the range 65-95%. For tensile strains below about 65% strain therefore the fatigue life is virtually infinite[78]. The magnitude of e_0 is extremely important since most elastomer components subjected to repeated loading will be designed to work below it. However in a component of complex geometry and loading it is not easy to determine the actual magnitude of the strains and it is not easy to determine whether the working conditions are below T_0.

2.4.3 Fatigue life determination

The crack growth rate at tearing energies $T>T_0$ is found to be a function of T until catastrophic failure occurs at T_c,

$$dc/dn = f(T) \qquad (2.4\text{-}8)$$

If the fatigue life is defined as the number of cycles n required for a crack to grow from a crack length c_1 to a length c_2 then,

$$n = \int_{c_2}^{c_1} \mathrm{d}c / [f(T)] \tag{2.4-9}$$

This integral can be evaluated provided that the relationship between T and c is known and that values of T can be calculated for the particular sample shape and type of deformation. For a through-thickness edge crack (Figure 2.4-5) the energy release rate in simple extension is given by[42]:

$$T = 2k_t Wc \tag{2.4-10}$$

where W is the elastic strain energy density in the bulk of the material and for large strains, k_t departs from the classical value of π, being given approximately by:

$$k_t = \frac{\pi}{\sqrt{\lambda}} \tag{2.4-11}$$

where λ is the extension ratio[79].

In the intermediate tearing energy region, Equation 2.4-8 often approximates to the simple power law relationship mentioned in Equation 2.4-1, of the form:

$$\mathrm{d}c/\mathrm{d}n = B_t T^{\beta} \tag{2.4-12}$$

where B_t, β are constants and T is the maximum value of the tearing energy during a cycle. Substitution for T from Equation 2.4-10 and integration yields, for the number of cycles, n, for a crack to grow from length c_1 to length c_2 in an article subject to a fixed maximum extensions with a constant maximum value of $2k_t W$

$$n = \frac{1}{(\beta - 1)B_t (2k_t W)^{\beta}} \left(\frac{1}{c_1^{\beta - 1}} - \frac{1}{c_2^{\beta - 1}} \right) \tag{2.4-13}$$

For elastomers, values of β commonly range from 2 to 6. The value tends to be lower, at the higher mechanical hysteresis exhibited by the material at high strains. Thus if c_2 is appreciably greater than c_1, the second term in the brackets in Equation 2.4-13 may be neglected. Further, when no initial cut or crack is present, if it is assumed that growth will initiate from a natural flaw, then Equation 2.4-13 may be rewritten as,

$$N = \frac{1}{(\beta - 1)B_t (2k_t W)^{\beta} c_0^{\beta - 1}}, \tag{2.4-14}$$

where N is the fatigue life or number of cycle to failure and c_0 the equivalent crack length of the largest naturally occurring flaw that is present.

In general, the fatigue life N of any elastomer component can be predicted by integrating Equation 2.4-8:

$$N = \int_{T_i}^{T_c} \left(\frac{1}{\mathrm{d}T / \mathrm{d}c} \right) \frac{\mathrm{d}T}{f(T)} \tag{2.4-15}$$

where T_i is the initial tearing energy, which depends on the size of the starting crack and T_c is the catastrophic tearing energy. The validity of this approach was examined by carrying out experiments on tensile samples containing inserted cuts of various lengths. Extended to uncut specimens, the fatigue life of tensile samples made it possible to deduce the apparent initial flaw sizes using Equation 2.4-14. Gent *et al*[71], Lake and Lindley[49], Lake[80] and Greensmith[81] found defects having an apparent size in the range between 25 and 70 μm. Of course, these values represent effective sizes reflecting a given value of T. However an elastomer component initially contains a wide distribution of flaw sizes and therefore initial values of tearing energies. The flaw giving the highest tearing energy will typically be the critical one responsible for catastrophic fracture.

2.4.4 Effect of frequency or strain rate

Most fatigue crack growth tests are carried out at a constant applied frequency. But as the strain is increased to cover the range of tearing energies, the strain rate increases. Both the effect of frequency[82] and the strain rate[83] have been studied and the results show distinct differences in behaviour between non-crystallising and strain-crystallising elastomers.

For the case of non-crystallising elastomers like SBR, the crack growth during each cycle was considered as the sum of two components[82]: the time dependent and the dynamic/cyclic component of the crack growth. The first component depends only on the time duration a specimen is under a given load and crack growth occurs under a static loading. The second component is the increment of crack growth due to the cyclic process itself.

At high frequencies or large strain rates, the second of these contributions dominated and the crack growth rate at a given tearing energy decreased when the frequency was increased. Over a range 10-1000 cycles per minute (cpm), the crack growth rate decreased by a factor three[82]. At low frequencies (below 10 cpm), the time dependent component of crack growth dominated and the crack growth per cycle was inversely proportional to the frequency. From the point of view of the strain rate, the behaviour was of course similar. For a CIIR (Chlorobutyl) compound, studied by Young[83], a partially crystallising elastomer, the crack growth rate at a given tearing energy decreases[83] over a range of strain rates from 1 to 20 s^{-1}. This was attributable to the time dependent component of crack growth. The longer time period the specimen was under stress, at low strain rates, the quicker the crack advanced. Young[83] did not account for this behaviour to an energy effect and a visco-elastic effect where a reduction of the hysteresis as the strain rate decreases would be responsible for the reduction of the energy dissipated. He suggested there was a dominant role played by a damaged zone around the tip of the growing crack. The compound was experiencing more damage at the lower strain rate, because the material in the area of the crack tip was under load for a longer time.

For crystallising elastomers, the rate of extension and therefore the frequency have little effect on the high strain or crack growth behaviour. Very little effect of

frequency on fatigue crack growth[80] has been observed over the range of 10^{-3} to 50 Hz.

If the frequency is too high, however, especially for thick sample, excessive heat generation results. The predominant cause of failure is now no longer mechanical fatigue but rather an elevated temperature degradation. This type of failure may lead to the blow out of solid tyres.

2.4.5 Non-relaxing conditions

Many elastomer springs are subjected to an oscillating load superimposed on a dead load, and thus the non-relaxing behaviour may be of a prime importance. It has been shown that if complete relaxation of a sample to zero strain did not occur during each deformation cycle[72, 84] then the crack growth and the fatigue resistance of crystallising elastomers was considerably enhanced. As if the minimum applied force was sufficiently high, the crystalline structure at the tip of the crack and its associated hysteresis would be at least partially retained and would impede the advance of the crack tip profile. Figure 2.4-6[85] shows cyclic crack growth rates for an unfilled NR plotted as a function of maximum tearing energy per cycle. In this instance if the minimum T is 5.6% of the maximum tearing energy instead of zero, the crack growth rates are reduced by a significant factor of about 10. Enhancement in crack growth resistance was also observed in non-strain-crystallising elastomers like SBR[86] under non-relaxing conditions. This improvement in crack growth and fatigue resistance for non-strain-crystallising elastomers under non-relaxing conditions was mainly attributable to a reduction in the strain energy of the cycle.

2.4.6 Effect of temperature

The effect of the temperature on fatigue crack growth follows broadly what might be expected from the influence of temperature on tear behaviour. As with the tear behaviour, the fatigue crack growth is governed by the nature and the extent of mechanical hysteresis[74] at high strains. NR exhibits a pronounced mechanical hysteresis due to crystallisation at high strains at the tip of the crack. Because the origin of this hysteresis for NR compounds is little affected by the temperature[87], the

crack growth characteristics are not significantly modified by the temperature[88]. In the case of SBR, the hysteresis is solely governed by the internal viscosity of the material. The internal viscosity decreases considerably with increasing temperature[52, 82]. This behaviour was clearly shown by Lake and Lindley[82] when a 10^4 fold decrease in fatigue life was observed for unfilled SBR on heating from 0 to 100°C, in contrast to unfilled NR, which exhibited only a four fold decrease (Figure 2.4-7).

2.4.7 Different energy dissipation mechanisms

The energy dissipation processes described in the section 2.3.3 on tearing measurements also constitute reinforcing mechanisms in the case of fatigue crack growth.

Lake and Lindley[82] studied the effect of carbon black on the crack growth rate of several elastomers containing 50 pphr MT (Medium Thermal) or HAF (High Abrasion Furnace) carbon black-filler (Figure 2.4-8). Because of its interaction with the elastomer and its particle sizes (26-30 nm), HAF carbon black is a reinforcing filler. MT carbon black is a non-reinforcing filler, its particle sizes ranging between 200-500 nm. In all the cases the addition of carbon black caused a strengthening which corresponded to a decrease in the crack growth rate for a given tearing energy. The threshold tearing energy T_0 in the case of the HAF carbon black filled elastomers was increased by about a factor of two, but the MT carbon black had little effect on T_0. The decrease in the cyclic crack growth rate was attributed to the additional source of mechanical hysteresis, to an effective increase in T_0 with the HAF carbon black and in an increased propensity to crack tip blunting and branching.

The different fatigue crack growth resistances for different elastomers as shown in Figure 2.4-8 were mainly attributed to the various degrees of mechanical hysteresis in each material. The value of the power law exponent β from Equation 2.4-12 is usually found to be equal to 2 for either filled or unfilled NR. For non-strain crystallising elastomers like SBR, the value of β is usually around 4 and the value is thought to be related to the degree of mechanical hysteresis at a large strain.

The type of vulcanising system used can also produce various degrees of mechanical hysteresis in the resulting cross-linked elastomers. Lake and Lindley[82]

found that the fatigue life of NR containing polysulphidic cross-links was twice that for systems with mono-sulphide and peroxide cross-links. They concluded that the superiority of the polysulphidic cross-linked elastomer might be due to the labile nature of polysulphidic cross-links, which were able to break and reform in the strained state, thus relieving the stress concentration at the tip of the crack. Yanyo[89] made a similar observation for carbon black-filled NR elastomers.

2.5 Fracture of non-simply loaded components

We showed previously that using the fracture mechanics approach, and calculating the level of the tearing energies generated in the sample could give a prediction of the crack growth rate and then an estimation of the fatigue life. One difficulty in applying this approach is the determination of the correct value of the tearing energy. For simple geometric shapes as the ones described earlier analytical solutions are available. Analytical solutions have also been developed for more complex cases than tensile, trouser or pure shear test-pieces and examples of these solutions are reviewed in this section.

2.5.1 Analytical evaluation of the tearing energy

Lindley[79] showed that the tearing energy approach was valid for components of non-uniform thickness and for components with non-uniform stress and thickness. He experimented with the test-pieces shown in Figure 2.5-1. Test-piece B corresponded to one of non-uniform stress, C to non-uniform thickness and D combined both. The corresponding analytical expressions for tearing energies were slight modifications of those for simple extension with an edge crack.

For the semi-circular test-pieces, the energy released U_r due to a crack of length c was formulated in the same manner as for simple extension

$$U_r = k_t c^2 t W \qquad (2.5\text{-}1)$$

but with k_t being a function of c. c, t and W are respectively the crack length, the thickness and the *e.s.e.d.* function. Then, when U_r was differentiated with respect to c to obtain T, an extra term due to the differentiation of k_t appears. In the case of a simple extension wedge, from dimensional considerations, U_r became a function of c^3 and the relation between the crack area a and c was required to calculate T. For the semi-circular wedge case D, the energy loss was experimentally determined against the crack-surface area to calculate T. No significant differences were observed in the variation of cyclic crack growth rate with tearing energy for these different test-piece geometries.

The earlier sections 2.3 and 2.4 dealt with crack growth behaviour in thin sheets using a plane stress analysis. Lindley and Teo[90] studied the crack growth behaviour of elastomers under plane strain (25 mm thick sheet) and under plane stress (2 mm thick sheet). Their plane strain experiments consisted of single or double rectangular cross-section shear springs of height h (Figure 2.5-2) with an introduced crack along the bond. Because the situation was identical to that of a pure shear when the crack was long enough $(c \geq 3h)$, the tearing energy was given by the same expression. The plane stress test used for comparison was a simple extension test-piece. They[90] showed that there were no differences, within the limits of the experimental reproducibility, between the crack growth behaviour under plane stress or plane strain (Figure 2.5-3).

Fatigue crack growth in a circumferentially cracked circular cylinder of an elastomer under torsion has also been studied by Aboutorabi *et al*[91]. They derived the energy release rate by treating the elastomer as a linear elastic material both analytically and with FEA computation. Crack growth results[92] expressed as a function of the energy release rate showed good agreement when compared with tension plane stress measurements[72] (Figure 2.5-4).

Although compressive stresses would simplistically appear to close a crack, early work by Cadwell *et al*[84] pointed to failures of elastomer cylinders under repeated compression cycles. Thus for bonded elastomer cylinders in compression, cracks grew to remove the elastomer which, at the maximum compression, bulged outside the original profile of the cylinder[93] as shown on Figure 2.5-5. Stevenson[93] derived the tearing energy as follows. For an increase in crack length dc, there will be

an increase in crack area da and in a volume of elastomer dV from which strain energy is released. The energy loss dU_r is thus:

$$dU_r = W dV \tag{2.5-2}$$

so that

$$T = W\frac{dV}{da} \tag{2.5-3}$$

Experimental observations have demonstrated that the propagation was stable in this geometry and, that T was then independent of the crack length. The expression (2.5-3) was rewritten as:

$$T = W\frac{\Delta V}{a_c} \tag{2.5-4}$$

where ΔV was the volume of elastomer removed by crack growth, W was the average elastic strain energy density and a_c was the total area of crack surface. ΔV and a_c were functions of the dimensional parameters of the elastomer cylinder. Generally, if small compressive strains are applied in-situ then a linear elastic analysis is adequate. Shear strains occur throughout the cylinder and their elastic energy is additional to that of the normal strains, giving rise to an effective compression modulus E_c, greater than the Young's modulus.

$$E_c = 3E_s(1 + 2S_p^2) \tag{2.5-5}$$

where E_s is the average small strain shear modulus and S_p the shape factor equal to the cross-sectional area to total-free surface area. Although the elastic strain energy density will not in general be uniform, an average strain value may be expressed to a first approximation as:

$$W = \frac{1}{2} E_c e_c^2 \qquad (2.5\text{-}6)$$

where e_c is the compression strain. Results of crack growth rates in compression were found to correlate well with values obtained in tension, as shown in Figure 2.5-6. The experimental tearing energy is derived from the slope of the curve ΔU_r versus the crack area a, ΔU_r being the energy loss due to the given amount of crack growth.

2.5.2 Finite Element based fracture mechanics analysis

As mentioned in section 2.3.1, two different approaches are available when dealing with highly non-linear elastic material: the energy release rate (tearing energy for elastomers) and the Rice *J*-integral. The first one is a generalisation of the Griffith's energy balance approach and the second a contour integral characterising the stress and strain field in the crack tip region. In both cases, it is necessary to have available an *e.s.e.d.* function which can be inserted into the FEA programme and which can be utilised to calculate both the elastic energy stored and that released on crack growth.

Several approaches have been used to calculate the energy release rate. The energy release rate can be estimated by computing the change in total energy between two neighbouring positions of the crack tip (Figure 2.5-7). The methods based on this concept are usually called virtual crack extension methods (VCE). The simplest application of this concept consists in running two full analyses to compute the elastic strain energy density of the model for two slightly different crack lengths. More sophisticated approaches have attempted real virtual crack extension by only running one full analysis and with the possibility of computing the energy release rate in any directions of the 2D or the 3D crack front. Formulations and computations of the energy release rate using a real VCE method were proposed initially by Hellen[94] and Parks[95] for linear elastic materials. These formulations were extended for elastic-plastic material behaviour by Parks[96] and for non-linear elastic (elastomer) material behaviour by Pidaparti *et al*[97]. It has been proposed by Pidaparti *et al*[97]and Claydon[98] in a 3D models and by Hellen[94] in 2D that the energy release rate distribution varies sinusoidally with inclination of the direction of the virtually extended crack. They

consequently obtained negative values of the energy release rate when the crack is virtually extended in a backward direction with respect to the expected crack propagation direction. These results are clearly erroneous as it would mean that the crack would absorb energy whilst propagating. As an example, Figure 2.5-8 shows the geometry and the results found by Hellen[94]. It appears then that the computation of a real VCE method using only one analysis and capable of correctly predicting the magnitude of the energy release rate in any directions at the crack front is not yet available.

Another method to evaluate the energy release rate is the Virtual Crack Closure Technique or VCCT. Irwin[99] showed that the work required to close a crack an infinitesimal distance is equal to the energy released during an infinitesimal advance. The VCCT determines the energy release rate by calculating the work necessary to close one element length. If we call a the area of the crack face which is closed during the virtual closure, F_n the component of the nodal force normal to the crack plane and u_n the normal displacement of the node directly behind the crack tip (Figure 2.5-9), then the energy release rate is given by:

$$G = \frac{1}{a}\int_0^u F_n \mathrm{d}u_n \qquad (2.5\text{-}7)$$

If the relationship between F_n and u_n is assumed to be linear, then:

$$G = \frac{1}{2a} F_n u_n \qquad (2.5\text{-}8)$$

Rybicki and Kannimen[100] successfully implemented this method to predict the crack growth rates of internal cracks in cord/elastomer structures[101]. With a truck tyre, the critical regions can have more than one crack opening mode active during a loading, and the deformations associated with each mode are not necessarily in phase. The VCCT makes it possible to estimate the energy release rate for each mode, and the crack growth rate associated with that mode. The total crack growth rate is assumed to be the sum of the contribution from each mode. Implicit in this approach, is the assumption that the crack growth rate for a given energy release rate is independent of the mode of deformation. This assumption is valid for monotonically loaded cracks

on simple thin geometries[80] and it is an ongoing study on thick geometries and multiaxial deformations.

The *J*-integral was first proposed by Rice[102] as a fracture parameter for two dimensional, non-linear elastic, and small displacement gradient analyses. It has since been extended to large displacement gradients[44] and 3-D crack fronts[103]. Finite element formulation has been developed for the evaluation of *J*-integral[104]. As a consequence, the *J*-integral option also called contour integral is readily available in commercial FEA software.

2.6 Review on fractography and roughness measurements for elastomers

2.6.1 Roughness measurement techniques

Most studies of the nature of fracture surfaces of elastomers have been qualitative with a few significant quantitative works due to Schallamach[105], Gent and Pulford[106], Deuri and Bhowmick[107], Thavamani and Bhowmick[108], Fukahori and Andrews[109] and Ganesan *et al*[110]. The reasons for such limited studies despite the recent significant advances in techniques of surface mapping and in data processing results from a general non-availability of proper methods and intrinsic parameters to describe the roughness of a surface. This review describes two different approaches based on a two-dimensional (2D) or on a three dimensional surface images (3D).

The 2D information consists generally of pictures or micrographs of fracture surfaces obtained using either optical or electron microscopy. Fukahori and Andrews[109] counted the number of steps crossing a reference line and weighted each of these steps according to their apparent depth. They assumed that the broader these step lines, the deeper the steps, as deeper steps cast more shadow. Gent and Pulford[106] measured the distance between steps. Ganesan *et al*[110] used an image processing technique. After digitising the 2D picture, the image surfaces were represented in terms of local textures and the authors suggested that the frequency of occurrence of these textures should be a characteristic measure of the roughness of the surface. These local textures were described mathematically using a set of polynomial functions and the detection of the textures was realised with the use of a mathematical criterion. Another popular technique using either optical or electron microscopy is

that consisting of stereo microscopy. This method consists of using a stereoscopic image pair constituted of two images displaying the same object before and after a tilt by a certain small angle, of a couple of degrees. As the direction of the tilt axis is parallel to the viewed image, the tilt can only yield horizontal shifts between a point in the first image and in the second image. If the parallel projection can be applied at magnification greater than ×1000 then the shifts can be related through simple trigonometric laws to the height of the point with respect to the object plane. It is then theoretically possible to map the whole scanned area. But the use of a magnification greater than ×1000 limits the scanned area to typically 100 by 100 μm which might prove too small to be representative of the whole surface. This method could prove to be limited also by the depth of field especially if the surfaces are very rough and by the ability of the software utilised to recognise the same point in the 2 stereo images.

The 3D mapping of fracture surfaces involves in general mechanical contact, electromagnetic radiation or sometimes contact with fluid either a gas or liquid. In the case of elastomers, mechanical contact methods have been mostly used and no published work has been found using the two other approaches. The mechanical contact approach use in general an apparatus called a Talysurf. It uses the principle of a phonograph or a gramophone, where a sharp probe traverses the elastomer surface and transforms its minute irregularities into electrical oscillations. The form of the stylus is a pyramid with a 90° included angle between opposite faces. But because of the finite dimensions of the stylus, it could fail to follow very steep peaks or too small valleys faithfully and would produce a distorted record of the surface. As the dimensions of the stylus are finite, so also is the load. Although the load is small, generally not more than 70 mg, the area in contact is also small and hence the pressure may be sufficiently high to cause significant local elastic deformation of the surface being measured. This could happen in the case of relatively soft materials like elastomers. Non-contacting techniques involving electromagnetic radiation are the alternative. They usually consist in the use of a light beam as a non-contacting stylus. The rays of light from the optical probe are reflected by the object surface. As the distance between the object surface and the objective changes as the surface is scanned, the focus is maintained by repositioning the objective lens. Monitoring the movement of the objective lens allows profile measurement to be made. The detection of the diffuse reflection from the object surface could also be used as a surface

measurement. But in case of either reflected or diffused light, extremely rough surfaces may have areas that are immeasurable due to extremely steep surface facets reflecting the measuring beam away from the sensor.

2.6.2 Main observations

Fracture surfaces of torn elastomer specimens have been studied[111, 117, 51] in the past. In general, at high tearing energies and fast crack growth rates (see Figure 2.3-4), smooth fracture surfaces are observed in both crystallising and non-crystallising elastomers and in filled and unfilled elastomers. At lower tearing energies stick-slip behaviour (Figure 2.3-8) and associated rougher surfaces are observed[111, 117, 51]. This roughness is associated with the formation of secondary cracks. This secondary cracking being dependent upon the materials properties and effect such as strain crystallisation, internal viscosity, carbon black content and strain induced anisotropy.

Fukahori and Andrews[109] found a direct relationship between their measured fracture surfaces roughness and the hysteresis or the visco-elastic behaviour of the material. The smoother fracture surfaces corresponded to the more hysteritic material because the stress decay away from the crack tip would be more significant and only the inherent flaws close to the crack tip would be involved in crack growth and this reduced the texture of the fracture surface. Similarly, Gent and Pulford[106] ascribed crack growth and the texture of their fracture surfaces to the joining of secondary cracks originating from stress-raisers (inherent flaws and filler particles). These authors tried to quantify the surface roughness of torn samples by measuring the distance between steps of the surface texture. They observed that step spacings were larger in weaker materials. They also observed that the more tear resistant a material was, the greater the heights of the steps.

observations to the density of the stress-raising features and the stress distribution in the crack tip neighbourhood. They affirmed that the more numerous these stress-raisers and the more diffuse the stress distribution, the stronger the material. This is in direct contradiction with the arguments of Fukahori and Andrews[109] who say that the stronger a material the larger the stress decay away from the crack tip. Cho *et al*[112] in comparing the fracture surfaces of unswollen and swollen SBR at the same tearing energy noticed that the later exhibited much smoother surfaces with more widely

spaced steps, the latter being weaker than the former. From the strength point of view, the fact that the less viscous material (swollen SBR) was weaker agrees with the Fukahori and Andrews[109] conclusions but the surface behaviour would appear to be in contradiction to their proposed roughness rationale. Clearly great care must be taken when making comparisons of fracture surfaces as it is necessary to be certain of the exact mechanical and environmental conditions under which the surfaces are generated. Comparing fracture surface roughness is clearly not an easy task as there is no universal roughness parameter. Any measured value would depend for example on the scale that the roughness is looked at. Recent tear measurements pursued at QMW[51] have shown that oil swollen SBR appears to have a smoother fracture surface than unswollen SBR when compared at a equivalent tearing energy but would appear rougher when compared at the same rate of tear. Although there is general agreement on the fact that rough crack growth is probably due to the propagation of secondary cracks joining the main crack[106, 109], the mechanisms governing the propagation of these secondary cracks are still unclear.

As far as the author is aware, fracture surface observations of fatigue tested specimens, unlike those for tear measurements, are limited to descriptive studies[112, 107] and no systematic observations comparing fracture surfaces for various test parameters such as tearing energy, strain rate, crack growth rate, temperature and strain induced anisotropy or the various material characteristics such as internal viscosity, carbon black contents and cross-link density have been reported.

2.7 Programme of study

The concern of this thesis is the investigation of life prediction for systems of gradually increasing complexity in an attempt to draw general rules for real components such as anti-vibration devices for the automotive industry. For this it is necessary to have an *e.s.e.d.* (elastic strain energy density) function for the material applicable in all loading modes. Knowledge of such functions for carbon black filled elastomers is a necessary pre-requisite as a crack is usually driven by the release of elastic strain energy. The type of *e.s.e.d.* function proposed in this study, depending only on I_1, the first strain invariant, are able to predict the behaviour of filled elastomers under uniaxial, equi-biaxial loading and in some cases in general bi-axial

loading. But there is only limited evidence that these *e.s.e.d.* functions will allow the calculation of the strain energy for more complex situations. In addition carbon black filled elastomers can exhibit significant non-elastic behaviour not predictable by an elastic strain energy approach. One of the objectives of this work is to tackle some aspects of these problems. This will consist of:

- As mentioned in this review, Yeoh[15] showed that a cubic *e.s.e.d.* function was able to produce acceptable predictions of general bi-axial extension behaviour. But his *e.s.e.d.* function was derived from equi-biaxial measurements, a very similar loading mode to the general bi-axial. A more demanding test of this approach is proposed here. It is proposed to investigate the prediction of bi-axial stress-strain data from a uniaxially derived *e.s.e.d.* function designed for filled elastomers.

- Another proposal to test the validity of the elastic strain energy approach is the application of one of Rivlin's analytical solutions[7, 113, 114] for multi-loading modes and inhomogeneous deformations. It appears from this review that no such work has been carried out using an *e.s.e.d.* function derived from filled materials. The particular Rivlin's solution to be utilised gives the forces to maintain simultaneous extension, inflation and torsion in an uniform circular cylindrical tube. This can be tested by repeating the same experiment or with a similar experiment consisting in inclining (30 degrees in our case) a pure shear test-piece and extending it vertically.

The review on the fracture of elastomers showed that the major reinforcement process in carbon black filled elastomers is knotty-tearing (section 2.3.4.2). This consists of crack deviation whose origin is not totally understood but is believed to be due to the occurrence of sufficient strength anisotropy around the crack tip [67, 60, 65, 66]. In order to get a better understanding of this phenomenon, it is proposed here to study the effect of induced anisotropy on the development of knotty-tearing.

The review of fatigue life prediction for non-simply loaded components (section 2.5) showed that this technique is still in its early development. Published works [71, 90, 91, 92, 93] are limited generally to simple loading (tension, torsion, compression and shear) either in plane stress or plane strain. But fatigue crack growth in complex loading situations have been rarely tackled and the aim of this work is to

investigate in non simply loaded components the effect of the most important variables on crack growth rates.

The review on finite element based fracture mechanics has opened up the possibility of resolving situations where components are complexly loaded. But some erroneous results[94, 97, 98] found in the literature reveal that this method is not totally understood and care should be taken when using this method.

The review on quantitative measurement of fracture surfaces roughness conclude that 3D mapping of the surfaces using non-contacting method are the simplest and the most suitable for soft materials like elastomers.

The work proposed at the light of the fracture review is as follow:

- Study fatigue crack growth behaviour of a pre-strained pure shear sample in which the pre-strain produces the induced anisotropy and a bi-axial stress field. The effects will be studied in strain crystallising and non-strain crystallising elastomers and in elastomers containing different carbon black contents in an attempt to determine the role of these materials variables on crack growth. Fracture surfaces will be examined in an attempt to study local crack paths and their relationship with the material anisotropy.
- Investigation and prediction using FEA of the crack growth behaviour of a modified pure shear test-piece (inclined 30 degrees from the horizontal) which is pulled vertically inducing simultaneously a pure shear and a simple shear deformation modes.
- Study the crack growth behaviour of a pure shear sample subjected to a short strain history (a loading cycle along the long axis) to estimate its effect on the development of knotty-tearing.

The next chapter will describe the experimental methods employed to fulfil the tasks outlined above.

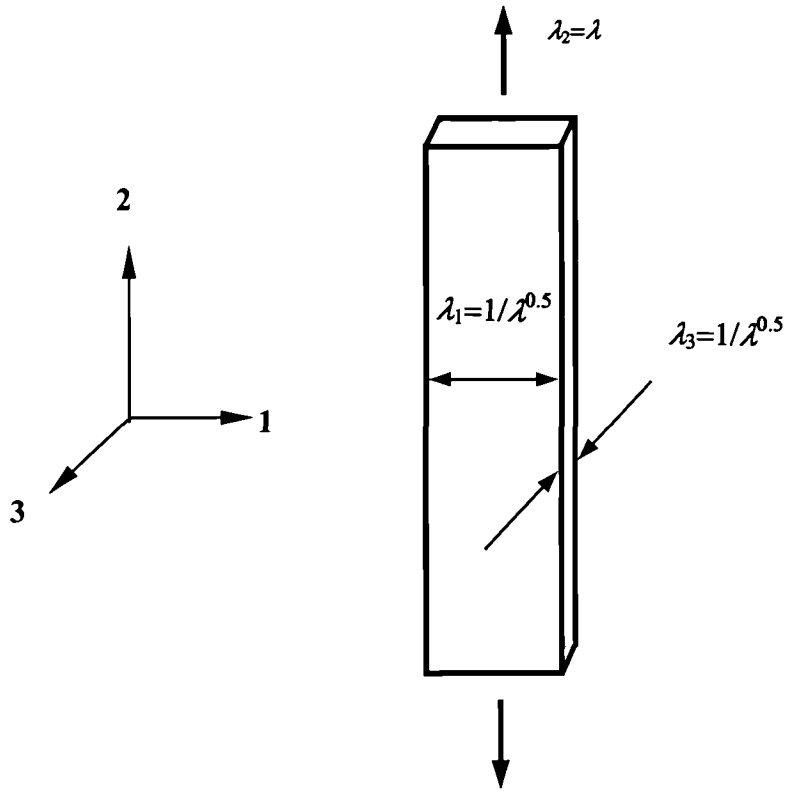

Figure 2.2-1 Values of the principal extension ratio for a tensile test-piece, the test-piece being pulled in the principal direction 2.

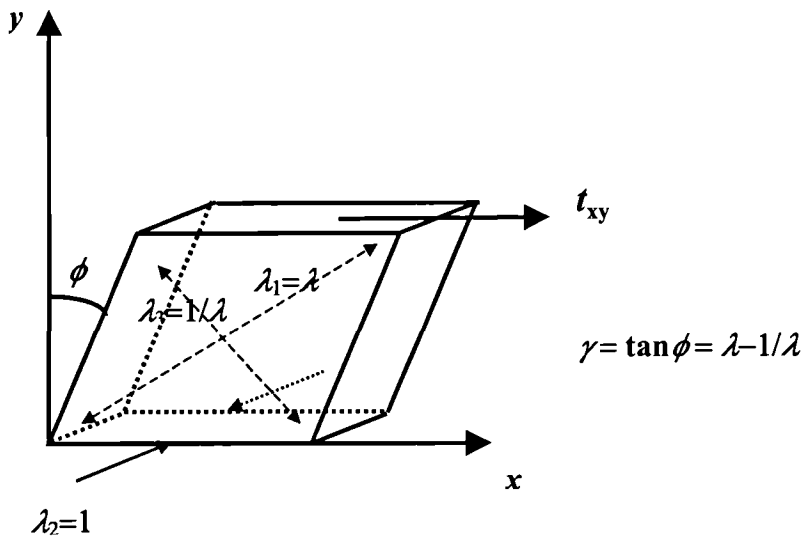

Figure 2.2-2 Values of the principal extension ratios for a simple shear test-piece.

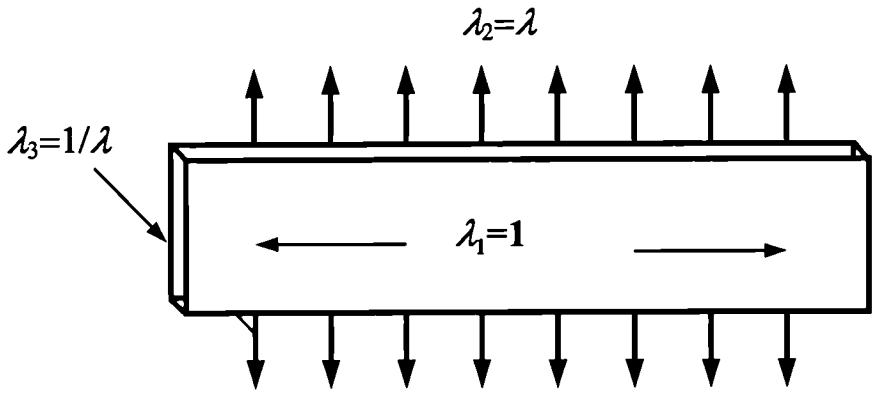

Figure 2.2-3 Values of the principal extension ratio for a pure shear test-piece, the test-piece being pulled in the principal direction 2.

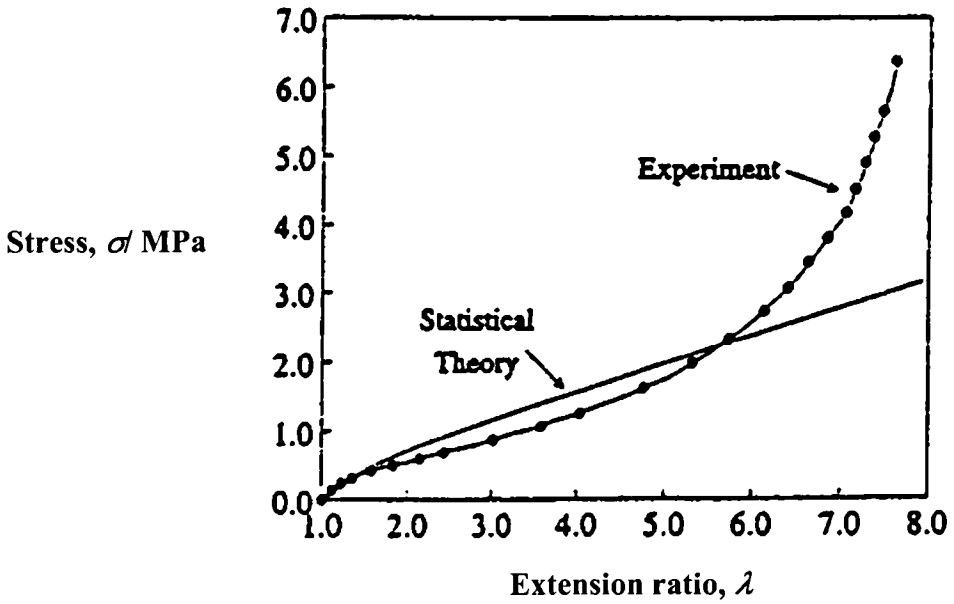

Figure 2.2-4 Comparison of statistical theory with experiment for unfilled elastomers by Treloar[3].

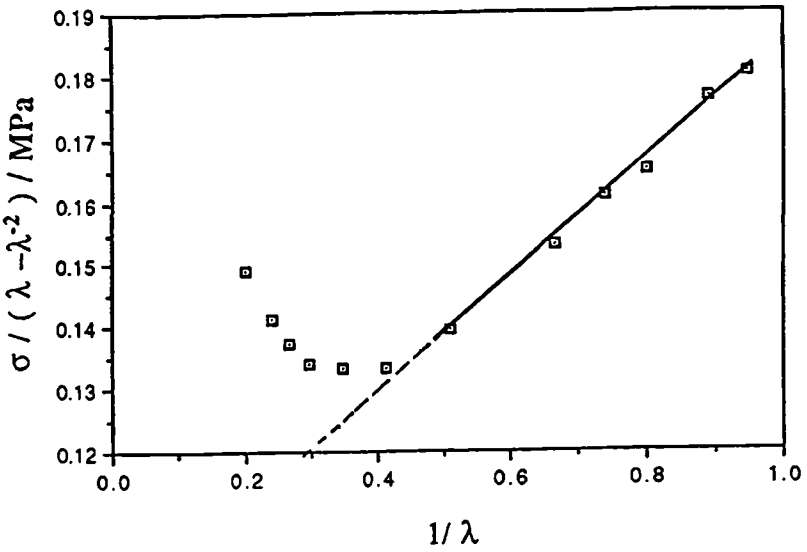

Figure 2.2-5 Mooney plot for an unfilled natural rubber cured with peroxide by Treloar[3].

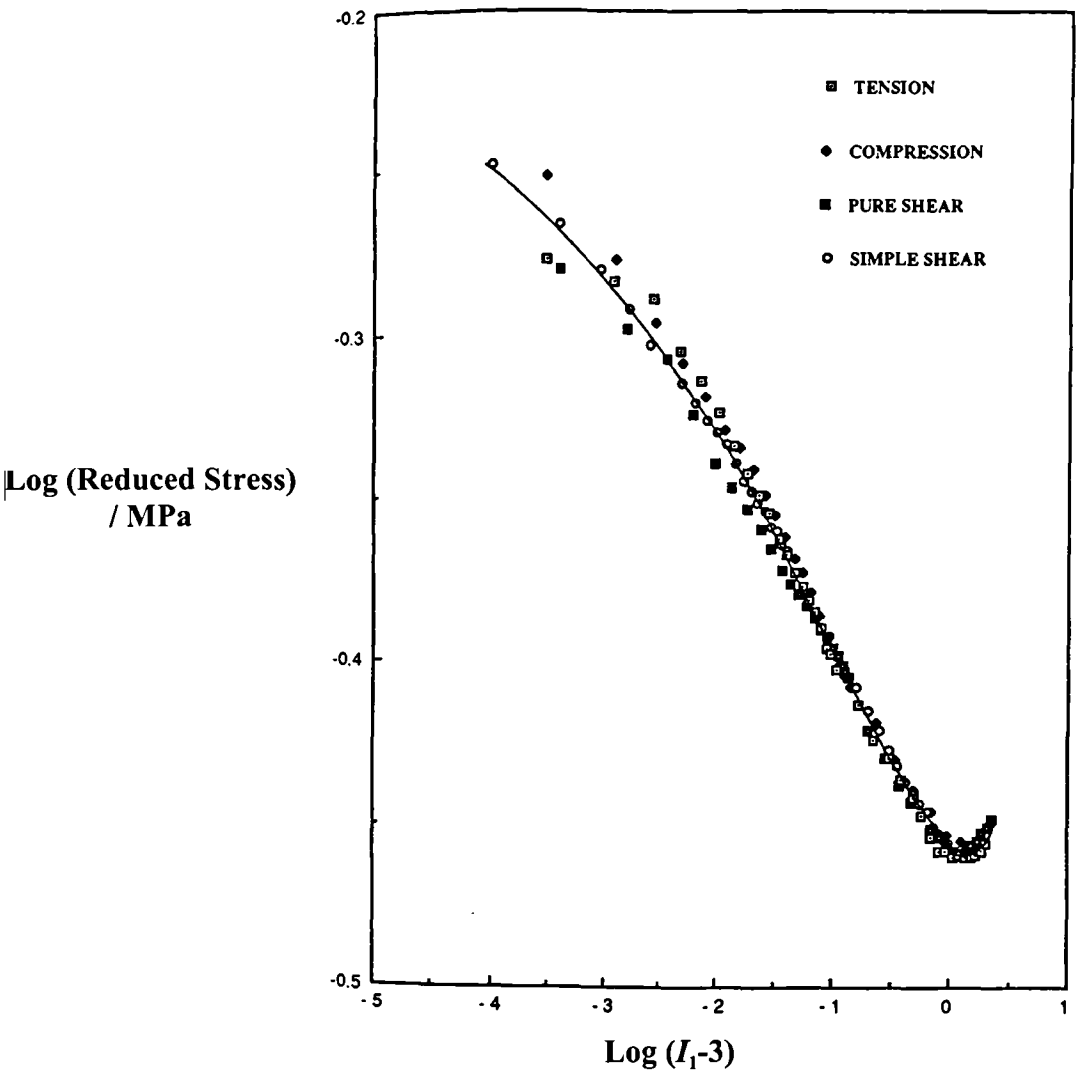

Figure 2.2-6 Derivation of the *e.s.e.d.* (elastic strain energy density) function due to Davies *et al*[23], Equation 2.2-40 (line) using measurements in four different loading modes using a 23 pphr (parts per hundred rubber) HAF carbon black filled natural rubber.

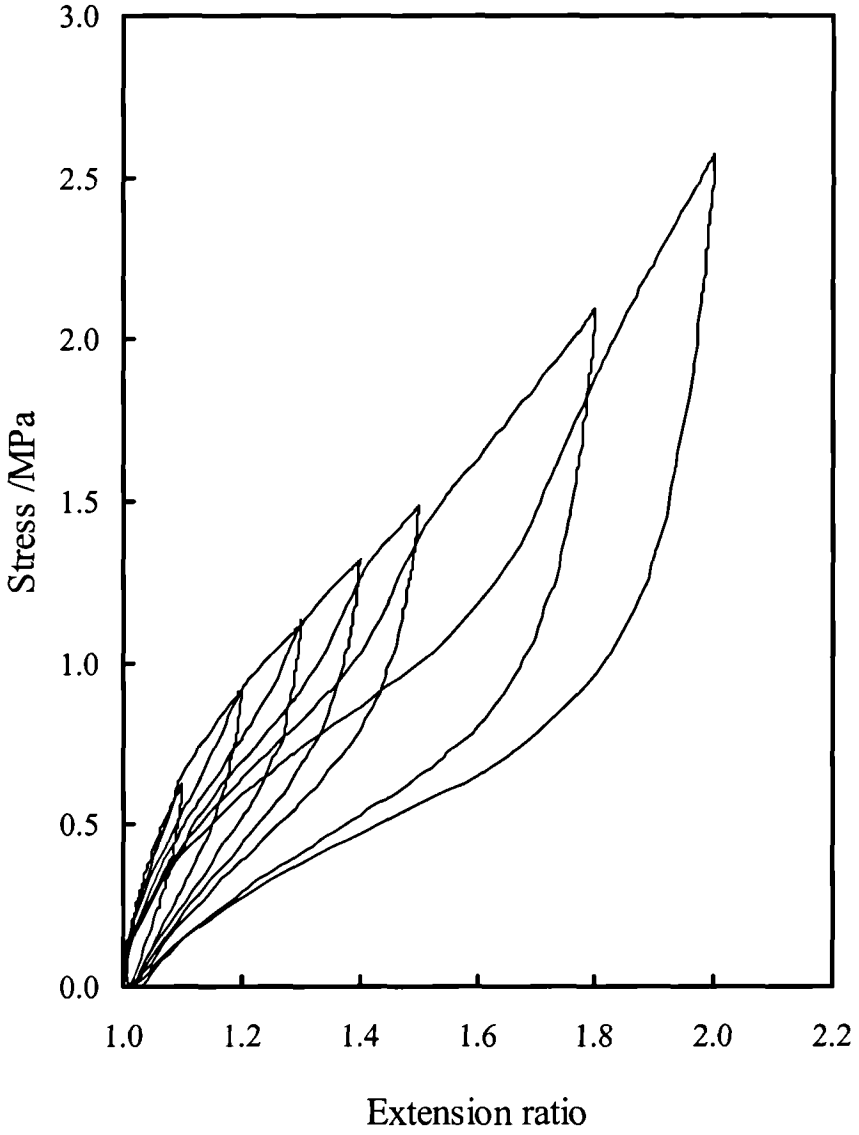

Figure 2.2-7 Schematic illustration of the hysteresis and the stress-softening behaviour for a highly filled natural rubber 59 pphr HAF carbon black[115].

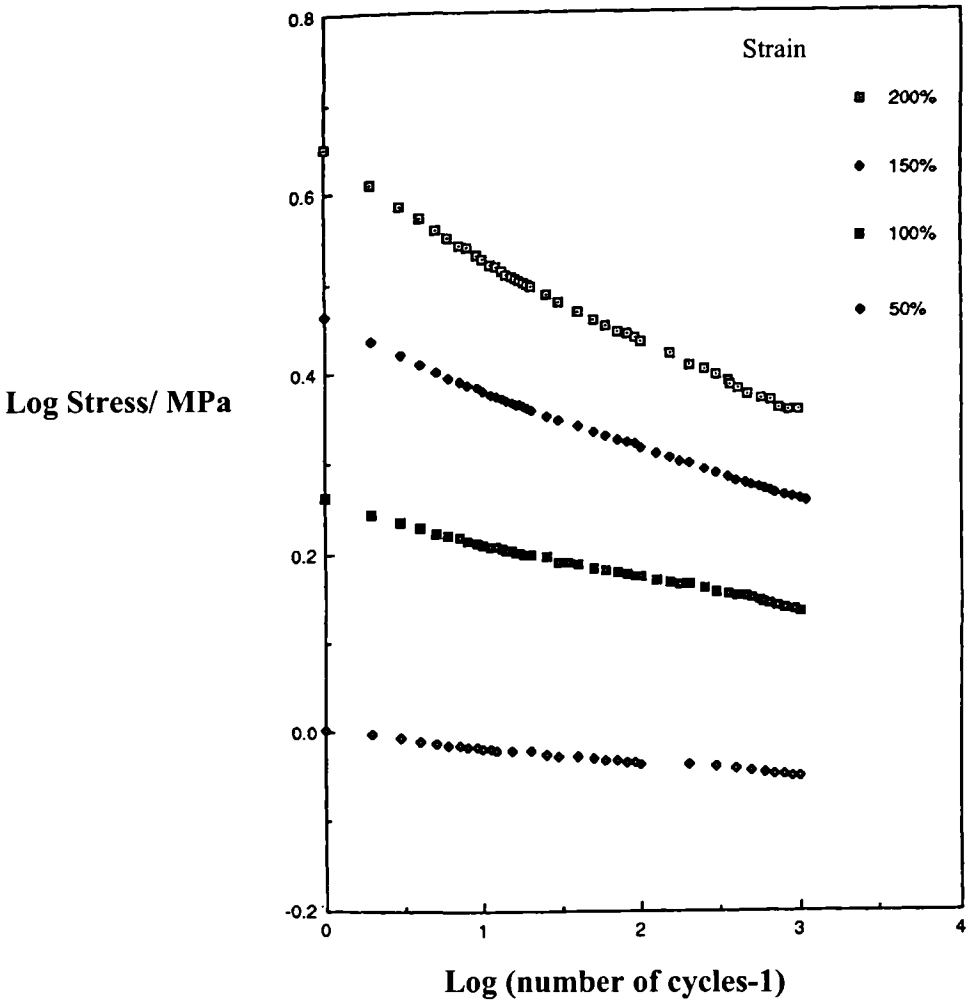

Figure 2.2-8 An illustration of Mullins effect under cyclic deformations: decrease in stress as functions of cycles at different cyclic tensile strains for a 49 pphr HAF carbon black filled elastomer[116].

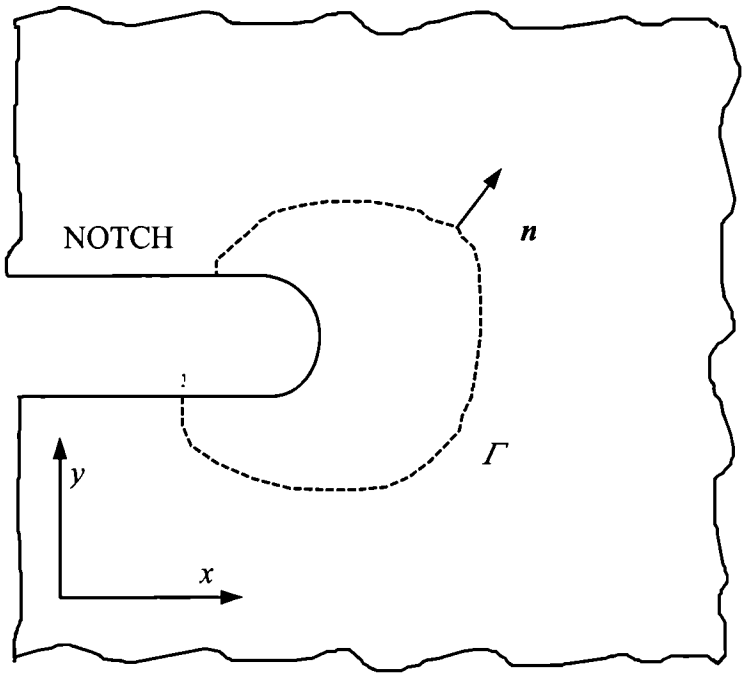

Figure 2.3-1 Flat surfaced notch in two-dimensional deformation field. Γ, the integration path for the J-integral, is any curve surrounding the crack-tip. $\boldsymbol{n}$ is the outward normal along Γ.

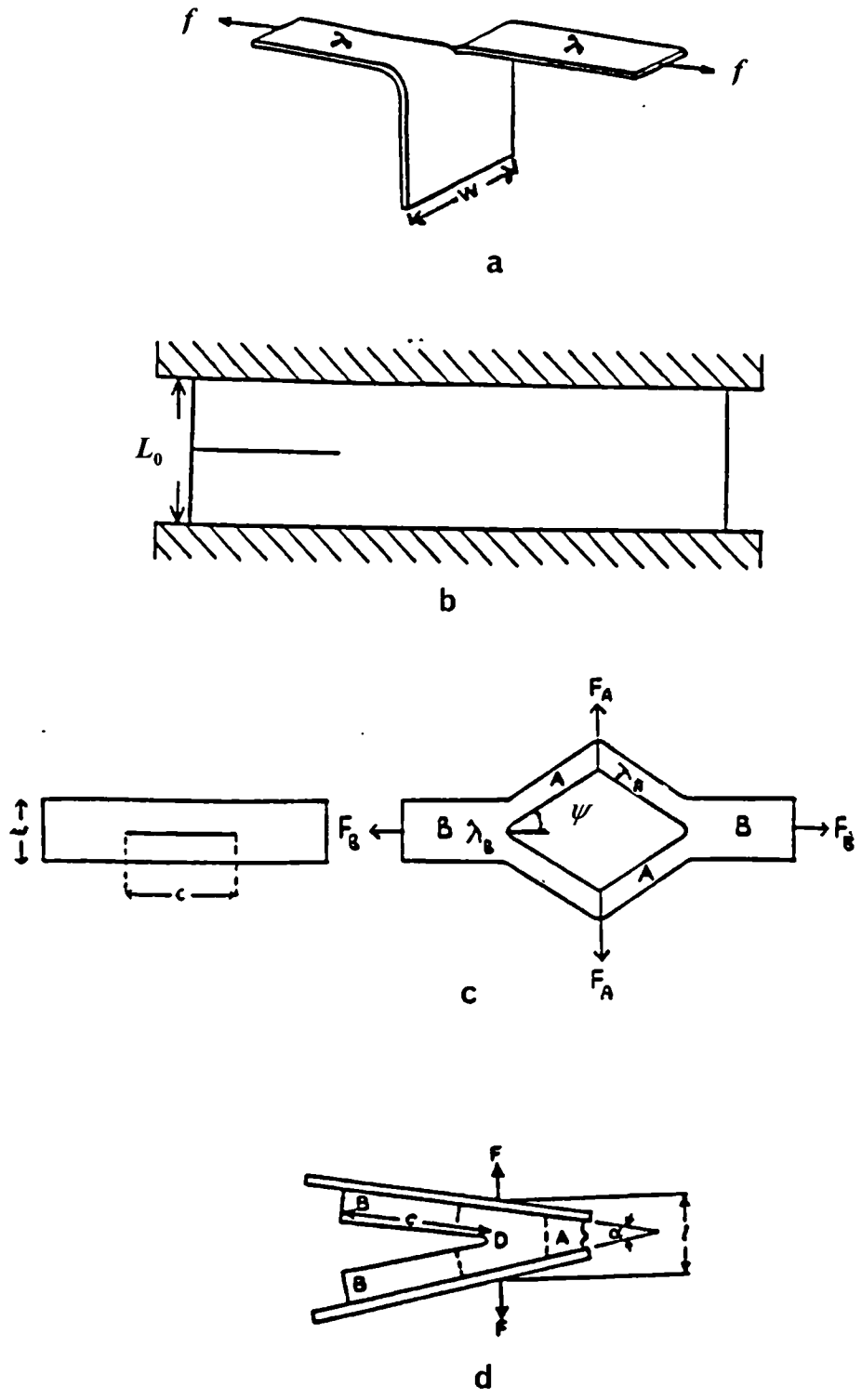

Figure 2.3-2 Types of tear test-pieces (a) simple extension (trouser) test-piece (b) pure shear[42] test-piece, (c) split test-piece[45] and (d) angle test-piece[46].

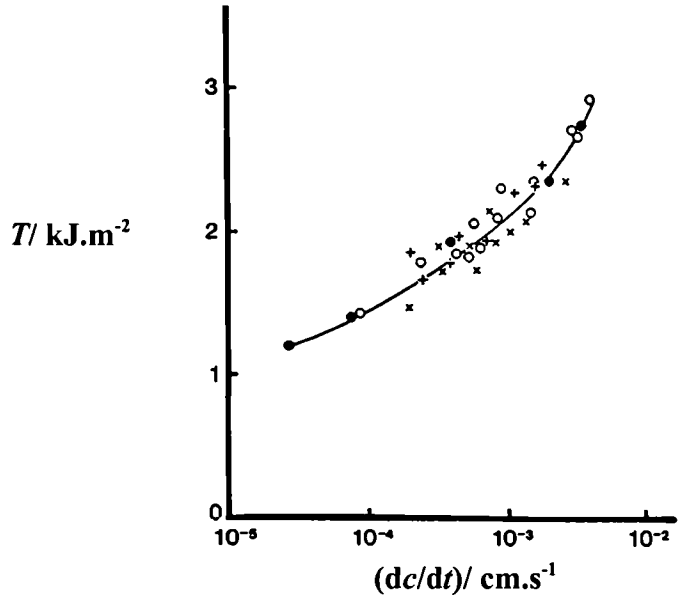

Figure 2.3-3 Tearing energy versus tear rate for a gum SBR elastomer obtained from the three test pieces shown in Figure. 2.3-2 (a), (b), (c) and (d): ×, simple extension (trouser); +, pure shear; o, split test-piece; •, angle test-piece[46].

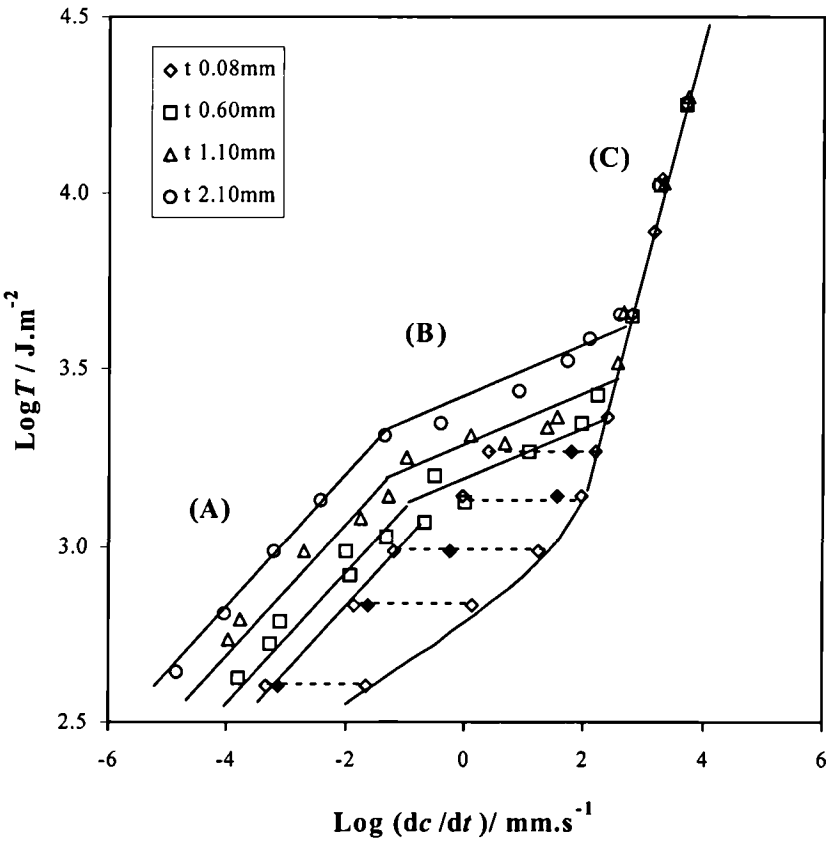

Figure 2.3-4 Tearing energy against rate for unfilled SBR showing the different crack growth behaviours and the effect of the thickness *t*. Regions (A), (B) and (C) correspond respectively to the rough, stick-slip and smooth tearing[51].

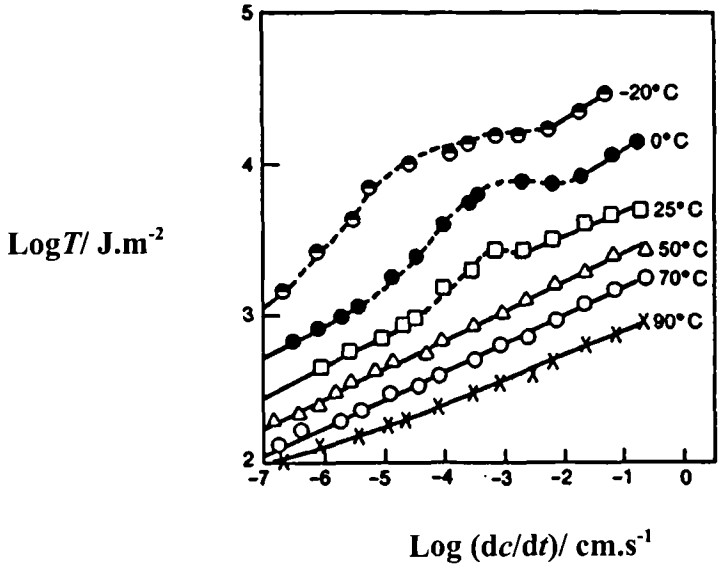

Figure 2.3-5 Dependence of tearing energy on rate and temperature for an unfilled SBR elastomer[117].

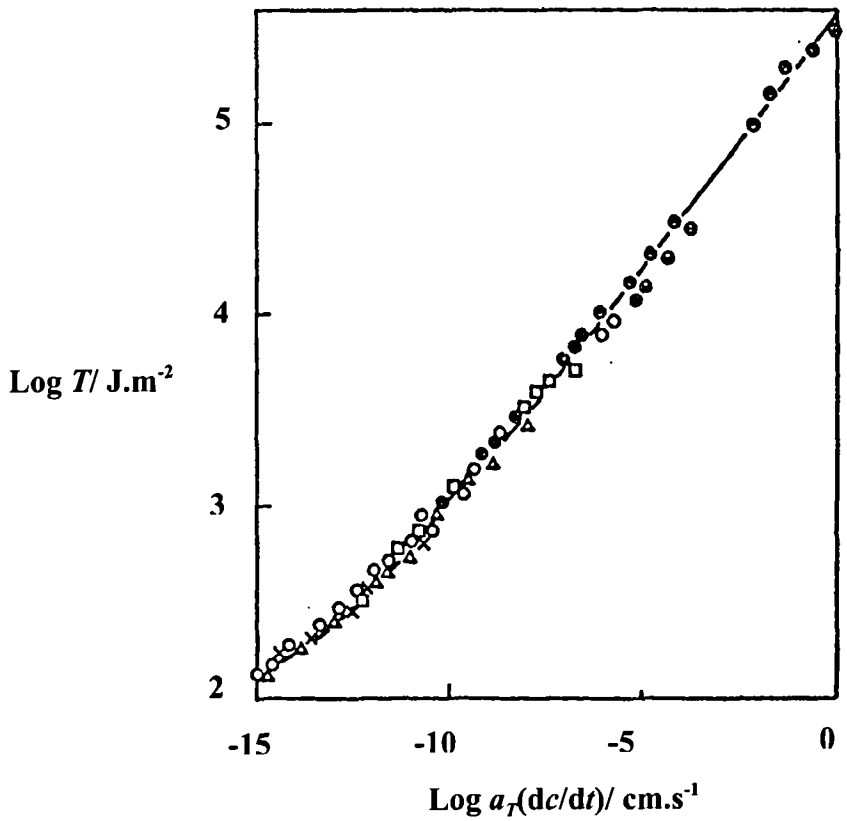

Figure 2.3-6 WLF master curve for characteristic fracture energy in an unfilled SBR[52].

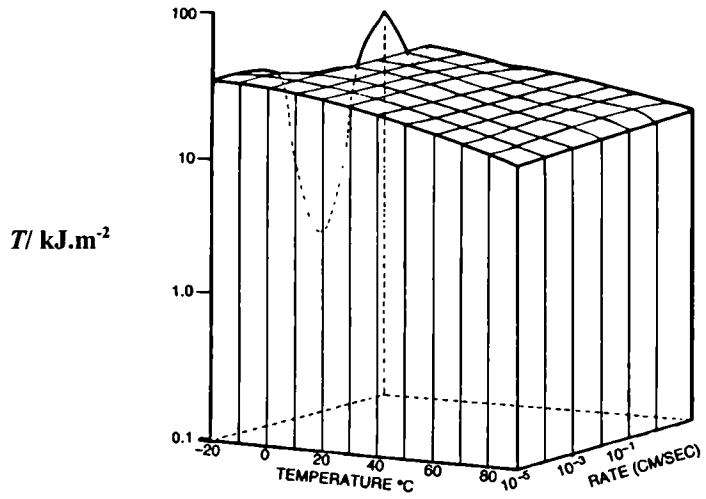

Figure 2.3-7 Tearing energy surfaces for an unfilled strain-crystallising NR[117].

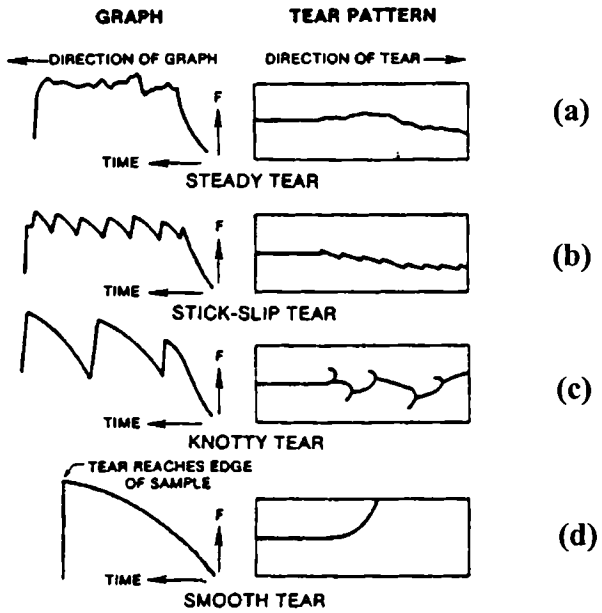

Figure 2.3-8 The four types of tear behaviour[58].

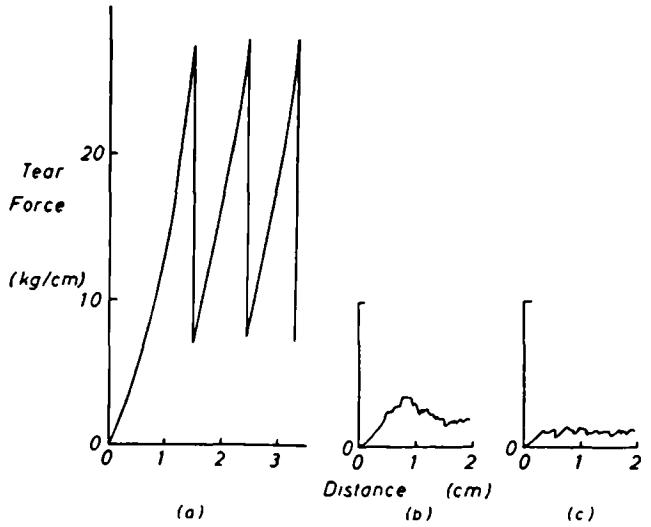

Figure 2.3-9 Tear force relation for (a) a filled elastomer without constraints, (b) the same material with the tear confined to a linear path (+/-0.005 cm) and (c) the unfilled elastomer with or without constraints[54].

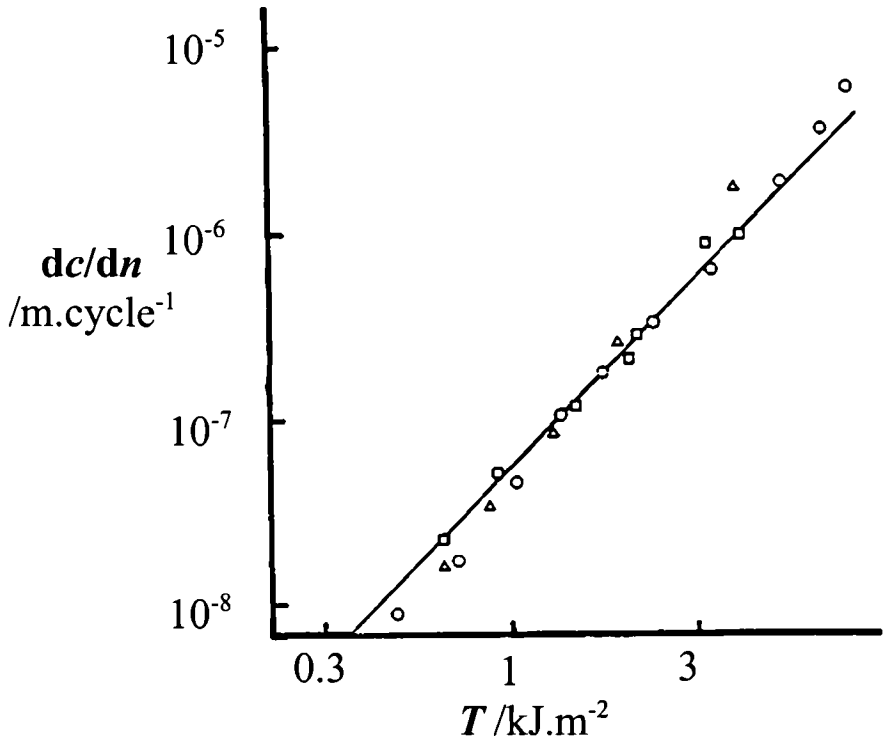

Figure 2.4-1 Cyclic crack growth rate d*c*/d*n* versus tearing energy *T* for an unfilled NR obtained using various test pieces: □ , trousers; Δ , pure shear; ○ , tensile strip with an edge crack[71].

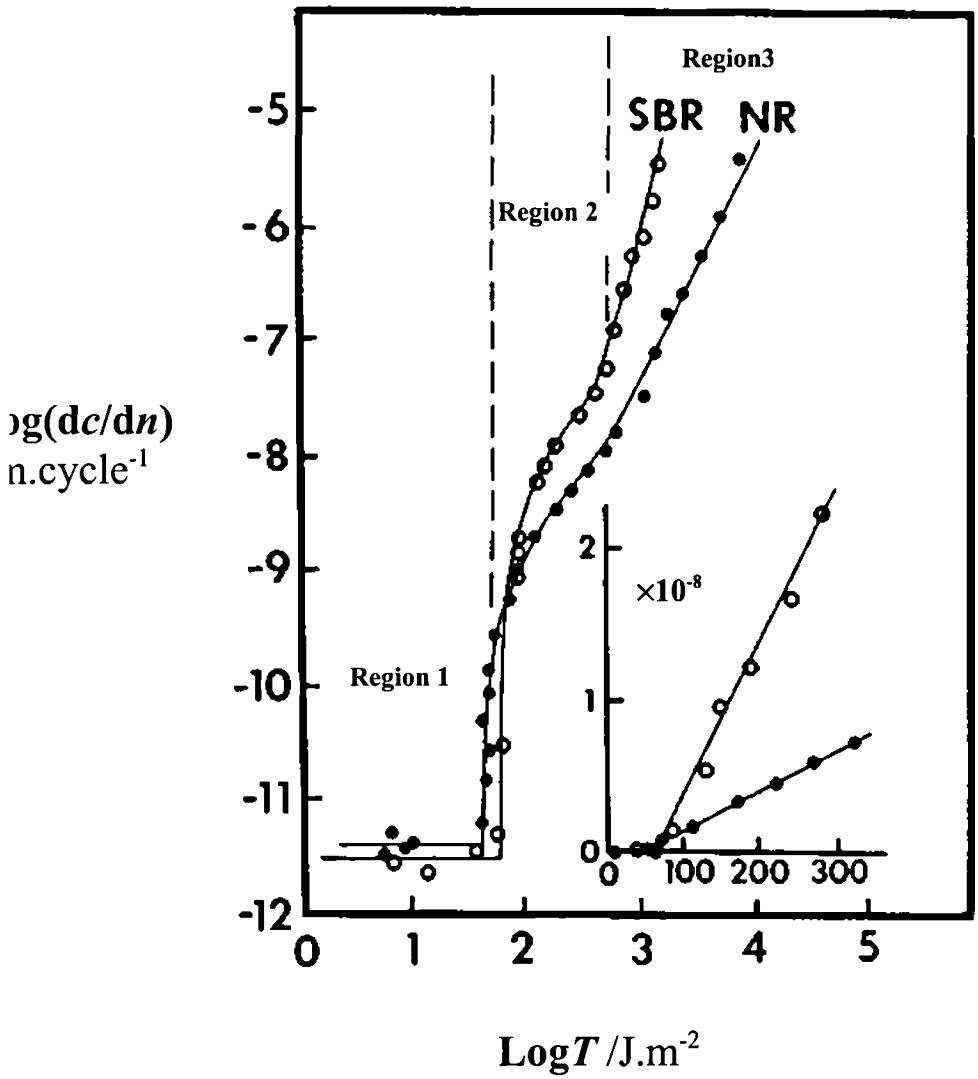

Figure 2.4-2 Cyclic crack growth behaviour for unfilled NR and SBR compounds. Inset shows the region near the threshold tearing energy T_0 for mechanical fatigue, plotted on linear scale[80].

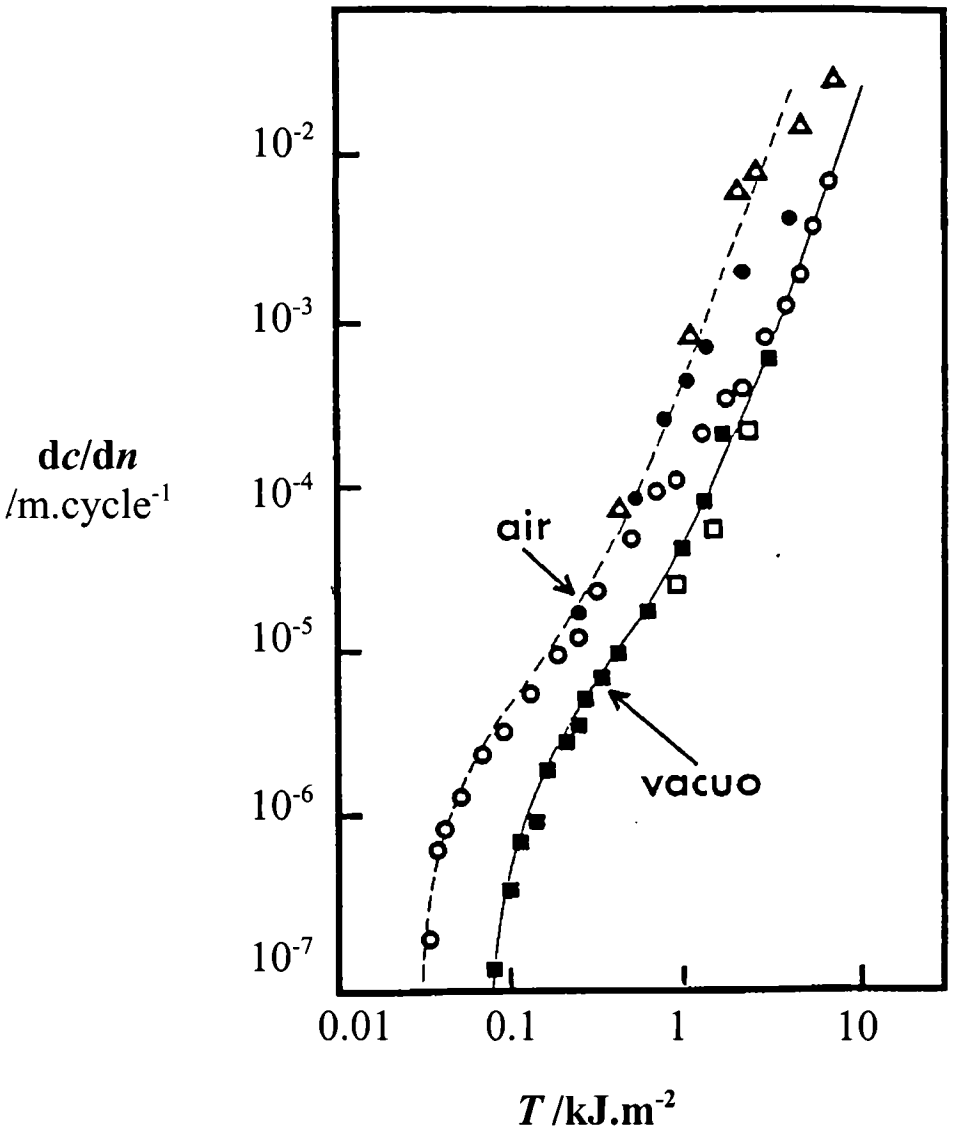

Figure 2.4-3 Effect of atmosphere and frequency on cyclic crack growth in NR containing no added anti-flex cracking agent. Experiments at atmospheric pressure; o, approximate frequency 2 Hz; ●, 0.02 Hz; Δ, 0.0002 Hz. Experiments in vacuo (<10^{-2} torr): ■, 2 Hz; □, 0.02 Hz[74].

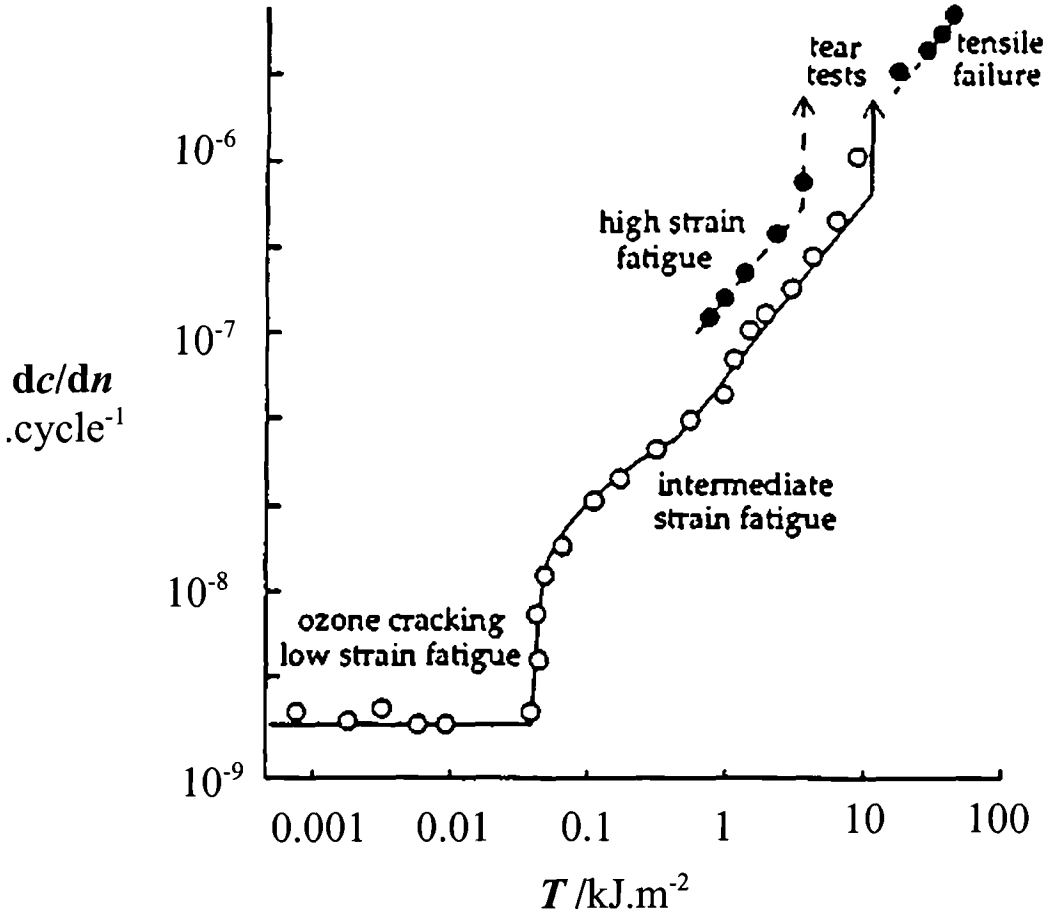

Figure 2.4-4 Cyclic crack growth characteristics for a NR compound with the indication of the different type of failure to which the different regions are relevant. The behaviour illustrated at the highest tearing energies takes place when the bulk of the elastomer has become partially crystalline; if this had not occurred, different behaviour is observed, with the growth rate accelerating considerably in the region denoted "tear test" and becoming time dependent above this[76].

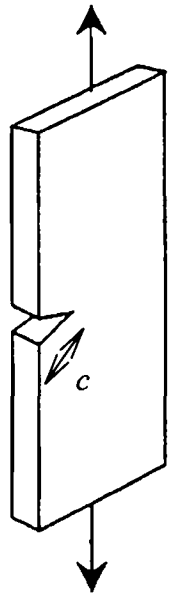

Figure 2.4-5 Tensile strip test piece with an edge crack of length *c*.

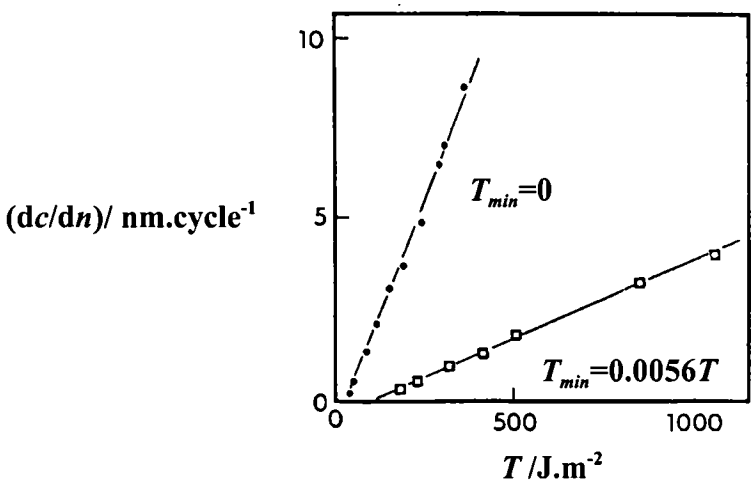

Figure 2.4-6 Effect of non-zero minimum tearing energy (non-relaxing conditions) on cyclic growth in NR. Cyclic crack growth rate d*c*/d*n* versus maximum tearing energy T of the cycle with minimum tearing energy, T_{min}, zero and with T_{min} equal to 5.6% of the maximum[85].

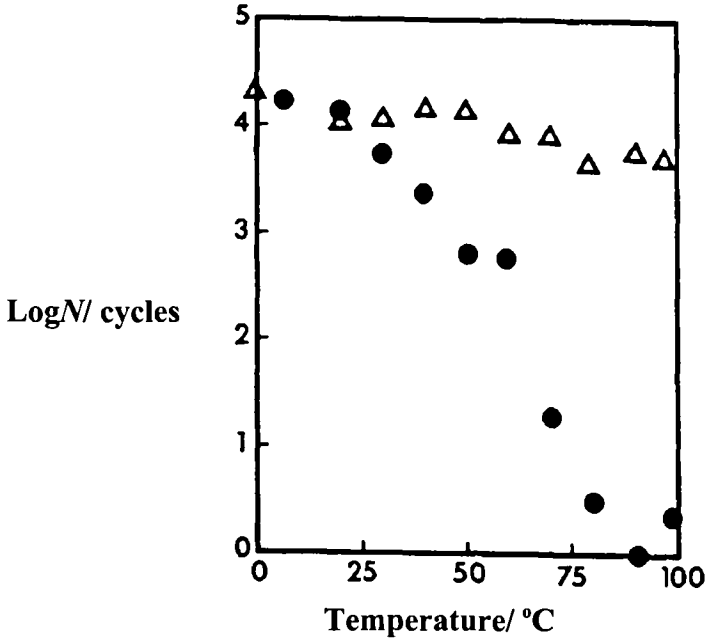

Figure 2.4-7 Effect of the temperature on the dynamic fatigue life of dumbell test-pieces at 1000 cycles/minute:●, SBR at 175% maximum strain; Δ , NR at 250% maximum[82].

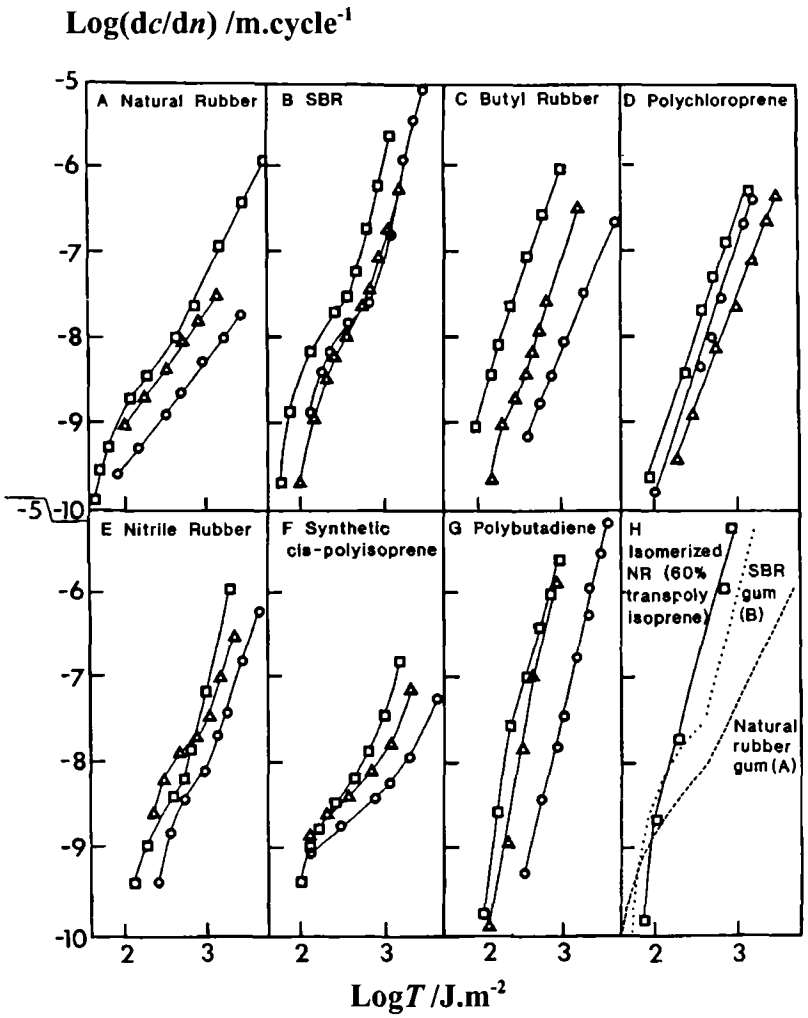

Figure 2.4-8 Mechanico-oxydative crack growth characteristics of compounds from different polymers:□, unfilled; △, with 50 pphr MT carbon black;○, with 50 pphr HAF carbon black at room temperature[72].

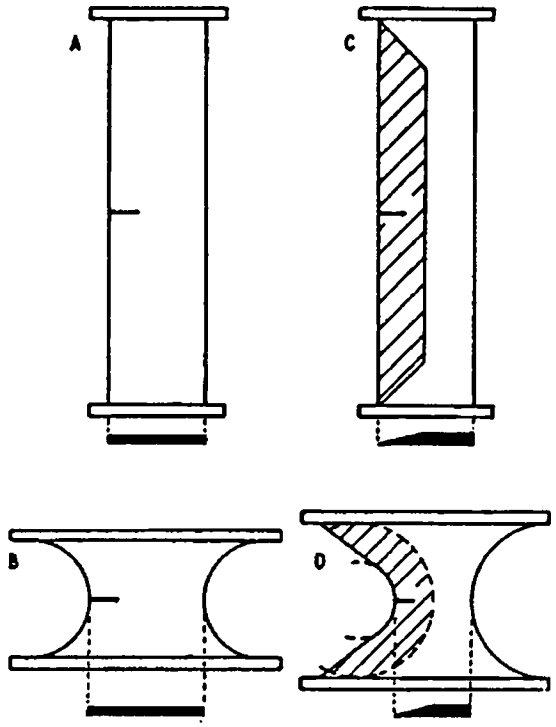

Figure 2.5-1 A Simple-extension strip. B Semicircular test-piece. C Simple-extension wedge. D Semicircular wedge. Cross-sections along the line of the cracks are shown solid. Wedge areas are hatched[79].

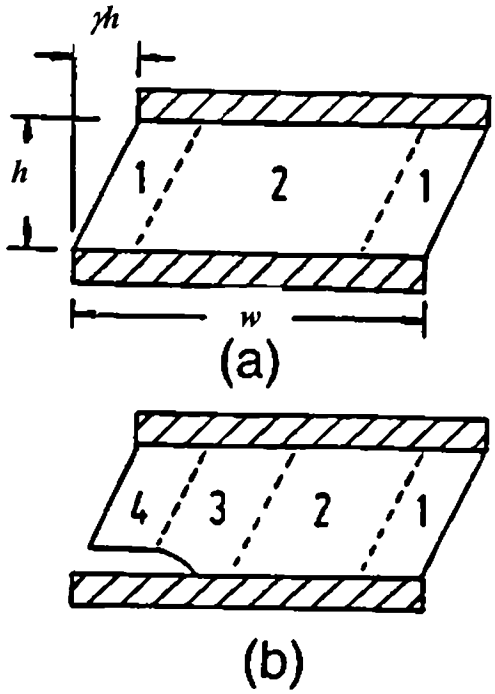

Figure 2.5-2 Bonded unit subjected to simple shear strain γ: (a) with no crack and (b) with a crack adjacent to a bonded surface[90].

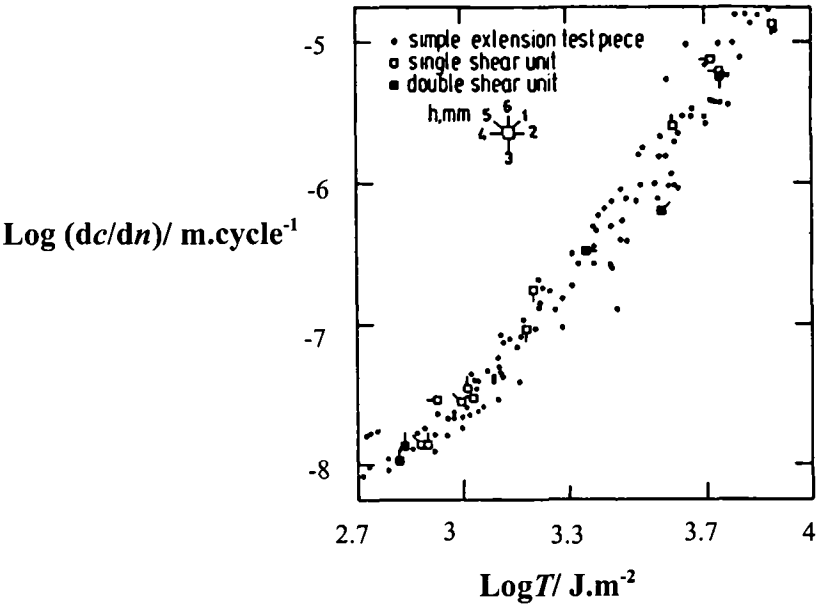

Figure 2.5-3 Comparison of crack growth rate d*c*/d*n* as a function of tearing energy *T* using unfilled NR for plane stress specimen (simple extension test-piece) and plane strain (single and double shear unit)[90]. *h* refers to the dimension showed in Figure 2.5-2.

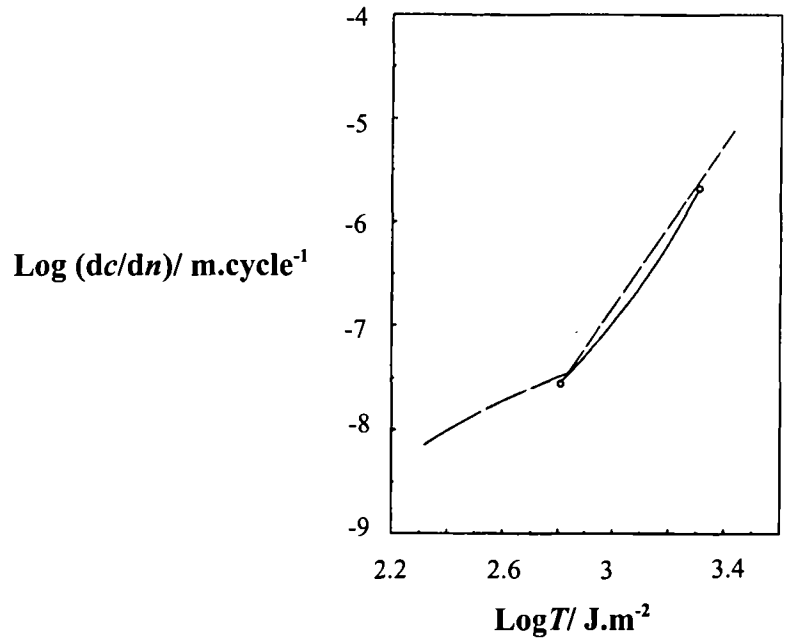

Figure 2.5-4 Crack growth rate d*c*/d*n* as a function of tearing energy *T* for a circumferentially cracked circular cylinder in torsion for a 50 pphr carbon black filled SBR (line)[92] compared with results in tension (broken curve)[72].

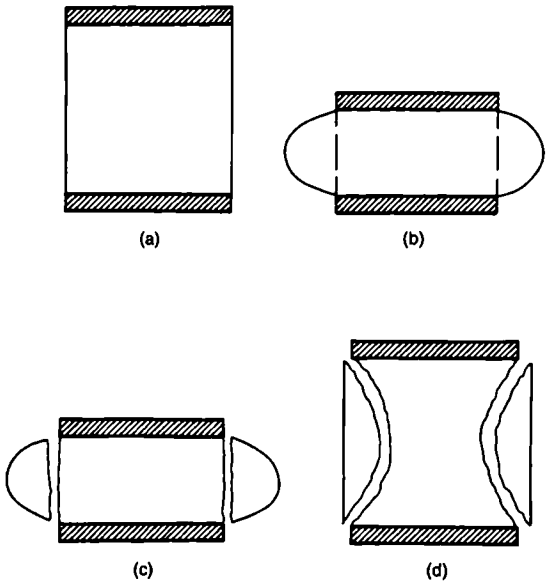

Figure 2.5-5 Typical stages of crack growth in compression: (a) unstrained; (b) compressed-crack initiation at bound edges; (c) compressed-bulge seperates from core; (d) unstrained -showing parabolic crack locus[93].

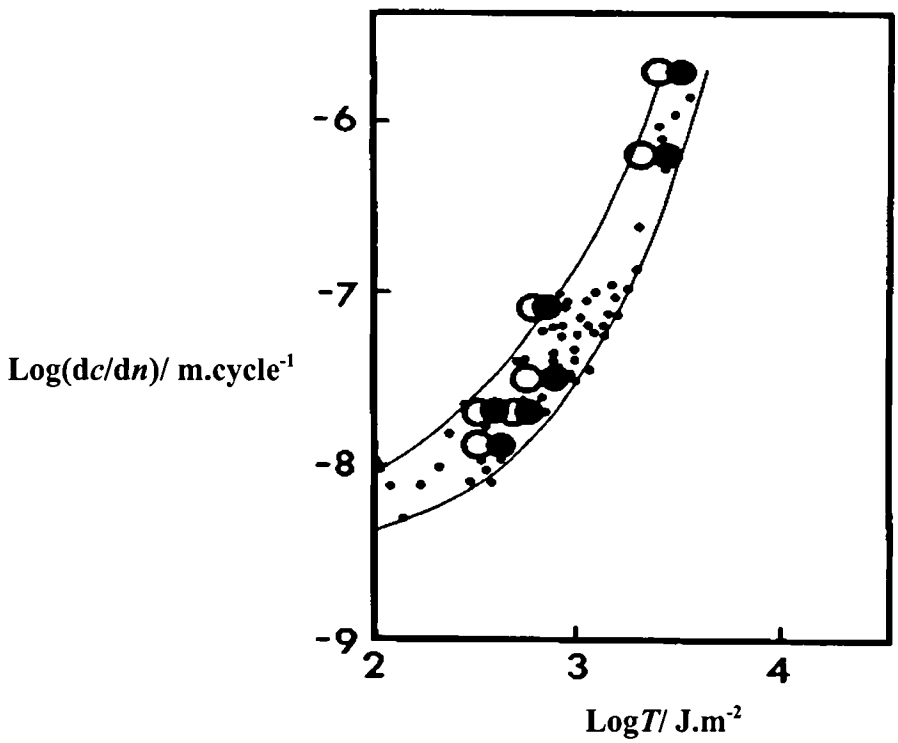

Figure 2.5-6 Crack growth rate as a function of tearing energy :●, compression-experimental results; ○ compression-theoretical results; •, simple extension-experimental results[93].

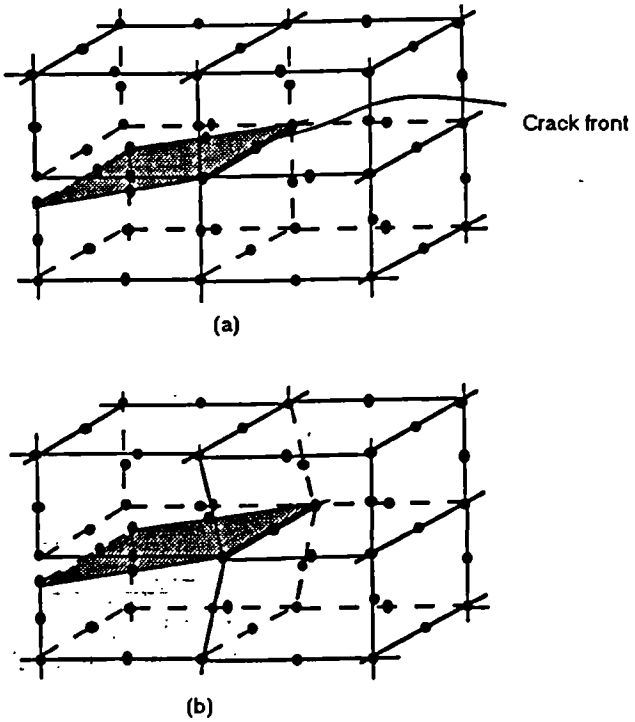

Figure 2.5-7 Finite element model around the crack front using 20-node quadratic isoparametric elements showing the virtual crack extension method: (a) crack front prior to extension, (b) virtual extension of the crack front[97].

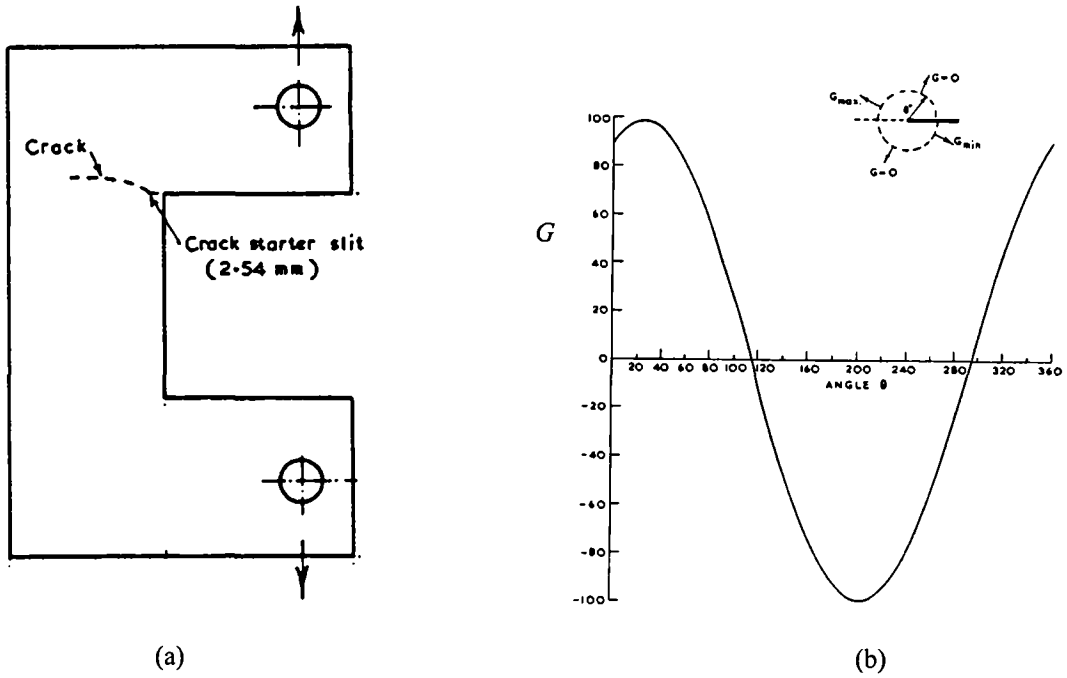

Figure 2.5-8 (a) Geometry used by Hellen[94]. (b) Plot of G (energy release rate normalised to 100) against angle of crack propagation.

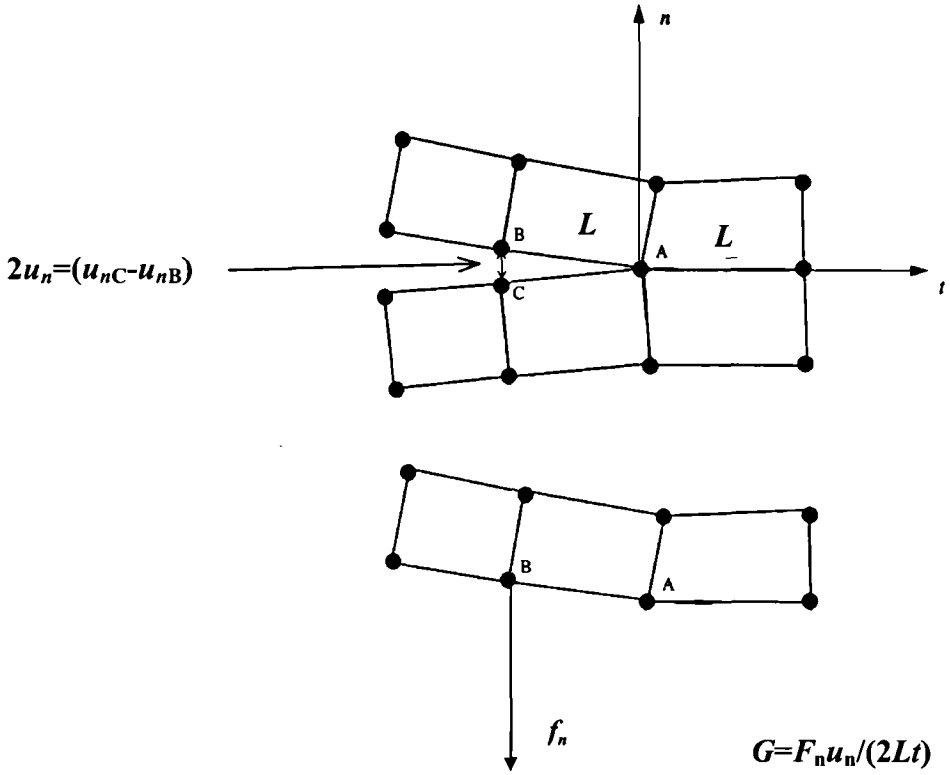

Figure 2.5-9 Virtual crack closure for a 2-D model.

REFERENCES

[1] Kuhn K., *Kolloid-Z.*, **76**, 258 (1936).

[2] Treloar,L. R. G., *Trans. Faraday Soc.*, **39**, 36 (1943).

[3] Treloar L.R.G., "The Physics of Rubber Elasticity", Oxford Univ. Press, 3rd ed. **4**, 59 (1975).

[4] Love A. E. H., "The mathematical Theory of Elasticity", 4th ed., Cambridge University Press (1927).

[5] Rivlin R. S., "Rheology vol. 1", Eirich, F.R. Ed, Academic Press, New-York, **10,** 351 (1956).

[6] Rivlin R. S., *Rubber Chem. Technol.* **65**, G51 (1992).

[7] Rivlin R. S., *Phil. Trans Roy. Soc.* A, **242**, 173 (1949).

[8] Wang M. C. and Guth E., *J. Chem. Phys.*, **20**, 1144 (1952).

[9] Krigbaum W. R. and Koneko M., *J. Chem. Phys.*, **36**, 99 (1964).

[10] Ball R. C., Doi M., Edwards S. F. and Warner M., *Polymer*, **22**, 1011 (1981).

[11] Prager S. and Frish H. L., *J. Chem. Phys.*, **46**, 1475 (1967).

[12] Gent A. N. and Rivlin R. S., *Proc. Phys. Soc.* B, **487** (1952).

[13] DiMarzio E. A., *J. Chem. Phys.*, **36**, 1563 (1962).

[14] Mooney M., *J. Appl. Phys.*, **11**, 582 (1940).

[15] Yeoh O. H., *Rubber Chem. Tehnol.*, **63**, 792 (1990).

[16] Charlton D. J., Yang J. and Teh K. K., *Rubber Chem. Technol.*, **67,** 481 (1994).

[17] Tschoegl N. W., *Rubber Chem. Technol.*, **45**, 60 (1972).

[18] James A. G. and Green A., *J. Appl. Polym. Sci.*, **19**, 2319 (1975).

[19] Gregory M. J., *Plastics and Rubber: Materials and Applications,* **4,** 184 (1979).

[20] Kabatawa A. and Kawai H., *Adv. Polym. Sci., 24*, 89 (1977).

[21] Seki W., Fukahori Y., Iseda Y. and Matsunuga T., *Rubber Chem. Technol.*, **60**, 856 (1987).

[22] Fukahori Y. and Seki W., *Polymer*, **33**, 502 (1992).

[23] Davies C. K. L., De D. K. and Thomas A. G., *Rubber Chem. and Technol.*, **67**, 716 (1994).

[24] Natural rubber engineering data sheets, MRPRA, Hertford, UK (1987).

[25] Stacer R.G., Hubner C. and Husband D. M., *Rubber Chem. Technol.*, **63**, 488 (1990).

[26] Verga O. H., "Stress-strain behaviour of Elastic materials", John Wiley and Sons, New-York (1966).

[27] Ogden R. W., *Rubber Chem. Technol.*, **59**, 361 (1986).

[28] Valanis K. C. and Landel R. F., *J. Appl. Phys.*, **38**, 2997 (1967).

[29] Rivlin R. S. and Sawyers K. N., *Trans. Soc. Rheo.*, **20**, 545, (1976).

[30] Gent A. N., *Rubber Chem. Technol.*, **69**, 59 (1996).

[31] Mullins L., *Rubber Chem. Technol.*, **42**, 339 (1969).

[32] Harwood J. A. C., Mullins L. and Payne A. R., *J. Polymer Sci.*, **B3**, 119 (1965).

[33] Bueche F., *J. Polymer Sci.*, **4**, 107 (1960).

[34] Harwood J. A. C., Mullins L. and Payne A. R., *J. Appl. Polym. Sci.*, **9**, 3011 (1965).

[35] Kawabata S., Yamashita Y., Ooyama H. and Yoshida S., *Rubber Chem. Technol.*, **68**, 311 (1995).

[36] Gent A. N. and Kim H. J., *Rubber Chem. Technol.*, **51**, 35 (1978).

[37] Hawkes J., Harris J., Stevenson A., Becker E., Miller T. and McMullen R., *Proceedings of the International Rubber Conference*, Manchester (1996).

[38] Chow C. L. and Cundiff C. H., *Tire Sci. Technol.*, **15**, 73 (1987).

[39] Westergaard H. M., *J. Appl. Mech.*, **61**, A49-A53 (1939).

[40] Rice J. R., *J. Appl. Mech.*, **35**, 379 (1968).

[41] Griffith A. A., *Phil. Trans. Roy. Soc. London* A, **221**, 163 (1920).

[42] Rivlin R. S. and Thomas A. G., *J. Polym Sci.*, **10**, 291 (1953).

[43] Rice J. R., *Fracture*, Ed. by Liebowitz, Academic Press, **2**, 191 (1968).

[44] Chang S. J., *Z. Angew. Math. Phys.*, **23**, 149 (1972).

[45] Thomas A. G., *J. Appl. Polym. Sci.*, **3, 8,** 168 (1960).

[46] Lake G. J., Lindley P. B., and Thomas A. G., *Proceedings of the International Conference on Fracture,* Brighton (1969).

[47] Thomas A. G., *J. Polym. Sci.*, **18**, 177 (1955).

[48] Lake G. J. and Thomas A. G., *Proc. Roy. Soc. London* A, **300**, 108 (1967).

[49] Lake G. J. and Lindley P. B., *J. Appl. Polym. Sci.*, **9**, 1233 (1965).

[50] Bhoumick A. K., Gent A. N. and Pulford P., *Rubber Chem. Technol.*, **56**, 226 (1982).

[51] Tsunoda K., Busfield J. J. C., Davies C. K. L. D. and Thomas A. G., (in press) Submitted to *J. Mat. Sc.* (2000).

[52] Mullins L., *Trans. Inst. Rubber Ind.*, **35**, 213 (1959).

[53] Williams M. L., Landel R. F. and Ferry J. D., *J. Amer. Chem. Soc.*, **77**, 3701 (1955).

[54] Gent A. N. and Henry A. W., *Proceeding of the International Rubber Conference,* Brighton, 193 (1967).

[55] Stacer R. G., Von Meerwall E. D., and Kelley F. N., *Rubber Chem. Technol.*, **58**, 913 (1985).

[56] Andrew E. H., *Rubber Chem. Technol.*, **36**, 325 (1963).

[57] Andrews E. H., *Proc. Roy. Soc. London* A, **277**, 562 (1964).

[58] Glucklich L. and Landel R. F., *J. Appl. Polym. Sci.*, **20**, 121 (1976).

[59] Greensmith H. W., *J. Polymer Sci.*, **21**, 175 (1956).

[60] De D. and Gent A. N. *Rubber Chem. Technol.*, **69**, 834 (1996).

[61] Andrews E. H., *J. Appl. Phys.*, **32**, 542 (1961).

[62] Hamed G. R, Kim H. J. and Gent A. N., *Rubber Chem. Technol.*, **69**, 807 (1996).

[63] Hamed G. R. and Zhao J., *Rubber Chem. Technol.*, **71**, 157 (1998).

[64] Kendall K., *Proc. R. Soc. London* A, **344**, 287 (1975).

[65] Andrews E. H., *J. Mech. Phys. Solids*, **11**, 231 (1963).

[66] Medalia A. I., paper no 1 presented at a meeting of the Rubber Division, American Society, New-York, NY, April 8-11, (1986).

[67] Greensmith H. W., *J. Polymer Sci.*, **21**, 175 (1956).

[68] Liebowitz H., "Fracture", Ed. by Eirich F. R. and Smith L.T., Academic Press, New-York, **7**, 411 (1972).

[69] Gent A. N. and Lindley P. B., *Proc. Roy. Soc. London* A, **249**, 195 (1958).

[70] Bhowmick A. K., "Fractography of rubbery materials", Ed. by Bhowmick A. K. and De S. K., Elsevier Applied Science, **4**, 101 (1991).

[71] Gent A. N., Lindley P. B., and Thomas A. G., *J. Appl. Polymer Sci.*, **8**, 433 (1964).

[72] Lake G. J., and Lindley P. B., *Rubber J.*, Oct, 24 and Nov., 30, **146** (1964).

[73] Gent A. N., *J. Appl. Polym. Sci.*, **6**, 497 (1962).

[74] Lake G. J., *Rubber Chem. Technol.*, **45**, 309 (1972).

[75] Gent A. N and Hindi M., *Rubber Chem. Technol.*, **63**, 123 (1990).

[76] Lake G. J., *Rubber Chem. Technol.*, **68**, 435 (1995).

[77] Thomas A. G. and Whittle J. M., *Rubber Chem. Technol.*, **43**, 222 (1970).

[78] Derham C. J., Lake G. J. and Thomas A. G., *Rubber Int. Malaysia*, **22**, 191 (1969).

[79] Lindley P. B., *J. Strain Anal.*, **7**, 132 (1972).

[80] Lake G. J., *Prog. Rubber Technol.*, **45**, 89 (1983).

[81] Greensmith H. W., *J. Appl. Polym. Sci.*, **7**, 993 (1963).

[82] Lake G. J. and Lindley P. B., *J. Appl. Polym. Sci.*, **8**, 707 (1964).

[83] Young D. G., *Rubber Chem. Technol.*, **59**, 809 (1986).

[84] Cadwell S. M.,Merrill R. A., Sloman C. M. and Yost F. L., *Ind. Eng. Chem., Anal. Ed.*, **12**, 19 (1940).

[85] Lake G. J and Thomas A. G., "Engineering with rubber, How to design rubber components", Ed. by Gent A. N., Hanser Publishers, **5**, 95 (1992).

[86] Ellul M. D., "Engineering with rubber, How to design rubber components", Ed. by Gent A. N., Hanser Publishers, **6**, 129 (1992).

[87] Gent A. N., "Science and Technology of Rubber", Ed. by Eirich F. R., Academic Press, New-York, **10**, 419 (1956).

[88] Young D. G. and Danik J. A., *Rubber. Chem. Technol.,* **67**, 137 (1993).

[89] Yanyo L. C., *Int. J. Fracture*, **39**, 103 (1989).

[90] Lindley P. B. and Teo S. C., *Plastics and Rubber: Materials & Applications*, **4**, 29 (1979).

[91] Aboutorabi H., Ebbott T., Gent A. N. and Yeoh O. H., *Rubber Chem. Technol.,* **71**, 76 (1997).

[92] De D. K. and Gent A. N., *Rubber Chem. Technol.,* **71**, 84 (1997).

[93] Stevenson A., *Int. J. Fract.*, **23**, 47 (1983).

[94] Hellen T. K., *Int. J. Numer. Meth. Engng.*, **9**, 187 (1975).

[95] Parks D. M., *Int. J. Fracture* **10**, 487 (1974).

[96] Parks D. M., *Comput. Meth. Appl. Mech. Engng.*, **12**, 353 (1977).

[97] Pidaparti R. M. V., Yang T. Y. and Soedel W., *Int. J. Fracture,* **39**, 255 (1989).

[98] Claydon P. W., *Engng. Fracture Mech.*, **42**, 961 (1992).

[99] Irwin G. R., "Fracture", *Handbuch der Physik,* **6**, 551 (1958).

[100] Rybicki E. F. and Kamminen M. F., *Engng. Fracture Mech.*, **9**, 931 (1977).

[101] Ebbott T. G., presented at the twelfth annual meeting of the Tire Society, The University of Akron, Akron, OH, March 23-24 (1993).

[102] Rice J. R., *J. Appl. Mech.*, **35**, 379 (1968).

[103] De Lorenzi H. G., *Int. J. Fracture,* **19**, 183 (1982).

[104] Shish C. F., *Int. J. Fracture,* **39**, 79 (1986).

[105] Schallamach A., *Wear,* **1**, 384 (1958).

[106] Gent A. N. and Pulford C. T. R., *J. Mater. Sci.*, **9**, 3612 (1984).

[107] Deuri A. S. and Bhowmick A. K., *J. Appl. Polym.*, **35**, 327 (1988).

[108] Thavamami P. and Bhowmick A. K., *J. Mater. Sci.*, **28**, 1351 (1993).

[109] Fukahori Y. and Andrews E. H., *J. Mater. Sci.* **13**, 777 (1978).

[110] Ganesan L., Bhattacharrya P. and Bhowmick A. K., *Rubber Chem. Technol.*, **68**, 144 (1994).

[111] Greensmith H. W., *J. Appl. Polym. Sci.*, **3**, 183 (1960).

[112] Cho K., Jang W. J., Lee D., Chun H. and Chang Y-W., *Polymer*, **41**, 179 (2000).

[113] Rivlin R. S., *Phil. Trans* A, **241**, 379 (1948).

[114] Rivlin R. S., *Proc. Roy. Soc.* A, **195**, 463 (1949).

[115] Deeprasertkul C., Ph.D. Thesis, University of London (2000).

[116] De D. K., Ph.D. Thesis, University of London (1994).

[117] Greensmith H. W. and Thomas A. G., *J. Polymer Sci.*, **18**, 189 (1955).

Maso mahita tsy mi tondra mody

(*Malagasy proverb: "Eyes that can see will not bring you home")*

3

Experimental approach and procedures

3.1 Introduction

In section 2.6 the proposed programme of study which will constitute the main body of this thesis was described. This chapter details the experimental procedures utilised to carry out this study. As the main application of the results of this work will be to anti-vibration devices, the main materials used are commercial engineering compounds. Typically these compounds are Natural Rubber (NR), filled with various amount of carbon black, as supplied by BTR-AVS. In addition carbon black filled Styrene Butadiene Rubber (SBR), supplied by TARRC (Tun Abdul Razak Research Centre) formerly known as MRPRA (Malaysian Rubber Producer Research Association) will be studied to obtain comparative data from a non-strain crystallising elastomer. The experimental work will consist of stress-strain measurements with the purpose of mechanically characterising these materials as well as to obtain results by loading them in a range of non-simple deformations. Fatigue crack growth rate measurements in simple and more complex loadings will be carried out in parallel with fractography studies which will consist of SEM examination and roughness estimations of the fractured surfaces. The only experimental work not described in this section but referred to in the programme of study, in section 2.6, are the FEA investigations and the predictions for the crack growth behaviour which will be presented in Chapter 5.

3.2 Materials and formulations

The base elastomers used in this study were either Natural Rubber (NR), cis 1,4 polyisoprene, or poly-styrene-butadiene rubber (SBR), whose respective repeat units are shown diagrammatically in Figure 3-1 and Figure 3-2. NR is a strain-crystallising elastomer in contrast to SBR which is a random co-polymer of styrene and butadiene which does not crystallise because the phenyl unit along the polymer chain causes a steric hindrance effect when the elastomer molecule is stretched. These polymers behave as viscous fluids and need to be cross-linked (or vulcanised) to form 3-D networks which exhibit the highly elastic mechanical properties described in the previous chapter. The cross-linking reactions consists of forming mainly covalent bonds, sulphur bonds in the present case, between different elastomer chains (Figure 3-3). These cross-linking reactions, are accelerated using accelarator/activator ingredients which are usually a combination of a fatty acid (generally stearic acid), zinc oxide and accelerators. The combination of the vulcanising agent (sulphur), the activators and accelerators is frequently called the vulcanising system. Table 3-1 details the formulation of the unfilled and the carbon black filled elastomers used in this work. The cross-links consist either of mono-, di-, or polysulfide covalent bonds and the proportions of these different bonds depends in a complex manner on several parameters due to the complexity of the chemical reactions involved.

According to the formulation shown in Table 3-1, there were 2 types of vulcanising systems. NR21 and NR29 contain a higher ratio accelerators to sulphur compared to the other compounds. This type of vulcanising system, usually called efficient vulcanising (EV) system, will have a network predominantly containing monosulphidic cross-links. The other compounds is called a conventional vulcanising system with a network predominantly containing polysulphidic cross-links.

Two types of carbon black were used in this study. The first one called HAF (High Abrasion Furnace) or N330 according to the ASTM (American Society for Testing Materials) number, is the product of incomplete combustion of organic material (oil or coal tar) and is the most commonly used filler in elastomers for engineering purposes. HAF designates the grade of this carbon black meaning a particle diameter of 25-40 nm. It is a reinforcing carbon black because of its ability to form a filler network on top of the elastomer network and because of its extent of

interaction with the elastomer. The other filler used in this study is called MT (Medium Thermal) or N990 according to the ASTM number and is the product of thermal decomposition of oil in the absence of oxygen. It is a non-reinforcing carbon black, having a large particle size diameter between 200-500 nm.

Three carbon black-filled NR elastomers NR21, NR29 and NR59 containing respectively 21, 29, 59 pphr (parts per hundred rubber by mass) of HAF carbon black and two SBR elastomers, SBR30 and SBR50, respectively filled with 30 pphr HAF carbon black and with 50 pphr MT were chosen for this work. SBR materials filled with reinforcing carbon black tend to behave like crystallising elastomers, while SBR materials filled with non-reinforcing carbon black do not. The reinforcing and non-reinforcing carbon blacks were both used in the SBR materials to make a comparison of these relative effects.

The physical properties of the elastomer network depend to a large extent on the cross-link density. Hence, the choice of the appropriate compounds among the large number of compounds available from BTR-AVS and TARRC to keep this cross-link density constant is crucial as the carbon black content and the ability to strain-crystallise were to be used as the material variables in this work. This is not an easy task as commercial compounds are formulated to fulfil specific requirement from customers. The actual cross-link densities $[X]_{act}$ for each of the chosen compounds, whose determination will be detailed later, are given in Table 3-1. These values were in general around 10×10^{-5} mole.g^{-1} RH (rubber hydrocarbon) except for NR21 which had a lower value of 6.7×10^{-5} mole.g^{-1} RH. Using Equation 2.2-20 in Chapter 2, such a difference in the cross-link density could be estimated as a 50% drop in the shear modulus, from 0.45 to 0.3 MPa. This fact will be then taken into account when discussing the results.

3.3 Sample preparations

The NR materials were mixed at BTR-AVS with the formulations given in Table 3-1 and were moulded at QMW using an electrically heated press. The SBR compounds were mixed and moulded at TARRC. The vulcanisation process was carried out using compression moulds in order to obtain flat sheets used for tensile and pure shear test specimens. A pressure of 20 MPa was applied and the temperature

was controlled on the top and bottom platens and inside the mould using three thermocouples. The uniformity of the temperature between the two platens is important as it could affect the uniformity of the cross-link density throughout the flat sheet. The temperature of each platen was controlled at an accuracy of $\pm 2^{\circ}C$ and the differences in temperature between the two platens did not exceed 4°C. A significant effect on the cross-link density was observed for some initial samples where temperature differences higher than 10°C between the two platens was recorded. An example of a possible effect on crack growth, when the temperature was not monitored properly, is seen in Figure 3-4 and Figure 3-5. These specimens correspond to longitudinally pre-strained pure shear (25% strain) for a tearing energy T=1500 $J.m^{-2}$. Figure 3-4 shows some elastomer threads observed on one side of the fatigue pure shear specimen between the fracture surfaces. Figure 3-5 shows on the same specimen angled crack front signifying a variation in crack growth rate from one side to the other side of the test-piece. Effectively, one side, the one exhibiting the threads, did not show any crack propagation while the other did (Figure 3-5 region A) and the two crack fronts joined together when a larger deformation was applied (Figure 3-5 region B). It hence appeared that one side of the test-piece was stronger than the other and this was attributed to significant differences in curing temperatures between the two platens when moulding the flat sheet.

The size of the flat sheets was $195 \times 195 \times 2\text{-}2.5$ mm. The curing times and temperatures used were 10 minutes and 155°C for all the NR elastomers and 60 minutes and 150°C for the SBR elastomers. These vulcanisation times were determined using an oscillation disc cure meter.

3.4 Determination of the cross-link density

Equilibrium swelling was a suitable method for investigating the cross-link density of the carbon black filled elastomers and to check the consistency of the cross-link densities of different moulded flat sheets from batch to batch. The elastomer specimens were weighed in air accurately using an electronic analytical balance and were then immersed in n-decane. The change in mass of the elastomer samples was recorded as a function of time. The volume of solvent absorbed was calculated from the difference between the mass of the swollen and the unswollen samples. Hence, the volume fraction of elastomer in the swollen elastomer network was calculated using the following equation.

$$V_{rn} = M_0 \frac{M_{rn}}{M_t} \rho_{RH} \qquad (3\text{-}1)$$

Where V_{rn} is the volume of the elastomer network, M_0 the mass of the elastomer specimen, M_{rn} is the mass of the elastomer hydrocarbon *(RH)* and the sulphur combined, M_t is the total mass of mix formulation, and ρ_{RH} is the density of elastomer hydrocarbon which is equal to 0.92g/cm^{-3}. The volume fraction of the elastomer was calculated, knowing the volume of the elastomer network V_{rn} from Equation 3-1:

$$v_r = V_{rn}/(V_{rn} + V_s) \qquad (3\text{-}2)$$

where V_s is the volume of solvent absorbed. V_s is obtained from the mass uptake after swelling. The cross-link density was determined using the Flory-Rehner equation[1] which expresses the swelling condition as a balance between the free energy increase due to the mixing and the configurational entropy decrease due to the expansion of the network:

$$\ln(1 - v_r) + v_r + \kappa v_r^2 + 2\rho_{RH} V_0 [X]_{phy} (v_r)^{1/3} = 0 \qquad (3\text{-}3)$$

where V_0 is the molar volume of the solvent, 195.88 cm^3 for n-decane and κ is the elastomer/solvent interaction parameter, equal to 0.42 and 0.64 respectively for NR/n-decane and SBR/n-decane. $[X]_{phys}$ is the sum of the chemical cross-links (covalent bonds either carbon-carbon or sulphur-carbon) and the physically manifested cross-links (chain entanglements or physical bonds). For a network containing tetra-functional cross-links only, the number of network chains is twice the number of cross-links. If M_c is called the average molecular mass between cross-links, the cross-link concentration expressed in mole of cross-links per gram of rubber hydrocarbon is given by:

$$[X]_{phys} = \frac{1}{2M_c} \tag{3-4}$$

However, the carbon black itself had been observed[2] to restrict the mobility of the elastomer during the swelling process and would hence give larger apparent values of $[X]_{phys}$ than the actual values of $[X]_{phys}$ observed for corresponding unfilled elastomers. Porter[2] developed an empirical relationship which corrected the physical cross-link density in carbon black (HAF) filled elastomers:

$$[X]_{act} = \frac{[X]_{phy}}{(1 + K\Phi)} \tag{3-5}$$

where $[X]_{act}$ is the actual physical cross-link density in the vulcanised network and K is a numerical constant, characteristic of the filler, equal to 2.6 for HAF carbon black and Φ is the volume fraction of the carbon black. Equation 3-5 was used here to calculate the actual cross-link densities of the carbon black filled elastomers given in Table 3.1. While this procedure works well for elastomers filled with a reinforcing HAF carbon black it will result in an underestimation of the cross-link density for the SBR materials containing the non-reinforcing carbon black (MT).

3.5 Mechanical testing techniques

All the mechanical tests were carried out at room temperature, nominally 20°C. Tensile and pure shear test-pieces were cut with a die-stamp from the moulded flat sheets. The thickness of these sheets was measured with a dial gauge. The accuracy of the thickness measurement was estimated to be 2-2.5 ± 0.02 mm. All the mechanical tests are performed on an Instron n° 1122 with a 5KN capacity load cell, at roughly the same strain rate of 50 % per minute for the various test pieces. It had been checked that at this strain rate, the load cell was capable of giving a true reading of the load by stopping a running test and by verifying that the load reading did not continue to rise.

The load cell was always calibrated with weights before any new test. Weights were hung on the load cell and the readings were compared with the forces generated by the weights. During a test the force-time curves were recorded on a Phillips X-Y plotter using the outputs from the Instron load cell for the Y-axis and a set pen speed on the plotter for the X-axis. The displacement on the graph was converted into displacement of the cross-head and then into sample strain using the appropriate scaling factor.

Tensile Test

The dimensions of the parallel-sided specimens, $100 \times 10 \times 2\text{-}2.5$ mm were measured as the average of 5 measurements of each dimension, with the following accuracy: 100 ± 1 mm for the height and 10 ± 0.1 mm for the width. A Vernier was used for the width and the length between the grips. Two gauge marks parallel to one another were drawn 100 mm apart using a silver pen. The sample was clamped along one of those lines by the upper grip which was attached to the load cell. The lower grip was used to clamp the sample along the other line. Two screws along with two springs on each grip were used to clamp the sample (Figure 3-6). With this type of test piece, the grip separation can be used as a fair measure of the sample elongation, if the initial length between the grips was determined accurately, provided no slippage from the grips occurred during testing. To avoid any slippage, the grips had to be carefully tightened. This tightening is always accompanied by a small change in the zero force due to a compressive force on the elastomer generated by the grips. This

compressive force was balanced off by moving the cross-head down slowly to attain again zero force. If the screws were tightened excessively, which created a large compressive force that made it difficult to measure the unstrained height and which led to an early failure of the specimen in that region.

Pure shear test

Pure shear deformation, illustrated previously in Figure 2.2-2 in Chapter 2, is achieved by straining a rectangular sheet in its height direction, to produce an extension ratio λ_1, while maintaining the perpendicular or transverse dimension unchanged (λ_2=1). Pure shear deformation requires the application of a tensile force F_1 in one direction and F_2 in the transverse direction. However, if the width of the sheet is very much longer (minimum 6 times) than its height then the direct application of a transverse force is not required, the force being automatically generated as a result of the restraints introduced by the grips. Except in the immediate vicinity of the free edges, the state of strain in such a test piece is a substantially uniform homogeneous pure shear.

The dimensions of the test-pieces used in this study were 175 or 240 mm in width (according to the grips used) ×18-22 mm in height ×2-2.5 mm in thickness. Therefore the specimen width was approximately 10 times the height. The dimensions were measured using the same procedure adopted for the tensile test specimens. The unstrained height was measured at 4 different positions along the grips using a Vernier. For each test condition, four specimens were tested. Tests were carried out at a strain rate of 10 mm/minute (50% strain per minute if the unstrained height was exactly 20mm). As with the tensile test, the gripping constituted a significant experimental difficulty. The same adjustments were necessary to compensate for the compressive forces. Because of the width of the geometry, grips non-uniformly tightened or inaccurate parallelism of the grips can lead to a non-homogeneous stress-field in the specimen and make it more difficult to determine the unstrained height hence rendering the obtained stress-strain curve less accurate.

Pre-strained pure shear test piece

Strips were cut from flat sheets of the following dimensions: 175 or 240 mm in width (according to the grips used) ×25-40 mm in height (according to the amount

of pre-straining) ×2-2.5 mm in thickness. They were then clamped and stretched along the longitudinal direction with a one sided sliding rectangular frame. The strip of pre-strained elastomer was then gripped along its free edges with the pure shear grips as in Figure 3-7. The pre-strained test-piece was then extracted from the frame by cutting at the pure shear grip ends. The pre-strain remains applied due to the constraint of the grips except in the immediate vicinity of the edges. The state of strain in such a test piece is substantially uniform homogeneous (longitudinally) pre-strained pure shear. An example of the extent of this homogeneous deformation state on a 100% pre-strained sample is shown on Figure 3-8 where grid lines that were initially spaced 5 mm were drawn on the specimen. The region of homogeneous pre-strained pure shear can be estimated as the region where the vertical grid lines (5 mm apart) are straight which corresponds to the region approximately 6 spacings, i.e. 30 mm away from the edges. This edge zone will be re-evaluated more accurately in Chapter 5 using FEA techniques.

As the edges were in a complex deformation state, as the buckling of the edges demonstrated (Figure 3-8), when the test-piece was set onto the jigs of the Instron to perform force-displacement measurements, difficulties arose. The situation is illustrated in Figure 3-9 which shows the profile view of the set-up. Because of the compressive forces and the free rotation of the upper jig about the long axis of the test-piece, the zero force position is obtained with the axis of the upper and lower jigs misaligned at a maximum angle of 15° from the vertical. The determination of the unstrained height, measured at 4 different positions between the grips using a vernier, is then underestimated. This was readily seen when a test is carried out, as the initial slope of the force displacement curve was not representative of the stiffness of the material due to the realignment of the jigs. This was much lower than that exhibited by the real stiffness of the material at higher strains, as shown in the experimental curve on Figure 3-10. The starting point of the curve is not for an extension ratio of 1 but below, nominally $1/\sqrt{\lambda_1}$, λ_1 being the longitudinal extension ratio due to the pre-strain (50% in Figure 3-10). The correction on the stress-extension ratio curve consisted in increasing the measured unstrained height such that the stress-extension ratio curve shows a continuously decreasing modulus at small strains and that the initial data was unaltered at high strain. This correction of the unstrained height was

estimated on the force-deflection curve shown in Figure 3-11. This was done systematically for all materials and all pre-strains.

The initial height L_0' (the prime sign signifying that initial height is measured in the deformed state) after the pre-strain was applied varied from 19-26 mm depending on the magnitude of the pre-strain. For each test condition, four specimens were tested, and tests were again carried out at an extension ratio of 10 mm/min.

30° inclined pure shear test piece geometry

This consisted of inclining the pure shear test piece by 30° and then straining it in the vertical direction (Figure 3-12). The specimen was then under a combination of a pure shear and a simple shear deformation. Experimentally, the pure shear grips were mounted on a triangular metal block whose hypotenuse was inclined at 30° to the horizontal. The extent of the inclination controls the amount of shear deformation and 30° was chosen arbitrarily As shown on Figure 3-12, the position of the grips on the two triangular blocks was adjusted to obtain a 20 mm specimen height which aligned in the direction of the tensile axis. The first difficulty resulted from the fact that the height of the test piece was not exactly 20 mm. Hence, the load cell of the Instron was hence subjected to side forces even before the specimen was strained. This affected the determination of the zero load position. In addition, side forces were produced due to the geometry of the test-piece itself during the test, as a simple shear deformation mode is generated. Hence the effect of side forces on the measured load was investigated. Side forces were generated by pulling horizontally a spring fixed to the load cell to produce forces from 10 to 100N when the load cell was already subjected to vertical loads. It was observed that the load cell was not at all sensitive to these side forces and hence provided reliable measure of the tensile force alone.

3.6 Fatigue crack growth rate test procedures

The test-piece used to investigate cyclic crack growth under dynamic conditions was a pure shear test-piece. The principal reason for this choice was that the tearing energy (T) at a given extension for this test piece is independent of the crack length as formulated previously[3]:

$$T=WL_0 \qquad (3\text{-}6)$$

where W is the elastic strain energy density function (or *e.s.e.d.* function) remote from the crack tip and L_0 is the unstrained height. This characteristic of the pure shear test is particularly useful in a crack growth test as it is possible to monitor the crack growth rate over any convenient interval of crack growth at a specific strain level and hence a given tearing energy. As explained in section 2.4.2, the relation between the crack growth rate dc/dn where c is the crack length and n the number of cycles and the tearing energy T should constitute a materials characteristic.

These experiments were carried out at room temperature by imposing a sinusoidal waveform in specimen extension at a frequency of 5 Hz using a servo-hydraulic testing machine. The pure shear test-piece was strained to a maximum strain amplitude of between 5-35% and was relaxed to zero strain in each cycle. This is known as a fixed-displacement fully relaxing test. To determine the tearing energy using Equation 3-6, the *e.s.e.d.* density has to be determined for each of the extended conditions. Hence a force-deflection curve was plotted at the given temperature and given strain rate or frequency of test, and the integration of this curve divided by the volume of the specimen gives the elastic strain elastic density. The force-deflection curves were plotted with a Phillips X-Y plotter and the integration was carried out manually using the trapezium method. As mentioned previously in section 2.2.4 stress-softening occurs in filled elastomers and although most of it occurs during the first hundred cycles, the force-deflection curves are altered as the specimen is cycled. This stress-softening effect also increases the initial unstrained height L_0 as the specimen is cycled and a modified expression for Equation 3-6 is derived in the next chapter to circumvent this problem.

An initial horizontal cut of 40 mm in length was introduced on the central axis at one edge of the test piece using a razor blade. This placed the crack/cut tip sufficiently far from the edge to avoid any edge effects as will be demonstrated using a finite element technique in Chapter 5. The initial rapid crack growth rate, which occurred over the initial increase of crack length of range 0.05-0.5 mm due to extreme crack tip sharpness resulting from the razor blade incision[4] was neglected. The width of the specimen was either 175 or 240 mm depending on the grips used. The initial height L_0 was in the range 18-22 mm. The specimen thickness was between 2-2.5 mm. The crack length was measured with the aid of a video camera to an estimated precision of 0.2 mm and the load-displacement curves were simultaneously recorded. The crack growth rate results were plotted on a log-log plot of dc/dn versus T.

When cyclic crack growth rate tests were carried out using either the pre-strained, the inclined geometry or a combination of both test methods, the machine and specimen specifications were as described above but with the appropriate jigs mounted on the servo-hydraulic machine. A photograph of the inclined geometry set-up is shown in Figure 3-13. For this the same experimental difficulties as for the force-deflection measurement were encountered. In the case of a pre-strained test-piece, the presence of a crack at one end rendered this edge of the test-piece free. The buckled material in a compressive deformation state at the other end made the overall deformation state non-symmetrical. When the specimen was cycled, because of the non-symmetry of the deformation state and also because the upper jig was free to rotate about the vertical axis caused the jig to twist. This was circumvented by guiding this upper jig with two metal guides that restrained any movement except in the vertical direction (Figure 3-13).

3.7 Fractography procedures

As mentioned in the literature review, two different methods appear to be most appropriate for investigating the roughness of elastomer fracture surfaces. These use either the scanning electron microscopy (SEM) or a non-contacting profilometer such as an infrared laser profilometer. The two methods necessitate the same specimen preparation, cutting the sample from the specimen and gold coating. A description of this specimen preparation method is given below.

3.7.1 Specimen preparation

One of the fracture surfaces was cut from a fatigue test specimen using a razor blade to produce a parallelepiped of unstrained material (Figure 3-14). This sample was then gold coated using a sputter method. In an almost argon atmosphere in the specimen chamber where the pressure was between 0.05 to 0.1 mbar, a high voltage was applied to a gold target as the cathode and the specimen table was made the anode. This creates a high voltage field where free electrons collide with the argon atoms introduced into the chamber forming positively charged argon ions. These ions are accelerated to the cathode and release gold atoms as they impact the target. The released gold atoms and the residual gas molecules in the specimen chamber produce repeated collisions resulting in a wide scattering of the gold atoms forming a diffuse cloud of these atoms that coat the specimen evenly from all sides. A standard procedure (30 μA current under 0.05 mbar pressure for 30 seconds) was followed during this process. There exists a risk of overheating the specimen for temperature sensitive materials, like elastomers. In order to assess any such effects on the sample in the conditions used, the most highly carbon black filled samples were examined in the SEM before and after coating. This is possible for carbon black filled elastomers, as they are often conductive enough to allow reasonable imaging without a gold coating. Examples of the micrographs observed at ×200 and ×900 are shown in Figures 3-15 and 3-16. These micrographs show that the coating procedure does not alter the surface appearance and that gold-coating improves the resolution.

Using this sputtering method, even very rough surfaces are homogeneously coated with an approximately 20 nm thick gold layer with sufficient conductivity for SEM examination and providing sufficient reflectivity for the infrared profilometer.

3.7.2 SEM fractography

For the SEM, the gold coating provided a conductive path to the earthed specimen stage to prevent charging up of the poorly conducting specimens when they were irradiated by the electron beam. But as mentioned in the previous section, highly carbon black filled elastomers may not require gold coating. However, as poorly conducting unfilled elastomers were also examined, a gold-coat was applied to all

samples to maintain the same conditions. The main reason why charging of the sample surface should be avoided is because it deflects the primary beam and affects the efficiency of secondary electron collection, impairing the image quality; another reason being to increase the secondary electron production and with it increase the signal to noise ratio.

The specimen examination was carried out using a JEOL 6300 SEM at an accelerating voltage of the primary beam of 15kV with a 15 mm working distance (distance between the specimen surface and the objective lens). 5 to 6 samples were introduced into the specimen chamber at a time. Each sample was initially viewed from the top (Figure 3-17) at a magnification of $\times 200$ a and then laid down on the holder tilted between 5 to 20 degrees (Figure 3-18) to observe the scale of the surface roughness at a magnification of $\times 50$. A higher magnification was selected for the top view, as the aim of this exercise was to study the details of the fracture surface in that case.

The large depth of field of the SEM allowed the examination of rough surfaces, which would not be possible with optical microscopy. But a problem occurred when the sample was tilted: the large side surfaces were exposed (Figure 3-18) and charging of these surfaces tended to occur even on the gold-coated samples for the lightly carbon black filled and unfilled elastomers. This produced very wide bright features resulting in poor contrast making the fracture profile difficult to examine. Reducing the accelerating voltage reduced the charging effect but the corresponding drop in resolution made this method non-viable.

3.7.3 Profilometer

The working principle of this profilometer is as follows: infrared light which is reflected from the object surface is focused to a spot by an objective lens. When the lens/ object surface distance changes due to the modifications of the surface topography during scanning, a feedback control circuit moves the objective lens accordingly to restore the focus. This lens movement is proportional to the surface height variations and gives a measure of the surface profile. Strongly scattering or highly absorbing (*i.e.* black surfaces) can make measurements impossible. As the majority of the elastomers analysed in this work were carbon black filled, gold

coating was used to avoid this problem by increasing the reflectivity of the surfaces and improving the resolution.

The light spot of 1μm diameter could be considered as the resolution of this apparatus. One millimetre is the largest amplitude height variation detectable in the fracture profile as the objective lens has a maximum vertical displacement of $\pm 500\mu m$. This proved insufficient when looking at the inclination of some of the surfaces. In these cases, profile measurements were restricted to a limited region and these were conducted only when the possible scanning length was greater than 1 mm. In the literature, striations of separation 20 to 70 μm are reported on fatigue cracks[5]. SEM profile observation of the roughest surfaces found at the high tearing energies in highly carbon black filled materials showed repetitive features between 100 and 300 μm in length. A minimum scanning length of 1 mm appeared then necessary to obtain a reasonable representation of the whole surface. Another limiting factor of this technique was the detection of the reflected signal. If the surface was too steep, the reflected signal was not within the reach of the sensor. The manufacturers' specification stated that not more than a maximum inclination of $\pm 15^{\circ}$ should be studied which appeared to be acceptable for most of the cases in this work.

The acquisition and the analysis of the data were carried out using a software set-up on a PC. This software allowed profile measurements to be recorded along a line. Three different profile measurements were realised for a given specimen on three different positions across the thickness. The positions were chosen at least 0.4 mm away from the edges of the approximately 2 mm thick specimens to avoid the edge effects as the fracture profile observations on the SEM generally showed a smoother profile near the edges than in the centre of the specimen. From the profile measurements, the UBM software proposes a filter command to make the distinction between what is called the waviness and the roughness. The concept of dividing a surface morphology in its waviness and roughness emerged from the fact that engineering surface profiles are usually the result of a cutting-tool. Then the roughness, also called primary texture, is the result of the action of the cutting-tool used to produce the surface and the waviness also called secondary texture is possibly caused by imperfections in the cutting-tool, such as a vibration or a badly grinded wheel. In our fatigue crack growth tests, the imperfections are mainly attributed to

inhomogeneities, inadvertent inclusion of foreign materials, gel particles, areas of unequal cure or poor dispersion of the filler responsible of the secondary texture or waviness. Consequently, the length of the largest repetitive feature along a one millimetre scanned length of material was taken as the cut-off wavelength to filter out the waviness from the roughness.

Adopting this filtering procedure, the software enables the calculation of several roughness parameters from the profile measurements to be carried out. Examples are the maximum peak to valley height of the entire measurement, the average distance between peaks of certain heights, the ratio of the stretched length to the actual length of the profile or the root mean square. This last one also called (R_q) is the most universally accepted measure of surface roughness. It is defined as follow:

$$R_q = \sqrt{\frac{1}{n}\sum_{i=1}^{n}(y_i - y_m)^2} \qquad (3\text{-}7)$$

where n is the number of points recorded on the profile by the software, y_i are the heights of these points and y_m is the average height of the n points. Because this parameter does not take into account any information in the x-direction (like the distance between peaks, the frequency of occurrence of the peaks for example), there is no need to add any correction factor when fracture surfaces obtained under pre-strain have their roughness estimated in the undeformed/non-pre-strained state.

3.8 Finite Element based fracture mechanics procedures

According to Chapter 2, section 2.5.2, three different methods are available to estimate the energy release rate or tearing energy. These are namely the Virtual Crack Extension method (VCE), the Virtual Crack Closure Technique (VCCT) and the J-integral method. As the VCE and the VCCT are in principle equivalent techniques, based on the energy balance approach, only the VCE and the J-integral methods were used in this study. The VCE method will be used in its simplest application of the energy balance concept, by running two full analyses to compute the elastic strain energy of the model for two slightly different crack lengths. The aim of this finite element investigation is to estimate the magnitude of the energy release rate or tearing

energy as a function of the crack propagation direction, hence permitting a prediction of the direction of the crack growth.

The finite element work was performed using Silicon Graphics workstations on which was mounted the finite element software ABAQUS[6]. Two-dimension models in plane stress deformation condition were utilised and similar models were used both for the pre-strained pure shear geometry (Figure 3-19) and the 30° inclined pure shear geometry (Figure 3-20). The dimensions of the model in the undeformed state are a length of 175 mm, a height of 20 mm and an initial crack length of 40 mm. The mesh is formed by rectangular elements far from the crack tip, and the crack tip region meshing consists of concentric circles spaced 1.429 mm apart with radial lines spaced at 7.5 degrees (Figure 3-19). This type of meshing of the crack tip region is called a focused mesh. This mesh made it possible to open up the crack every 7.5 degrees intervals with the VCE method and to have sufficiently accurate stress and strain magnitudes around the crack tip for the use of the J-integral technique. But accurate J-integral results can be obtained even with a relatively coarse mesh[6].

The procedures for these two different techniques are as follow:

(1) for the VCE method, the elastic strain energy (Δu) between 2 neighbouring positions of the crack (producing a variation of one of the fractured surfaces of Δa) needs to be estimated. The tearing energy is then approximated by $\Delta u/\Delta a$. In this study, a crack extension was obtained by releasing the crack tip nodes that were initially tied together. By releasing the appropriate nodes it was possible to model the appropriate direction of crack growth. Figure 3-21 shows that two sets of elements of the focused mesh, separated by the crack, are both tied to a node, one free and the other one bound to the rest of the model.

(2) for the Rice J-integral method which consists in estimating a path integral taken around the crack tip (Equation 2.3-4, in Chapter 2), a built-in option called CONTOUR INTEGRAL in ABAQUS[6] was used to estimate the magnitude. The integral can be estimated along several contours. The first contour being the ring of elements immediately adjacent to the crack tip, and the subsequent contours are generated automatically as contours passing through the nearest neighbouring elements, moving out from the crack tip. The number of contours along which the integration is carried out is chosen by the user. Theoretically the J-integral is path independent however the estimation of the J-integral using FEA converges after only

a certain number of contours away from the crack tip because of the discretisation and numerical errors. It was found here that the estimated integral converged usually after the fourth contour and the value of the integral displayed for the fifth contour was used in this study. The focused mesh of the crack tip have a triangular form but are plane stress collapsed quadratic elements in case of the *J*-integral estimation.

Both the cubic and the Davies *et al e.s.e.d.* functions (respectively Equations 2.2-45 and 2.2-40) were implemented into the finite element models. The coefficients of the cubic function were directly entered in the programme as a Mooney-Rivlin series. A Fortran subroutine (Appendix 2) was called in the finite element programme to input the coefficients of the Davies *et al* function.

M=68

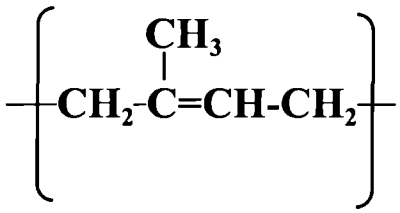

Figure 3-1 Repeat unit of Natural Rubber (NR), cis 1,4 poly-isoprene and the relative molar mass (M) in $g.mol^{-1}$.

M=54 M=105

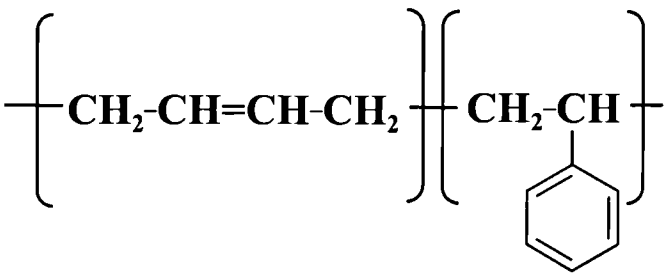

Figure 3-2 Repeat unit of polystyrene butadiene rubber (SBR) and the relative molar mass (M) in $g.mol^{-1}$.

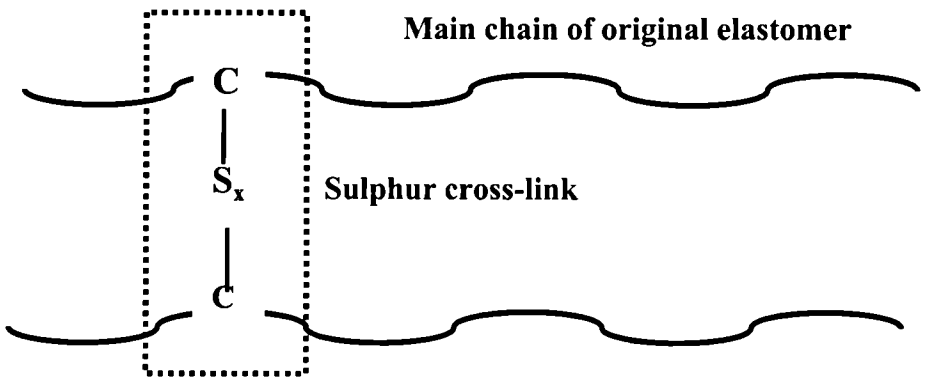

Figure 3-3 Schematic showing the formation of an elastomer network with the covalent bonds of either mono-, di- or polysulfides between the original elastomer chains.

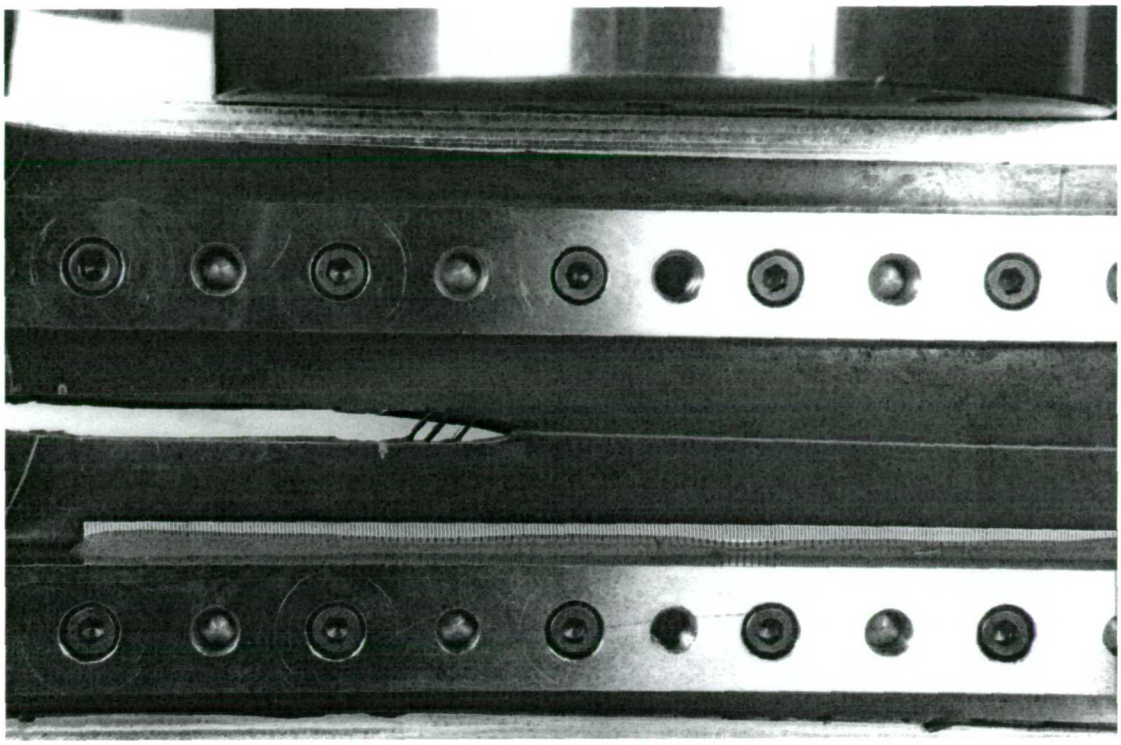

Figure 3-4 Fatigue crack growth test on a pre-strain pure shear test-piece (NR 29, pre-strain, PS=50% and T=1500 J.m^{-2}) showing elastomer threads between the two open fracture surfaces presumably due to differences in strength of the elastomer through its thickness.

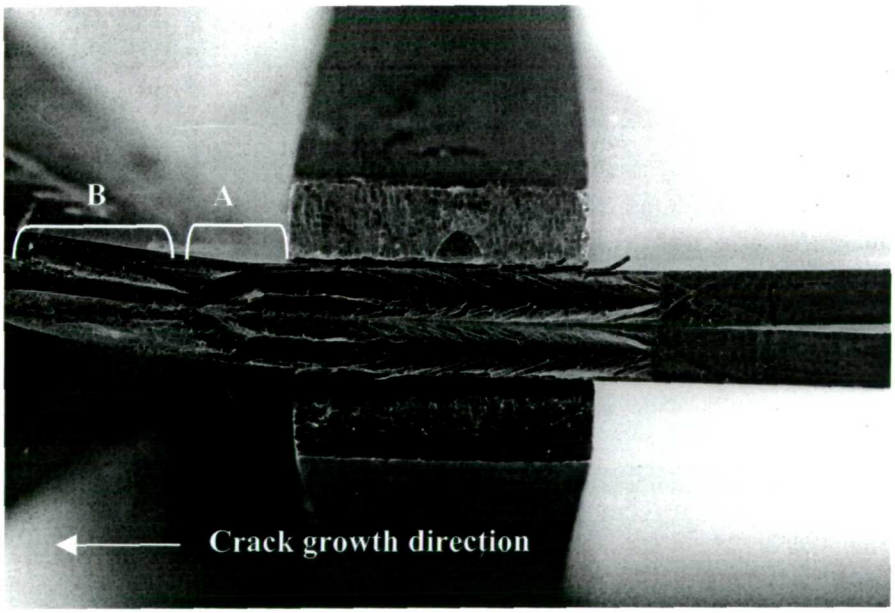

Figure 3-5 The two fractured surfaces from the actual specimen shown in Figure 3-4 exhibiting an angled crack front (region A) and a straighter crack front when a larger cyclic strain was applied (region B).

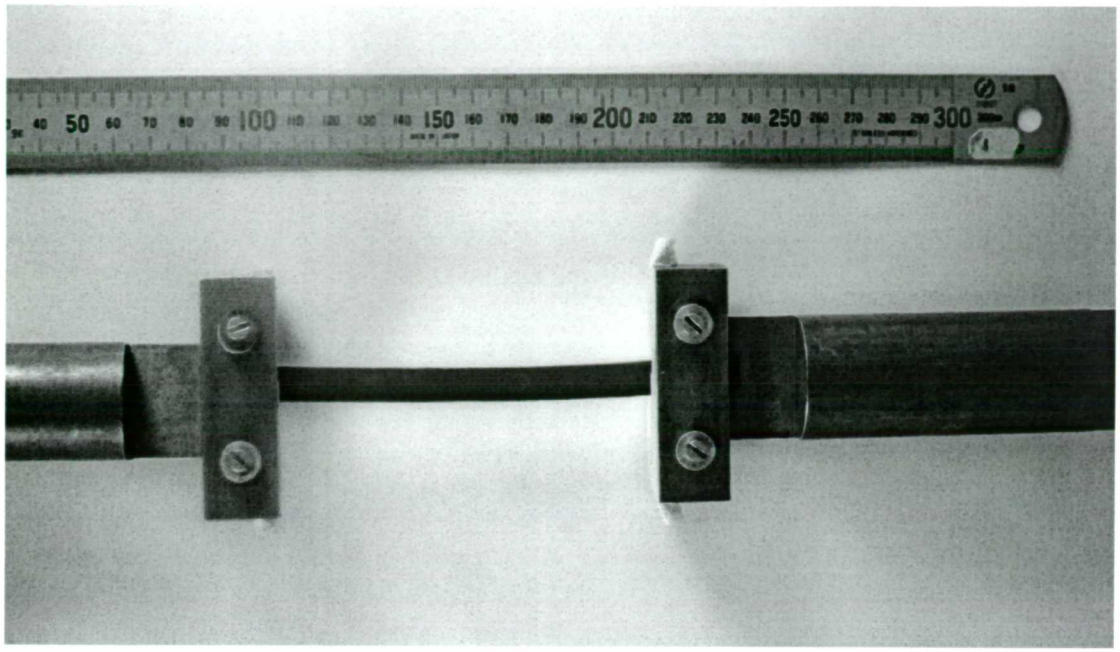

Figure 3-6 Tensile testing grips.

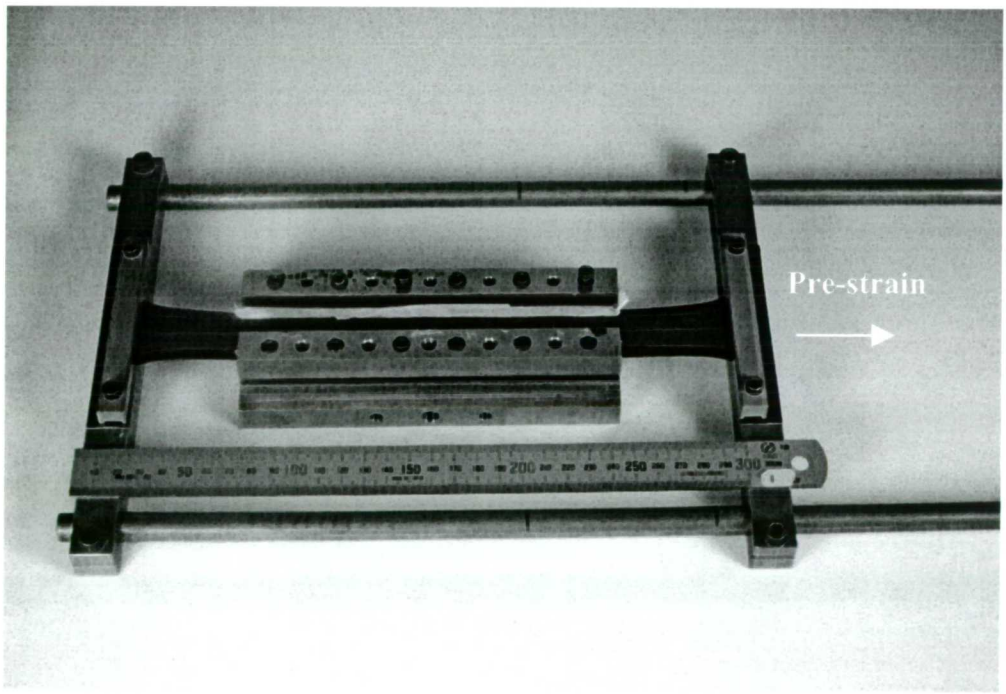

Figure 3-7 The frame used to longitudinally pre-strain a pure shear test-piece.

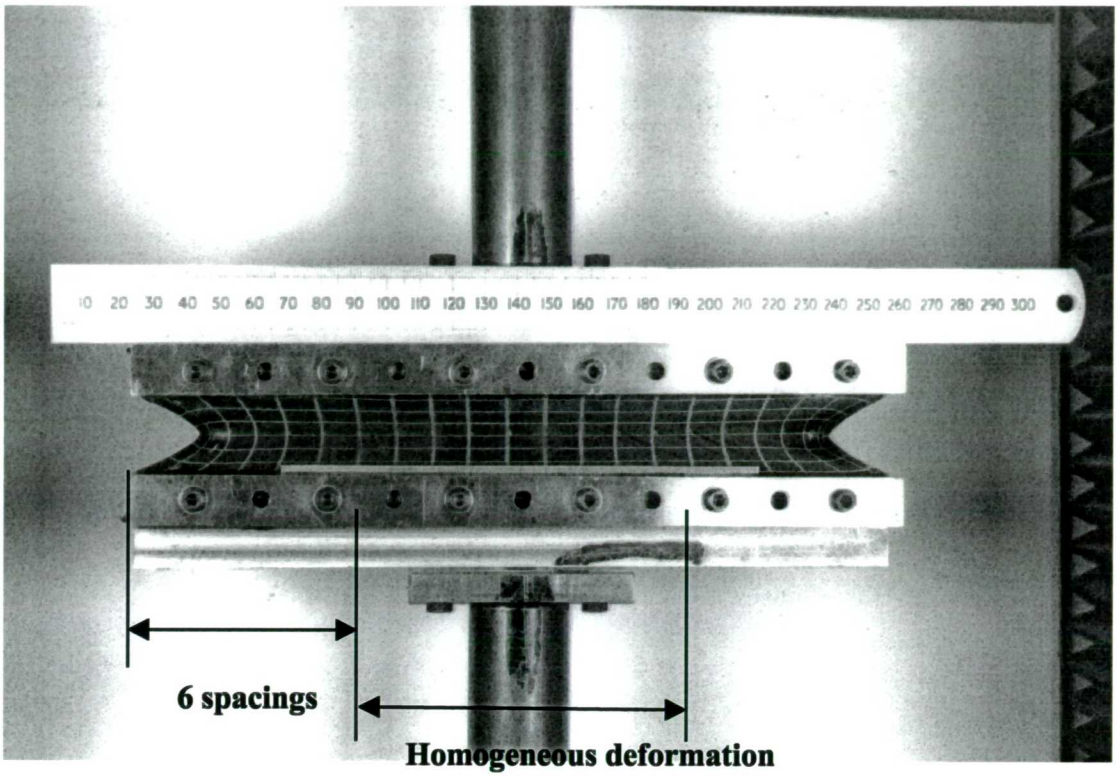

Figure 3-8 The region of homogeneous pre-strained pure shear deformation can be estimated as the region where the vertical grid lines remain vertical which corresponds to a region approximately 6 spacings, i.e. 30-35 mm away from the edges. This sample with an initial height L_0 equal to 20 mm was pre-strained to 100%. The distance from the edges to be in a region of homogeneous deformation scaled to L_0 gives a ratio equal to 1.5-1.75, to be compared with the FEA results in Chapter 5.

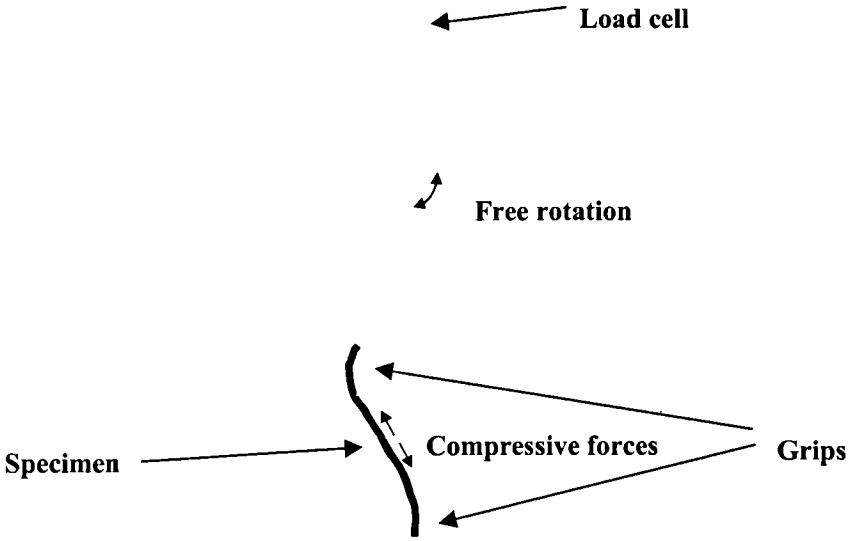

Figure 3-9 Schematic showing an exaggerated representation of the misalignment of the upper and bottom jigs when a pre-strained pure shear test-piece is set-up on the Instron machine.

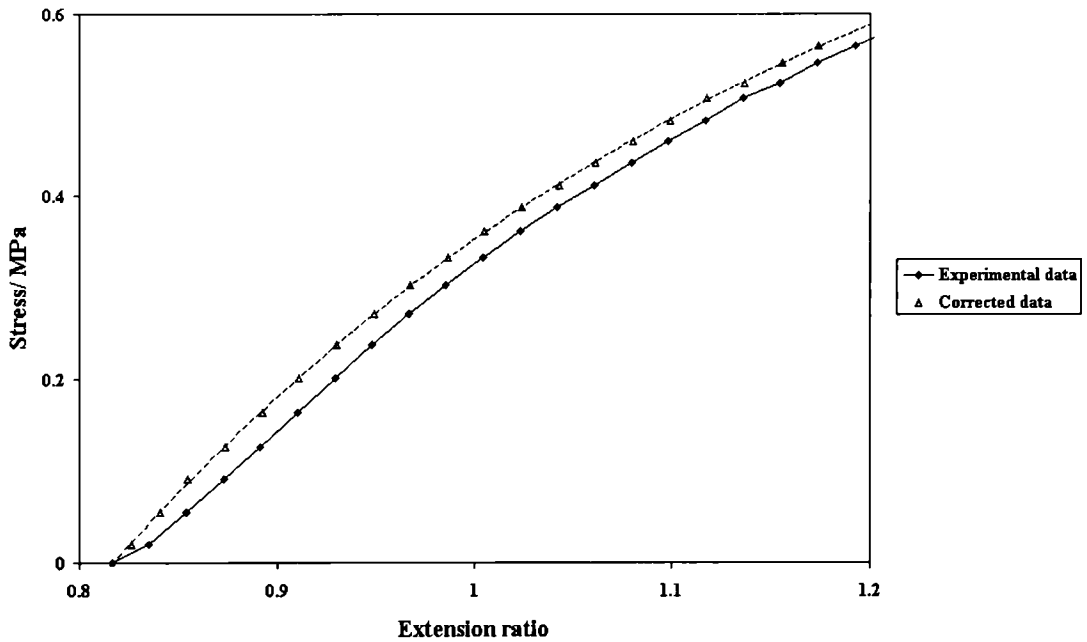

Figure 3-10 The correction adopted to counteract the problem of the misalignment of the jigs on the Instron machine which is made by re-evaluating the unstrained height. These data are for NR21 pre-strained by 50%.

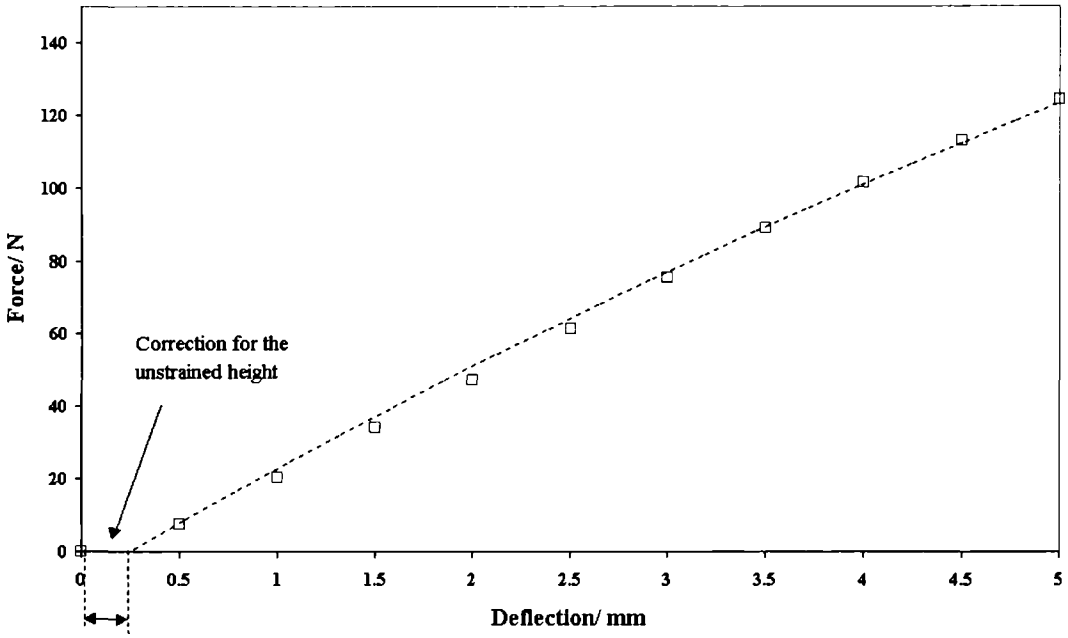

Figure 3-11 Estimation of the underestimation on the unstrained height measurement by extrapolating the initial small strain data points to obtain a continuously decreasing slope.

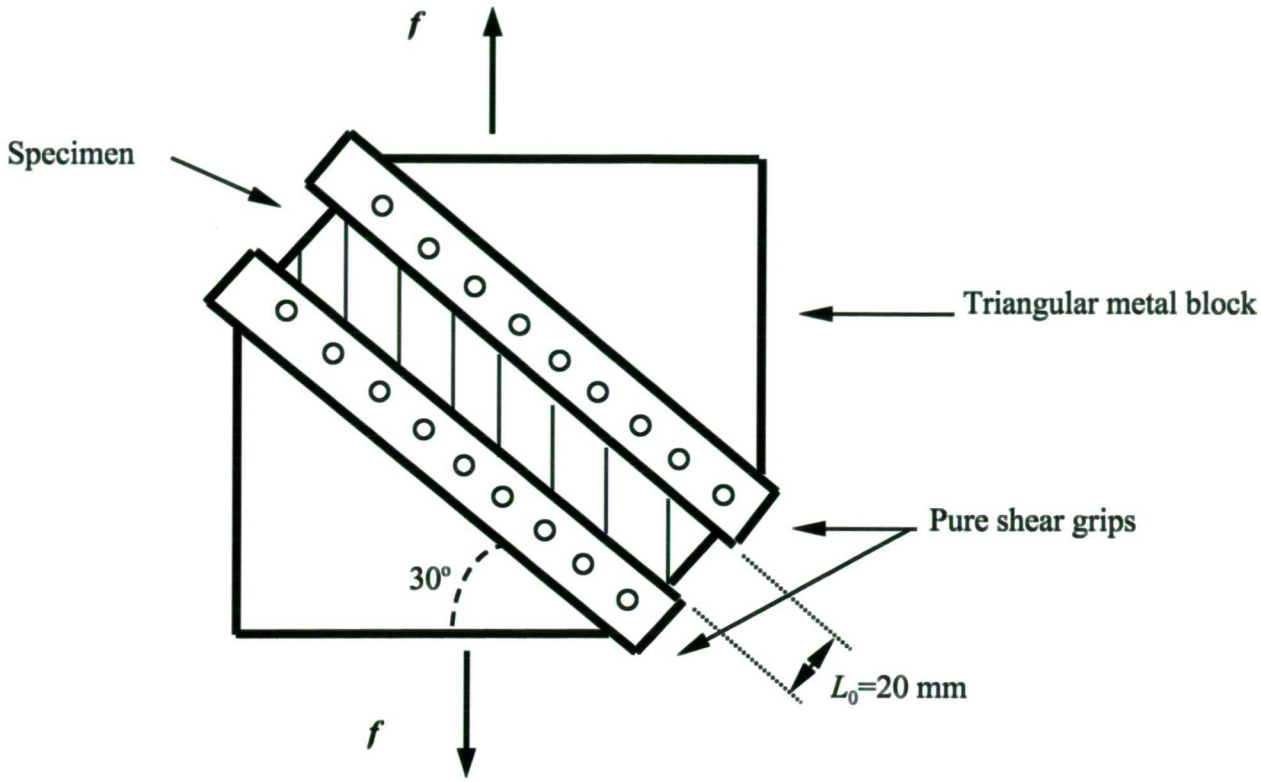

Figure 3-12 Thirty degree inclined pure shear test piece: the pure shear grips are mounted on two triangular metal block and pulled in the vertical direction. The set-up is designed to have an alignment of the axis of traction if the unstrained height of the specimen is 20 mm.

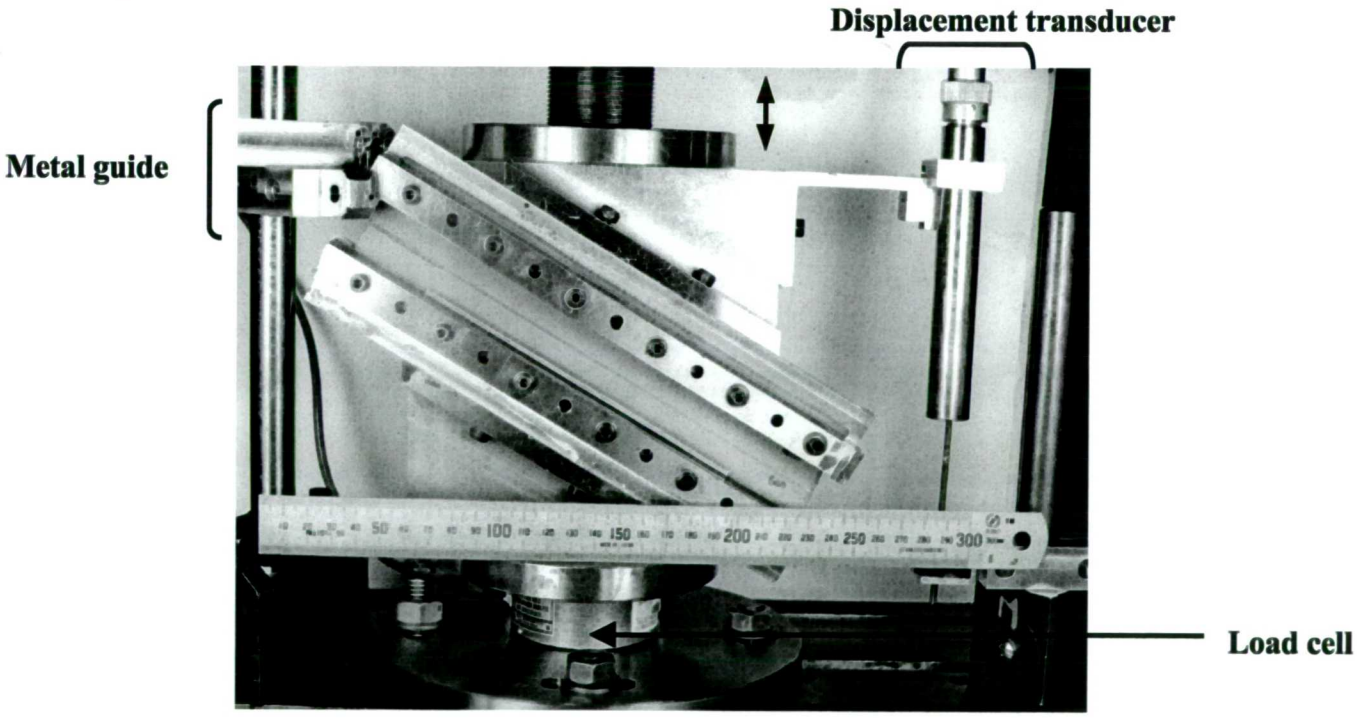

Figure 3-13 Inclined pure shear or inclined pre-strained pure shear set-up on the jigs of the fatigue servo-hydraulic machine.

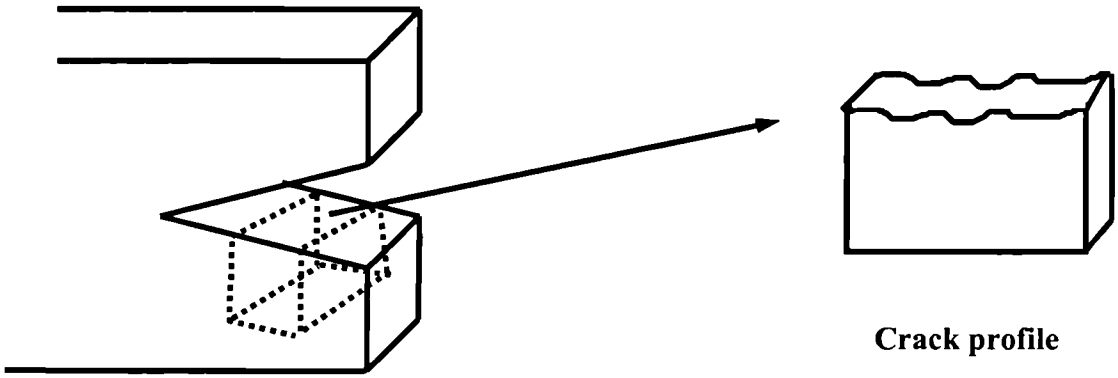

Figure 3-14 Extraction procedure for the samples used for fractography studies.

Figure 3-15 SEM micrographs comparing a non-gold coated (top) and a gold-coated (bottom) sample (NR59) observed at (×200) magnification.

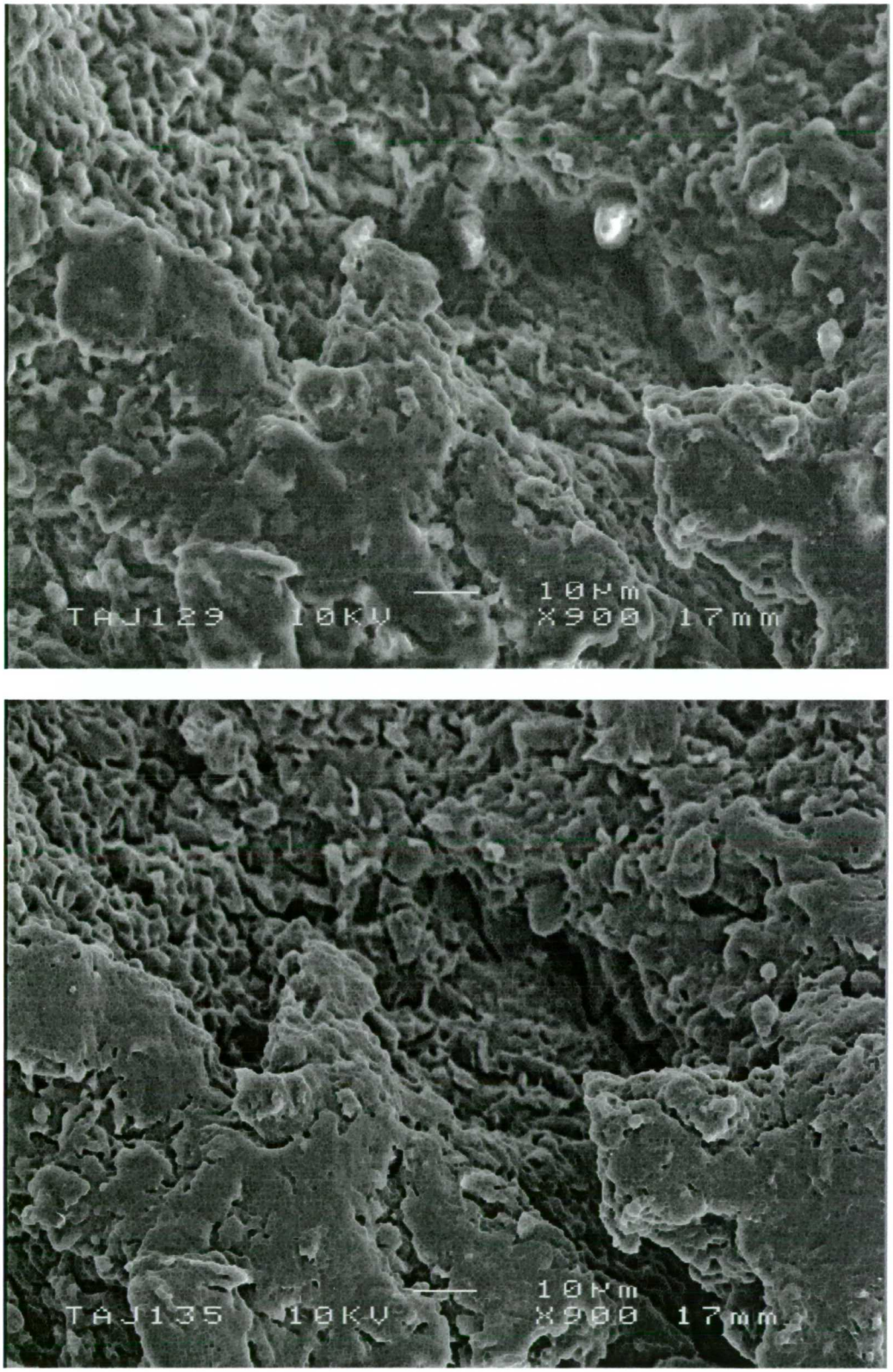

Figure 3-16 SEM micrographs comparing a non-gold coated (top) and a gold-coated (bottom) sample (NR59) observed at (×900) magnification.

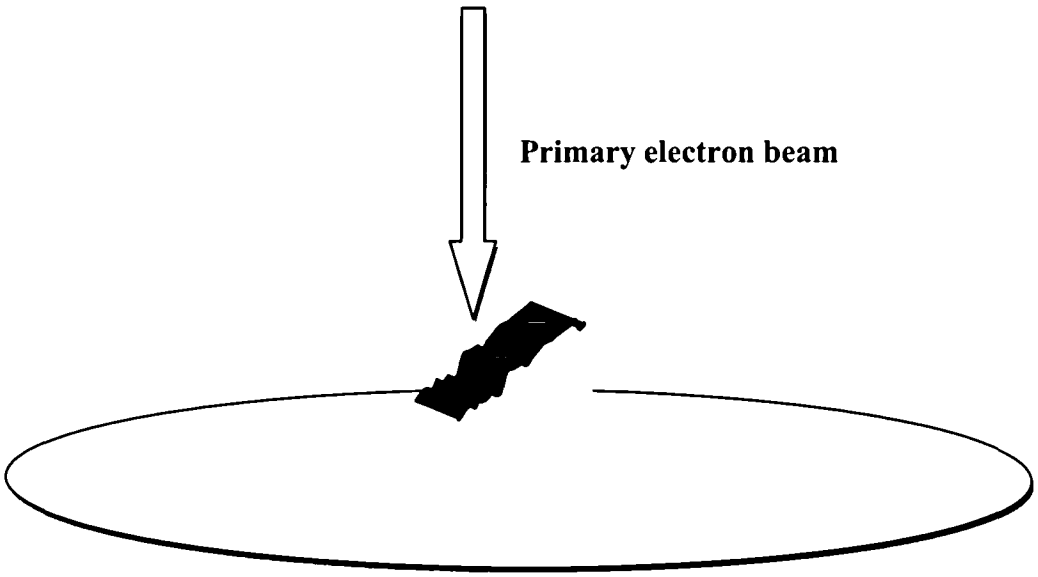

Figure 3-17 Schematic of the fracture surface top view examination on the SEM.

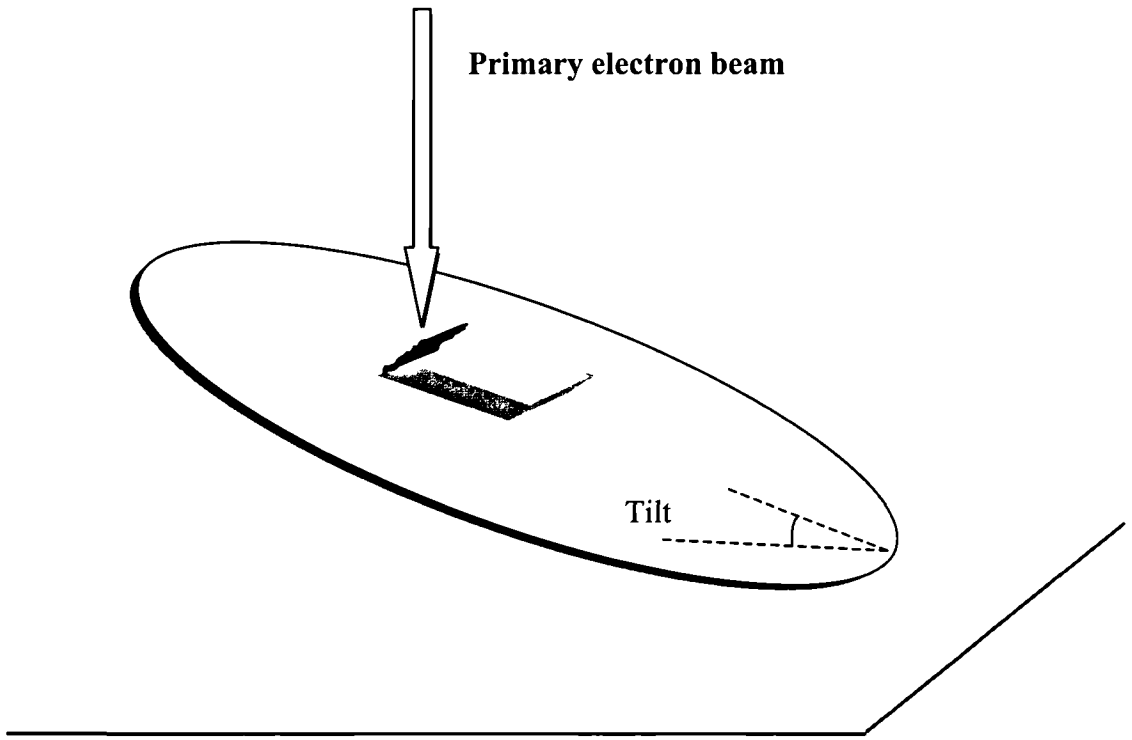

Figure 3-18 Schematic of the fracture profile view examination on SEM.

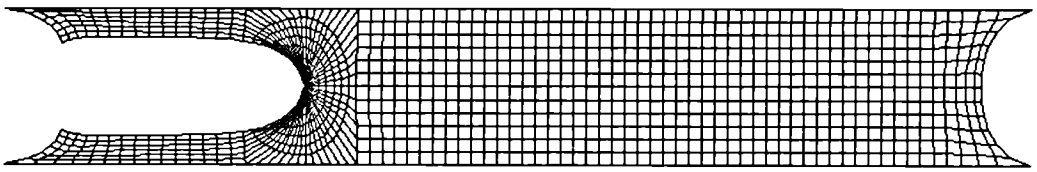

Figure 3-19 Finite element model under a longitudinal pre-strain (PS=50%) which is deformed in the vertical direction.

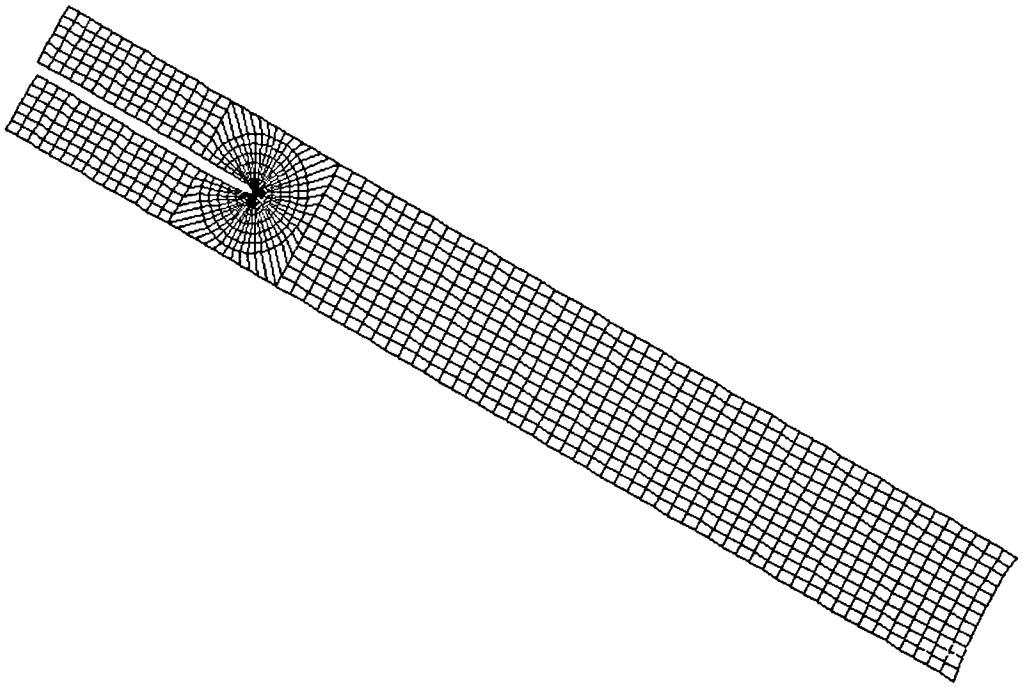

Figure 3-20 Finite element model for the 30° inclined pure shear test-piece, pulled in the vertical direction.

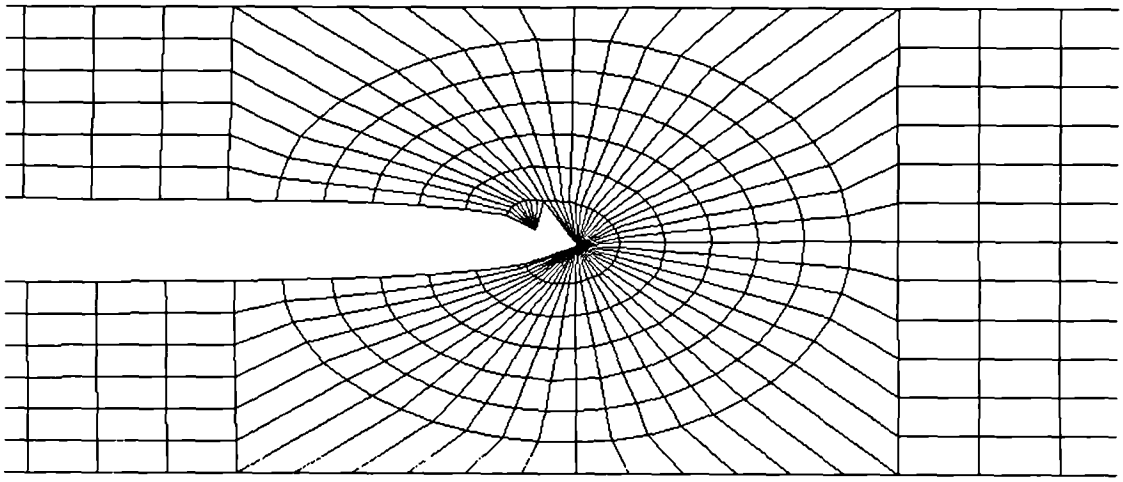

Figure 3-21 Illustration of the VCE (Virtual Crack Extension) method: two sets of elements of the focused mesh, separated by the crack, are both tied to a node, one free and the other one bound to the rest of the model.

INGREDIENTS (pphr parts per hundred rubber in mass)		NR0	NR21	NR29	NR59	SBR0	SBR30	SBR50
NR (SMR CV60[i])		100	100	100	100	-	-	-
SBR (Intol 1500 [ii])		-	-	-	-	100	100	100
HAF,N330 carbon black		-	21	29	59	-	30	-
MT, N990 carbon black		-	-	-	-	-	-	50
Volume fraction (rubber)		0.99	0.92	0.88	0.8	0.99	0.89	0.83
Volume fraction (carbon black)		0	0.08	0.11	0.2	0	0.11	0.17
ZnO		5	2.8	5.7	2	5	-	-
Stearic acid		2	0.5	0.5	0.5	2	-	-
Anti-oxidant (6PPD[iii])		3	2	2	1	-	1	1
Anti-ozonant (wax)		-	2	3	2	-	-	-
Accelerators	CBS[iv]	2.3	1.2	-	1.7	1	1.1	1.1
	TMTD[v]	-	-	1.1	-	-	-	-
	TBBS[vi]	-	-	1.4	-	-	-	-
	MBT[vii]	-	1.55	-	-	-	-	-
Sulphur		1.5	1	1	2.7	1.75	2	2
Cure temperature/ °C		150	155	155	155	150	150	150
Cure time/ minutes		16	10	10	10	50	60	60
V_r		0.3197	0.3033	0.3692	0.4077	0.4993	0.5388	0.5373
$[X]_{phys}/(10^{-5}\,\text{mol/g.RH})$		9.2	8	13.3	17.3	11.3	16.8	16.7
$[X]_{act}/(10^{-5}\,\text{mol/g.RH})$		9.2	6.7	10.6	11.8	11.3	12.9	11.6
M_c/ g.mole^{-1}		5050	7463	4717	4237	4425	3876	4191

Table 3.1 Formulations for NR and SBR elastomers.

[i] SMR CV60: Is a high-quality grade Standard Malaysian Rubber with an assurance of freedom from particulate contamination like sand or bark. The absence of contamination reduces the inherent flaw size and helps to avoid the complications associated with premature failure arising from that source. CV60 means Constant viscosity with producer's viscosity limited between 55-65.

[ii] Intol 1500: Is a grade produced by cold emulsion polymerisation. It contains 23.5% by mass of styrene, the molecular proportion of units in the chains being one styrene to approximately six butadiene.

[iii] 6PPD: N-(1,3-Dimethyl-butyl)-N'-phenyl-p-phenylenediamine.

[iv] CBS: N-Cyclohexylbenzothiazole-2-sulphenamide.

[v] TMTD: Tetramethylthiuram disulphide.

[vi] TBBS: N-ter-Butyl-2-benzothiazolylsulfenamide.

[vii] MBT: Mercaptobenzothiazole.

REFERENCES

[1] Flory P. J. and Rehner J., *J. Chem. Phys.*, **11**, 512 (1943).

[2] Porter M., *Rubber Chem. Technol.*, **40**, 866 (1967).

[3] Rivlin R. S. and Thomas A. G., *J. Polym. Sci.*, **10**, 291, (1953).

[4] Lake G. J. and Yeoh O. H., *J. Polym. Sci., Polym. Phys. Ed.*, **25**, 1157 (1987).

[5] Bhowmick A. K., "Fractography of rubbery materials", Ed. Bhowmick, Elsevier Applied Science, London and New York, **4**, 101 (1991).

[6] ABAQUS/Standard, User's Manual. Hibbit Karlsson & Sorenssen Inc., Version 5.8 (1998).

4

Stress-strain behaviour of filled elastomers under non-simple loading

4.1 Introduction

This chapter will report on and discuss the results of the mechanical characterisation of the various elastomer compounds to be used in this thesis, details of which were given in sections 3.2 and 3.3. In addition, the mechanical behaviour of these compounds when loaded in more complex deformations than the usual uniaxial tests will be investigated as proposed in section 2.6. First, the mechanical characterisation carried out using tensile and pure shear test-pieces will be reported followed by the results for the non-simple deformation modes consisting of a longitudinally pre-strained pure shear test-piece with an induced bi-axial stress field and an inclined pure shear test-piece with induced simultaneous pure shear and simple shear. The ability to predict the mechanical behaviour of these non-simply loaded filled elastomers using the elastic strain energy density function (or *e.s.e.d.* function) approach described in section 2.2.3 will constitute the main interest of this chapter. From the programme of study section 2.6, a cubic *e.s.e.d.* function proposed by Yeoh[1] was to be used here but as this function has not previously been fitted to stress-extension data for these compounds its reliability is unknown. However, the Davies *et al* function[2] reported in section 2.2.3.2, has been fitted in the past and has been found to work reasonably well[3]. Both of these functions will be hence tested and compared.

4.2 Materials characterisation and *e.s.e.d.* function determination

Under the hypothesis of an incompressible ideal elastic solid subjected to an isothermal pure homogeneous deformation, Rivlin[4] has shown that a set of relationships exist between the principal true stresses, t_1, t_2 and t_3, the principal extension ratios λ_1, λ_2 and λ_3, and the partial derivatives of W with respect to the invariants I_1 and I_2. These relationships were identified as Equations 2.2-27 to 2.2-29 in Chapter 2. In case of the simple deformation modes of interest in this study, namely tension and pure shear, these relationships given respectively as Equations 2.2-30 and 2.2-32 in Chapter 2 are reproduced here with new equation numbers (4-1) and (4-2) respectively:

Tension:

$$\frac{\sigma}{(\lambda-\lambda^{-2})}=2\left\{\frac{\partial W}{\partial I_1}+\frac{1}{\lambda}\frac{\partial W}{\partial I_2}\right\} \tag{4-1}$$

Pure shear:

$$\frac{\sigma}{(\lambda-\lambda^{-3})}=2\left\{\frac{\partial W}{\partial I_1}+\frac{\partial W}{\partial I_2}\right\} \tag{4-2}$$

In these equations, σ is the engineering stress i.e. the force divided by the unstrained cross-section area. The left-hand sides of these relationships are known as the reduced stresses. The assumptions, for carbon black filled elastomers that W was largely dependent only on the strain invariant I_1 and that the second invariant I_2 had minimal effect for filled rubbers (i.e. $\partial W/\partial I_2 = 0$) was proposed by Gregory[5] and Davies *et al*[2]. On that basis, two different strain energy functions were proposed for this work. The first function, developed at Queen Mary and Westfield college by Davies *et al*[2] was designed to predict the behaviour of carbon black filled elastomers from small strains to at least 100% strain in the simplest possible form:

$$W=\frac{A}{2(1-\varphi/2)}(I_1-3+C^2)^{(1-\varphi/2)}+\Lambda(I_1-3)^2 \tag{4-3a}$$

where A, φ, C and Λ are material constants from which we can derive $\partial W/\partial I_1$:

$$\partial W/\partial I_1 = \frac{A}{2}(I_1 - 3 + C^2)^{\frac{-\varphi}{2}} + 2\Lambda(I_1 - 3) \qquad (4\text{-}3b)$$

The second function proposed by Yeoh[1], which we will call the cubic function is a third degree polynomial in $(I_1 - 3)$ derived from Rivlin's power series given in Chapter 2 as Equation 2.2-25. Although its prediction abilities are not as good as the Davies *et al* function at small strains, it is a very attractive function for fracture mechanics use, as it is easy to obtain the magnitude of the constants and simple to input into commercial FEA software. It has the following form:

$$W = C_{10}(I_1 - 3) + C_{20}(I_1 - 3)^2 + C_{30}(I_1 - 3)^3 \qquad (4\text{-}4a)$$

C_{10}, C_{20} and C_{30} being material constants, at a given temperature and strain rate. In this case, $\partial W/\partial I_1$ is given by:

$$\partial W/\partial I_1 = C_{10} + 2C_{20}(I_1 - 3) + 3C_{30}(I_1 - 3)^2 \qquad (4\text{-}4b)$$

In order to determine the magnitudes of the constants in the strain energy functions for the different compounds used here, their stress-strain curves have to be calculated in the form of the engineering stress (force per unit cross-sectional area referred to the unstrained state) as a function of extension ratio. Then for each stressing mode (tension or pure shear), the same data are plotted in the form of the reduced stress versus $I_1 - 3$. The plots for the different stressing modes should superimpose if the assumption that W depends only on I_1 is valid. In this case as the reduced stress is equal to $\partial W/\partial I_1$, the magnitudes of the constants in W can be obtained by fitting the reduced stress curves using a regression analysis.

4.2.1 Stress-strain behaviour

The tensile and pure shear tests were carried out using the procedures described in section 3.4. The tests were performed on all the materials detailed in Table 3.1 except for the unfilled SBR, SBR0 which was only available in a quantity which limited its use to the fracture study. Tests were carried out to the maximum possible strain either before the onset of specimen slippage in the grips or up to the specimen breaking extension. The stress-strain behaviour of the different materials will be either discussed from a stress point of view with respect to the stress-extension curves or from a shear modulus point of view with respect to the reduced stress against $I_1 - 3$ plots. It was shown in Equation 2.2-36 that the reduced stress or $2\partial W/\partial I_1$ was equal to the chord shear modulus. This is validon the assumption that W is largely dependent only on I_1 and not on I_2.

Stress-extension ratio plots

The stress-extension curves are shown on Figure 4-1 for pure shear and Figure 4-2 for tension.

It can be seen in Figures 4-1 and 4-2 that the stress at a particular extension ratio increases with increasing carbon black for the NR compounds. In this respect the large difference between the curves for NR21 and NR29 is also partly due to the significant difference in cross-link density mentioned in section 3.2. The carbon black reinforcement ability depends on several parameters: the size and the distribution of primary carbon black particles, the size, shape and the distribution of aggregates (the smallest dispersible unit usually composed of coalesced particles) and the surface activity of the carbon black surface (chemical reactivity or adsorption capacity). For the NR compounds, the size and shape of the primary carbon black particles as well as their surface activity are supposed to be constant, as the same filler is used. On the other-hand, the size, the shape and the distribution of the aggregates will be a function of the carbon black content. These aggregates can eventually associate to form agglomerates leading to what is usually termed a secondary structure or a filler network. The presence of this network, when it exists, influences the small strain modulus, the latter increasing the more developed the filler network[11, 12]. This

secondary structure is believed to be broken at large strains and to be transformed into discontinuous sub-networks. These sub-networks will interfere with the elastomer matrix by hindering the free movement of the elastomer chains. The simplest model considering the disruption of an elastomer network by solid spheres showed an increase of the Young's modulus with the concentration of solid particles[6, 7]. This phenomenon is sometimes called the strain amplification effect, due to the large increase of the local strains in the elastomer network caused by the presence of solid particles which make the bulk material appear stiffer. Qualitatively, the increase in the stress at a given strain (i.e. the modulus) with carbon black content for the NR compounds is then understandable. The other mechanisms proposed to explain the reinforcing effects of carbon black (occluded and bound rubber) will not be detailed as they do not constitute the major interest of this work.

In case of the SBR compounds, the type of carbon black differs between the two compounds. SBR30 and SBR50 are respectively loaded with HAF, N330, a reinforcing carbon black and MT, N990 a non-reinforcing one. Although SBR30 is less loaded with carbon black than SBR50, the size and shape of the primary particles make the former system possess a more developed carbon black structure and stronger filler-elastomer interactions. In consequence, the disturbance of the elastomer network is larger in SBR30. Another explanation would be that the disruption of the network by the filler be reduced by slippage and/or detachment of the rubber molecules on the filler surface, which mainly depend on the elastomer-filler interactions[8]. The larger disturbance of the network of SBR30 is attributable to the higher surface activity of HAF, N330 carbon black in comparison to MT, N990. It hence results as shown on Figure 4-1 and 4-2, in SBR30 exhibiting higher stresses than SBR50, for a given strain, especially at high strains. Furthermore, SBR30 behaves more like a strain-crystallising elastomer, with high failure strains and stresses, with SBR50 being significantly weaker.

The effect of strain-crystallisation[9] and finite extensibility[10] of the elastomer chains are observable in Figure 4-2 for the tensile data of NR0 which shows a rapid increase of the stress at strains around 400-450%

Reduced stress versus $I_1 - 3$ **plots**

The plots of the reduced stress (or $2\partial W/\partial I_1$ if $\partial W/\partial I_2$ is negligible) versus the invariant $I_1 - 3$, the later being a measure of the strain, for the two different deformation modes studied are shown on Figures 4-3 and 4-4. It should be noticed that not all the small strain data shown in the stress-extension ratio plots are shown on these reduced stress curves. The inaccuracy of this small strain data is not of such a magnitude as to be evident on the stress-extension ratio plots. However, the mathematical form of the reduced stress functions (Equations 4-1 and 4-2) are such that a small error in the initial strain measurement leads to large errors in the magnitude of the reduced stress. Furthermore, a five per cent error in the measurement of the unstrained height L_0 can result in an apparent increase in the reduced stress (or shear chord modulus) with increasing strain, at small strains, which would be physically unrealistic behaviour.

These curves in pure shear represent the variation of the chord shear modulus as the latter corresponds to the reduced stress in pure shear (see Equation 2.2-32 in section 2.2.3.1). But either in tension or in pure shear and either for filled or unfilled elastomers, the variation of the reduced stress shows a similar pattern. A rapid decrease at small strains is first observed corresponding to a decrease of the chord shear modulus. This phenomenon was extensively studied by Payne[11, 12] from strains as little as 1% to intermediate strain levels (20-40%) and is often termed as the Payne effect. This modulus reduction is usually attributed to the interaggregate interactions and the carbon black secondary structure. The existence of a carbon black network in an unstrained elastomer was demonstrated by Voet and co-workers[13, 14], evaluating the electrical conductivity of filled elastomers. Many workers[15, 16, 17] attributed this decrease in the modulus at small strains to the breakdown of the filler network upon straining and their investigations usually involved dynamic tests, the extent of the loss modulus (energy dissipated under dynamic strain) exclusively depending on the carbon black properties.

According to Figure 4-3, this is also observed, to a lesser extent, for the unfilled NR compound, NR0. Hence, other mechanisms than that proposed for filled materials are anticipated. Yeoh[1], who also observed this drop in the reduced stress at small strains, contested the usual explanation of the breakdown of the carbon black structure

as being the most significant effect for the decrease in the modulus for filled compounds. It was suggested that the drop in the modulus for unfilled compounds could be the result of the breakdown of the physical entanglements or the orientation and the rearrangement of the elastomer chains at small strains. Support for this is given by the fact that entanglements have been shown to make their largest contribution at small strains[18].

If the tension and pure shear curves in Figure 4.3 and 4.4 superimposed for each material then this would be good evidence that the appropriate *e.s.e.d.* function is only a function of I_1 and a negligible function of I_2; that is to say $\partial W/\partial I_2$ being zero. This premise clearly holds good for the filled NR materials but is less reliable for the unfilled NR and the SBR materials. However even for these materials the differences tend to be exaggerated on these plots. If the data for SBR50 is taken (the worst case) and a cubic expression is fitted to the pure shear data (Equation 4.4b), then when this resulting expression is used to predict the tensile data the differences in experimental and calculated points are not that large (Figure 4.5).

Nevertheless, it should be noted that the pure shear data are consistently above that in simple extension when differences are observable. A possible reason for this observation is the contribution of a non-zero $\partial W/\partial I_2$ that is to say a non-negligible dependence of W on I_2. The expression for the reduced stress (previously Equation 2.2-29, in Chapter 2), as follows:

$$\frac{t_2 - t_3}{\lambda_2^2 - \lambda_3^2} = 2\left\{\frac{\partial W}{\partial I_1} + \lambda_1^2 \frac{\partial W}{\partial I_2}\right\} \tag{4-5}$$

shows that the influence of $\partial W/\partial I_2$ on the reduced stress is larger in the pure shear case than in tension. The factor in front of $\partial W/\partial I_2$ in Equation 4-5 is $\lambda_1^2 = 1$ for the pure shear and $\lambda_1^2 = 1/\lambda_2$, where λ_2 is the extension ratio in the direction of straining in tension. If we assume that the magnitude of $\partial W/\partial I_1$ is similar in both deformation modes, it is then understandable that the reduced stress data is higher in pure shear than in tension. These differences in reduced stresses appear larger in the case of the SBR compounds, SBR30 and SBR50, than for the NR compounds. The reasons for this

are not known. Possible types of molecular rationale given in the literature review for the existence of $\partial W/\partial I_2$ were summarised by Trelaor[19] and are the following: Non-Gaussian chain or network statistics, internal energy effects, chain entanglements, irreversible effects and non-random packing effects. Given the voluminous benzene ring of the styrene group it is probable that the resulting stearic hindrance of SBR is greater than for NR, this probably causing an increase in $\partial W/\partial I_2$. In general, for both unfilled[20] and filled[21] elastomers, $\partial W/\partial I_2$ is shown to initially increase and then decrease. Because the form of this change followed that predicted for the contribution of physical entanglements to the total stress[22], Gent[23] attributed the $\partial W/\partial I_2$ contribution to the role played by the physical entanglements.

Gent and Thomas[24] suggested that for unfilled NR the contribution of I_2 to the *e.s.e.d.* function could be represented by Equation 4-6, to a first approximation:

$$W = W_1 + W_2 \ln(I_2/3) \tag{4-6}$$

with W_1 being a function of $I_1 - 3$ and $W_2 = 2.18C_{01}$ and where C_{10} and C_{01} are the Mooney constants as described in section 2.2.3.2 in Chapter 2. This form for W was chosen as it yields values of $\partial W/\partial I_2$ which decrease rapidly with increasing strain as observed for unfilled NR[20]. While this equation was not developed for filled elastomers it clearly can be used to represent the sometimes observed decrease in $\partial W/\partial I_2$ with increasing strain[21]. It is to be used here to investigate how such a contribution of $\partial W/\partial I_2$ would affect plots of reduced stress versus $I_1 - 3$ for different deformation modes as illustrated in Figures 4-3 and 4-4. It was decided to add a contribution of $\partial W/\partial I_2$ to the data points for NR29 (Figure 4-3) and to compare this with the results for SBR30 and SBR50.

This was done by using the Davies *et al* function for W_1 in Equation 4-6 giving:

$$W = \frac{A}{2(1-\varphi/2)}(I_1 - 3 + C^2)^{(1-\varphi/2)} + \Lambda(I_1 - 3)^2 + W_2 \ln(I_2/3) \tag{4-7}$$

The values of A, φ, Λ, C for NR29 were taken from Table 4-2 calculated as described in section 4.2.2. To determine the value of W_2 it was necessary to determine the Mooney constant C_{01} for NR29 using Equation 2.2-34 in Chapter 2:

$$\frac{\sigma}{\left[\lambda - \lambda^{-2}\right]} = 2\left[C_{10} + C_{01}\lambda^{-1}\right] \tag{4-8}$$

by plotting $\sigma/\left[\lambda - \lambda^{-2}\right]$ versus $1/\lambda$ and determining the slope, $2C_{01}$. The resulting value of C_{01} was 0.17 MPa and W_2 was set equal to 0.37 MPa. Consequently, the expression for $\partial W/\partial I_2$ which is the partial derivative of W with I_1 constant is as follows:

$$\partial W/\partial I_2 = W_2/I_2 \tag{4.9}$$

As the purpose of this exercise was to determine the sense and form of a $\partial W/\partial I_2$ contribution, the exact numerical value of W_2 was not that important. Equation 4-7 was also partially differentiated with respect to I_1 and an identical expression to Equation as 4-3b was obtained. $\partial W/\partial I_1$ and $\partial W/\partial I_2$ (Equation 4-9) were inserted into Equation 4-5 for both tension and pure shear. These functions were plotted in the form of a reduced stress versus $I_1 - 3$ plot in Figure 4-6. As can be seen the predicted pure shear data laid above that for tension at all strains. The form of these recalculated curves for NR29 was now similar to the measured behaviour for both SBR30 and SBR50, suggesting that it was a $\partial W/\partial I_2$ contribution which results in the non superposition of the curves derived from different deformation modes. Why the contribution from I_2 to the *e.s.e.d.* function should be apparently significant for filled SBR materials but not for filled NR materials is unclear.

4.2.2 Determination of the e.s.e.d. functions

The pure shear data was used to obtain the values of the constants in the two strain energy functions for the materials studied. This data is shown fitted with the cubic and the Davies *et al* functions in Figures 4-7 and 4-8 respectively. The pure shear data was used for this purpose as the stress-strain and crack growth behaviour of pre-strained pure shear test-piece were to be studied.

The strain energy functions were hence determined by curve fitting the plots of $\partial W/\partial I_1$ as a function of $I_1 - 3$ shown on Figures 4-7 and 4-8. The coefficients of the cubic strain energy function proposed by Yeoh[1] were obtained by fitting these plots with a second degree polynomial using the trendline function in Microsoft Excel®. The Davies *et al* strain energy functions were also determined using Microsoft Excel®, fitting by "eye" the $\partial W/\partial I_1 = f(I_1 - 3)$ experimental plots.

Because of its mathematical form, the cubic strain energy function was unable to fit the experimental data over the whole range of strain studied. As described previously, the experimental curves $\partial W/\partial I_1 = f(I_1 - 3)$ showed a sharp decrease at small strains and then a regular increase with strain, particularly for filled compounds. Because the change in slope was quite marked, these two parts of the curve could not be fitted simultaneously with a second-degree polynomial (the derivative of the cubic function with respect to I_1). Predominance was given here to the intermediate/large strain data (from 50-70% strain or for $(I_1 - 3) \geq 0.6 - 1.3$) when fitting with the cubic function. This ensured that the large strain data were reliably fitted. As the main purpose of its use was for a fracture mechanics based finite element modelling of crack growth, the behaviour at the small strains was not required to be known accurately. A plot of the predicted stress-strain behaviour in pure shear for NR59 and for SBR30 from the corresponding fitted cubic function is given in Figure 4-9 and shows that the inaccuracy of the fitting at small strains does not lead to significant errors on the stress-strain plot.

The magnitudes of the coefficients determined for this cubic function are given in Table 4-1. The general trend is an increase in the magnitude of the coefficients as the carbon black content increases, describing the increase in modulus. The exception being for C_{30} between NR0 and NR21. The negative values of C_{20} for these 2

compounds signify that the minima of these curves (parabolic form) occur for positive values of $I_1 - 3$. The parabolic form of the fitting curves in these cases partially describes the change in behaviour between the small strains and the higher strains. For the other compounds, the decrease in the reduced stress or shear modulus at small strains is not described by the cubic function as the values of C_{20} are positive.

Concerning the Davies *et al* model, the present results confirm the previous work of De[3] that this model is able to fit the experimental data from small strains to up to 200% strain. The values of the material coefficients for this model are given in Table 4-2. According to the mathematical expression for the Davies *et al* model, this formulation is the sum of two opposing contributions. The first one containing the parameters A, φ and C is a monotonically decreasing function of $I_1 - 3$ and dominates the behaviour at small strains. Whereas, the other contribution, containing the parameter K is monotonically increasing. A and Λ determine the magnitude of the modulus respectively at small strains and higher strains but because Λ is generally small, A actually influences the magnitude of the modulus over the whole range of strain. A also represents the shear modulus at 100% strain according to Equation 2.2-38 in Chapter 2. As expected then, the parameters A and Λ increase with the carbon black content for NR compounds. A value of 0.45 MPa is obtained for the parameter A for NR0 which is comparable to 0.44 MPa[25] found in the literature for a similarly cross-linked unfilled natural rubber. It appears that for the SBR compounds, the value of A is greater for the MT, N990 carbon black filled. The reason for this result will be explained when the variation of the parameter C with the material variables is discussed. The difference in the reinforcing abilities of HAF-N330 and MT-N990 carbon blacks is observable in the magnitudes of Λ. This supports the fact that the difference in the reinforcement capability of a carbon black is visible at high strains; the more reinforcing the carbon black the larger the disruption of the flow of the elastomer chains.

The parameter φ describes the rate of the drop of the modulus at small strains. It is then expected that the more developed the carbon black secondary network, the more important would be the breakdown of this network and the higher the absolute value of the slope, that is to say the value of φ. The formation of this carbon black structure is mainly a function of the distance between aggregates (which mainly

depends on the carbon black content) and the surface activity of the carbon black. For the NR compounds, there is no significant difference in the value of φ between NR0 and NR21 probably meaning that the carbon black structure is almost non-existent in the latter compound. No significant difference is also observed between NR32 and NR59 which would mean a similar degree of breakdown of the carbon black structure in the two compounds. In case of the two SBR compounds, the value of the parameter φ appear to be slightly higher for the HAF-N330 carbon black filled material than the MT-N990 carbon black filled material, confirming that the latter exhibits a less developed carbon black structure although it has higher carbon black loading.

The parameter C was introduced by Davies *et al*[2] in their strain energy function model to give a finite value of the modulus at small strains. Equation 2.2-41 in Chapter 2 related the small strain modulus to C:

$$\left(\frac{\tau}{\gamma}\right)_{\gamma\to 0} = AC^{-\varphi} \qquad (4\text{-}10)$$

According to this expression, the smaller the magnitude of C, the larger the small strain shear modulus. In this work, the precision of the measurements at small strains did not allow to us to relate the calculated value of C to the measured value of the small strain modulus. It is however found that the higher the carbon black content, the lower is the magnitude of C, as shown in Table 4-2 for both NR and SBR compounds. But the values of C for the filled SBR compounds are higher than expected giving for example for SBR30 a predicted small strain modulus equal to 1.5 MPa compared to a measured value of the dynamic tensile storage modulus of the same compound of approximately 3 MPa[26]. Because the apparent values of C are large for the SBR compounds, the magnitude of the parameter A does not predict the value of the shear modulus at 100%. In fact the value of the parameter A was found to be larger for SBR50 than for SBR30 opposite to the observed difference in shear modulus at 100% strain.

4.2.3 Conclusions

It has been shown that the two *e.s.e.d.* functions proposed can represent reasonably well the stress-strain behaviour in different deformation modes of carbon black reinforced NR compounds. As the functions were chosen to depend on I_1 only it follows that the contribution to the reduced stress of $\partial W/\partial I_2$ must be small. For unfilled NR and the filled SBR compounds there appears to be a $\partial W/\partial I_2$ contribution which reduces the universality of the proposed functions. However even in these cases values of the constants in the functions can be chosen such that they predict the stress-strain behaviour in a given deformation mode adequately.

4.3 Stress-strain behaviour of a pre-strained pure shear test-piece

The pre-strained pure shear geometry described in Figure 3-7 in Chapter 3 is to be used for crack growth studies. It is hence necessary to test the validity of the strain energy functions determined using simple uniaxial deformation modes (section 4.2) to predict the stress-strain behaviour of this more complex deformation mode. From a practical point of view, differences in the stiffness due to the effect of an existing or a previous pre-strain are of considerable interest. For example, many applications of elastomers involve bi-axial deformation, in tyres and other inflated devices or in anti-vibration components. Measures of the uniaxial stiffness alone might hence be misleading.

In this study, the effect of different magnitudes of pre-strain on the stress-strain behaviour of elastomers with various carbon black contents will be determined. This experimental data will be compared to that predicted using the strain energy functions determined in section 4.2.2.

4.3.1 Stress-extension ratio, reduced stress curves and prediction calculations

The conversion of the measured load-displacement curve to a stress-extension ratio curve should be carried out carefully. All the dimensions used to calculate the

stresses and the extension ratios should be referred to the unstrained dimensions. If we call λ_p the value of the pre-strain (Figure 4-10), we have:

$$\lambda_1 = \lambda_p \tag{4-11}$$

$$\lambda_3 = \frac{1}{\lambda_2 \lambda_p} \tag{4-12}$$

It should be noted that the initial extension ratio in the direction of vertical loading is equal to $1/\sqrt{\lambda_p}$ as at that stage $\lambda_2 = \lambda_3$. This value is then below unity. Tests are performed from that initial extension ratio, $1/\sqrt{\lambda_p}$, to at least $1+1/\sqrt{\lambda_p}$ that is to say an increase of at least 100% strain.

Using Rivlin's set of relationships between the principal true stresses and the principal extension ratios (Equation 2.2-29 in Chapter 2), as well as the relationship between the true stresses and the engineering stresses ($t_i = \sigma_i \lambda_i$) and substituting Equations 4-11 and 4-12 for λ_1 and λ_3, we find:

$$\frac{\sigma_2 \lambda_2^3 \lambda_p^2}{\lambda_2^4 \lambda_p^2 - 1} = 2\frac{\partial W}{\partial I_1} \tag{4-13}$$

which is the expression used to calculate the reduced stress. The variation of the reduced stress as a function of $I_1 - 3$ will be compared for the pure shear and the pre-strain samples. The results will be discussed in the next section, 4.3.2.

The knowledge of the coefficients for the cubic and the Davies *et al e.s.e.d.* functions, determined previously for the compounds studied from pure shear data, should make it possible to predict the stress-strain behaviour of a pre-strained pure shear specimen. From the expressions of the respective *e.s.e.d.* functions, Equations 4-3b and 4-4b, we can derive the stress-strain relationships, σ_2 against λ_2 by:

$$\text{Cubic: } \sigma_2 = 2\frac{(\lambda_2^4 \lambda_p^2 - 1)}{\lambda_2^3 \lambda_p^2}\left[C_{10} + 2C_{20}(I_1 - 3) + 3C_{30}(I_1 - 3)^2 \right] \tag{4-14}$$

$$\text{Davies } et\ al\text{: } \sigma_2 = 2\frac{(\lambda_2^{\,4}\lambda_p^{\,2}-1)}{\lambda_2^{\,3}\lambda_p^{\,2}}\left[A/2\ (I_1-3+C^2)^{-\varphi/2}+2\Lambda(I_1-3)\ \right] \qquad (4\text{-}15)$$

However, it should be noted that there is a hidden dependence on λ_2 in the terms on the right-hand containing I_1-3. These predicted curves will be compared with the experimental data in the next section.

4.3.2 Results and discussion

The reduced stress versus I_1-3 data for the pre-strained specimens are shown in Figures 4-11 and 4-12. This reduced stress, as given by Equation 4-13, of the form $\sigma_2\lambda_2^3\lambda_p^2/(\lambda_2^4\lambda_p^2-1)$ reduces to σ_2/λ_2 at significant values of λ_2. σ_2/λ_2 is the chord elastic modulus on the plots of σ_2 versus λ_2 shown on Figures 4-13 and 4-14. On these plots are also shown the stress-strain curves predicted using the numerical values of the cubic and Davies *et al e.s.e.d.* functions derived from non pre-strained specimens. Finally in all cases, the magnitudes of the pre-strains (PS) are expressed as percentage strains varying from 0% to 200%.

The plots of the reduced stress versus I_1-3 shown in Figures 4-11 and 4-12 all show that the initial points in I_1-3 move to higher values with increasing pre-strain, as the magnitude of I_1-3 increases with any increase in strain. For all materials the reduced stress (chord elastic modulus) increases in magnitude for a given value of I_1-3 with increasing pre-strain. This shows that pre-strain in one direction has increased the subsequent stiffness in a direction at right angles, for both filled and unfilled materials. However, the magnitude of the effect increases with increasing HAF carbon black content.

It is proposed here to assess if the contribution of $\partial W/\partial I_2$ could explain this increase in stiffness with increasing pre-strain. If we assume that the functional form of W in the pre-strained deformation is the same as for the uniaxial deformations (pure shear and tension, Equation 4-7), $\partial W/\partial I_2$ (Equation 4-9) is then a monotonically

decreasing function of I_2. As I_2 is a more rapidly increasing function of I_1 in the pre-strain deformation states than in the uniaxial ones (Figure 4-15), the contribution of $\partial W/\partial I_2$ to the reduced stress will be smaller for the pre-strain deformations than in uniaxial ones. This is confirmed (G.T. model on Figure 4-11) by substituting both Equation 4-7 for $\partial W/\partial I_2$ and Equation 4-3b for $\partial W/\partial I_1$ in the reduced stress expression, Equation 4-5 with the materials parameters of NR29 and adding an arbitrary constant (equal to 0.55 MPa) to shift the curves upward for clarity. For three different pre-strain (PS=0%, 50% and 100%), it is observed that initially the values of the reduced stress for a given $I_1 - 3$ increases with increasing pre-strain but that these curves converge to that for pure shear as $I_1 - 3$ increases. This predicted behaviour has some similarity to that observed for NR29 but is very different to that observed for NR0, NR21 and NR59 and the SBR materials. It is hence unlikely that a contribution from $\partial W/\partial I_2$, assuming that its functional form is the same as in uniaxial conditions, could explain the observed variation of the reduced stress with pre-strain for the current tests.

Whatever the contribution of $\partial W/\partial I_2$, from a physical point of view, the major contribution to this observed stiffness increase with pre-strain must be due partly to molecular orientation and partly due to the role of the carbon black. The carbon black will both increase the molecular orientation due to strain amplification and by the development of carbon black structure. The reduced stress (chord modulus) initially decreases in all cases with increasing strain for both filled and unfilled materials. However, the effect is most marked for the highly filled elastomers, suggesting that the breakdown of the carbon black structure plays some role. It was anticipated that as the specimens were strained further, the effect of the pre-strain would eventually become masked by the orientation developed in the new straining direction. This would have resulted in the curves of reduced stress versus $I_1 - 3$ for a given material being superimposed at large strains for all pre-strains. While there is some tendency for this to occur for NR29, in general, at the strains studied, it does not take place. This suggests that it is not easy to remove orientation developed by straining in one mode by subsequent additional straining in different mode. If this is the case it will of course

not be possible to produce an *e.s.e.d.* function to represent deformation in a number of deformation modes.

Some of the data from Figures 4-11 and 4-12 are shown as plots of $\sigma_2 = f(\lambda_2)$ in Figures 4-13 and 4-14. Also shown are the cubic and the Davies *et al e.s.e.d.* functions containing constants derived from non pre-strained specimens. As expected the experimental curves all lie above the predicted curves as the measured chord moduli σ_2/λ_2 are all increased with increasing pre-strain, the effect being greater for the highly filled materials. Both *e.s.e.d.* functions hence underestimate the actual elastic strain energy stored in the specimen by as much as 40%.

4.4 Stress-strain behaviour of a 30° inclined pure shear test-piece

The 30^0 inclined pure shear geometry described in Figure 3-11 in Chapter 3 is, like the pre-strained test-piece, to be used for crack growth studies. It is hence necessary to test the validity of the strain energy functions determined using simple uniaxial deformation modes (section 4.2) to predict the stress-strain behaviour of this more complex deformation mode. This will be particularly useful for use within a finite element based fracture mechanics approach used to predict the direction of crack growth.

The study of the mechanical behaviour of a component loaded simultaneously in the two different deformation modes induced by this geometry (pure shear or constrained tension and simple shear) is also of interest in its own right as similar situations to this occur in many engineering components.

4.4.1 Derivation of the vertical force necessary to strain a 30° inclined pure shear test-piece.

The deformation behaviour of the test-piece can be modelled as illustrated Figure 4-16. The deformation is considered as a sheet extended by an extension ratio α_2 in the x-direction and then deformed to α_1 in the y-direction. This sheet is then subjected to a shear deformation parallel to the x-direction defined by an angle of shear ϕ and the amount of shear is defined as $\tan\phi = \gamma$. The analysis used here for this problem is a special case of the solution for the combined torsion, inflation and

extension of a uniform circular tube[27], as described in Appendix 1. In the present case, the equations can first be simplified by assuming the tube to be thin walled and of wall thickness t and radius a. Then if α_1 and α_2 replace λ_1 and μ in Rivlin's relationships[27], we have:

$$\gamma = a\alpha_2\varsigma \tag{4-16}$$

where ς characterises the magnitude of the torsion and is the angle of torsion per unit deformed height of the tube. The torsion couple M, the tensile forces to the end of the tube N and the force R_v, per unit area, measured in the deformed state, acting normally on the inner surface of the tube (that is to say the internal pressure) are related to the following stresses referred to the deformed dimensions; the shear stress, τ, the stress in the y-direction, t_1, and the stress in the x-direction, t_2:

$$\tau = \frac{M\alpha_1}{2\pi\alpha_2 a^2 t} \tag{4-17}$$

$$t_1 = \frac{F_t\alpha_1}{2\pi at} \tag{4-18}$$

$$t_2 = -\frac{R_v a\alpha_1\alpha_2^2}{t} \tag{4-19}$$

For a thin walled tube this is equivalent to the deformation of a flat sheet under biaxial and shear strain. Using the expressions for M, F_t and R_v in Appendix 1, we have the following expressions:

$$\tau = 2\gamma\frac{\alpha_1}{\alpha_2}\left(\alpha_1\alpha_2\frac{\partial W}{\partial I_1} + \frac{1}{\alpha_1\alpha_2}\frac{\partial W}{\partial I_2}\right) \tag{4-20}$$

$$t_1 = 2\left(\alpha_2^2 - \frac{1}{\alpha_1^2\alpha_2^2}\right)\left(\frac{\partial W}{\partial I_1} + \alpha_2^2\frac{\partial W}{\partial I_2}\right) - \frac{2\gamma^2}{\alpha_2^2}\frac{\partial W}{\partial I_2} \tag{4-21}$$

$$t_2 = 2\left(\alpha_2^2 - \frac{1}{\alpha_1^2\alpha_2^2}\right)\left(\frac{\partial W}{\partial I_1} + \alpha_1^2\frac{\partial W}{\partial I_2}\right) + 2\gamma^2\alpha_1^2\frac{\partial W}{\partial I_1} \tag{4-22}$$

The strain invariant expressions are given by:

$$I_1 = \alpha_1^2 + \alpha_2^2 + \frac{1}{\alpha_1^2\alpha_2^2} + \gamma^2\alpha_1^2 \tag{4-23}$$

$$I_2 = \frac{1}{\alpha_1^2} + \frac{1}{\alpha_2^2} + \alpha_1^2\alpha_2^2 + \frac{\gamma^2}{\alpha_2^2} \tag{4-24}$$

which allows $\partial W/\partial I_1$ and $\partial W/\partial I_2$ to be calculated in terms of α_1, α_2 and ν if W is known as a function of I_1 and I_2.

For the case of the forces on an inclined pure shear test-piece (Figure 4-16), α_1, α_2 and γ become:

$$\alpha_1 = 1 + \frac{\delta}{L_0}\cos\vartheta \tag{4-25}$$

$$\alpha_2 = 1 \tag{4-26}$$

$$\gamma = \tan\phi = \frac{\sin\vartheta}{L_0/\delta + \cos\vartheta} \tag{4-27}$$

where ϑ, δ and L_0 are defined in Figure 4-16 and are respectively the angle of inclination of the pure shear test-piece, the displacement along the vertical direction, and the unstrained height of the pure shear test-piece. We then have for the shear force f_s and the normal force f_n the following expressions:

$$f_s = 2tw\gamma\left(\alpha_1\frac{\partial W}{\partial I_1} + \frac{1}{\alpha_1}\frac{\partial W}{\partial I_2}\right) \tag{4-28}$$

$$f_n = 2tw\left[\left(\alpha_1 - \frac{1}{\alpha_1^3}\right)\left(\frac{\partial W}{\partial I_1} + \frac{\partial W}{\partial I_2}\right)\right] - \frac{2tw\gamma^2}{\alpha_1}\frac{\partial W}{\partial I_2} \qquad (4\text{-}29)$$

w being the width of the pure shear specimen. The total force f_t, the force measured during the test is:

$$f_t = f_s \sin\vartheta + f_n \cos\vartheta \qquad (4\text{-}30)$$

Relations (4-23) to (4-28) allow the measured force to be expressed in terms of the vertical displacement, δ, the dimensions of the test-piece (w, t and L_0) and the *e.s.e.d.* function. I_1 and I_2 are given by Equations 4-23 and 4-24 putting α_2=1. For the special case of $\partial W/\partial I_2 = 0$, which has been shown to be a reasonable assumption for NR filled elastomers (section 4.2) and as we have $\alpha_2 = 1$ (pure shear configuration), we obtain:

$$f_s = 2tw\gamma\alpha_1\frac{\partial W}{\partial I_1} \qquad (4\text{-}31)$$

$$f_n = 2tw\left[\left(\alpha_1 - \frac{1}{\alpha_3}\right)\frac{\partial W}{\partial I_1}\right] \qquad (4\text{-}32)$$

$$f_t = 2tw\frac{\partial W}{\partial I_1}\left[\frac{\delta}{L_0}\sin^2\vartheta + \left(\alpha_1 - \frac{1}{\alpha_1^3}\right)\cos\vartheta\right] \qquad (4\text{-}33)$$

Knowing $\partial W/\partial I_1$ or W from simple uni-axial data, it is possible to predict the force deflection behaviour of this inclined pure shear geometry test-piece for a given compound and to compare this with the experimental results.

4.4.2 Results and discussion

This 30° inclined pure shear geometry was tested on NR21, NR29 and NR59. The experimental results shown on Figure 4-17 were compared with predictions from the Davies *et al* and the cubic *e.s.e.d.* functions, utilising Equations 4-33, 4-23 and 4-25.

The Davies *et al* and the cubic functions predict reasonably well the experimental data. The observed discrepancies can be attributed to known experimental difficulties. One of them, common to all pure shear type experiments is the error in the determination of the zero force position. Whether this unstrained height is underestimated or overestimated, it results in a curve with lower forces for a given displacement. The side forces generated by the geometry itself mentioned in Chapter 3, section 3-4 (30° inclined pure shear test) might have been another source of experimental error but have been shown not to have a significant effect on the measurement of the vertical force.

As I_1 as a function of I_2 is not very different for the pure shear and the 30^0 inclined pure shear test (Figure 4-15), any variation in $\partial W/\partial I_2$ should not be largely different for the two deformation modes and would hence not produce any differences on a force deflection plot. In a sense, of course, this is another way of saying that as the deformation modes are not that different, one would expect a strain energy function derived for one to be applicable for the other.

4.5 Conclusions

The first section of this chapter dealt with the mechanical characterisation of the elastomer compounds to be used in this thesis. The use of two *e.s.e.d.* functions, a cubic form proposed by Yeoh[1] and a function proposed by Davies *et al*[2] depending only on the first strain invariant I_1 has proved to be a reasonable simplification for filled elastomers. The observed limitations could have been due to neglecting terms in I_2 in the *e.s.e.d.* function but this did not lead to significant errors in prediction of the stress-strain behaviour.

It has been demonstrated that pre-strain in one direction increases the elastic modulus of all the elastomer compounds, whether filled or unfilled, when subsequently strained in a direction at right angles. The pre-strain is inducing a stiffness anisotropy. From a molecular point of view, the introduction of the pre-strain in one direction restricts the molecular motion in the orthogonal direction and hence increases the modulus in this direction. The presence of carbon black amplifies this effect.

It is therefore difficult to use a strain energy function derived from a single deformation mode to predict the deformation behaviour following a pre-strain. Consequently, in the work on crack growth in pre-strained specimens described in Chapter 5, both an in-situ experimental method and a Finite Element Analysis based fracture mechanics method will be used to calculate tearing energies (energy release rates). For the 30° degree inclined pure shear test-piece, the uniaxial derived *e.s.e.d.* function predicts the deformation behaviour well and will be used in Chapter 5 to predict crack growth directions.

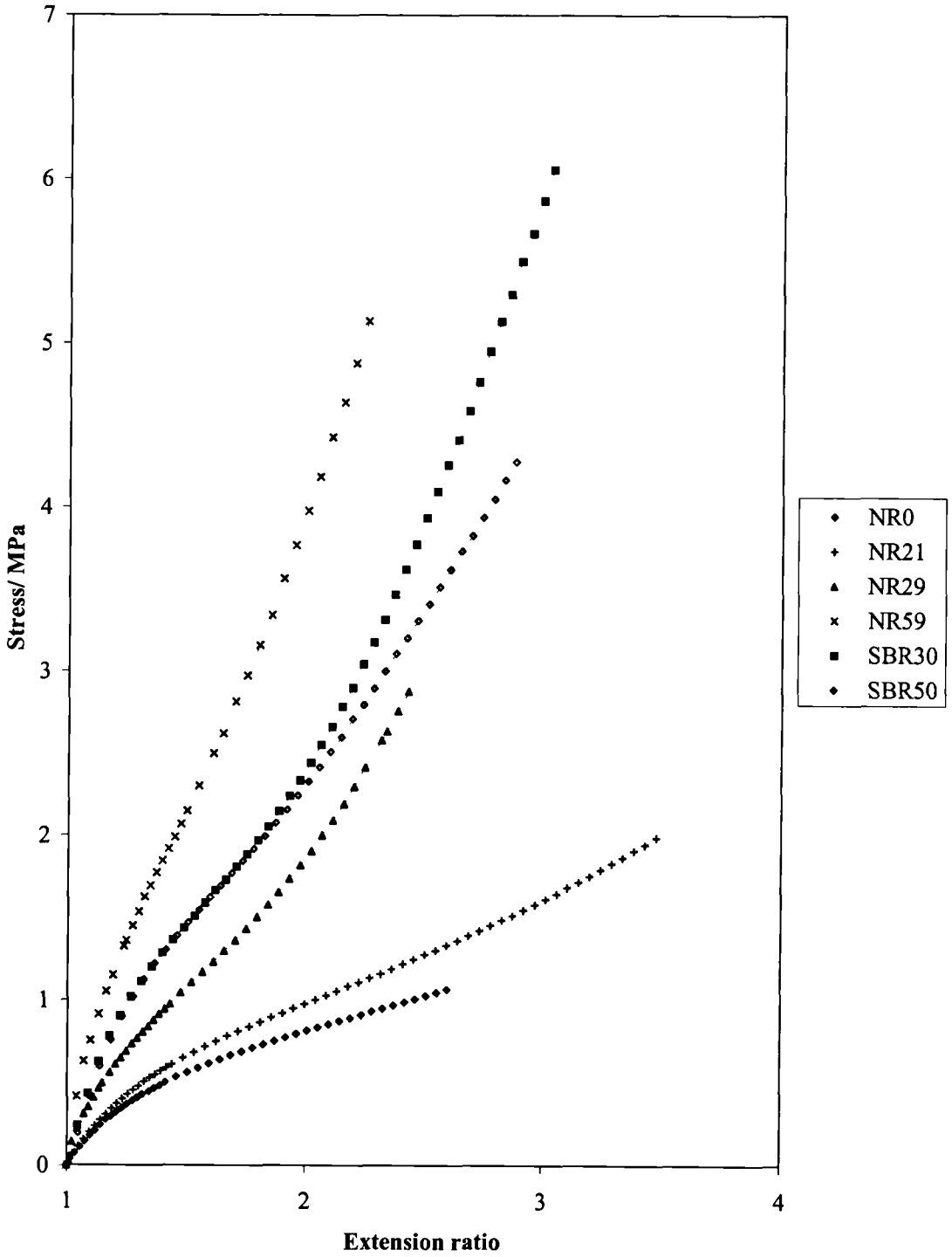

Figure 4-1 Stress-extension ratio curves for all compounds in pure shear.

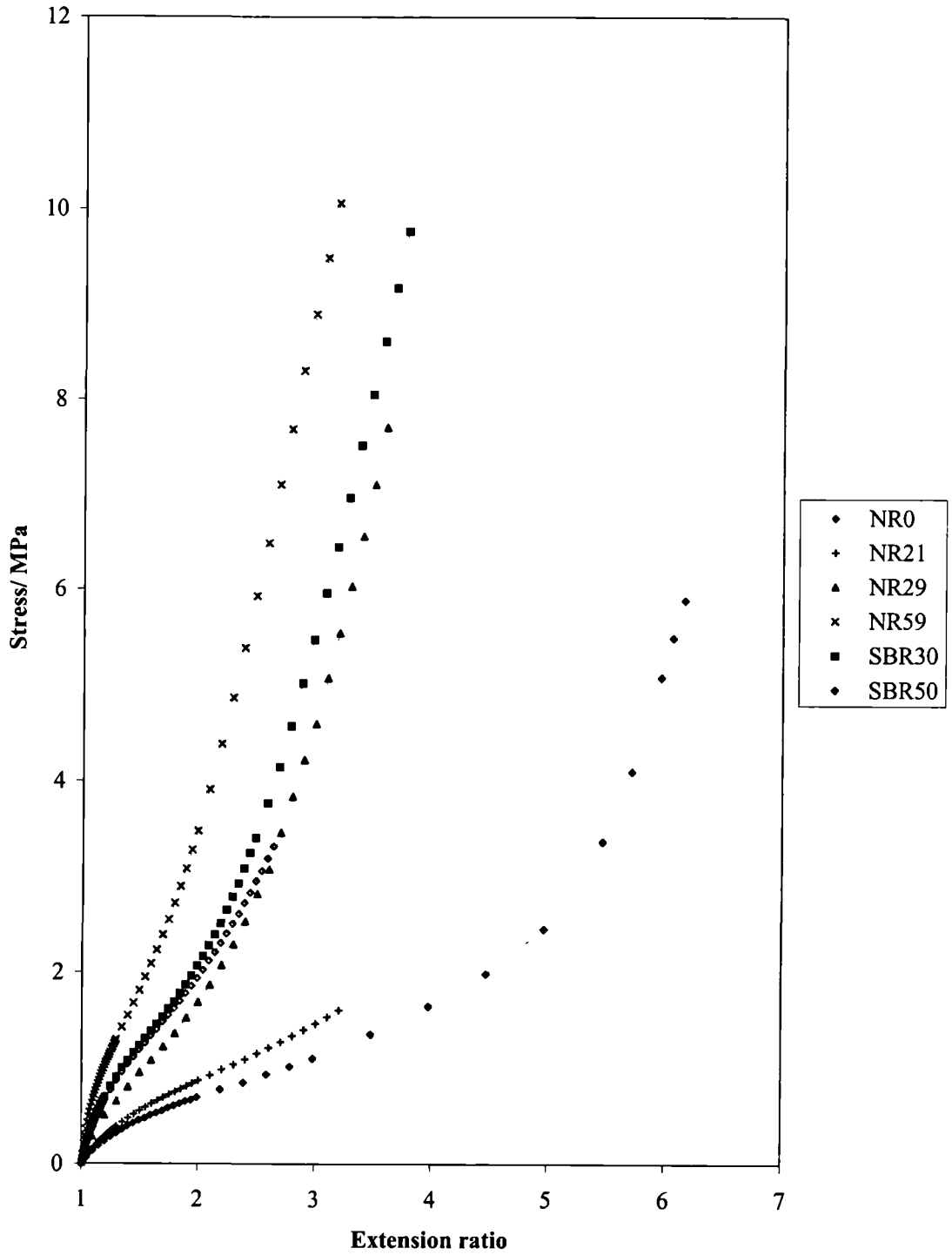

Figure 4-2 Stress-extension ratio curves for all compounds in tension.

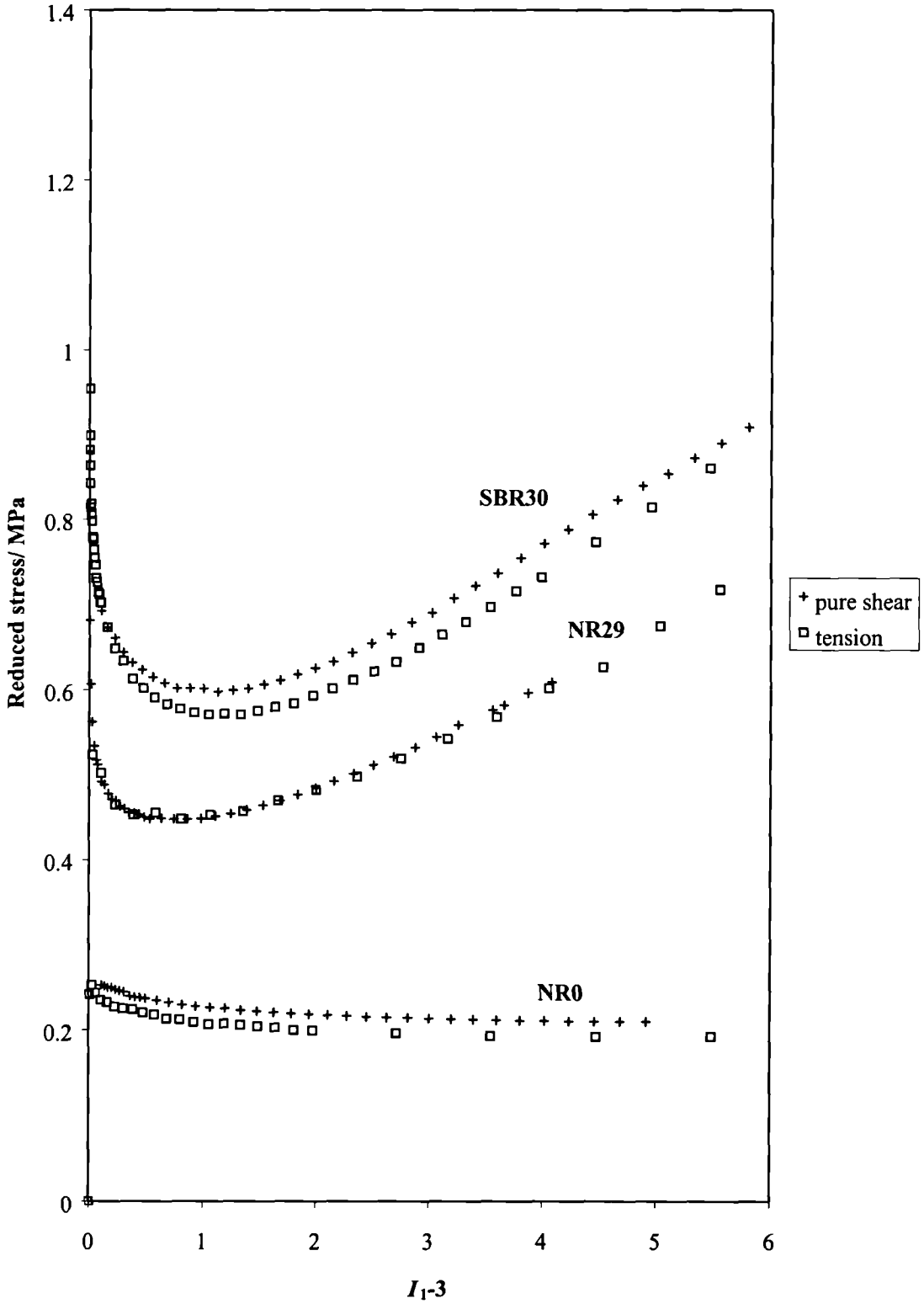

Figure 4-3 Reduced stress as a function of $(I_1 - 3)$ for NR0, NR29 and SBR30.

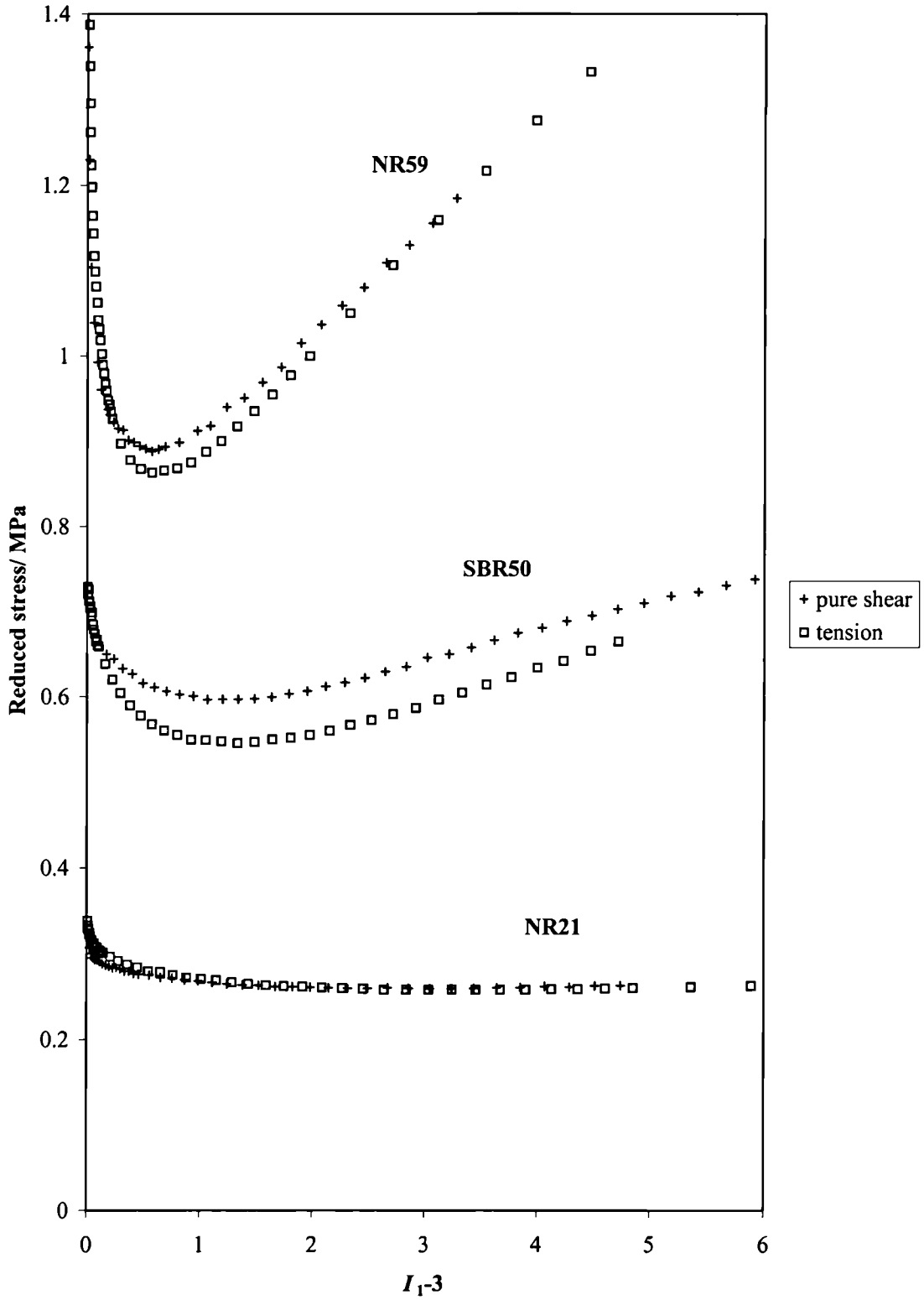

Figure 4-4 Reduced stress as a function of $(I_1 - 3)$ for NR21, NR59 and SBR50.

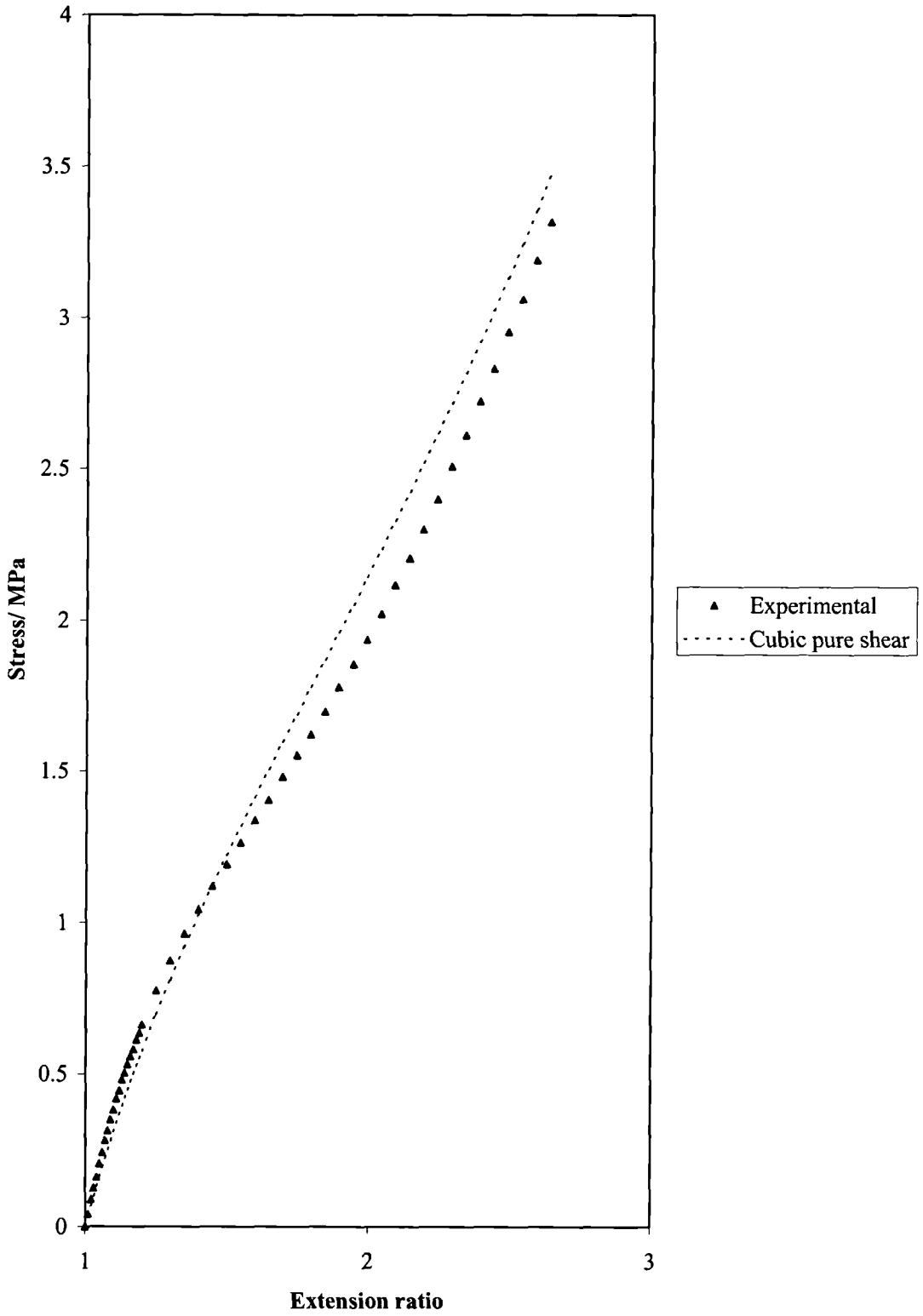

Figure 4-5 Prediction of the experimental data in tension with the cubic *e.s.e.d.* function derived from pure shear data for SBR50.

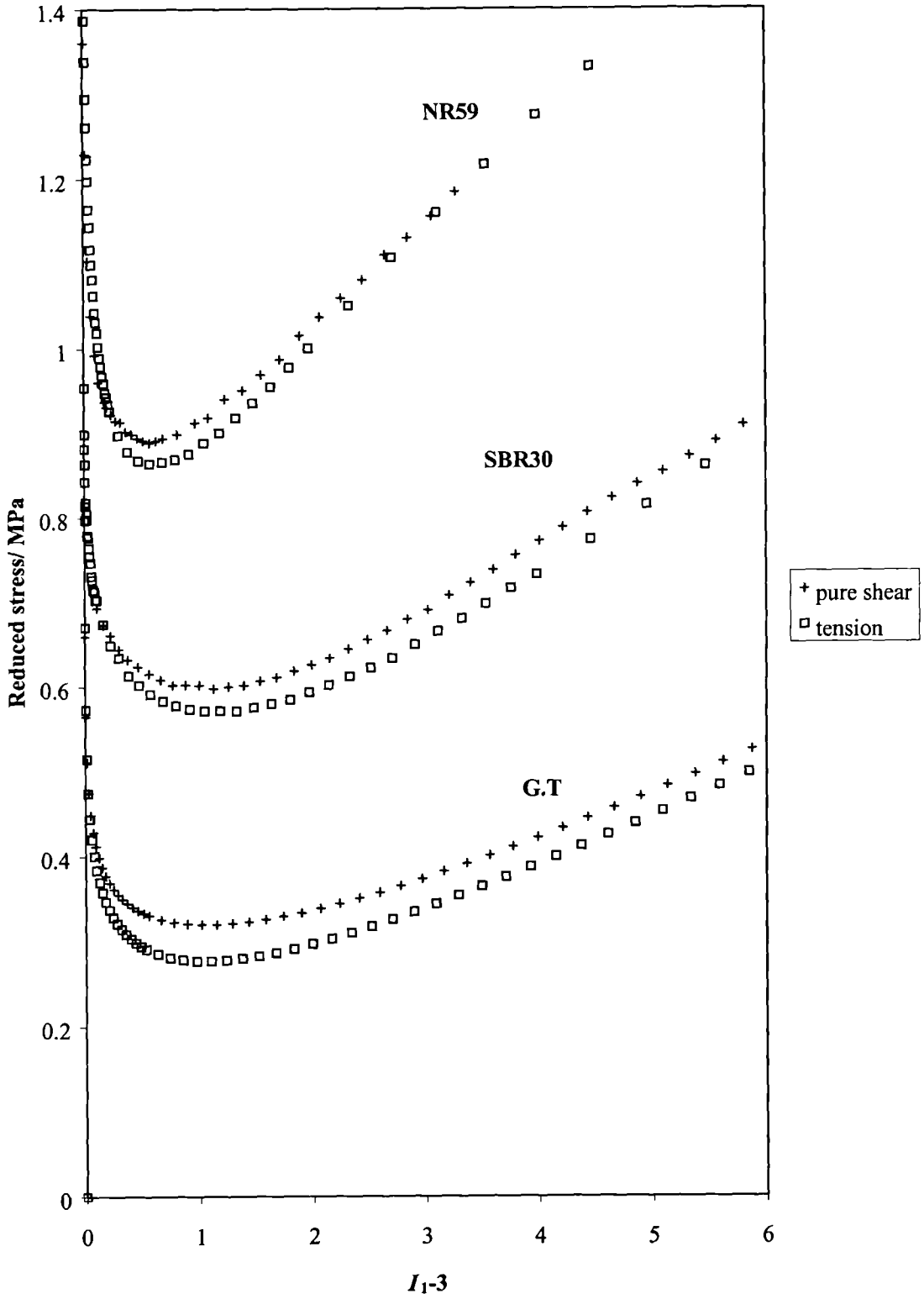

Figure 4-6 Predicted differences between pure shear and tension curves from a modified Gent and Thomas[24] (G. T.) *e.s.e.d.* function incorporating a term in I_2 and comparison with experimental data from SBR30 and NR59.

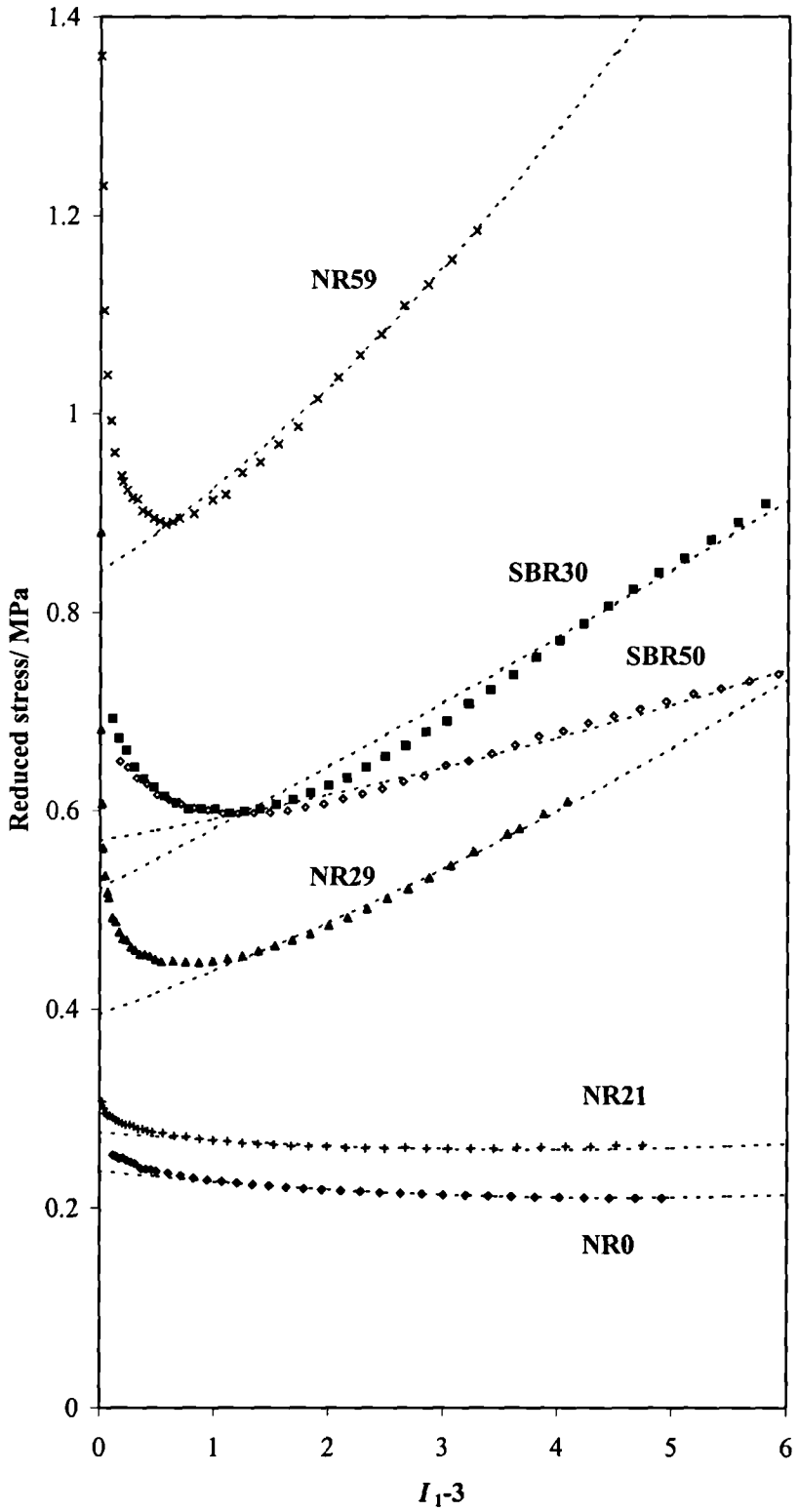

Figure 4-7 Fitting of the experimentally derived reduced stress versus $(I_1 - 3)$ data in pure shear with the cubic model.

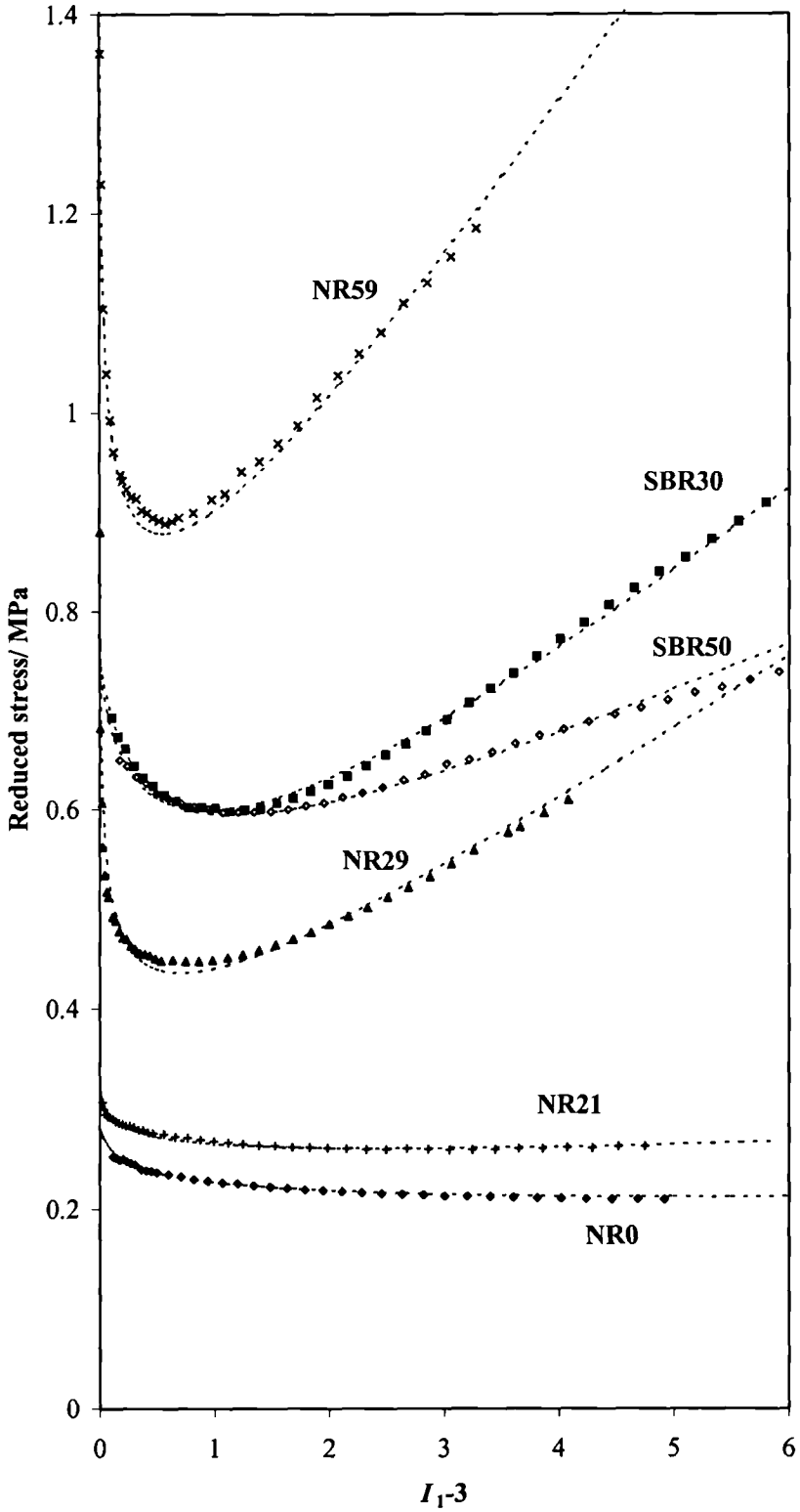

Figure 4-8 Fitting of the experimentally derived reduced stress versus $(I_1 - 3)$ data in pure shear with the Davies *et al* model.

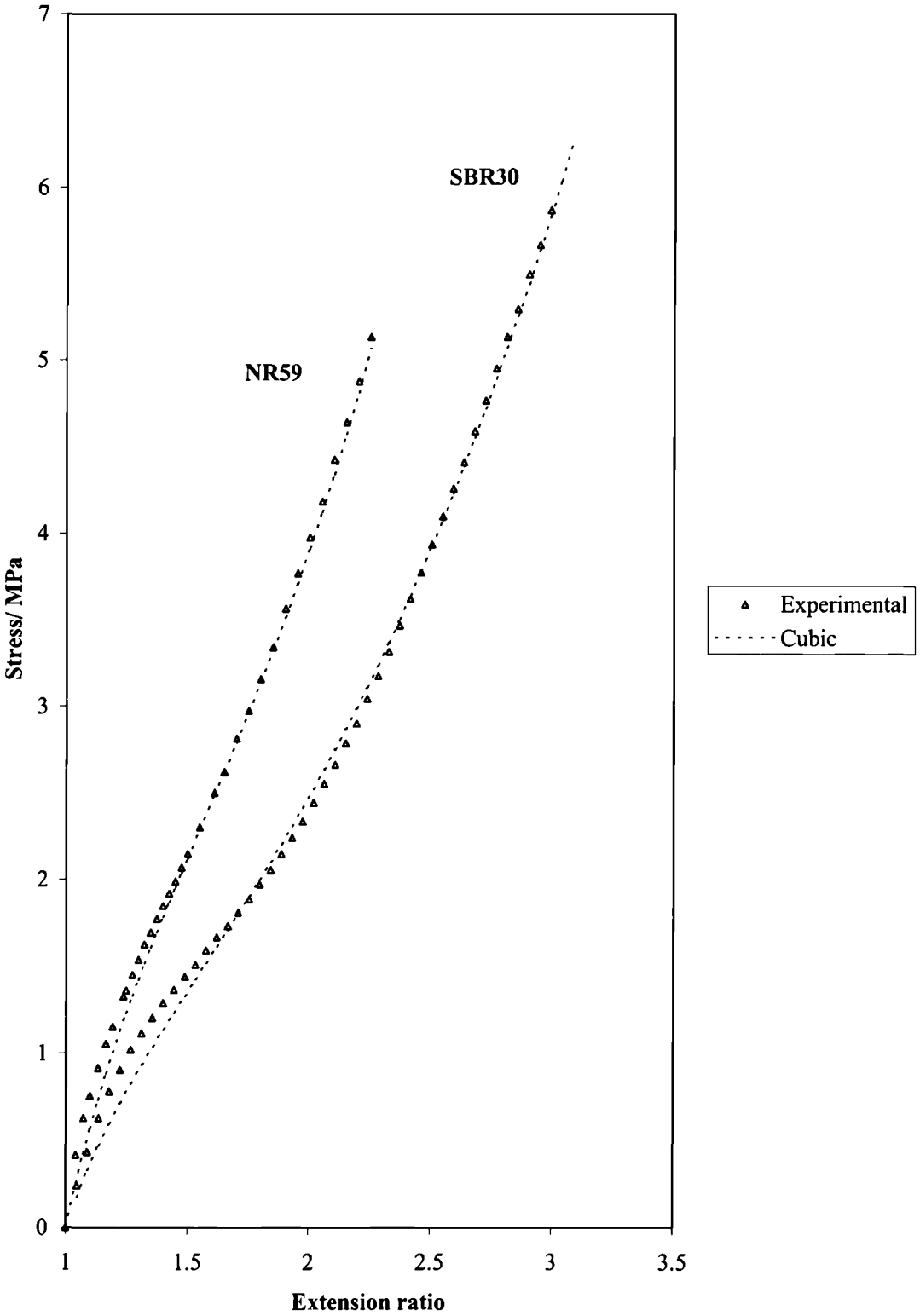

Figure 4-9 $\sigma_2 = f(\lambda_2)$ plots of the cubic function prediction compared with experimental data on NR59 and SBR30, in pure shear.

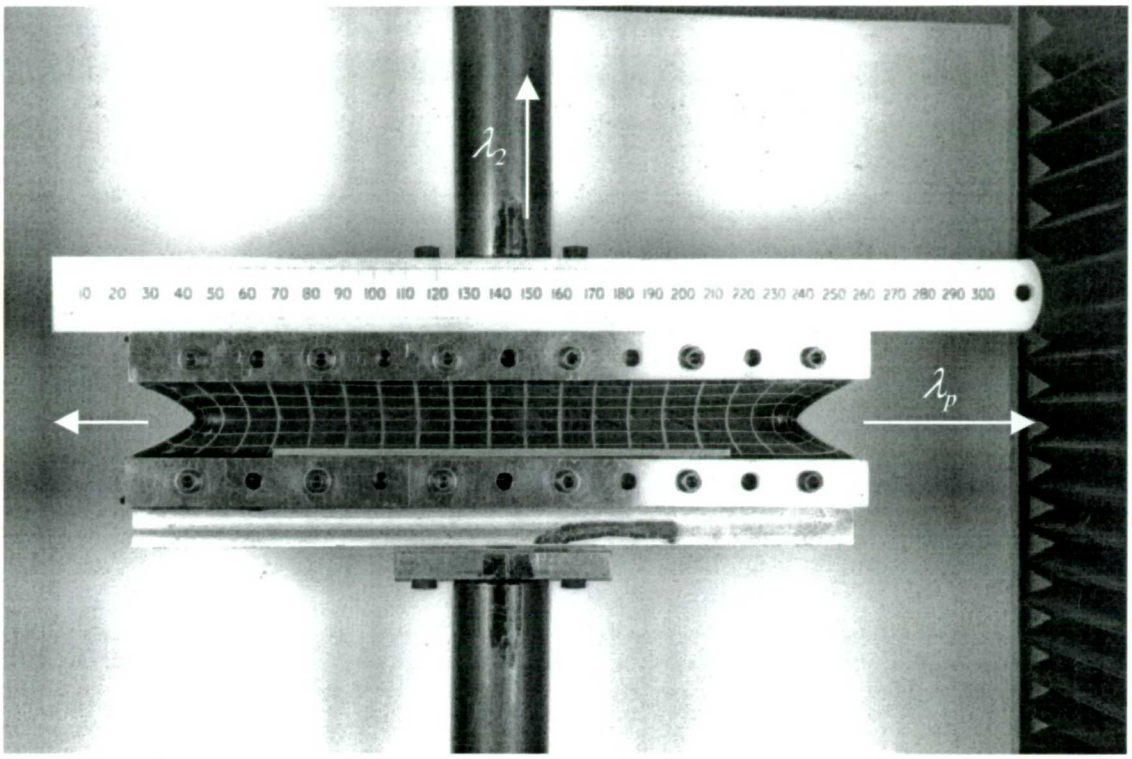

Figure 4-10 Principal extension ratios in the pre-strained pure shear test-piece, λ_p representing the magnitude of the pre-strain.

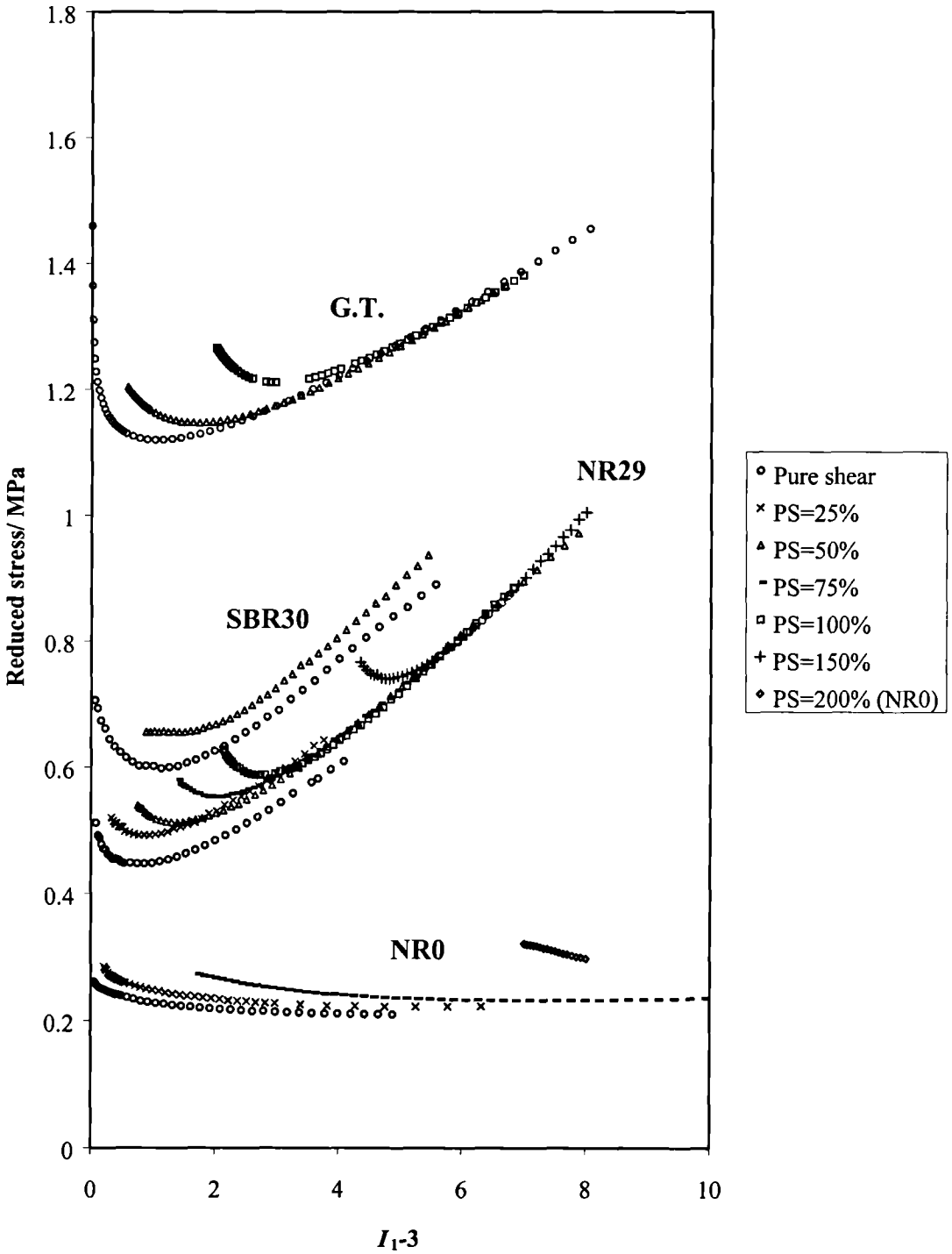

Figure 4-11 Reduced stress versus $(I_1 - 3)$ curves as a function of the magnitude of pre-strain (PS, expressed in percentage strain) for NR0, NR29 and SBR30. These curves are compared with a modified Gent and Thomas function[24] (G.T. model).

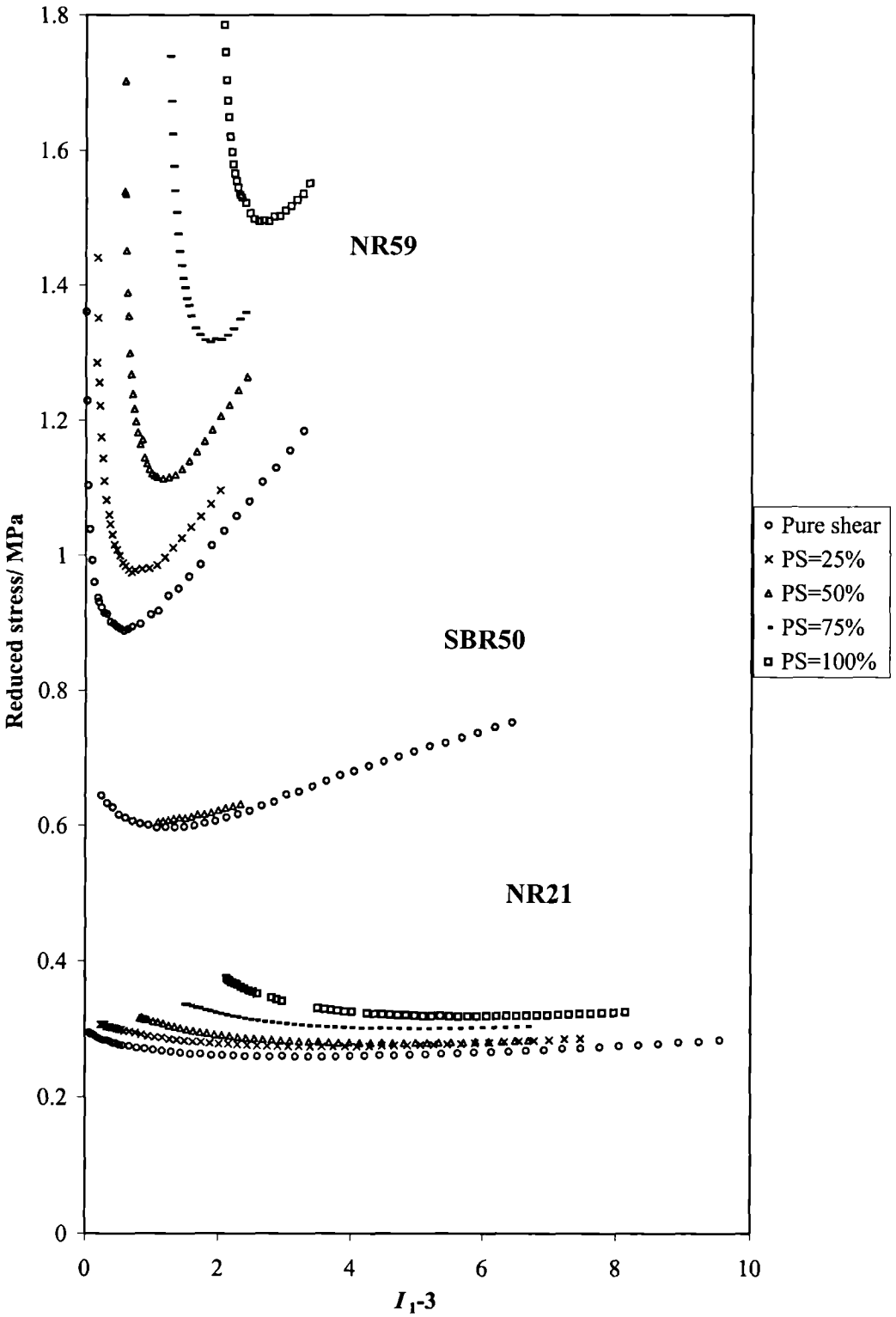

Figure 4-12 Reduced stress versus $(I_1 - 3)$ curves as a function of the magnitude of pre-strain (PS, expressed in percentage strain) for NR21, NR59 and SBR50.

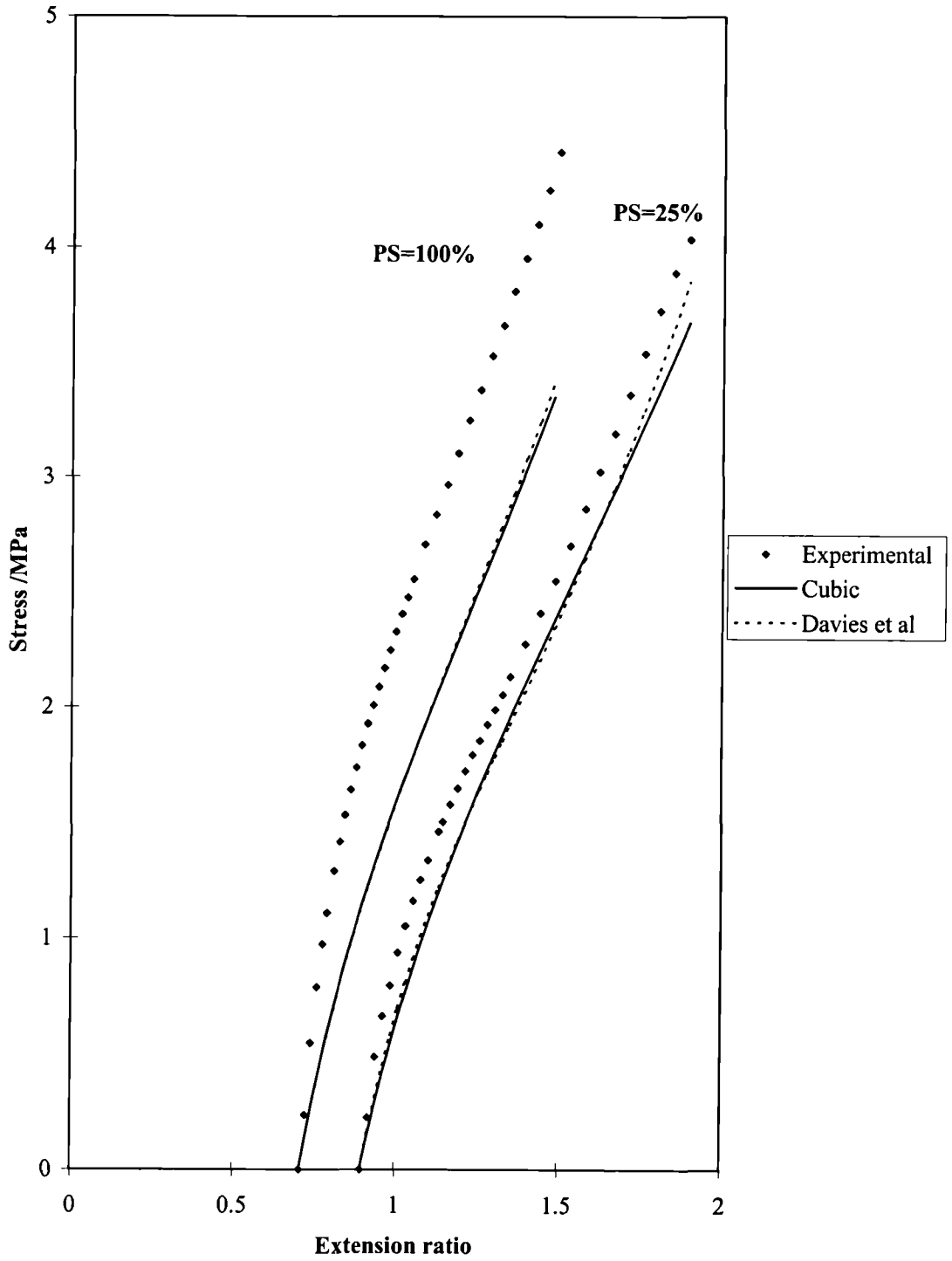

Figure 4-13 $\sigma_2 = f(\lambda_2)$ plots comparing the pre-strained pure shear experimental data (PS=25% and 100%) and the predicted curves (cubic and Davies *et al*) fitted from pure shear on NR59.

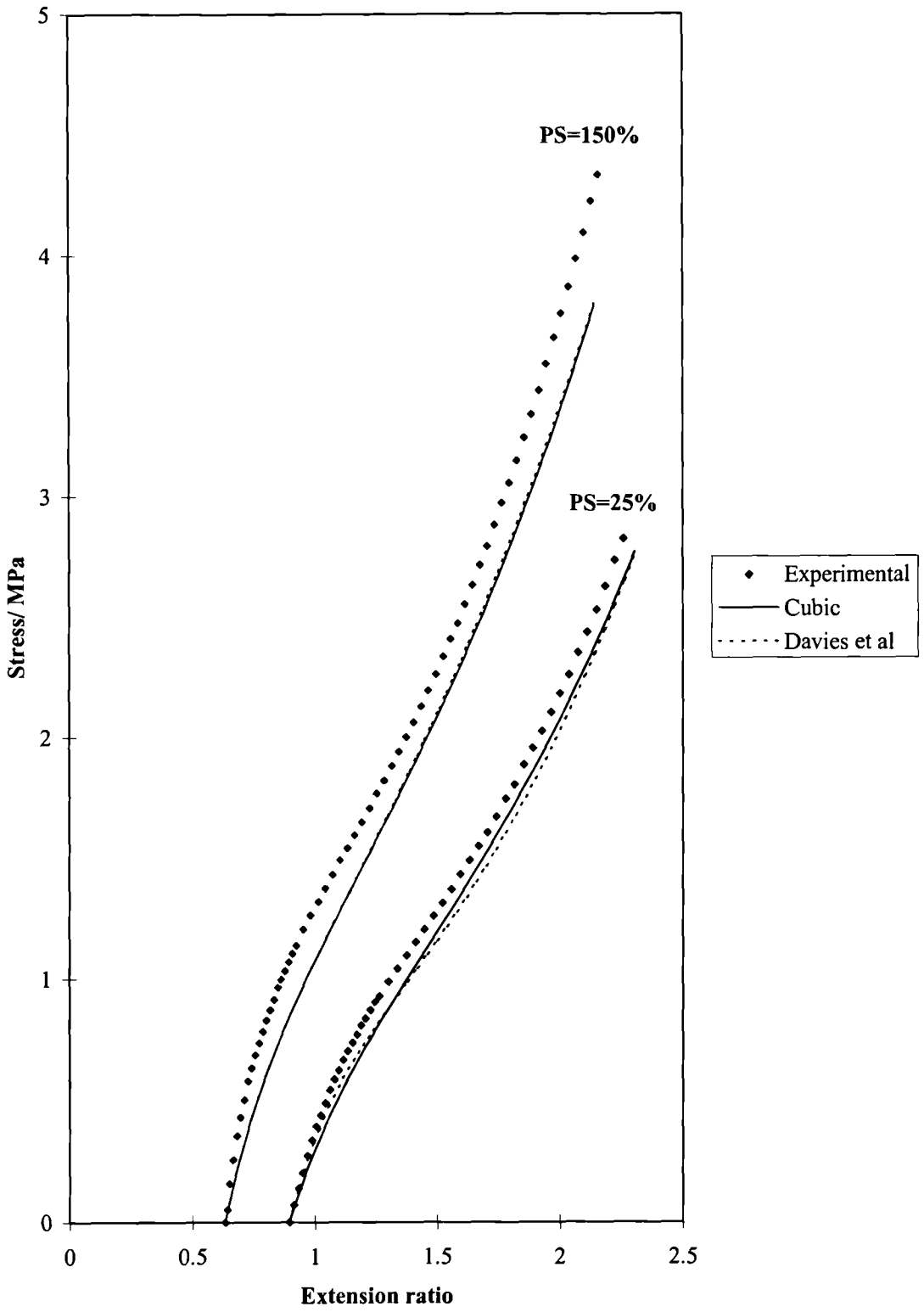

Figure 4-14 $\sigma_2 = f(\lambda_2)$ plots of comparing the pre-strained pure shear experimental data (PS=25% and 150%) and the predicted curves (cubic and Davies *et al*) fitted from pure shear on NR29.

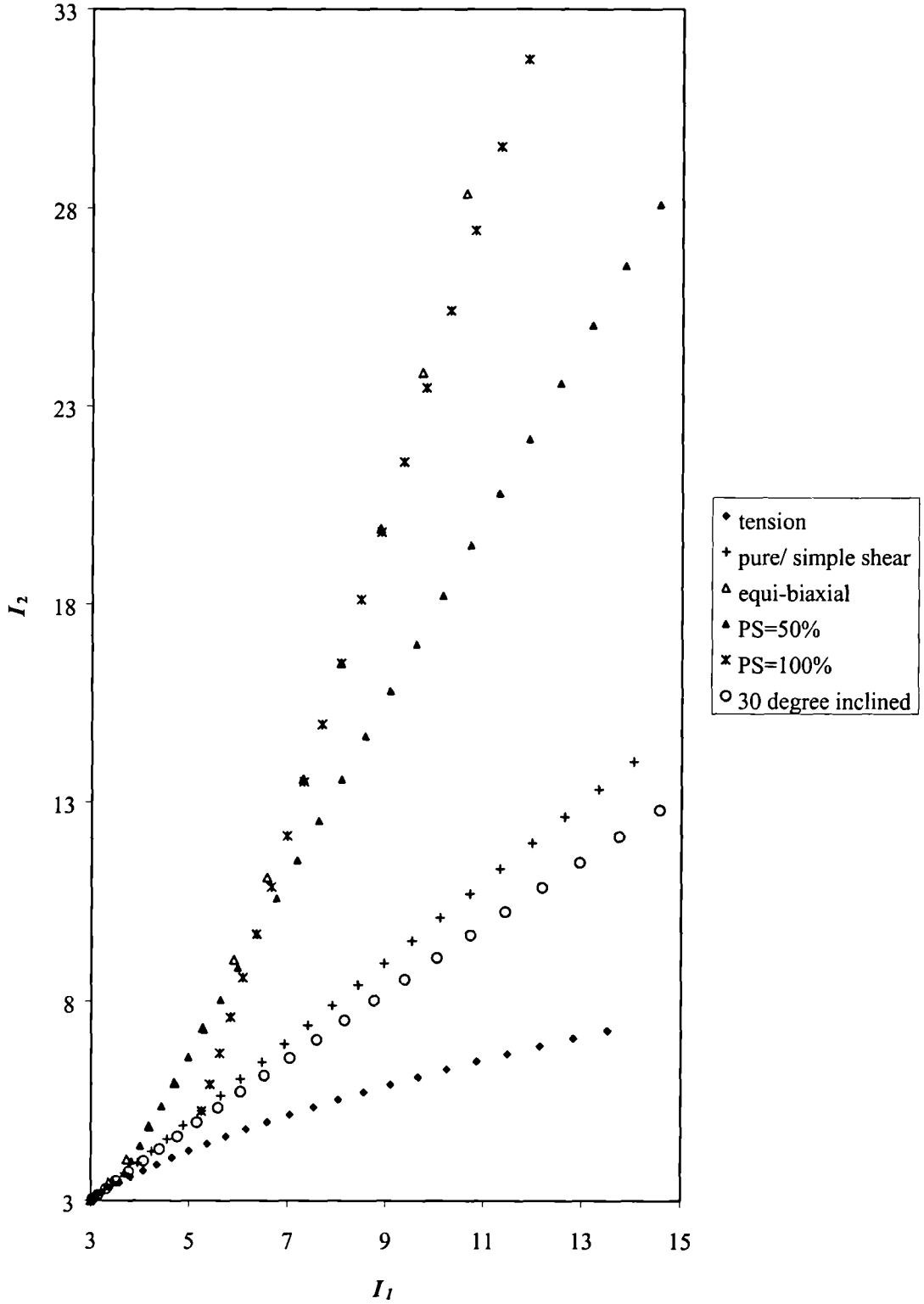

Figure 4-15 Plots of I_1 as a function of I_2 for various deformation modes (PS is the magnitude of the pre-strain expressed in percentage strain for the pure shear pre-strain geometry section 4.4).

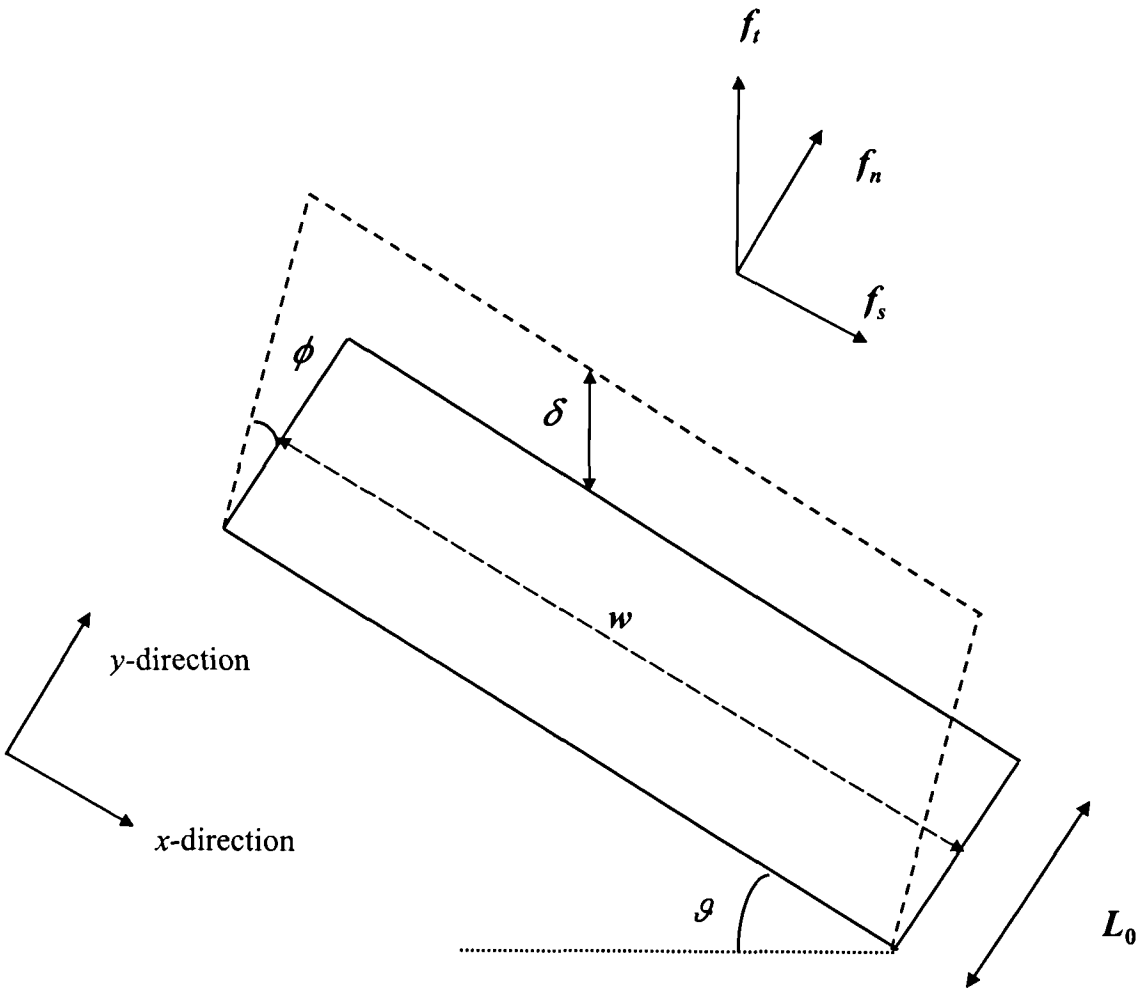

Figure 4-16 Schematic showing the different parameters defining the deformation of the 30° degree inclined pure shear geometry. These are: ϑ, the inclination of the pure shear geometry to the horizontal; ϕ, the angle defining the amount of shear; δ, the vertical displacement; w and L_0, respectively the width and the unstrained height of the pure shear geometry; f_s, f_n and f_t, respectively the shear, normal and total or measured forces.

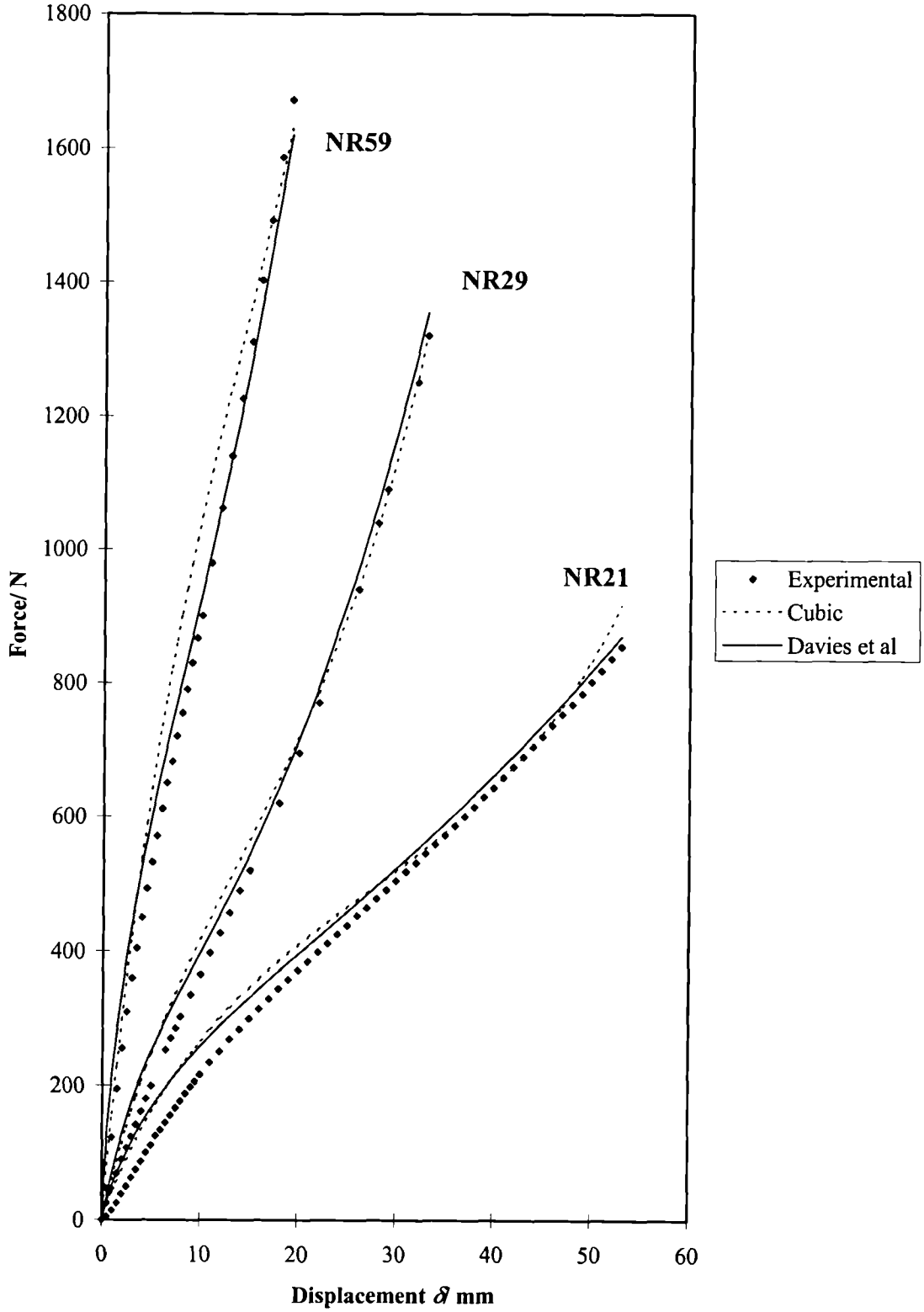

Figure 4-17 Comparison of the force-deflection data on the 30° inclined pure shear test-piece and the predictions from pure shear (Davies *et al* and cubic functions) for NR21, NR29 and NR59.

Compounds	C_{10}/ MPa	C_{20}/ MPa	C_{30}/ MPa
NR0	0.24	-5.9×10^{-3}	4.3×10^{-4}
NR21	0.28	-4.6×10^{-3}	4.7×10^{-4}
NR29	0.4	2.1×10^{-2}	8.3×10^{-4}
NR59	0.84	3.8×10^{-2}	3×10^{-3}
SBR30	0.52	3×10^{-2}	2.7×10^{-4}
SBR50	0.57	1×10^{-2}	4.7×10^{-4}

Table 4-1 Values of the material constants C_{10}, C_{20} and C_{30} of the cubic strain energy function for all compounds.

Compounds	A/ MPa	Λ / MPa	φ	C
NR0	0.45	1.3×10^{-3}	0.15	0.23
NR21	0.52	3.5×10^{-3}	0.11	0.15
NR29	0.72	4.0×10^{-2}	0.30	3.0×10^{-2}
NR59	1.45	9.0×10^{-2}	0.24	1.0×10^{-3}
SBR30	1.05	4.8×10^{-2}	0.45	0.45
SBR50	1.13	3.1×10^{-2}	0.35	0.59

Table 4-2 Values of the material constants A, Λ, φ and C of the Davies *et al* strain energy function for all compounds.

REFERENCES

[1] Yeoh O. H., *Rubber Chem. Technol.*, **63**, 792 (1990).

[2] Davies C. K. L., De D. K. and Thomas A. G., *Rubber Chem. and Technol.*, **67**, 716 (1994).

[3] De D. K., PhD Thesis, University of London (1994).

[4] Rivlin R.S., "Rheology vol. 1", Ed. Eirich F. R., Academic Press, New-York, **10,** 351 (1956).

[5] Gregory M. J., *Plast. Rubber Mater. Applications,* **4,** 184 (1979).

[6] Smallwood H. M., *J. Appl. Phys.*, **15**, 758 (1944).

[7] Guth E., *J. Appl. Phys.*, **16**, 20 (1945).

[8] Wolff S. and Wang M.-J., "Carbon Black", 2nd ed, Ed. Donnet J.-B., Bansal R. C. and Wang M.-J., Marcel Dekker, **9**, 289 (1993).

[9] Rivlin R. S. and Saunders D. W., *Phil. Trans. Roy. Soc. London* A, **243,** 251 (1951).

[10] Mullins L., *J. Appl. Polym. Sci.,* **6,** 257 (1959).

[11] Payne A. R., *J. Polymer Sci.*, **6**, 57 (1962).

[12] Payne A. R. and Whittaker R. E., *Rubber Chem. Technol.*, **44**, 440 (1971).

[13] Voet A. and Cook F. R., *Rubber Chem. Technol.*, **41**, 1208 (1968).

[14] Voet A., Sircar A. K. and Mullens T. J., *Rubber Chem. Technol.*, **42**, 874 (1969).

[15] Voet A. and Morawski J. C., *Rubber Chem. Technol.*, **47**, 765 (1974).

[16] Wolff S. and Donnet J.-B., *Rubber Chem. Technol.*, **63**, 32 (1990).

[17] Gerspacher M., "Carbon Black", 2nd ed, Ed. Donnet J.-B., Bansal R. C. and Wang M.-J., Marcel Dekker, **7**, 377 (1993).

[18] Prager S. and Frish H.L., *J. Chem. Phys.*, **46**, 1475 (1967).

[19] Treloar L. R. G., "The Physics of Rubber Elasticity", Oxford Univ. Press, 3rd Ed., **10,** 211 (1975).

[20] Obata Y, Kawabata S. and Kawai H., *J. Polymer Sci.* A**2**, **8**, 903 (1970).

[21] Kawabata S., Yamashita Y., Ooyama H. and Yoshida S., *Rubber Chem. Technol.*, **68**, 311 (1995).

[22] Prager S. and Frish H. L., *J. Chem. Phys.*, **46**, 1475 (1967).

[23] Gent A. N., "Engineering with rubber, How to design rubber components", Ed. Gent A. N., Hanser Publishers, **3**, 33 (1992).

[24] Gent A. N. and Thomas A. G., *J. Polym. Sci.*, **28**, 625 (1958).

[25] Natural rubber engineering data sheets, MRPRA, Hertford, UK (1987).

[26] Deeprasertkul C., PhD thesis, University of London (2000).

[27] Rivlin R. S., *Phil. Trans. Roy.* Soc. A, **242**, 173 (1949).

5

Fatigue crack growth under a biaxial loading

5.1 Introduction

The main concern of this thesis was an investigation of the fatigue crack growth behaviour of commercial elastomers used in anti-vibration components in the automotive industry. These materials were to be tested under non-simple loading. In the present case tests were to be carried out on pure shear test-pieces (Figure 5-1) on which a pre-strain was maintained in an orthogonal direction to the principal strain (Figure 5.2). By gradually increasing the loading complexity in this way, a better understanding of this issue could be developed and general rules could be drawn to predict the life of these systems. The crack growth process involved in this work is predominantly mechanical driven rather than chemical crack growth. The most suitable approach to describe the crack growth behaviour of highly deformable non-linear elastic material is an energy balance approach[1]. The crack growth process can be described as being governed by the energy release rate with respect to the fracture surface created and is called the tearing energy T for elastomers. It has been shown[2, 3] that the fatigue crack growth characteristics of a material can be described by the knowledge of the relationship between the crack growth rate dc/dn and the tearing energy T. This relationship is considered as being a material property, independent of the test piece geometry[4].

Adopting an energetic approach to examine fatigue crack growth, requires as pre-requisite that an investigation of the elastic strain energy density functions for filled elastomers, undertaken in Chapter 4, be completed. In the situation of a pre-strained test geometry, the elastic strain energy density should be used with care as an underestimation of up to 40% was observed as reported earlier.

The review of the literature on the strength (section 2.3), the fatigue crack growth (section 2.4) and the fracture of non-simply loaded components (section 2.5) showed that some aspects of fracture mechanisms of elastomers are not entirely understood. For example, the origin of crack tip blunting, the major reinforcement mechanism for filled elastomers, consisting of crack deviations sideways from the initial crack path is not completely known. The review of the work on fracture under non-simple loading has both revealed the need for further investigations on the topic as the majority of existing studies have been limited to uniaxial loading and as some incorrect results using a finite element based fracture mechanics has been found[5, 6, 7].

The most cited explanation for the occurrence of crack deviation is the occurrence of sufficient strength anisotropy in the crack tip region[8, 9, 10, 11] due to the orientation elastomer molecules, the filler or both. It was proposed as a first step to assess the effect of induced anisotropy in the form of a permanent pre-strain on fatigue crack growth behaviour (Chapter 5) of the materials presented in Chapter 3. Because the pre-strain also induces a complex loading (bi-axial loading) similar to the one encountered in real engineering components, this investigation is of interest from an engineering point of view to assess our ability to determine the elastic strain energy density function and the energy release rate (or tearing energy) under such conditions.

Fracture surfaces will be examined in an attempt to study local crack growth paths and their relationship to the material anisotropy. An attempt to quantify the roughness of these fracture surfaces will also be made.

Then, in Chapter 6, the effect of a transitory pre-strain on fatigue crack growth was assessed. The use of a test geometry which induces a simultaneous pure shear and simple shear deformation mode on the sample was also investigated. Finite element based fracture mechanics and its ability to predict the crack growth behaviour will be discussed where appropriate.

5.2 Preliminary tasks

The experimental set-up for the pre-strained pure shear test-piece was described in Chapter 3, sections 3.4 and 3.5.

The first section of this work will describe the derivation of a relationship between tearing energy and the elastic strain energy density for this particular geometry (section 5.2.1). The realisation of some preliminary tests prior to the investigation of the crack growth behaviour of the pre-strained pure shear test geometry were necessary. These included the estimation of the extent of the edge effects in this pre-strain condition (section 5.2.2), the evaluation of a correcting factor for the tearing energy estimation (section 5.2.3) and the effect of a strain history on the crack growth rate (section 5.2.4).

5.2.1 Tearing energy calculation

The tearing energy analysis for a pure shear test-piece was first carried out by Rivlin and Thomas[1]. Figure 5-1 illustrates such a pure shear test-piece containing a crack of length c and having an unstrained height L_0 and thickness t. If the specimen grips are held at constant displacement to produce a strain λ_2, the elastic strain energy density of the deformed pure shear specimen is not the same in all the different regions illustrated. Region A is undeformed and so the corresponding elastic strain energy u_A will be zero. In region B, around the crack tip, the stress field is complex and the elastic strain energy u_B is unknown. Region D is deformed in pure shear and the elastic strain energy is given by $u_D = WV_D$ where W is the elastic strain energy density in pure shear at the relevant strain and V_D is the volume of the specimen in region D. Region E is not deformed in pure shear because of its proximity to the ends of the specimen and so its corresponding elastic strain energy u_E is unknown. The tearing energy is obtained by estimating the drop in the magnitude of the elastic strain energy when the crack length increases by Δc. Because the magnitude of the elastic strain energy is unchanged in regions A, B and E as the crack grows, only region D contributes to the change in the total elastic energy and so the consequent drop in energy Δu is equal to:

$$\Delta u = -\Delta c t L_0 W \tag{5-1}$$

Consequently, the tearing energy in pure shear deformation is equal to:

$$T = -\frac{\Delta u}{\Delta A} = W L_0 \tag{5-2}$$

where ΔA is the area of one of the fracture surfaces created. This expression makes clear that the magnitude of the tearing energy is independent of the total crack length in this pure shear geometry. Problems in using Equation 5.2 for applications involving cyclic loading arise however due to the methodology in determining the elastic strain energy density W. The sources of these problems are both the mechanical hysteresis during a given cycle and the stress-softening behaviour between subsequent cycles. Concerning the first problem, the real elastic stored energy is situated somewhere between the measured loading and unloading curve, as both of these curves are affected by visco-elastic losses. Either loading or unloading curves could be used but the former was chosen in this work as it is easier to characterise. The stress-softening effect also known as the Mullins effect[12] is illustrated in Figures 2.2-7 and 2.2-8. These show that if the magnitude of W is estimated from the area under the first cycle stress-strain curve, it will lead to an overestimation in the magnitude of W as a crack grows in subsequent cycles. In addition, the permanent set resulting from the previous cycles changes the unstrained length. The only solutions to these problems is to measure the magnitude of W in situ after the appropriate number of cycles in a pure shear test-piece containing a crack as the crack grows. In principle this is straightforward as it is only necessary to record a cyclic force/displacement curve and to determine the elastic stored energy (u) from the area underneath the plot. Then if V is the volume of the specimen contributing to the force-deflection curve, $W = u/V$. If the elastomer is considered as an incompressible material, the expression for V referred to the unstrained dimensions is: $V = L_0 t(w - c)$ where L_0 is the unstrained height, t the thickness, w the width and c the crack length. This expression for the volume assumes that only the uncracked specimen volume contributes to the force-deflection curve and that the cracked part of the specimen carries no load and hence stores no energy. In practice De[13] found that a strip of width x of the cracked

specimen was not energy free, and x was found experimentally to be equal to 28 % of L_0 (the unstrained height), independent of the crack length. The actual specimen volume in which elastic strain energy was stored was hence given by $V = L_0 t(w - c + x)$, with the final expression for T as:

$$T = \frac{u}{t(w - c + x)} \tag{5-3}$$

In the present case, the magnitude of x will be estimated in section 5.2.3, using FEA. Here an expression for the tearing energy for a pre-strained pure shear test-piece is derived in a similar manner to that utilised by De[13] for the non-prestrained sample. The test-piece is pre-strained in the longitudinal direction by an amount λ_1 and Figure 5-2 illustrates the new dimensions of the test-piece. All the dimensions which refer to this pre-strained state will have a prime sign, that is to say t' for the thickness, c' the crack length, L_0' the height and w' the width. When the crack propagates a distance $\Delta c'$, only regions A and D have a change in their elastic strain energy. Hence if W_A and W_D are the elastic strain energy densities respectively in regions A and D, the resulting change in the total elastic strain energy Δu is given by:

$$\Delta u = -\Delta c' t' L_0' (W_D - W_A) \tag{5-4}$$

The change (ΔA) in surface area when the crack length increases by Δc' is:

$$\Delta A = \Delta c\, t = \Delta c'\, t' \; / \sqrt{\lambda_1} \tag{5-5}$$

Then as $T = -\frac{\Delta u}{\Delta A}$, T is given as,

$$T = \sqrt{\lambda_1} L_0' (W_D - W_A) = L_0 (W_D - W_A) \tag{5-6}$$

resulting in the following expression:

$$T = W_S L_0 \tag{5-7}$$

where W_S the elastic strain energy density uniquely due to the cyclic deformation and not due to the pre-strain. As before W_S is difficult to measure from first cycle force-deflection curves or from elastic strain energy functions based on these, due to the cyclic stress-softening effect. Hence W_S must be estimated from in-situ measurements utilising the area under the force-deflection curve for a particular cycle which we will call u_S, divided by the volume of the specimen contributing to this force-deflection curve. This volume is the volume of the uncracked specimen corrected by a term x'_P (Figure 5.2), represents a vertical strip of width x'_p of the cracked specimen, which in turn allows for the load-bearing contribution to the force-deflection curve by the cracked region and is given as:

$$V = L'_0 t' \left(w' - c' + x'_P\right) \tag{5-8}$$

We finally obtain utilising Equation 5-7:

$$T = \frac{u_S \sqrt{\lambda_1}}{t'(w' - c' + x'_p)} = \frac{u_S \lambda_1}{t(w' - c' + x'_p)} \tag{5-9}$$

The only non-directly measurable quantity in this expression is x'_p. It is known that $x'_p = \lambda_1 x_P$, where x_P corresponds to the width of the strip in the unstrained state for the pre-strained test-piece. However there is no direct evidence to suggest that x_P should be equal to x, the strip width for a non-prestrained sample as utilised in Equation 5-3. A similar problem exists as to the extent of edge effects in the longitudinally pre-strained specimens. This is important as specimens in this study are always pre-cracked to a length that is hoped to be long enough to take the tip of the crack out of the edge effect region. The question is hence similar to that for x, i.e. how does this necessary crack length depend on the extent of the longitudinal imposed pre-strain?

Finite Element Analysis will be used in an attempt to answer both questions in section 5.2.3.

5.2.2 Extent of the edge effects in a pre-strained test-piece

In previous work by De[13], an initial crack length C_0, of 40 mm (referred to the undeformed and non-prestrained dimensions) was introduced into a pure shear test specimen of initial height L_0, 16-18 mm. It was assumed to be sufficiently long to make the edge contribution to the stress field at the tip of the crack negligible. In the case of a specimen pre-strained in the longitudinal direction, the extent of the edge effect area was unknown. In the initial experiments here, it was assumed that such an initial crack of length 40 mm was sufficient to accommodate all pre-strain effects. This section aimed to verify this assumption using FEA. The influence of the edge effects on the tearing energy was assessed here by plotting the variation of the tearing energy against the crack length, $T = f(c)$, T being estimated using the Virtual Crack Extension (VCE) method referred to in section 2.5.2.1. Because of the symmetry of the pure shear geometry, only the upper half of the specimen was considered and modelled as a plane stress problem (Figure 5-3). A 200 mm length $\times$ 10 mm height geometry was meshed with 2×2 mm^2 plane stress elements. The material mechanical characteristics were inputted using the cubic strain energy function proposed by Yeoh[14] derived here in pure shear for NR29 (section 4.2.2). Both the application of the pre-strain and the clamping with the grips were simulated by imposing on each node of the upper edge geometry the necessary displacement to obtain the desired pre-strain. A non-prestrained sample (pure shear) and 50% and 100% pre-strained pure shear models were analysed. The strain applied in the vertical direction λ_2 was equal to 1.2 in pure shear and equal to 1 for the 2 pre-strained samples, which means that the models were stretched back to their initial heights.

However, it should be noted that the investigations on the ability of an elastic strain energy function approach to predict the stress-strain behaviour of a longitudinally pre-strained sample in section 4.3 have shown some limitations. Utilising the elastic strain energy function derived from non-prestrained pure shear data underestimated the actual elastic strain energy stored in pre-strained samples by as

much as 40%. However, as the objective of the current exercise was not to obtain the exact magnitude of the tearing energy T, but its variation with crack length, the exactitude of the elastic strain energy function was not crucial.

Figure 5-4 shows the calculated variation of T against the crack length c, referred to the initial unstrained state (non-prestrained, non-deformed).

From Figure 5-4, it can be seen that the tearing energy reaches 95-100% of its maximum value at crack length of 10-20 mm, 30-40 mm and 35-45 mm respectively for the 0%, 50% and 100% pre-strained pure shear samples. These results show that a crack length of c_0=40 mm (referred to the non-pre-strained sample dimensions) was sufficient to take the crack tip into the region of homogeneous deformation and avoid the complications due to edge effects. However the length necessary does seem to increase with increasing pre-strain. To generalise these results, they must be scaled to the initial height, equal to 20 mm, yielding values of c_0/L_0 equal to 0.5-1, 1.5-2 and 1.75-2.25 for the 0%, 50% and 100% pre-strain values respectively. The value for the 100% pre-strained sample of 1.75-2.25 compares well with the value estimated using drawn grids on the sample (Figure 3-8) of 1.5-1.75.

5.2.3 Evaluation of the correction factor x using FEA

As shown in Figures 5-1 and 5-2, x (or x_p for the pre-strained pure shear sample, referred to the non-prestrained dimensions) represents the width of a vertical strip of cracked material which contributes to the force-deflection curve of the uncracked material. It hence appears in the specimen volume term as a correction factor for the tearing energy in Equations 5.3 and 5.9.

To determine x (or x_p), 2 relationships needed to be plotted. The first one called F (crack) is the change in force predicted by the FEA on a strained specimen as a longer and longer crack is introduced. A straight line is shown drawn through these points in Figures 5-5, 5-6 and 5-7. Deviations from this line is seen for very short cracks due to the non uniform stress distribution at the pure shear test piece edges. The second curve F (uncracked) is the predicted force necessary to extend specimens of widths corresponding to the uncracked lengths. The two lines are essentially parallel and the force necessary to extend the cracked specimens is clearly greater due to the

fact that the force is not zero at the crack tip. De[13] found experimentally that x/L_0 was equal to 28% and that the values of x were independent of the crack length. Because the corresponding value of x for a pre-strained sample, called x_p here, had never been estimated, it was proposed to do so in this study using FEA.

The same FEA model used in the previous section, section 5.2.2 was utilised but with the node set "Right" constrained in directions 1 and 2 (Figure 5-3). The same procedures as performed by De experimentally were modelled here using FEA. The magnitudes of x and x_p were determined for the pure shear and the two pre-strained sample (50% and 100% pre-strains).

The results of this FEA investigation are shown on Figures 5-5 to 5-7. The values of x and x_p were found to be around 6 mm which gave x/L_0 equal to 30% for all pre-strains. These results confirm the experimental estimation found by De with x/L_0 =28%[13]. 30% for x/L_0 was taken for all the calculations for T. x_p', the measure of the width of the strip in the deformed state (pre-strained), is hence equal to $\lambda_p x$, where λ_p is the extension ratio due to the pre-strain.

5.2.4 Effect of the cyclic strain history on the crack growth rate and extent of transitory crack growth

As described in the experimental procedures section 3.6, when a fatigue crack growth test is performed, a single sample is used to obtain several data points on the $\log T$ versus $\log \mathrm{d}c/\mathrm{d}n$ plot. This method was adopted as it eliminates possible variations in the specimen and the materials as well as , set-up variables such as the initial specimen length and thickness. Also the setting-up of each new sample is time consuming. The disadvantage of this technique meant that a given sample, for a given test had previously been subjected to a series of cyclic deformations. In the various published studies related to fatigue crack growth in filled elastomers[3, 15, 16] such a problem had never been mentioned and it was believed that most authors performed their tests on virgin samples and hence did not repeat different tests on the same sample. As the main body of this work was focussed on pre-strained samples, the effect of the previous strain history on crack growth rate was particularly important.

The problem had two facets. The first being to establish that a crack grows at a given rate for a given tearing energy independent of the crack length and of the previous strain history of the sample; provided that the tearing energy is measured in-situ on the sample at the time of crack growth. The second was to establish, that even if the above were true, the extent of any transition region in crack growth rate when the extension and hence the tearing energy on a sample was changed.

Lake and Yeoh[17] investigated the crack growth behaviour of unfilled and filled elastomers initiated from a sharp tip (razor blade cut). They observed a sudden propagation in an abrupt manner of a crack with a very sharp tip and they called this phenomenon the small-scale tearing. The tearing energy at which such a jump occurred was much less than the tear strength as conventionally measured. The extent of this rapid transitory crack growth was typically within the range 0.05-0.5 mm until the crack growth took place at a tearing energy associated with a much "blunter" tip. The extent of such a phenomenon was unknown in the pre-strain configurations used in this study.

Consequently, the aim of this section was to investigate:

(1) the extent of transitory crack growth, if it existed, between a small amplitude cyclic strain test (low tearing energy) and a large amplitude cyclic strain test (high tearing energy).

(2) the effect of the cyclic strain history and the occurrence of any permanent changes during large amplitude cyclic strains on the crack growth rates.

These investigations necessitated the performance of a series of cyclic crack growth tests carried out in a given order. The test procedures were as for cyclic fatigue crack growth as described in section 3.6. Tests were conducted using the moderately filled compound NR29 for various pre-strains (15%, 25% and 100%). Sequences of several thousand cycles each of low to high to low tearing energy tests were performed as illustrated in Figures 5-8 to 5-10. The crack growth rates dc'/dn indicated on these graphs are referred to the deformed state, indicated by the prime sign.

A general trend was observed for the transition from low to high tearing energies as illustrated in Figures 5-11 to 5-16 which are the same plots as in Figures 5-8 to 5-10 but with magnified transition zones. Initially over from a couple of hundred cycles for PS=15% or a few thousand cycles for PS=25%, a more rapid crack growth occurred before the stabilised propagation took place at a lower crack growth rate.

These quicker crack propagations were probably initiated by the sharper crack tip resulting from the previous low tearing energy test; sharper with respect to the stabilised crack tip at the high tearing energy. This sharper crack tip prevailed for a few thousand cycles, after the large amplitude cyclic strains were applied, producing a higher crack growth rate. These transitory crack growth rates were not visible on all the tearing energy transitions of this study. They were primarily observed for the lower pre-strain tests (15% and 25%) and were much less pronounced for the highly pre-strained samples (100%). The pre-strain may be reducing the differences between the crack tip sharpness for different tearing energy magnitudes. Not surprisingly these differences between the initial and the stabilised crack growth rates also appeared also to be more pronounced the greater the difference between the low and the high tearing energy magnitudes. This was observed for the 15% pre-strain (Figures 5-11 and 5-13 or Figures 5-12 and 5-13). As a conclusion, these preliminary tests showed that the extent of the transitory crack growth was between a couple of hundred to a few thousand cycles. It was hence necessary to perform a test lasting significantly longer that a few thousand cycles prior to recording the stabilised crack growth rate for a given tearing energy.

The second part of this preliminary work was to investigate the effect of crack length and of intermittent large amplitude cyclic strains on the crack growth rate in a relatively low tearing energy test. This was achieved by comparing the crack growth rates of a given test before and after large cyclic strains were applied. The results illustrated in Figures 5-8 to 5-10 and are also summarised as crack growth rates in Table 5-1 for the different pre-strain tests. Experimentally, it was attempted to set the magnitude of the low tearing energies to be equal before and after the large amplitude cyclic strains were imposed. This was realised by setting the displacement amplitude of the jigs to be the same, but small discrepancies occurred due mainly to the imprecision in the displacement control of the jigs and to the permanent set (increase of the unstrained height) induced by the large amplitude cyclic strains. The tearing energy magnitudes before the large amplitude cyclic strains tended to be generally slightly higher than the ones following. This appeared reasonable if the displacements were assumed to be the same and the permanent set the only factor modifying the tearing energy magnitudes. More importantly, there were not any permanent changes in the crack growth rates, within the experimental scatter, as a result of the application

of intermittent large amplitude cyclic strains. This was a reassuring result for the bulk of the coming experimental work where several crack growth tests with different tearing energies were performed in succession on the same sample.

5.3 Results

5.3.1 Cyclic crack growth results

The effect of carbon black content, strain-crystallisation and different magnitudes of a longitudinal pre-strain on the crack growth characteristics were investigated. The results are presented as double log plot of dc/dn, the crack growth rate versus T, the maximum tearing energy during a cycle, in Figures 5-17 to 5-27. The amount of pre-strain applied (PS) is expressed in percentage strain.

The crack growth behaviour in region 3 (Figure 5-22) can generally be written as follows:

$$\log(dc/dn) = \beta \log T + b_t \qquad (5\text{-}10)$$

with β the slope value and b_t the intercept to the y-axis. The magnitudes of β and b_t are shown in Table 5-2.

It has also to be noticed that the extent of the experimental scatter can be as large as 20%, a value previously mentioned in the literature[18]. The calculation of the predicted experimental measurement errors alone produce relative errors of the order of 10% for both the tearing energy T and the crack growth rate dc/dn (Appendix 3). Adding to that the variability of the material properties, a 20% experimental scatter would not be unreasonable. The vertical and horizontal error bars (crosses) indicated on each graph corresponds to a 20% relative error both on dc/dn and T.

In the following discussion, the terms strength, strengthening, stronger (or weakening, weaker) would be related to the decrease (or increase) of the crack growth rates dc/dn at a given tearing energy T. Or conversely, an increase (or decrease) of T at a constant dc/dn.

5.3.2 Microscopic observations

SEM micrographs of the fracture surfaces and fracture profiles at magnifications of 200 and 50 times respectively were recorded for all tests. The micrographs are compared at whole values of the logarithm of the tearing energy (2, 2.5, 3....etc) in Figures 5-30 to 5-52. As the strength of the different materials varied largely and the magnitude of the pre-strains also greatly influences the strength, the microscopic observations were only possible for different ranges of tearing energies and sometimes these ranges did not overlap making comparisons difficult.

The profile views were used to give a qualitative estimation of the fracture roughness. The main structure visible on the top views was either the change of the average length of a step or the number of striations per unit area (Figure 5-55). But the real fracture surface morphologies could be somewhat more complex as for example one large step could have on closer examination smaller steps on its surface.

5.3.3 Roughness measurements

An infrared laser profilometer was used to measure the surface roughness as described in section 3.7.3. The results shown in Figures 5-61 to 5-67 are expressed as the root mean square R_q as a function of the tearing energy T. The values of R_q are the average of 3 measurements and the vertical bars represent the corresponding experimental scatter.

The aim of using this method was to produce a quantitative estimation of the roughness. As described in section 3.7.3, the estimation of the roughness is not straight forward as it depends on the choice of a cut-off wavelength to filter out the waviness from the roughness on the profile measurement. This cut-off wavelength was taken as the length of the largest repeating feature of the scanned profile. Though it is not an easy estimation, it appears that the evolution of the roughness with the experimental parameters (tearing energy and pre-strain) measured using this method correlates qualitatively with the evolution of the roughness on the profile view of the micrographs. It would hence appear that the roughness measurement using the profilometer is a reasonable way of quantitatively estimating the roughness.

5.3.4 FEA results

The procedures described in Chapter 3 section 3.8 to estimate the energy release rate or tearing energy were followed in this investigation. It was proposed to use both the VCE (virtual crack extension) technique and a contour integral technique, the *J*-integral. These procedures are applied here to estimate the variation of the tearing energy in a pre-strain pure shear geometry (PS=50%) as a function of the direction of crack growth. Both the cubic[19] and the Davies *et al*[20] elastic strain energy density functions were implemented using as numerical parameters the coefficients determined for NR29, in Chapter 4, section 4.2.2, Tables 4-1 and 4-2. The ABAQUS input file is shown in Appendix 4. However, according to these results from the stress-strain behaviour of a pre-strained sample, both elastic strain energy density functions underestimated the actual elastic strain energy stored in the specimen by as much as 40%. But as the focus of this work was on the relative magnitude of the tearing energy with respect to crack growth direction, inaccuracy in the absolute magnitude of the elastic strain energy is not critical.

The two strain energy functions differ in their abilities to predict the decrease in modulus at small strain (section 4.2.1). The results, Figure 5-68 are expressed in terms of the tearing energy T as a function of the advancing crack angle from the horizontal θ, define in Figure 5-69, for various vertical deformation expressed in extension ratios λ_2. The Davies *et al* predictions are all above the cubic ones which is in agreement with the fact that the former predicts a higher small strain modulus than the latter.

As the geometry is symmetrical, all the tearing energy distributions are symmetrical with respect to θ=0°. For λ_2=0.85, corresponding to a small vertical deformation compared to the pre-strain (PS=50% or λ_1=1.5), the tearing energy distribution showed two maximums, one slightly above θ=90° and its symmetrical. This means that the crack is likely to propagate at right angle to the initial crack direction. This is confirmed when looking at both contour plots of the elastic strain energy for λ_2=1 (Figures 5-70 and 5-71). The two symmetrical directions

corresponding to the largest decreasing gradient of the elastic strain energy (the largest energy release rate or tearing energy) are at right angles to the horizontal.

As the extension ratio λ_2 is increased (λ_2=1 and 1.05), the two maximums observed previously shift towards θ=0° and overlap to form a single but very shallow peak (λ_2=1.05).

The *J*-integral method predicts significantly different maximums except for the largest extension ratio (λ_2=1.05). The prediction of a drop in the tearing energy outside the region of the maximum is much more significant with the *J*-integral method. For angles greater than 90° from the maximum tearing energy direction (θ=0°), the tearing energies become negative. This would suggest that the specimen increases its elastic stored energy as the crack grows which is physically impossible. The inaccuracies of this method could be attributed to the fact that the *J*-integral estimation relies on the accuracy of the strain state in the neighbourhood of the crack tip. This accuracy is limited to the mesh refinement and the ability to predict very large deformations in that the crack tip region.

In conclusion, it is predicted that for NR29 under a pre-strain PS=50% that a crack would deviate sideways from the horizontal direction for a value λ_2 less than unity or for a tearing energy below 750 J.m^{-2} ($\log T = 2.86$). For tearing energies above this value, it is expected that the crack would grow straight ahead as only one maximum exists on the tearing energy against angle of crack growth curve (Figure 5-68). The actual experimental observations of crack growth show an even more complicated relationship. This is possibly due to the materials becoming anisotropic especially in the crack tip neighbourhood, an effect ignored by FEA.

5.4 Discussion

5.4.1 NR0 and SBR0 in pure shear (PS=0%)

The value of the slope β for the non-prestrain NR0 data in Figure 5-17 approximates to 3. This is to be compared with the value reported in section 2.4.2 and 2.4.7 of 2[21, 22]. As the present tests were performed at a constant frequency of 5 Hz, with the extensions increasing from 0.05 to 0.4, the strain rates vary from 0.5 to 4 sec^{-1}. Performing fatigue crack growth tests at constant strain rates, Young[15] observed little effect of the strain rate on the crack growth behaviour between 1 and 20 sec^{-1}. If we assume, as mentioned in section 2.3.3.2, that crack growth is governed by the high strain hysteresis (hysteresis up to the breaking point of the elastomer), the main contributor to this hysteresis is strain induced crystallisation for NR materials. As strain induced crystallisation in this range is practically rate or time independent, the findings of Young[15] are understandable. Consequently, the variability of the values of β reported by one author or another for unfilled NR materials can not be attributable to the various loading frequencies or strain rates employed but is probably due to differences in material compounding such as a change in cross-link densities that affects the way strain-crystallisation occurs at the crack tip (different degree or kinetics of crystallisation) or simply within a range of general experimental scatter.

The value of β for SBR0 also approximates to 3. This is lower than the value reported in the literature of 4 by Lake and Lindley[23] for a similar compound and tested at similar frequency. These differences in slope are both attributable to the experimental scatter which can be as large as 20% and the fact that slopes of 3 and 4 are not very different.

As expected and because of strain-crystallisation, NR0 is stronger than SBR0 which can be seen in Figure 5-17 and as shown by the values of b_t in Table 5-2.

It also has to be noted that as reported in the literature, the range of tearing energy in these tests overlaps both what is called region 2 and 3 in section 2.4.2. Because of the limited data in region 2, for all the current materials, the present data were considered as all being part of region 3 and falling on a same line though some

experimental points may be part of region 2. This may also be part of the reason for the variations in the value of β when compared with the data found in the literature.

Top view fracture surfaces in the non-prestrained state (PS=0%) of NR0 (Figure 5-30) and SBR0 (Figure 5-47) at a given strain rate ($\log(dc/dn) = -8.4$ and -6) show a very similar appearance. In both cases, there is a tendency for the steps to be more widely spaced as the tearing energy (or crack growth rate) increases. The roughness of these fracture surfaces as measured on the profilometer initially increases at $\log T = 3\text{-}3.4$ and decreases at $\log T = 3.4\text{-}3.6$ for NR0 (Figure 5-61). For SBR0, the roughness increases at $\log T = 2.3\text{-}3.1$ (Figure 5-65).

5.4.2 NR0 under pre-strain (PS=200%)

Though exhibiting similar values of β of around 3, the pre-strained NR0 (PS=200%) show a lower value of b_t (Table 5-2) making it weaker than the non-prestrained NR0 (Figure 5-18). Quantitatively, the pre-strain either increases the crack growth rate by a factor 25 at a constant tearing energy or decreases the tearing energy necessary to drive a crack at a given rate by a factor 3.

Gent and Kim[24] have argued, from very limited data, that the tearing energy should be calculated with respect to the deformed cross-section area after the application of the pre-strain. This cross-section area increased by a factor $\lambda_p^{1/2}$ where λ_p was the magnitude of the pre-strain, expressed in terms of the extension ratio. This increase was due to the fact that the extension ratio increased by a factor λ_p in the direction of the pre-strain and decreased by a factor $\lambda_p^{-1/2}$ in the orthogonal direction, through the thickness. In tear measurements, these authors managed to predict the drop in tearing energy for SBR materials, as a function of the pre-strain uniquely assuming that the weakening is due to the increase in cross-section area. A similar calculation carried out here on the NR0 data shifts the data equally towards lower tearing energies (Figure 5-19). Consequently, the calculated curve (PS=200% (calc.)) plotted taking the crack growth rate of PS=0% referred to the strained dimensions (dc/dn is changed into dc'/dn, with $c' = \lambda_p c$), can not predict the PS=200% data. The observed

weakening was consequently a real phenomenon and is not an artefact due to the way the tearing energy is calculated. Referring all the dimensions to the undeformed state (non-prestrained) for the calculation of the tearing energy (section 5.2.1) is a reasonable approach if results are to be compared with other test-piece results. It also has to be acknowledged that an exact calculation of the deformed cross-section area in the crack tip region is more complex than the one proposed by Gent and Kim.

According to the literature[25], an unfilled natural rubber like NR0 begins to strain-crystallise in the bulk at around 200-250% strain. According to Figure 4-2, strain-crystallisation in the bulk would occur at higher strain as the upturn on the stress-strain curve of NR0 starts from 400% strain onwards. Though this upturn is not directly associated with strain-crystallisation[26], it is a good indication of the onset of crystallisation. In the pre-strain condition, with PS=200% in the present test, crystallisation in bulk is not believed to have occurred.

One contribution of the pre-strain is to orientate molecules in the direction of the pre-strain. Clearly as a crack grows it is not necessary to reorientate all the molecules to the stretching direction (cyclic deformations) as this would increase the magnitude of T for a given dc/dn. Hence total recrystallisation would not occur at the crack tip. Only the few molecules oriented in a direction close to the stretching direction will actually strain-crystallise. In practise, where a crack grows in an oriented material it requires less work to be done, as it is breaking fewer molecules. The material is consequently exhibiting strength anisotropy.

The pre-strain, beyond its effect on the molecular orientation could potentially modify the high strain hysteresis and consequently the fracture processes. Measurements at small strains and low strain rates of the mechanical hysteresis (energy lost over the energy stored on loading), Figure 5-56 shows slightly larger hysteresis on the pre-strained sample than in pure shear (PS=0%). It is possible that this trend is retained at high strains and high strain rates which would mean that the effect of the strength anisotropy outweighs the effect of the hysteresis.

A comparison of the fracture surfaces of a non-prestrained and a pre-strained sample can be made with the aid of the sketches in Figure 5-59. The pre-strained samples exhibited smoother surfaces on a small scale (on a single step) but coarser surfaces on the bigger scale than a step (comparison of profile views for the same

tearing energy, Figures 5-30 (a) and 5-31 (c)). Because the cut-off wavelengths (section 3.7.3) are different for the pre-strained and the pure shear samples (Figure 5-59), the profilometer picks up the steps in case of the pre-strained samples producing larger R_q.

A trend is noticeable, for both PS=0% and 200%, concerning the evolution of the fracture surface morphologies with increasing T (Figures 5-30 and 5-31). The number of striations decrease and hence the distance between them, a step increases with increasing T. These are in general agreement with the literature[27, 28] which generally says that more widely spaced steps correspond to weaker materials. An initial presumption is that the length of a step corresponds to a single jump forward every cycle. Having cyclic crack growth rate magnitudes covering a range of 1×10^{-8}-10^{-6} m.cycle^{-1}, lengths of between 0.01-1 μm are expected which is 10 to 100 times smaller than those observed experimentally. Therefore, each step is the result of the application of 10-100 cycles. In reality, cracks grow in an irregular manner in/out of plane, across the whole or just part of the section probably at different local rates. It is possible, however, that the local sum of these small increments adds to a largely planar crack which only infrequently (i.e. at end of a striation) deflects out of plane in an observable manner.

5.4.3 SBR0 under pre-strain (PS=38%)

Figure 5-20 compares SBR0 in pure shear and in pre-strain conditions (PS=38%). This pre-strain was the largest applicable for this material because it is very weak when unfilled. The value of β is almost halved by applying the pre-strain and the pre-strained sample is weaker in the range of tearing energy studied. This result correlates with the results for NR0 where increased molecular orientation induced by the pre-strain results in specimen weakening. From the micrographs Figures 5-47 and 5-48, no significant differences are visible in the fracture surface morphologies and roughness.

5.4.4 Carbon black filled NR in pure shear (PS=0%)

5.4.4.1 Crack growth results

Figure 5-21 shows that NR21 and NR29 have slope values of β around 2 in contrast to NR59 which has a lower slope of 1.4, as indicated in Table 5-2. Figure 5-21 shows that filled NR materials are generally stronger than NR0 except for NR21 which does not show significantly different crack growth behaviour from NR0. As NR21 possesses the lowest actual cross-link density $[X]_{act}$ of all compounds (see Table 3.1), according to the findings of Brown *et al*[29], for similar cross-links this should cause a strength increase. But these authors also suggested that the ability of the polysuphidic cross-links, present in conventional systems, to reform after breaking make these compounds stronger than the monosulphidic cross-links of EV systems. Because NR21 has a formulation closer to an EV system, its lower strength can be explained by this last argument. It is also probable that for NR21, the carbon black network is not developed enough to have a significant reinforcing effect. The lower slope value of NR59 could be explained by the fact that it has a conventional vulcanising system.

From section 2.4.7[3] of the literature review, it was noted that the value of β was not expected to change with carbon black content but a lower intercept to the y-axis b_t for the filled compounds was expected. With the exception of NR21 this trend is followed here.

For the range of tearing energy covered in the present work, the crack growth behaviour can be described by a single linear region on the log-log plot for NR21 and NR29 (Figure 5-21) corresponding to region 3 in section 2.4.2. NR59 exhibits 2 linear regions (Figure 5-25) which correspond to regions 3 and 4 in reference to Figure 5-22. Region 4 has a slope value of 4.5. The reasons for the existence of such a regime is not clear but, as will be mentioned in the next section, it may result from the smoother fracture surfaces in this region. It is, however, not believed that this region coincides with the catastrophic crack growth region as the crack growth was stable and the tearing energy magnitudes are very small compared to the 50-80kJ.m^{-2} necessary for catastrophic tearing for a similar material[13].

5.4.4.2 Fracture surfaces

According to Equation 2.3-12 in section 2.3.2, the tearing energy can be expressed as follows[30]:

$$T = dW_b \tag{5-11}$$

where W_b is the work done in the crack tip region as it propagates and d is the crack tip diameter. According to the literature review section 2.3.3, the strengthening due to the addition of carbon black is associated with visco-elastic energy dissipation at the crack tip and to blunting of the crack which causes an increase in tip diameter. These effects both increase the tearing energy according to Equation 5-11. The increase in crack tip diameter was suggested by Figure 5-67 with higher magnitudes of (R_q) for the filled compounds compared to NR0. For example, for $\log T = 3$, (R_q) was below $5\,\mu m$ for NR0 and greater than $15\,\mu m$ for the filled NR compounds (NR21, NR29 and NR59). The more pronounced crack tip blunting and hence local molecular orientation ahead of the crack tip in a filled compound could be explained as follow. According to Figure 5-57, it was checked that at a given elastic strain energy density W and hence at a given tearing energy, the strain decreased with carbon black content as expected, and the stresses more than doubled from NR0 to NR59. Because the elastomer matrix constitutes the continuous phase of the filled materials, these higher stresses would correspond to higher local strain in the elastomer matrix (strain amplification effect due to the presence of the carbon black, see section 4.2.1) and hence a higher degree of orientation in the direction of the cyclic loading. This higher degree of orientation affects primarily the bulk of the material and should be partially retained in the region of the complex strain field ahead of the crack tip, though at the crack tip, whether for a filled or unfilled material, the role of strain-crystallisation is not very different as the molecules are fully extended. As a result, a more pronounced propensity for the secondary cracking to develop sideways from the main crack was expected the higher the carbon black content.

Detailed observation of NR59 profile views (Figures 5-42 (a) to (c)) show prominent secondary cracking, an illustration of which is given in Figure 5-60.

Because this secondary cracking is inclined and runs deep away from the main fracture surface, they are not detected by the infrared laser beam and make no contribution on the measurement of R_q. While the roughness of the filled NR compounds appear not significantly different according to the magnitudes of R_q, the occurrence of this secondary cracking contributes to make NR59 stronger than NR23 and NR29.

Figures 5-62 to 5-64 for the filled NR compounds and Figure 5-66 for SBR30 reveal that there is a tendency for R_q, in pure shear (PS=0%), to initially increase and then decrease for $\log T \geq 3-3.5$. Though not seen on Figure 5-64 for NR59, it is noticeable its roughness decreases from $\log T = 3.5$ to $\log T = 3.7$ on the micrograph Figure 5-42. As mentioned in section 5.4.1, the existence of a maximum in the variation of R_q was also exhibited by NR0. As mentioned in section 2.3.3.2, there is a competition ahead of the crack tip between the chain alignment which causes crack deviation preventing time-dependent crack growth[31] and catastrophic chain scission processes that tend to cause the crack to propagate rapidly straight ahead in a time-dependent manner. As there was no change of crack growth regime in the present range of tearing energies, it is still believed that the cyclic component of the crack growth dominates the crack growth behaviour. The low-intermediate tearing energies (low strain rates) allow the chain alignment to occur and this chain alignment increases as the tearing energy increases. The fracture surfaces become rougher with increasing tearing energy. For a large enough tearing energy (large enough strain rate), chain scissions occur before chain alignment and the fracture surfaces get smoother.

The fracture surfaces from the micrographs show two distinct types of surfaces which seem to be related to the formulations of the compounds. NR59 similarly as NR0 (and also the SBR compounds) show very sharp fracture surfaces in contrast with the blunter surfaces exhibited from NR21 and NR29. It appears from Table 3-1 and as mentioned in section 3.2, NR21 and NR29 have EV vulcanising systems. The way the vulcanising systems affect the fracture surfaces is not clear.

5.4.5 Carbon black filled SBR in pure shear (PS=0%)

Figure 5-23 shows that SBR30 is stronger than SBR0. Similar arguments explaining the strengthening due to the carbon black as the ones proposed for the filled NR compounds could be advanced with the exception that there are no significant differences in R_q between SBR0 and SBR30 (Figures 5-65 and 5-66). This would suggest that the reinforcing effect of carbon black on SBR is limited to increased visco-elastic energy dissipation. Crack tip blunting is much less important for filled SBR than for the filled NR which could have some relation with strain-crystallisation ahead of the crack tip promoting secondary cracking.

The similar magnitude of R_q is confirmed by the fact that there are no appreciable differences in fracture surface morphologies (number of striations per unit area or length of a step) between SBR0 and SBR30 at a given T (Figures 5-47(c) and 5-49(b)).

Similarly to NR59, in the range of tearing energy covered, SBR30 exhibits 2 linear regions which could be called regions 3 and 4 in reference to Figure 5-22. The values of β in regions 3 and 4 are respectively 2 and 12. Using the same arguments as in the previous section, in region 3, time-dependent/rapid crack growth is prevented by the formation of an anisotropic structure due to the chain alignment ahead of the crack tip. In region 4, because of the high rate of loading of the test-piece or more probably due to the high rate of loading of the region under high strain cycle ahead of the crack tip (Figure 5-58), it is probable that the anisotropic structure has not enough time to occur and the contribution of the time-dependent crack growth gets larger.

5.4.6 Carbon black effect compounds under pre-strain

5.4.6.1 Crack growth results

All materials

In general, as for the unfilled compounds, for a given crack growth rate dc/dn, the tearing energy T decreases as the pre-strain increases (Figures 5-24 to 5-27). Or vice-versa, at a given T, dc/dn increases as the pre-strain increases. The effect of the pre-strain mentioned in section 5.4.2, namely the molecular orientation in the direction of the pre-strain, no complete reorientation of molecules in the crack tip region and the modification (probably increase) of the high strain hysteresis could still be advanced to explain this weakening. The presence of the carbon black has the effect of amplifying the local molecular strain (strain-amplification effect), both in the direction of the cyclic loading and in the direction of the pre-strain. In the direction of the cyclic loading, it was checked, in the pre-strain condition, that for a given elastic strain energy W and then for a given tearing energy, the stresses increased with carbon black content. Therefore a more pronounced vertical molecular orientation is expected, in both the bulk and ahead of the crack tip, the larger the carbon black content. The effect of the pre-strain is described below.

The strain-amplification effect due to the pre-strain can be demonstrated by utilising Figures 5-28 and 5-29. These figures compare the extent of weakening of all compounds by plotting the relative drop in T (with respect to T for PS=0%), for a given crack growth rate $\log(dc/dn) = -8$, as a function of the pre-strain expressed as either strain or stress in the bulk of the test-piece.

Figures 5-28 shows that the pre-strain has the effect of decreasing the necessary tearing energy to drive a crack at a given dc/dn. The effect is the greatest for the higher carbon black content. Reproducing this plot as a function of the pre-stress rather than pre-strain, as shown in Figure 5-29, the behaviour of all the materials (either filled or unfilled and strain-crystallising or non-strain crystallising) is more similar. Expressing the pre-strain in terms of stress measures and compares the real local strain/stress borne by the elastomer matrix in compounds with different carbon black contents. The following conclusion can be made: the observed weakening under pre-

strain could be mainly attributed to the level of strain and consequently the degree of molecular orientation in the elastomer matrix. The carbon black content influences the strain level/degree of molecular orientation in the elastomer matrix and appears to be most significant effect of carbon black on the crack growth behaviour. Consequently, the degree of molecular orientation is intrinsically governing the crack growth behaviour in pre-strain situations outweighing other contributions.

It is also concluded that the strain-crystallisation in the bulk of the material, if it occurs even partially for some of these materials, has no influence on the observed weakening. And it appears, with a similar deduction as in section 5.4.2 using Figure 4-2, assuming that strain crystallisation would be induced at the same stress as for NR0 (for a stress corresponding to the up-turn on Figure 4-2 *i.e.* 2 MPa), strain-crystallisation in bulk is expected to start from approximately 50% for NR59, 100% for NR29 and 250% for NR21. Therefore, incipient strain-crystallisation in the bulk is probably occurring with NR59 and NR29 for the highest pre-strains used in this work, respectively PS=75-100% and PS=150%.

For PS=50%, there is a 6 fold increase in the crack growth rate dc/dn at constant tearing energy T for both NR29 and SBR30. Both materials, having similar carbon black content but different abilities to strain-crystallise, show a similar sensitivity to the pre-strain. It could be concluded that strain-crystallisation (due to the cyclic loading) at the crack tip of NR29, though reduced, is not totally suppressed. If it were the case for this material, it would be probable that the increase in dc/dn at a constant T would be greater than a factor 6.

It should also be noted that NR21 and NR29 do not exhibit any significant change in their crack growth behaviour $dc/dn = f(T)$ for pre-strains respectively between 100-150% and 25-100% (Figures 5-24 and 5-25). This is probably accounted by no significant changes in molecular orientation in these pre-strains ranges for these materials. As mentioned in sections 5.4.4 and 3.2, the fact that they are EV (efficient vulcanising) curing systems could once again be invoked but the relation is not clear. With more numerous monosulphidic cross-links, which are stronger chemical bonds than polysulphidic ones, scissions of main chains are more likely to occur. And because the polysulphidic bonds are able to reform after breaking, conventional vulcanising system (NR59) may induce a more pronounced anisotropy.

In the range of tearing energies covered in this study, all the compounds in pre-strain condition can be described by a single linear relationship of $\log(dc/dn) = f(\log T)$ with the exception of NR59, which exhibits either 2 or 3 different regions. This single linear relationship, defined as region 3 in reference to Figure 5-22, has for all materials the same value of β as in pure shear (PS=0%). The crack growth data of the pre-strained materials can be seen as being the result of translating the data of the corresponding pure shear to higher crack growth rates or smaller tearing energies. If this decrease in tearing energy was seen down to the lowest tearing energies, this weakening effect could be attributed to a decrease in the threshold tearing energy (T_0). Because of the molecular orientation induced by the pre-strain, less segments need to be broken across the material to open a crack. This effect is carried all the way up to higher tearing energies until the pre-strain is the cause of the occurrence of other phenomena, one of them is believed to be the cessation of strain crystallisation for NR59. That probably causes the change in regime observed on that material.

It should also be noted that NR21 and SBR30 show, for certain pre-strains (respectively PS=100% and 25%), a significant increase of R_q for the highest tearing energies but neither is accompanied with the appearance of crevasses (Figures 5-34(c) and 5-50(c)) nor a change in the crack growth behaviour as are observed for NR59, described next. It appears from these results that the pre-strain/bi-axial strain state can cause greater crack tip blunting than a pure shear/ uniaxial condition. As this significant crack tip blunting occurred for SBR30, it was not thought related to strain-crystallisation.

NR59

The crack growth behaviour of NR59 can be divided in 2 regions (3 and 6) for PS=75% and 100%, and in 3 regions (3, 4 and 5) for PS=25% and 50%. Regions 3, 4, 5 and 6 are identified in Figure 5-22.

Region 3 has a similar slope to the linear region in pure shear. This suggests that the behaviour can be related to the dominance of the dynamic/cyclic component of the crack growth due to the persistence of strain-crystallisation at the crack tip. Following a similar argument as for NR29, because the drop in relative tearing

energy is similar for strain-crystallising and non strain crystallising materials at a given crack growth rate $\log(dc/dn) = -8$ (effectively corresponding to region 3 for NR59), the main effect of the pre-strain in that region is to reduce the number of molecular chains a crack needs to break for it to grow.

Because of their similar high slope values, it would be tempting to attribute regions 4 and 6 to the dominant influence of the time-dependent component of the crack growth. But further investigations, described in the next paragraph, were not conclusive. It was nevertheless believed that strain crystallisation at the crack tip had been significantly reduced if not ceased causing this important change in crack growth regime. The reason strain-crystallisation ceased in these regions 4 and 6 (and not region 3) could be ascribed to the fact that fewer molecules can potentially strain-crystallise because of the pre-strain (in comparison to the pure shear condition) and at these rates of loading of the test-piece, corresponding to very high strain rates of molecules at the crack tip (Figure 5-58), the strain-crystallisation is inhibited. According to the literature[32], catastrophic/time-dependent crack growth happens in NR materials for $\log(dc/dn) = -6$ in pure shear condition. In the pre-strain condition of the present work, the onset of the regimes corresponding to regions 4 and 6 are for $\log(dc/dn) = -8$ to -7.5. These differences are reasonable because of the reduction in the number of molecular chains available to crystallise due to the pre-strain.

In case of region 6, observed for the highest pre-strain (PS=75% and 100%), the curves zoom up to crack growth rates of one micron per cycle. Mentioned in section 2.4.4, the concept of the time dependent and dynamic/cyclic components of crack growth was put forward to explain this observation. It was proposed that the time-dependent component of crack growth was dominating over the dynamic/cyclic component. This was investigated on NR59 for PS=75% and 100%. Tearing tests (identical set-up but under a static deformation), at different tearing energies, for PS=75% and 100% were performed (Appendix 5). As expected, a time-dependent crack growth was observed. These findings were also observed by Samsuri[33] in tear measurements of pre-strained NR compounds. From the present data, which were under the form

$$dc/dt = K_S T^{\beta} \qquad (5\text{-}12)$$

the calculation of the contribution of this static/time-dependent crack growth component to the total crack growth under cyclic loading needed Equation 5-12 to be integrated over one cycle. This calculation detailed in Appendix 3 produced the results shown in Figure 5-26, under the references PS=75%(s) and 100%(s). The result from PS=75%(s) showed a very similar slope with PS=75% but shifted to larger tearing energies. At a given tearing energy, the contribution of the time-dependent crack growth would appear to be negligible compared with the cyclic crack growth. Nevertheless the fact that a time-dependent crack growth was observed on the tear test on this NR compound is a strong argument to affirm that the time-dependent component of the crack growth plays a major role in region 6 despite the results observed in Figure 5-26. These lack of conclusive results is in part due to the fact that in region 6, the marked increase of crack growth rates are over a narrow range of tearing energy and slight discrepancies on both dc/dn and T can lead to large variations in the slopes. Similarly, the results from PS=100%(s) do not allow to draw either conclusive results. But it is also suspected that the time-dependent crack growth plays a major role for that regime.

The occurrence of region 5 is somewhat surprising for PS=25% and 50% as it was expected to see the crack growth rate to zoom up to catastrophic rates, to produce a behaviour similar as in region 6. Thus catastrophic crack growth seems to be retarded and shifted to higher tearing energies. As a result of the molecular orientation due to the pre-strain, which is expected to reduce the chain alignment in the direction of the loading, it appears that prominent crack deviations occur effectively increasing the crack tip diameter which prevents catastrophic crack growth. This severe blunting of the crack tip is confirmed both with the significant increase in R_q (Figure 5-64) and the prominent crevasses (wide secondary cracking) observed for example on the micrographs Figures 5-43(c) and 5-44(d). The microscopic observation of the flanks of the crevasses show smooth and rounded forms of the order of 10 μm in dimensions, on both pre-strained and non-prestrained samples (Figure 5-53). From Figure 5-54, it is likely that these rounded features on the flanks have the same origin as the single cavities shown on the micrograph. Hence, the formation of these crevasses could be attributed to the cavitation process, a mechanism described in section 2.3.3.2.

The bi-modal crack growth (rapid/ slow crack growth) for PS=50% and log$T$=3.6 is shown Figures 5-44 (b) and (c). This apparent instability in the crack growth rate is due to the competition between releasing the maximum energy during propagation and growing in the weakest direction as a result of material anisotropy. It is possible for quite a wide range of crack growth direction to all be equally likely. If the crack propagates in the horizontal direction then the crack growth is rapid and the crack tip remains sharp. If however the crack deviates then the crack tip is blunted and the rate is slowed.

5.4.6.2 Fracture surfaces

For $\log T \leq 3$, R_q is systematically lower in the pre-strained condition than for pure shear (PS=0%) (Figures 5-62 to 5-64 and Figure 5-66). In that range of tearing energies, the molecular orientation along the pre-strain dominates over the molecular alignment in the direction of the cyclic loading. For $\log T \geq 3$, R_q could either decrease or increase. In case of NR59, these variations are directly related to the changes in the crack growth behaviour and also the fracture surface appearances from the micrographs. For this material, the decrease and the increase in R_q correspond respectively to regions 6 and 5. In region 6, the crack growth rates zoomed up to high rates approaching catastrophical tearing. In region 5, this zoom up of crack growth rates seems to be somehow prevented by the occurrence of very rough fracture surfaces.

5.5 Summary and conclusions

The effect of a pre-strain, orthogonal to the direction of loading, is to weaken all the tested materials. This is attributed to the induced molecular orientation in the bulk of the material in the direction of the crack growth, which reduces the number of molecular chains across the plane of fracture hence reducing the resistance to crack growth. The major role of the molecular orientation in the bulk of the material with respect to the fracture process had been highlighted. It was shown that the reduction in tearing energy with increasing pre-strain is a unique function of the molecular

orientation, assuming that the latter could be reasonably estimated by the magnitude of stress borne by the elastomer matrix in the direction of the pre-strain.

Because this weakening effect due to the pre-strain would certainly be seen down to the lowest tearing energies, this effect could be presented as a decrease in the threshold tearing energy T_0 carried all the way up to higher magnitudes of T.

It was also speculated that the occurrence of strain crystallisation due to the cyclic loading was probably suppressed on the more highly filled material (NR59), for the highest pre-strain (PS=75% and 100%) for $\log T \geq 2.7$. For these regimes, the crack growth rates increased markedly over a narrow range of tearing energy, exhibiting very smooth fracture surfaces. Though the calculation of the predicted contribution of a time-dependent component of the total crack growth for these cases was not conclusive because of experimental uncertainties, such high rates of crack growth are bound to be related to time-dependent crack growth and especially as time-dependent crack growth was observed for this material, for these 2 pre-strains. From a molecular point of view, it was assessed from the stress-strain behaviour of NR59 that for $PS \geq 75\%$, incipient crystallisation in bulk would occur. However, these crystallites align in the direction of the pre-strain and reduce the number of molecular segments available to strain-crystallise at the crack tip in the direction orthogonal to the pre-strain. As observed, the material becomes much weaker.

The microscopic observations of wide secondary cracking (called crevasses) on NR59 revealed features which could be formed through a cavitation opening process. These very smooth rounded features were observed for non-prestrained and pre-strained samples. Causing the formation of very rough fracture surfaces, the occurrence of this phenomenon is linked with the crack growth behaviour corresponding to region 6 in Figure 5-22. This phenomenon could be seen as preventing the crack growth rates to zoom up to rates near the catastrophic tearing, which is otherwise observed in region 5.

It was confirmed in this work, for a range of materials and testing conditions, in agreement with the results from literature[27, 28], that the weaker a material the more widely spaced the crack growth steps.

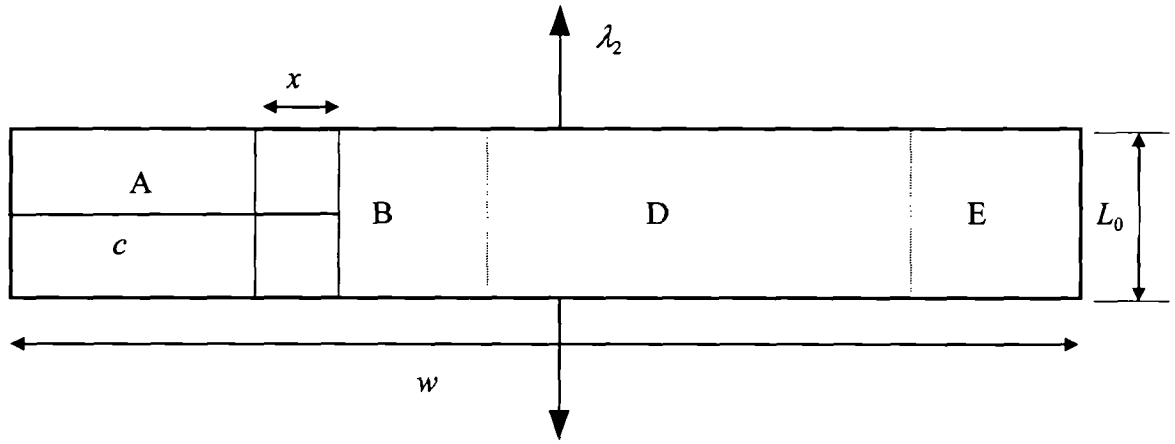

Figure 5-1 A schematic of the various regions according their state of deformation in a pure shear test piece with a crack length c, a width w and an initial height L_0. All the dimensions are referred to the undeformed state.

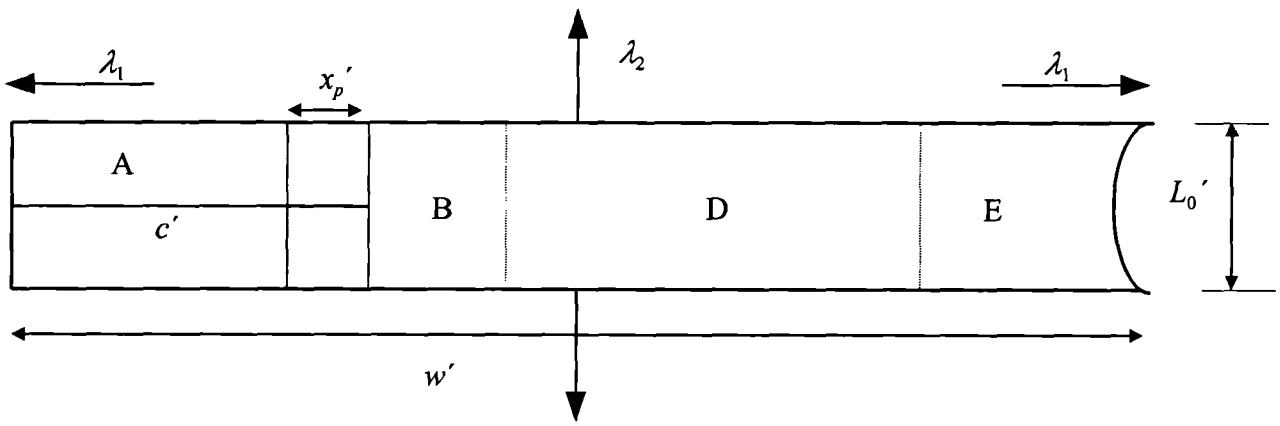

Figure 5-2 A schematic of the various regions according their state of deformation in a pre-strained pure shear test piece with a crack length c', a width w' and a height L_0' in the pre-strained state. All the shown dimensions with a prime sign are referred to the deformed pre-strained state.

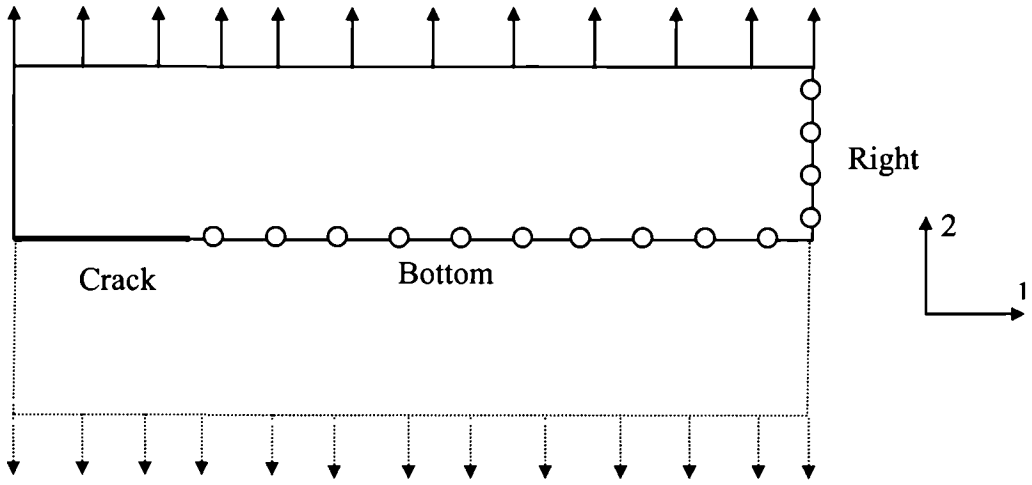

Figure 5-3 The solid lines show the half geometry modelled. Nodes along "Bottom" are constrained in the 1 and 2 directions. For the model used in section 5.2.2, nodes along "Right" are not constrained. They are constrained in the 2 and 1 directions for the model used in section 5.2.3.

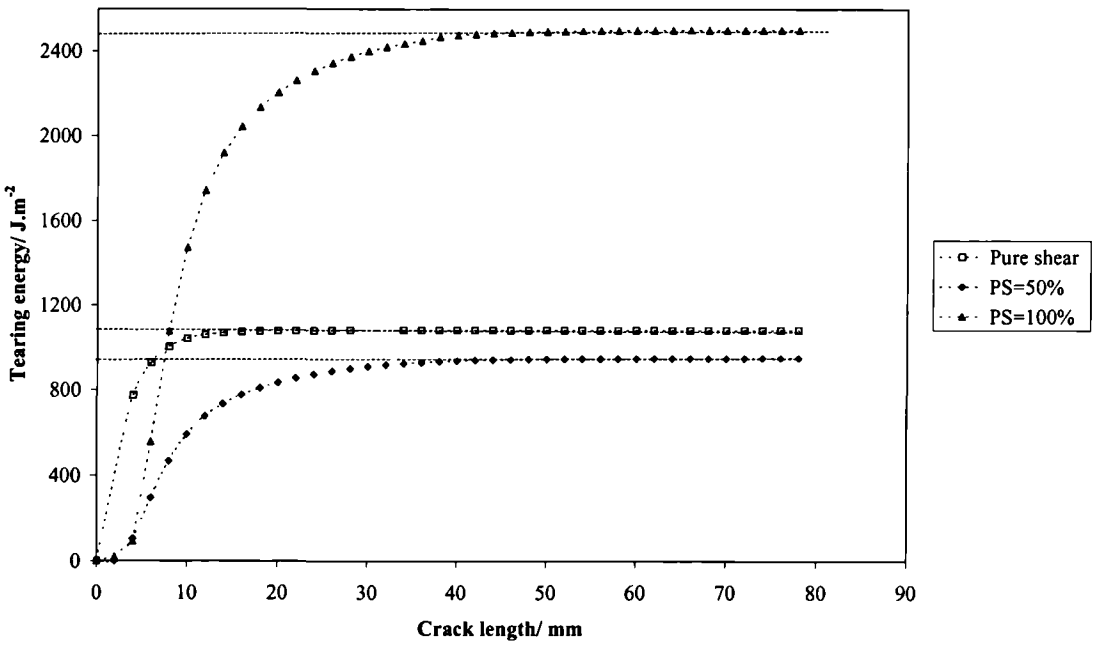

Figure 5-4 Extent of the edge effects estimated on a tearing energy against crack length plot for a pure shear, and test pieces pre-strained 50% and 100%. The magnitude of crack length is referred to the unstrained dimensions of a test-piece (non pre-strained, non deformed).

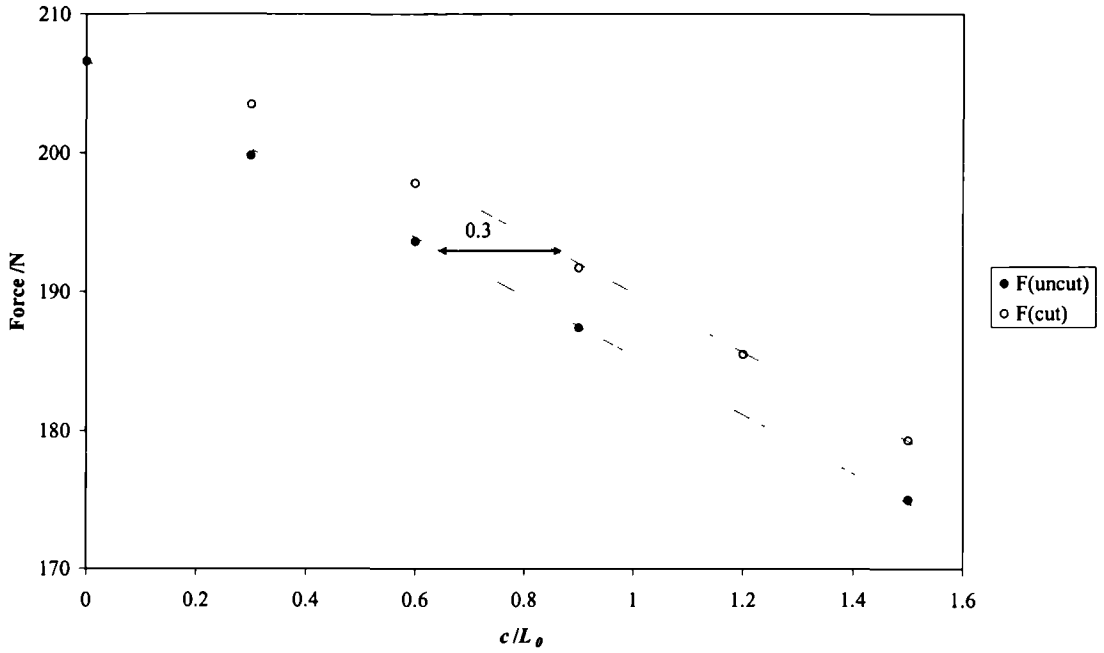

Figure 5-5 Determination of x for a pure shear with $\lambda_2 = 1.5$, using FEA. Plot of the crack length or reduction in width for the uncracked specimen c, scaled to the initial height L_0 versus the applied force: $x = 0.3L_0$

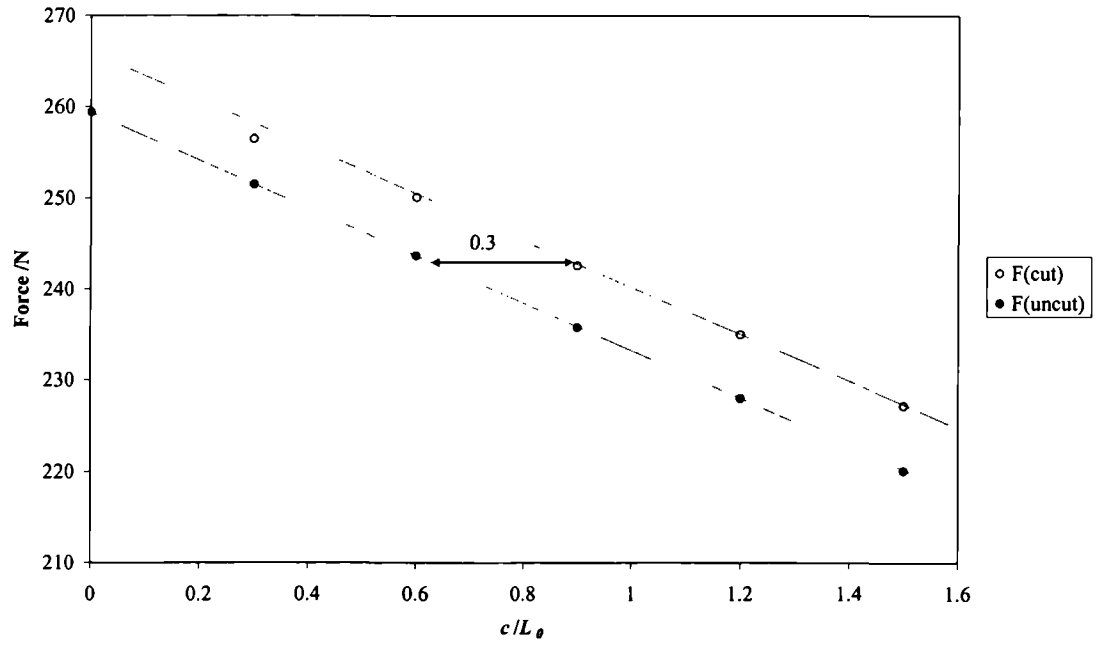

Figure 5-6 Determination of x_p' for a 50% pre-strained sample with $\lambda_2 = 1$, using FEA. Plot of the crack length or reduction in width for the uncracked specimen c, scaled to the initial height L_0 versus the applied force: $x_p' = 0.3L_0$

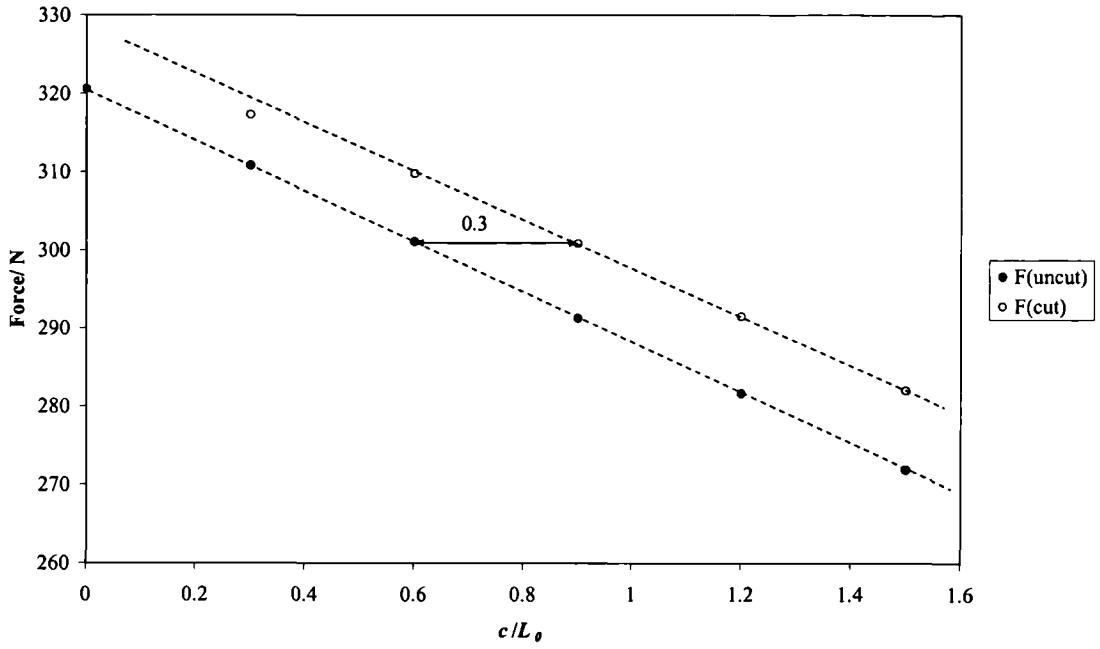

Figure 5-7 Determination of x_p' for a 100% pre-strained sample with $\lambda_2 = 1$, using FEA. Plot of the crack length or reduction in width for the uncracked specimen c, scaled to the initial height L_0 versus the applied force: $x_p' = 0.3L_0$.

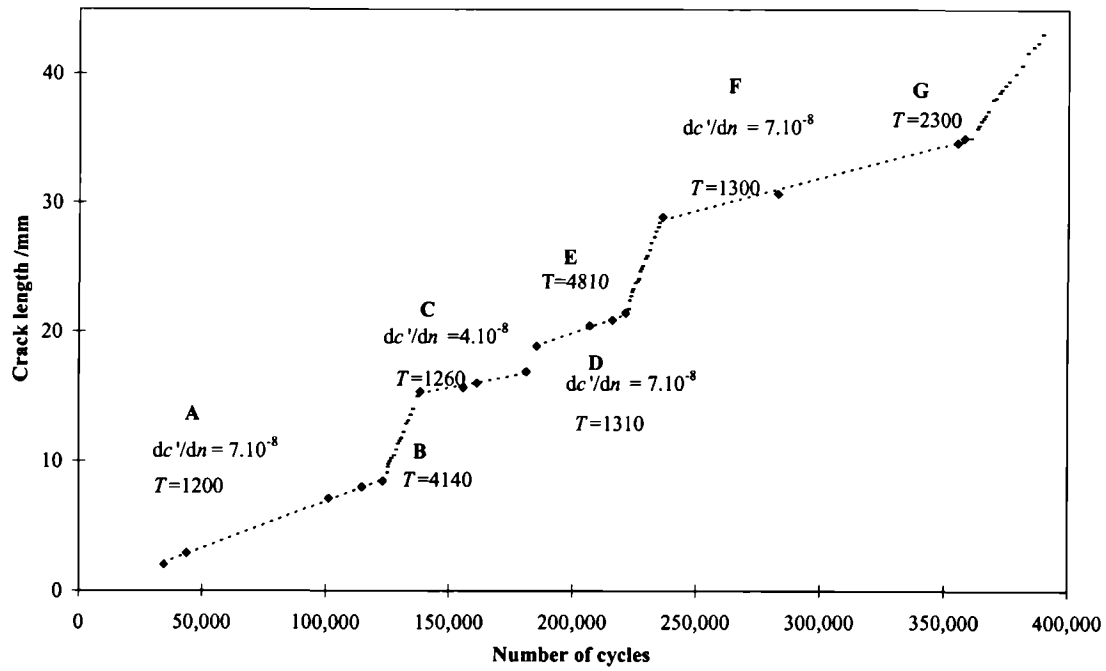

Figure 5-8 Sequences of low-high-low tearing energy tests on NR29 pre-strained 15%. The crack growth rates dc'/dn referred to the deformed state are in m.cycle^{-1} and the tearing energies T are in J.m^{-2}.

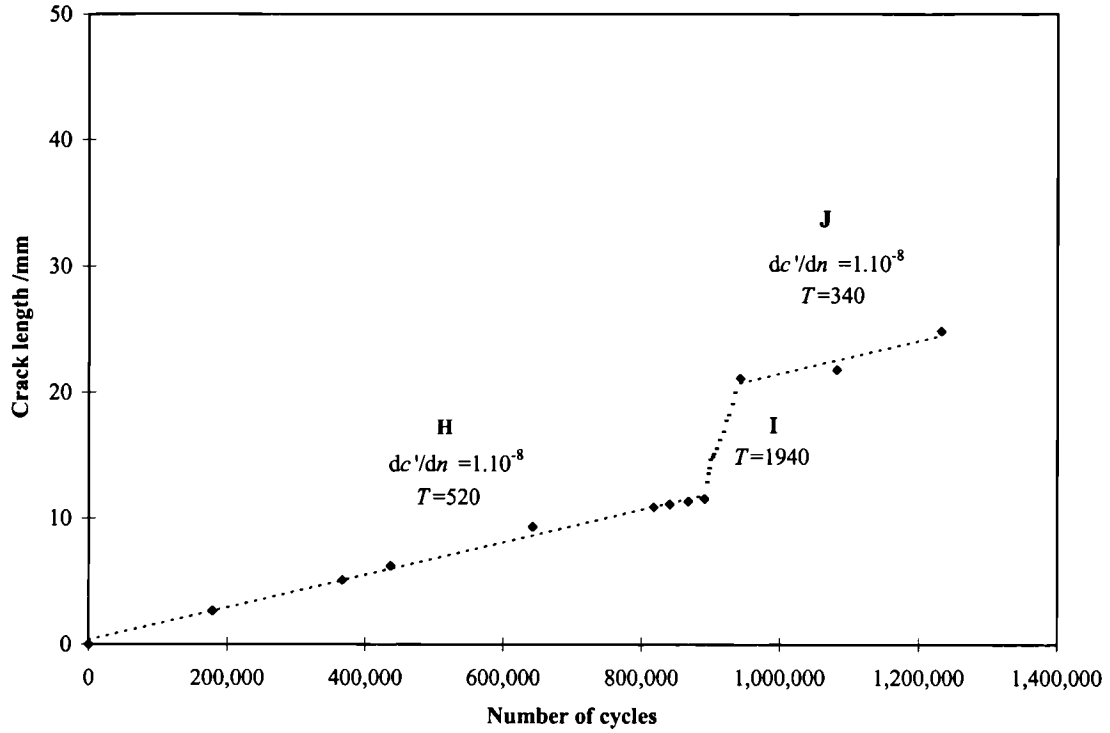

Figure 5-9 Sequences of low-high-low tearing energy tests on NR29 pre-strained 25%. The crack growth rates dc'/dn referred to the deformed state are in m.cycle^{-1} and the tearing energies T are in J.m^{-2}.

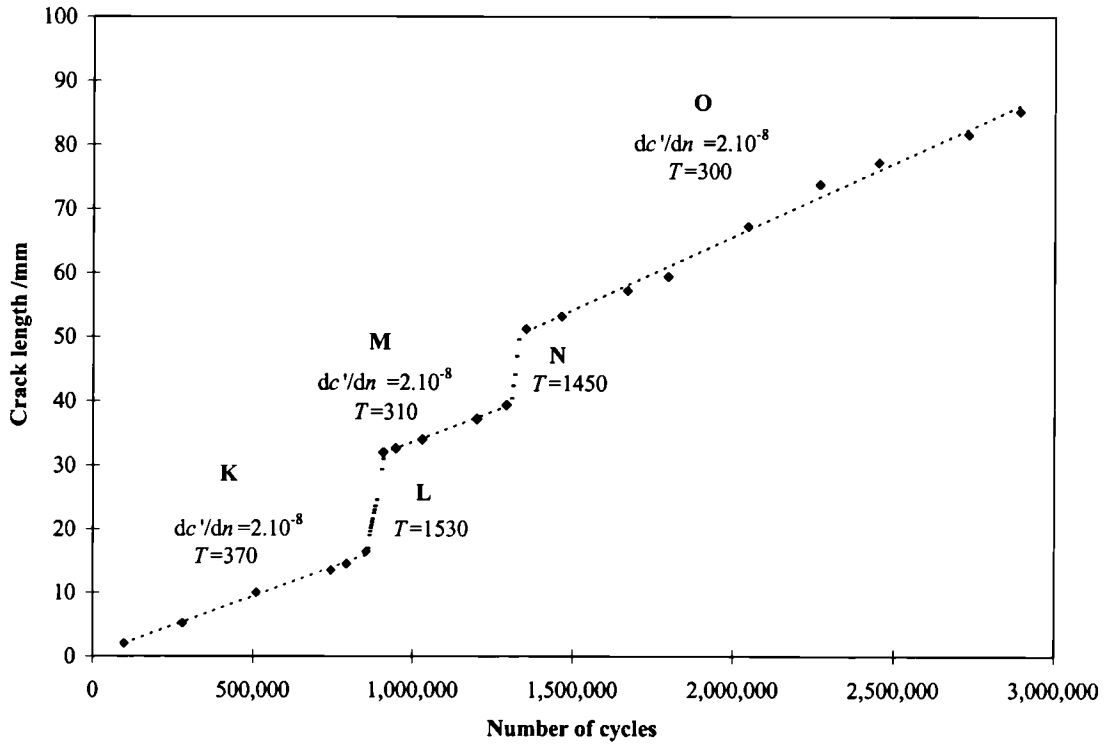

Figure 5-10 Sequences of low-high-low tearing energy tests on NR29 pre-strained 100%. The crack growth rates dc'/dn referred to the deformed state are in m.cycle^{-1} and the tearing energies T are in J.m^{-2}.

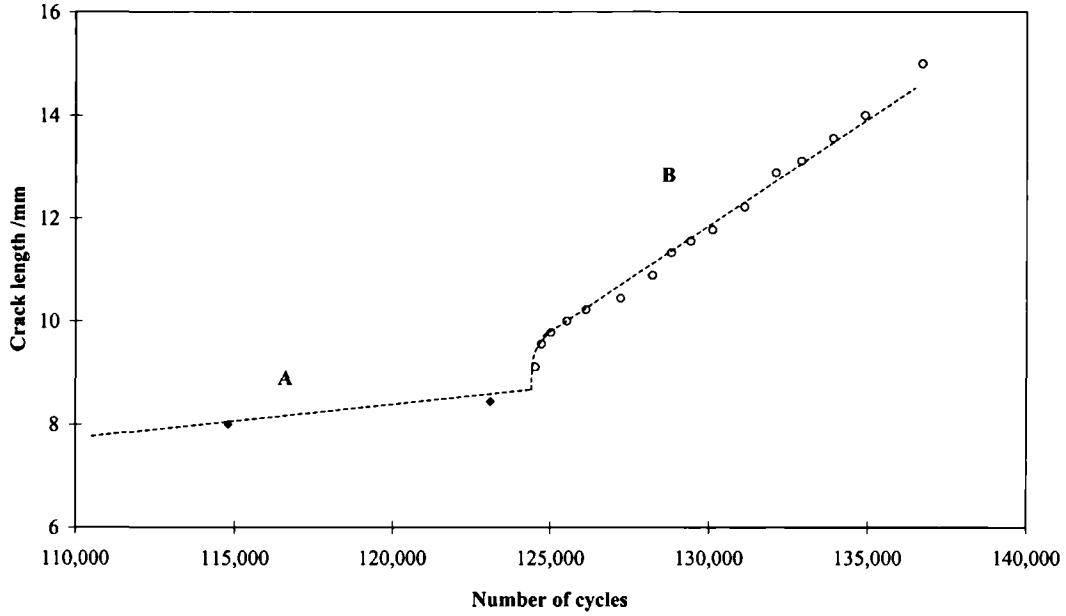

Figure 5-11 Magnification of the transition zone (A-B) showed on Figure 5-8 for NR29 pre-strained 15%.

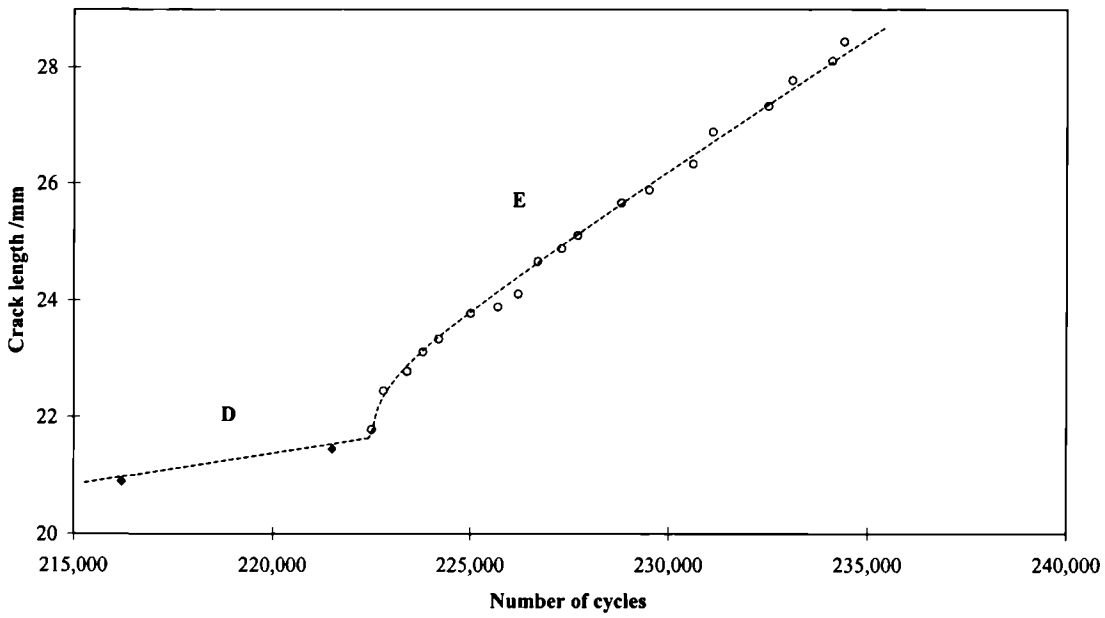

Figure 5-12 Magnification of the transition zone (D-E) showed on Figure 5-8 for NR29 pre-strained 15%.

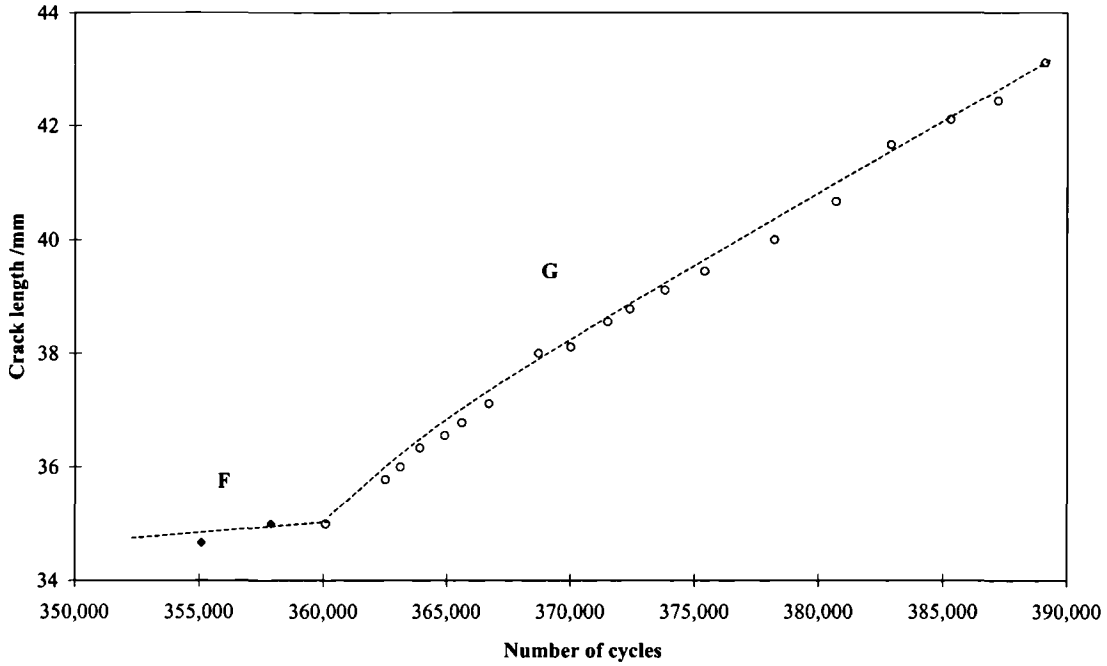

Figure 5-13 Magnification of the transition zone (F-G) showed on Figure 5-8 for NR29 pre-strained 15%.

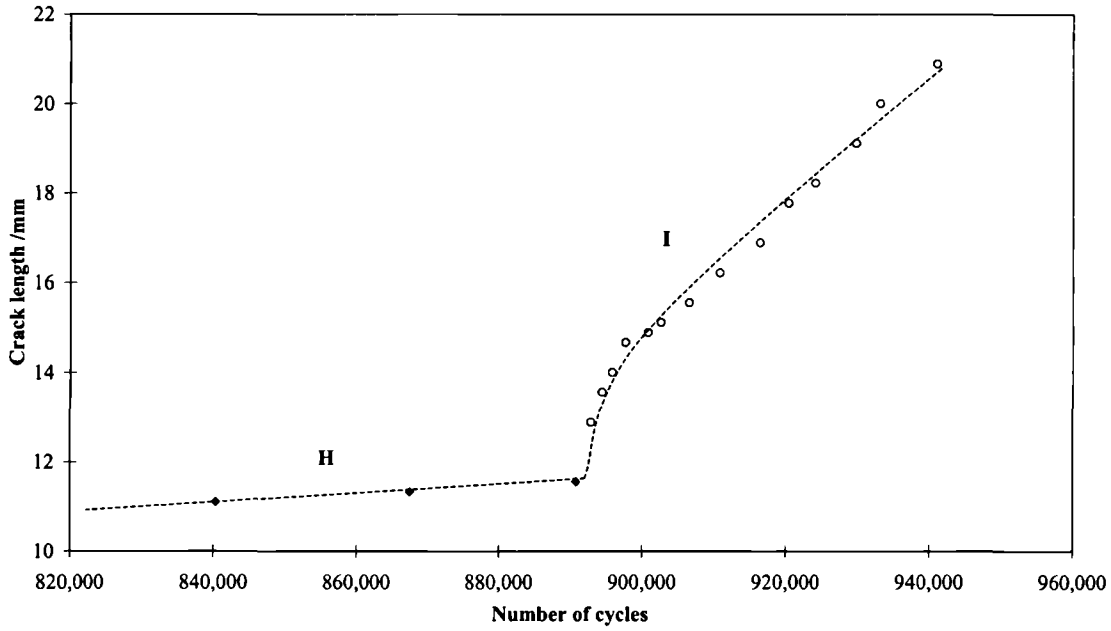

Figure 5-14 Magnification of the transition zone (H-I) showed on Figure 5-9 for NR29 pre-strained 25%.

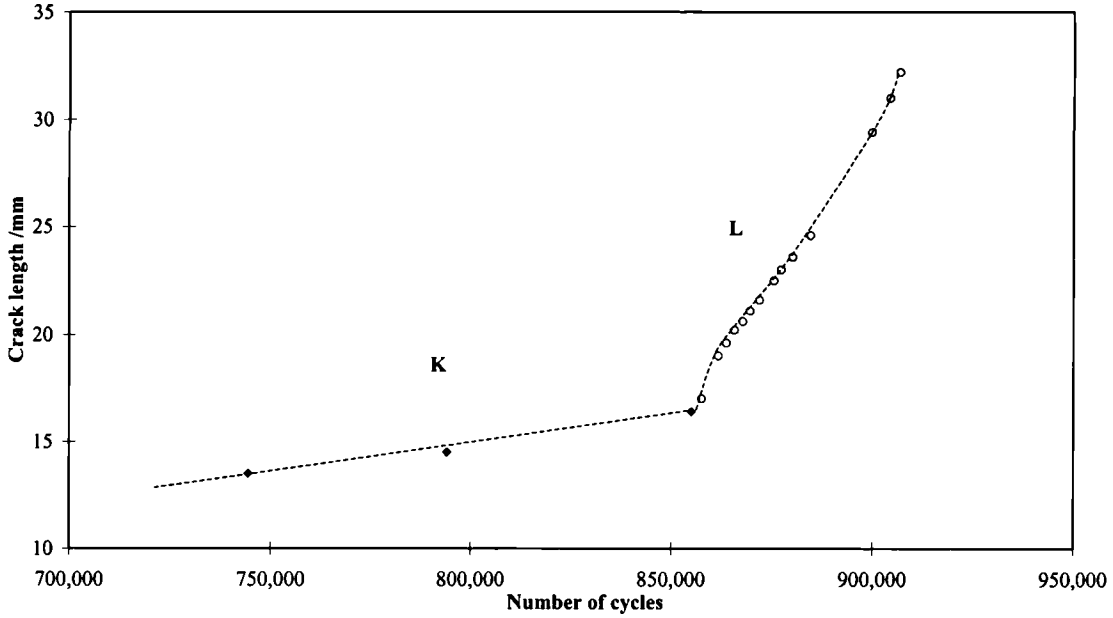

Figure 5-15 Magnification of the transition zone (K-L) showed on Figure 5-10 for NR29 pre-strained 100%.

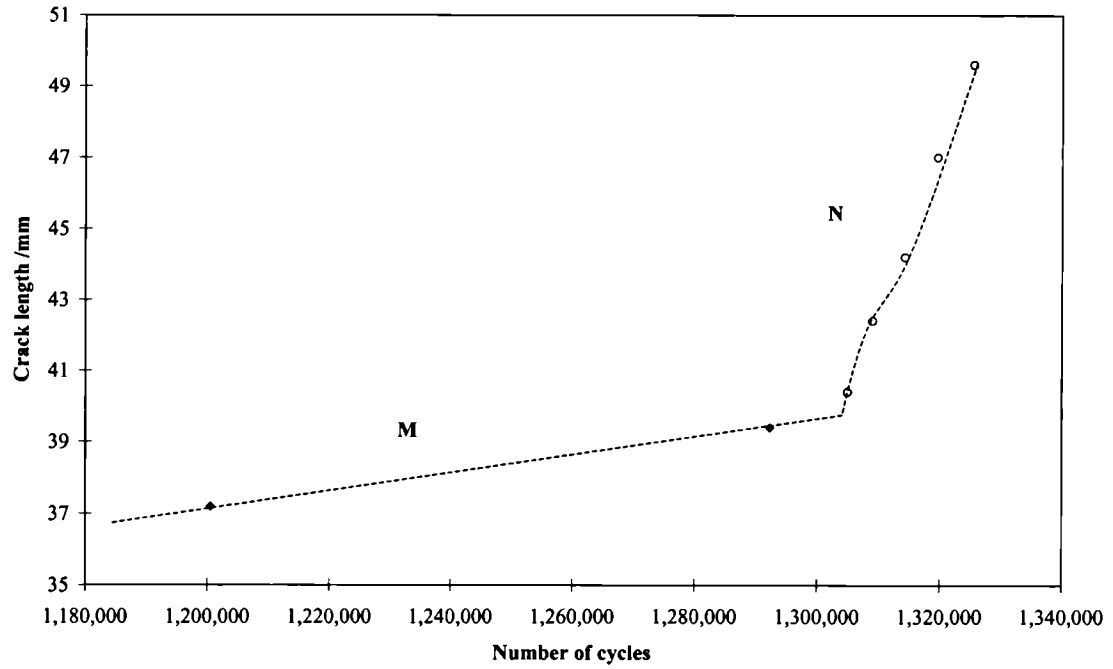

Figure 5-16 Magnification of the transition zone (M-N) showed on Figure 5-10 for NR29 pre-strained 100%.

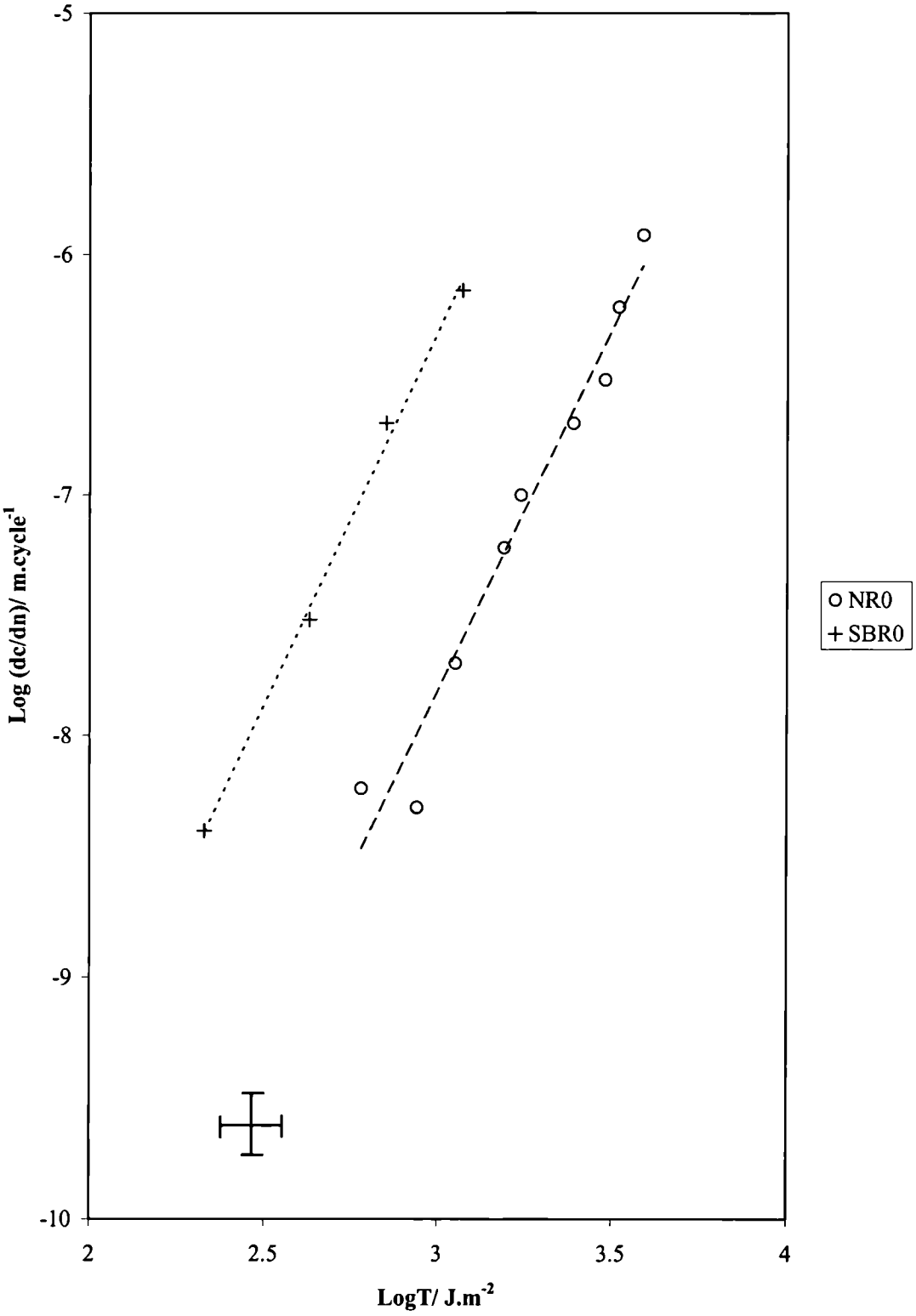

Figure 5-17 Crack growth per cycle (dc/dn) versus T comparing NR0 and SBR0.

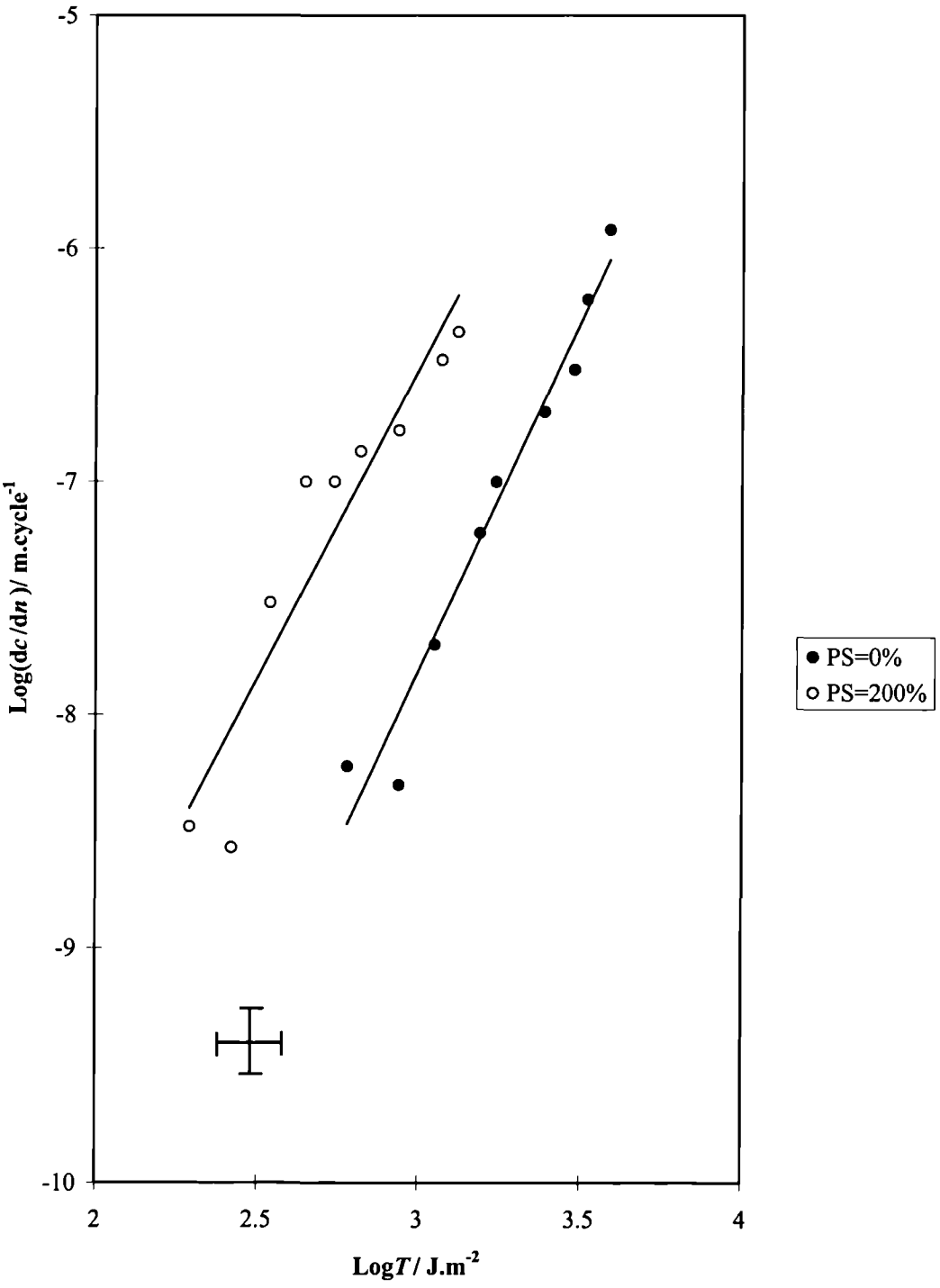

Figure 5-18 Crack growth per cycle (dc/dn) versus the tearing energy T for NR0 as a function of the pre-strain PS, expressed in percentage strain.

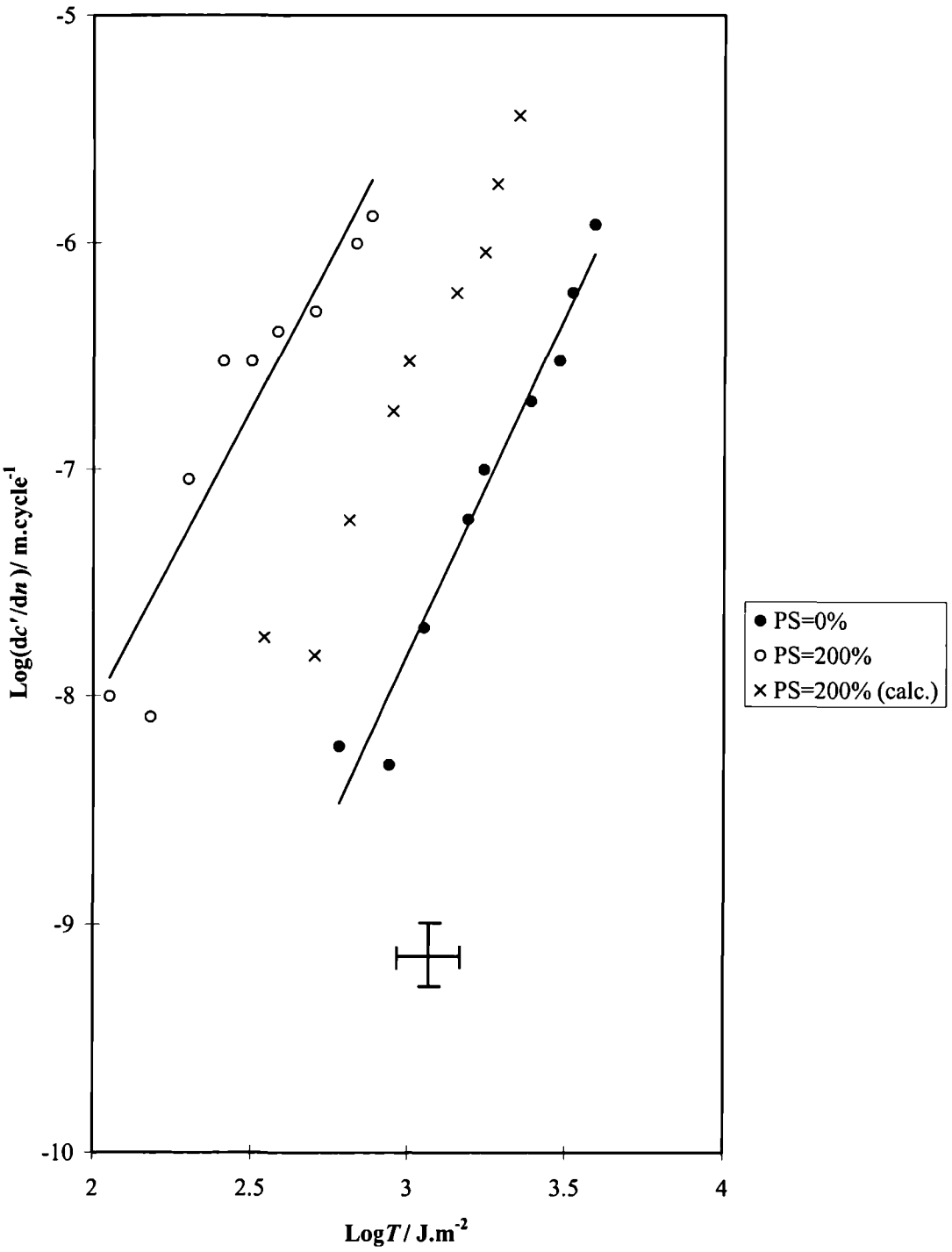

Figure 5-19 Prediction of the crack growth behaviour for NR0 of PS=200% (PS=200% (calc.)) assuming that the increase of the cross-section area in the pre-strain condition is the only factor making the pre-strained sample apparently weaker, compared with experimental results for NR0.

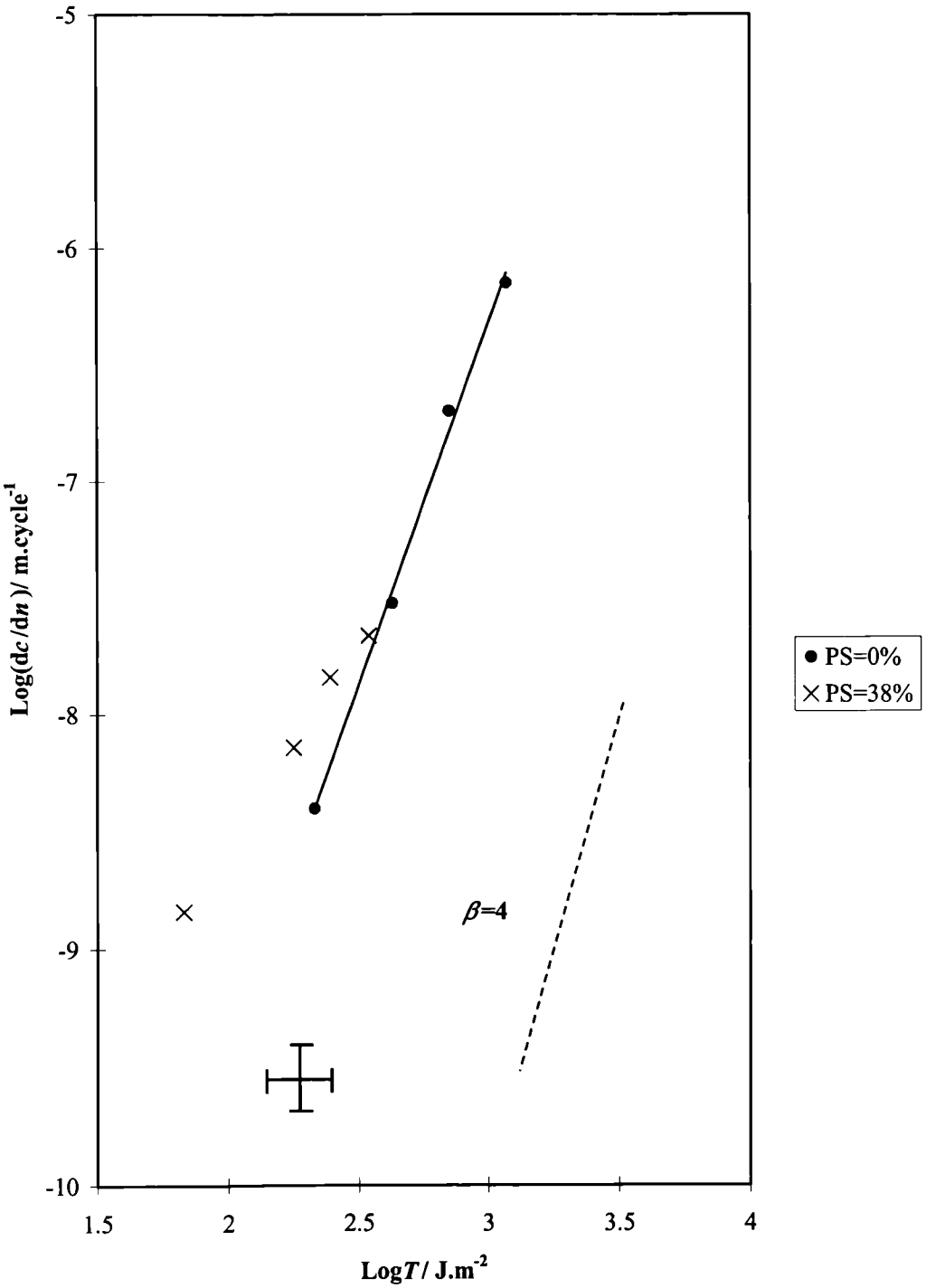

Figure 5-20 Crack growth per cycle (dc/dn) versus the tearing energy T for SBR0 as a function of the pre-strain PS, expressed in percentage strain. The dotted line represents a line with a slope value β of 4.

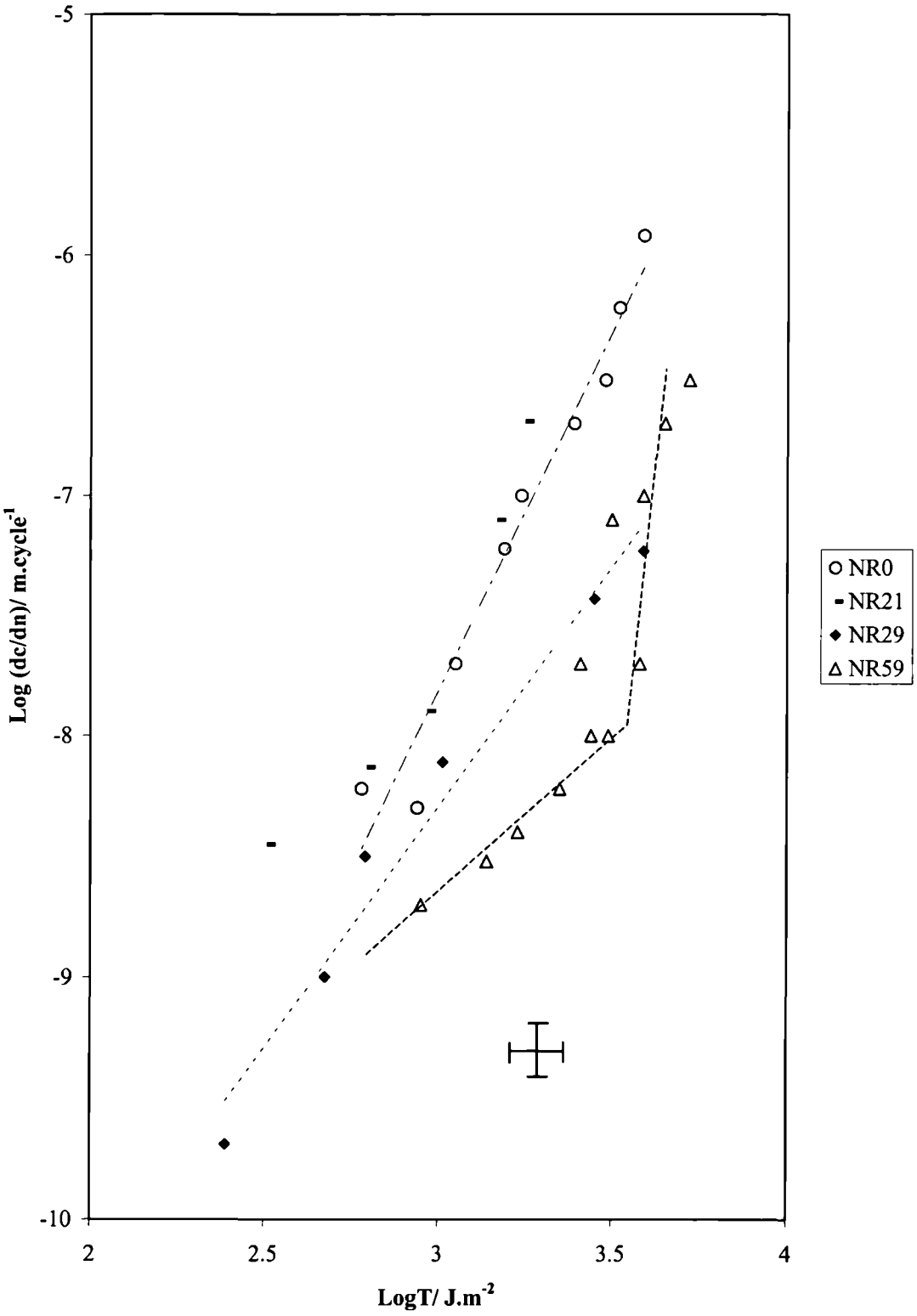

Figure 5-21 Crack growth per cycle (dc/dn) versus the tearing energy T comparing filled NR (NR21, NR29 and NR59) with NR0.

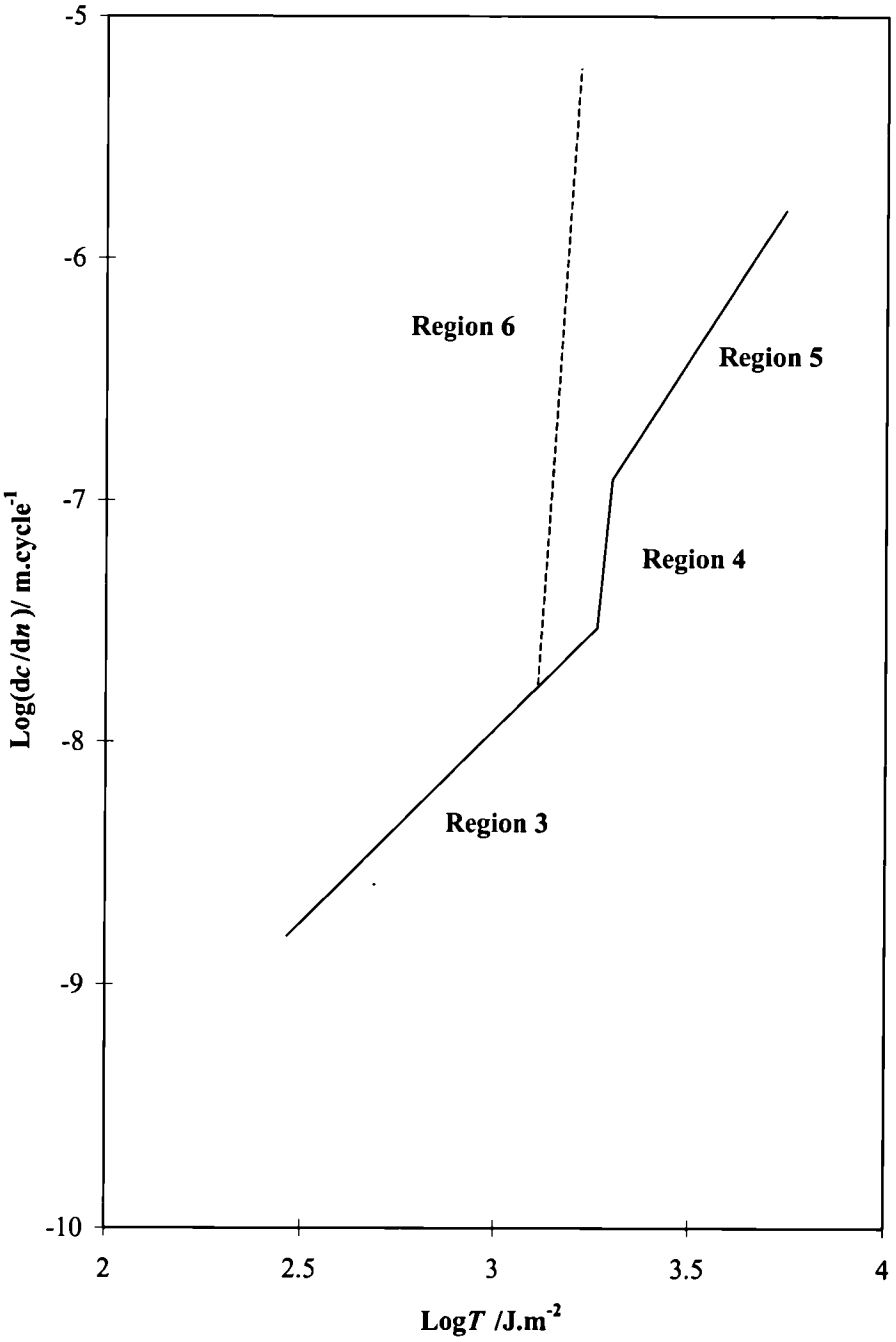

Figure 5-22 Various regions observed in the crack growth behaviour of SBR30 and NR59.

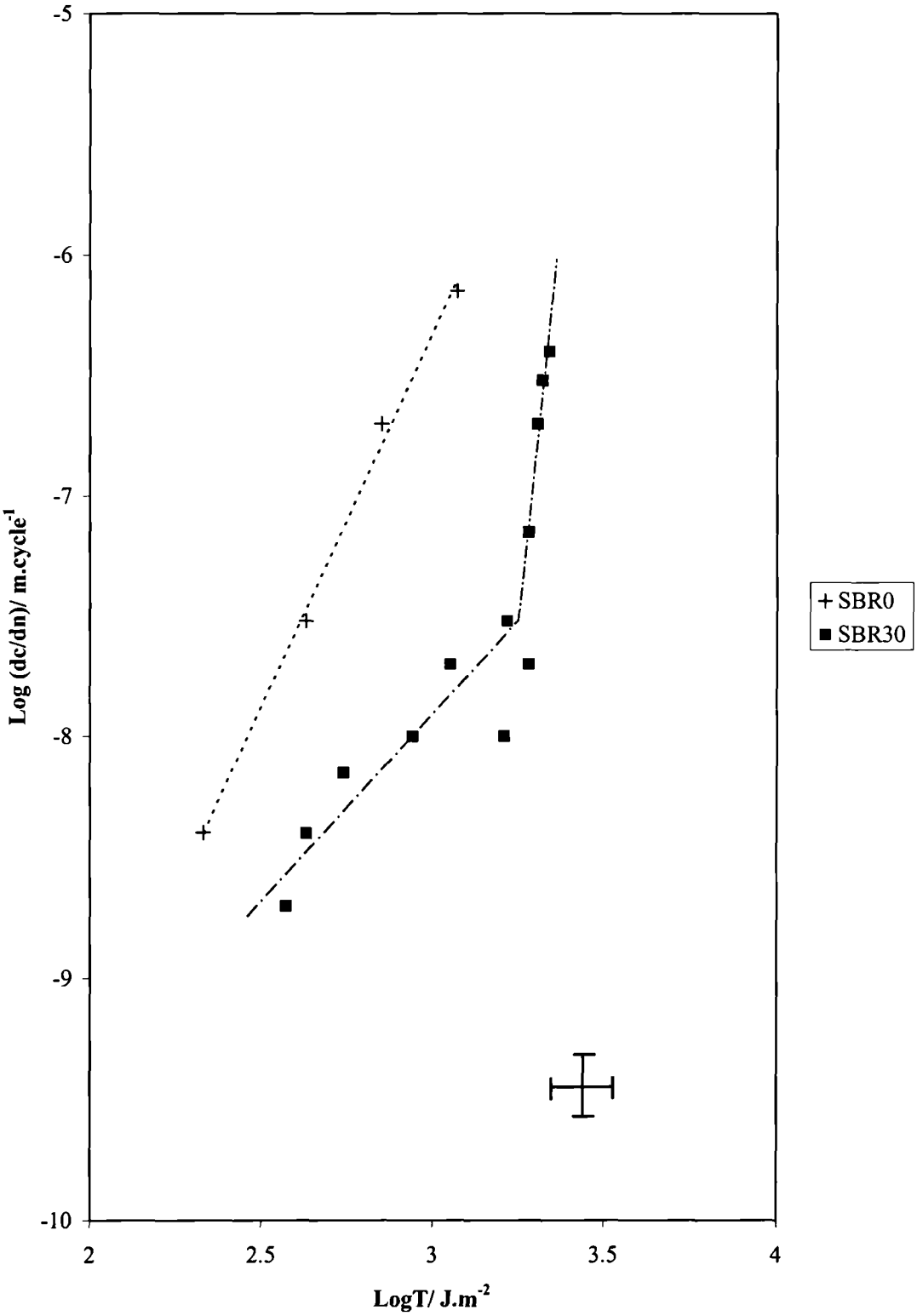

Figure 5-23 Crack growth per cycle (dc/dn) versus the tearing energy T comparing SBR0 and SBR30.

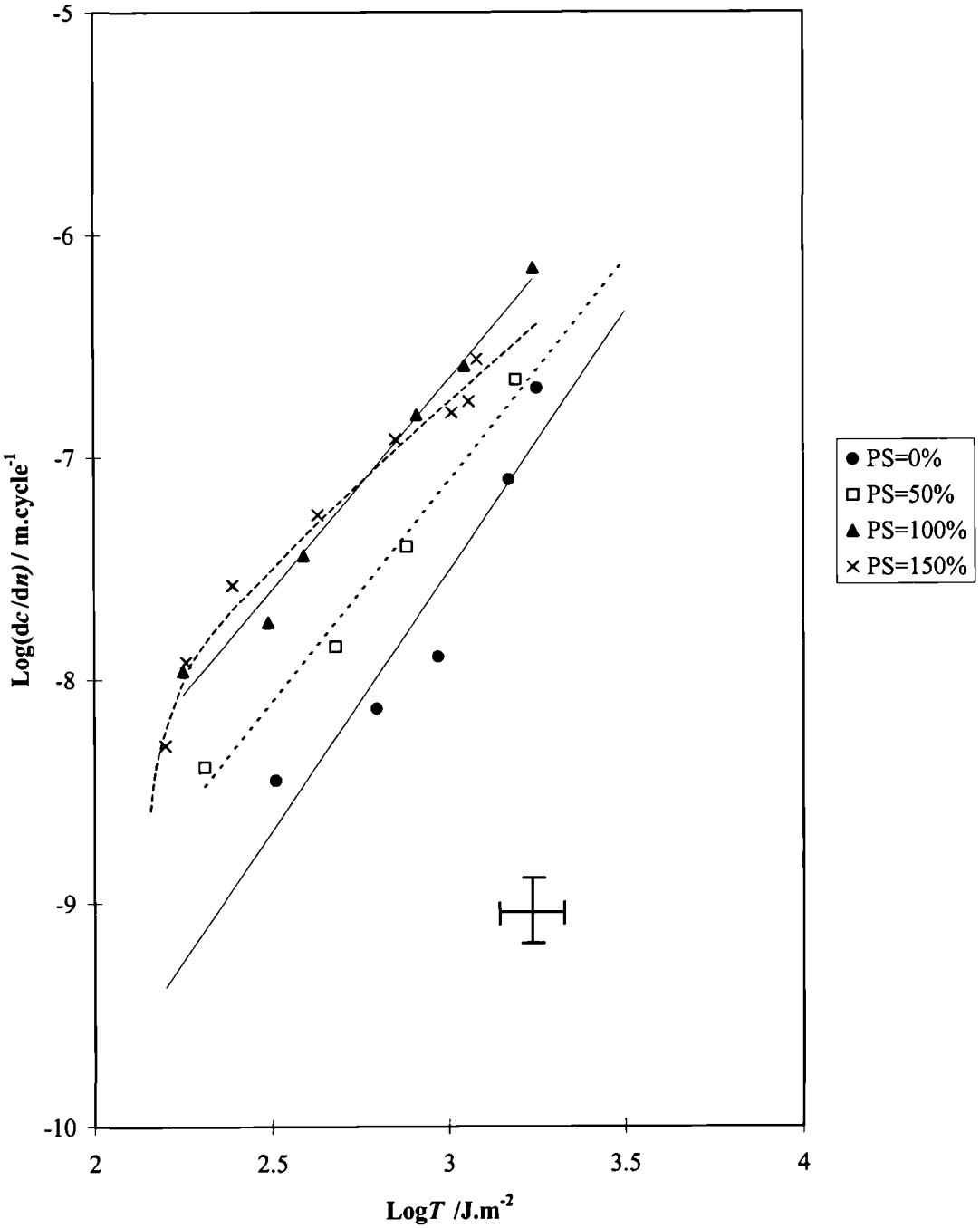

Figure 5-24 Crack growth per cycle (dc/dn) versus the tearing energy T for NR21 as a function of the pre-strain PS, expressed in percentage strain.

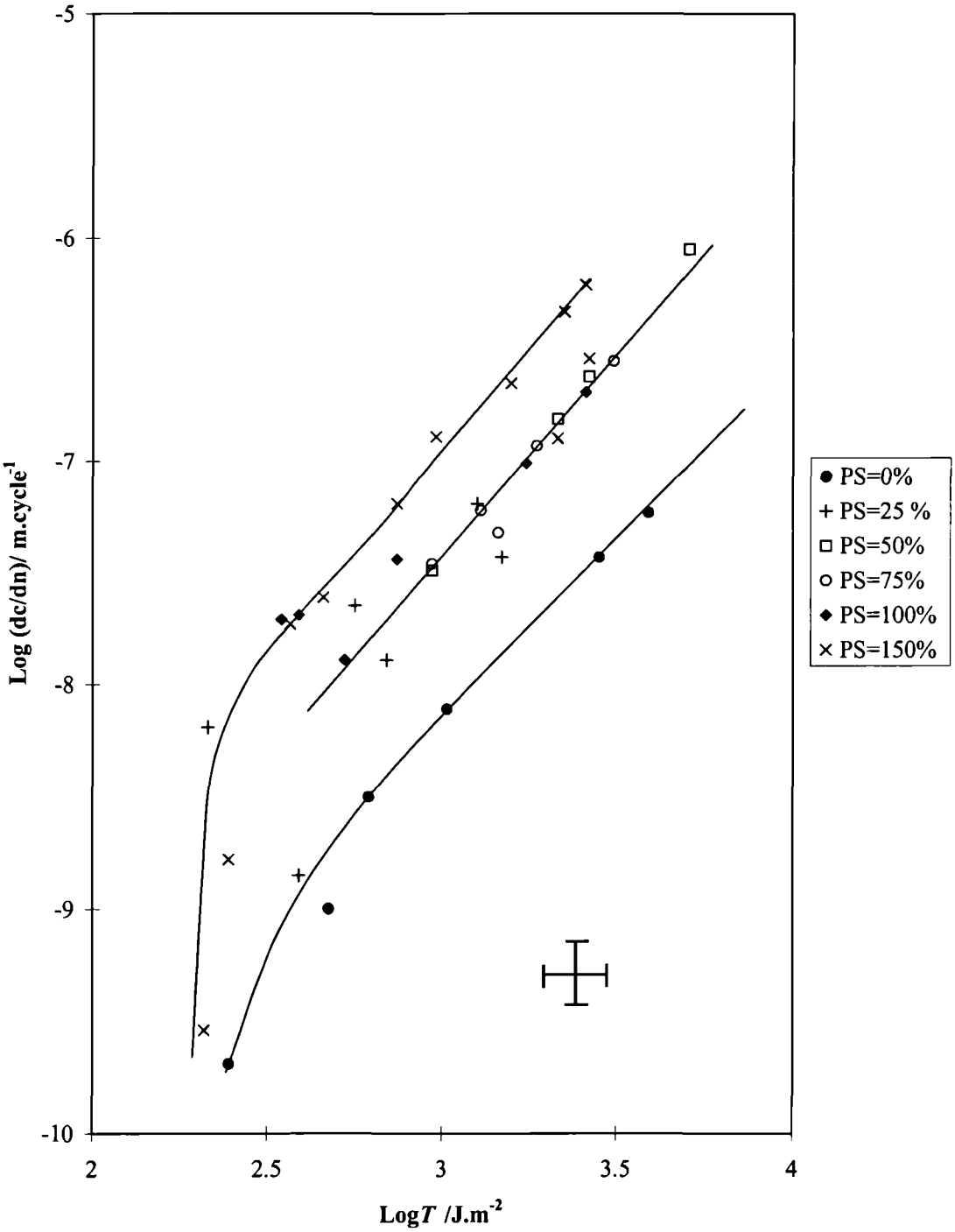

Figure 5-25 Crack growth per cycle (dc/dn) versus the tearing energy T for NR29 as a function of the pre-strain PS, expressed in percentage strain.

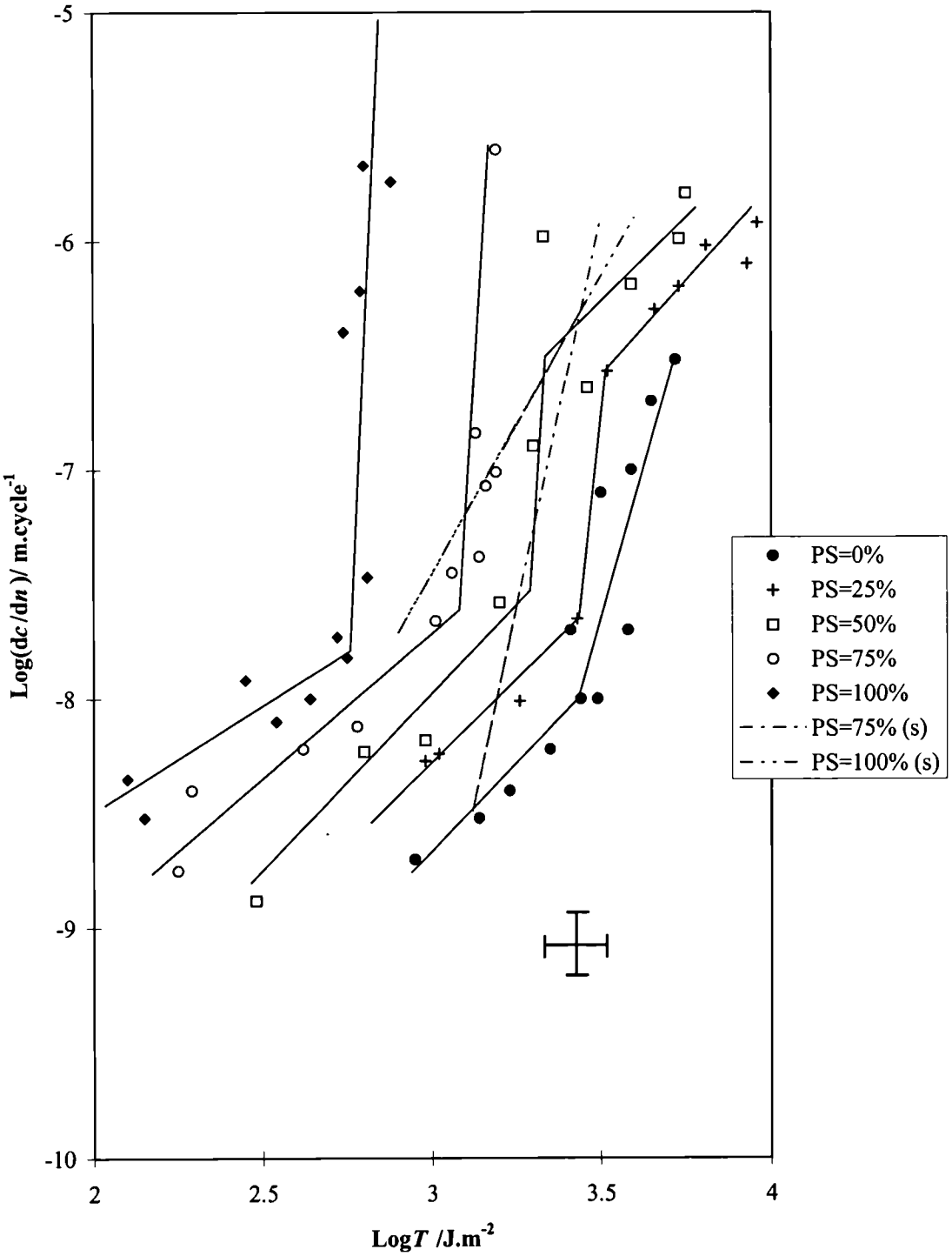

Figure 5-26 Crack growth per cycle (dc/dn) versus the tearing energy T for NR59 as a function of the pre-strain PS, expressed in percentage strain. The data PS=75%(s) and PS=100%(s) correspond to the estimated contribution of time-dependent crack growth for PS=75% and PS=100% (calculation detailed in Appendix 5)

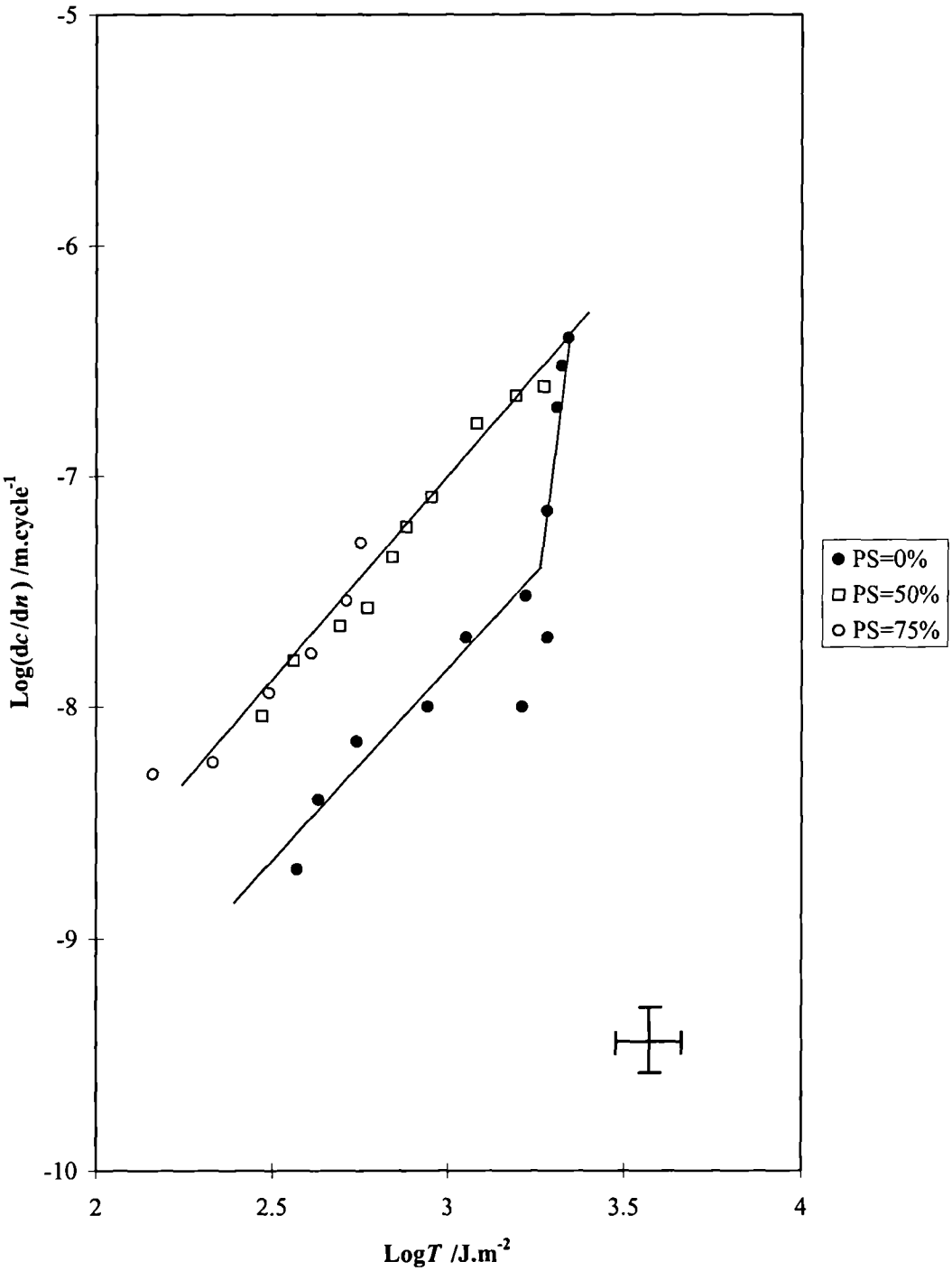

Figure 5-27 Crack growth per cycle (dc/dn) versus the tearing energy T for SBR30 as a function of the pre-strain PS, expressed in percentage strain.

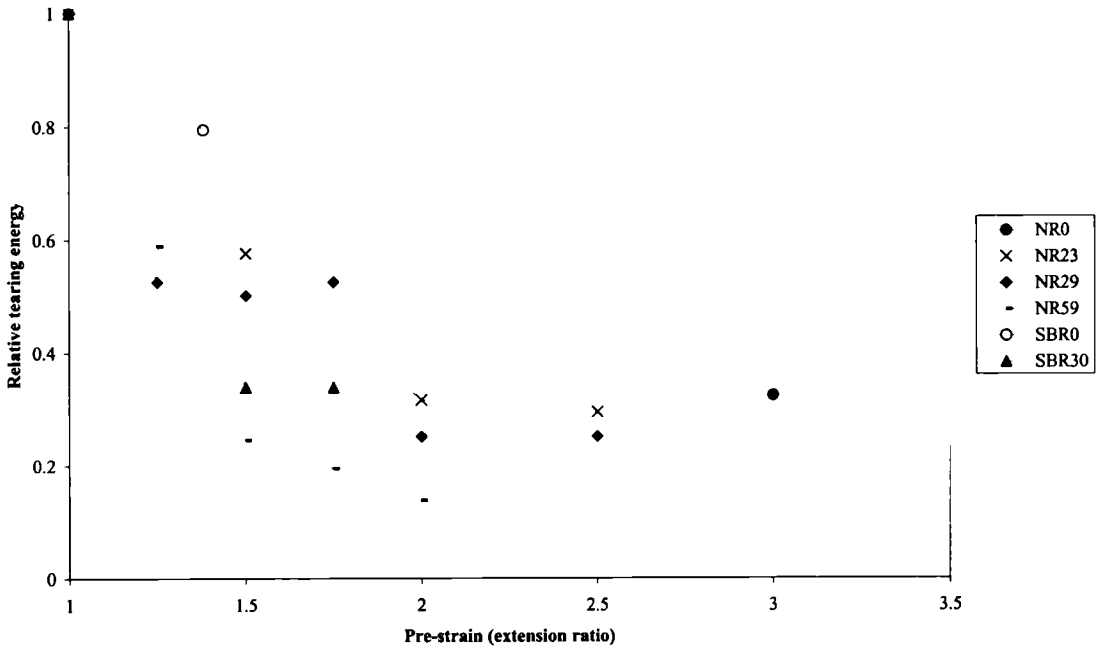

Figure 5-28 Plots of the relative tearing energy (relative to the tearing energy for PS=0%) at a given crack growth rate ($\log(dc/dn) = -8$), as a function of the pre-strain expressed in terms of extension ratio.

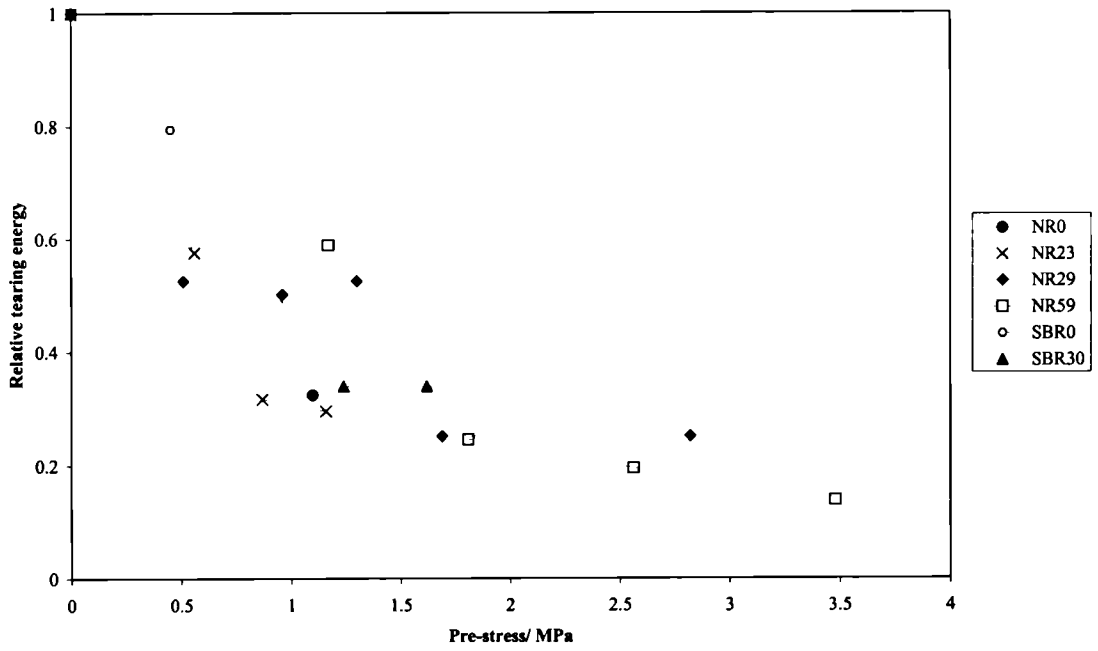

Figure 5-29 Plots of the relative tearing energy (relative to the tearing energy for PS=0%) at a given crack growth rate ($\log(dc/dn) = -8$), as a function of the pre-strain expressed in terms of stress (pre-stress).

Top views **Profile views**

log*T*=3 (log(d*c*/d*n*)=-8.4)

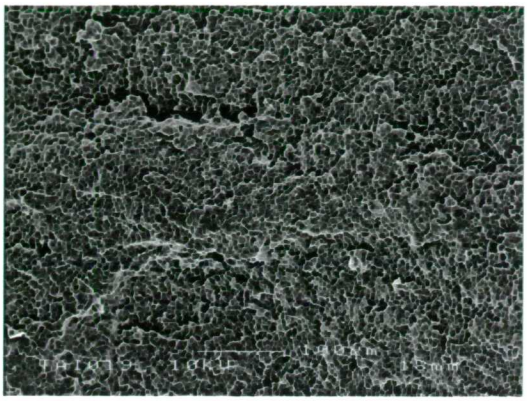

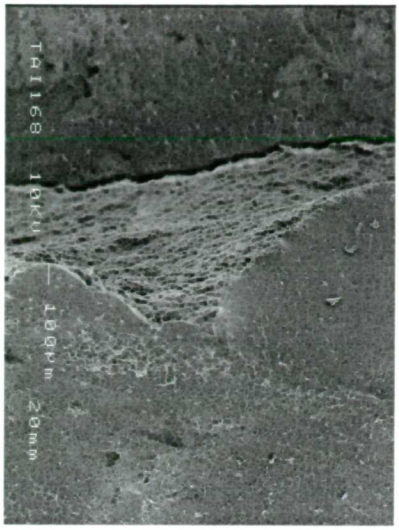

(a)

log*T*=3.4 (log(d*c*/d*n*)=-6.7)

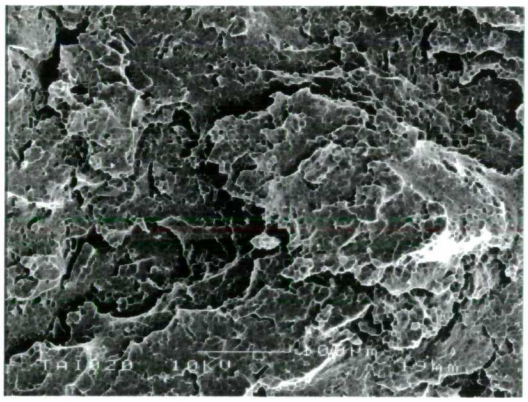

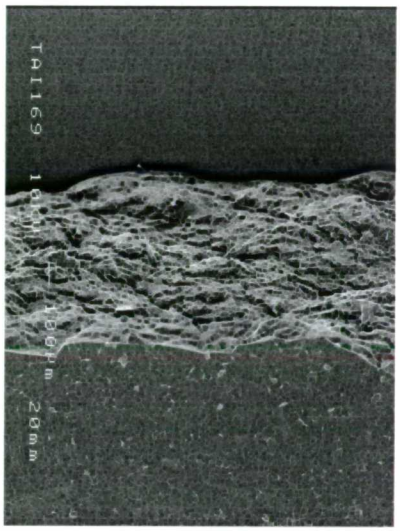

(b)

log*T*=3.6 (log(d*c*/d*n*)=-5.9)

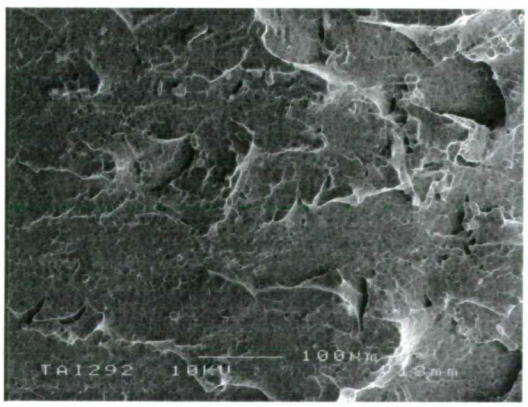

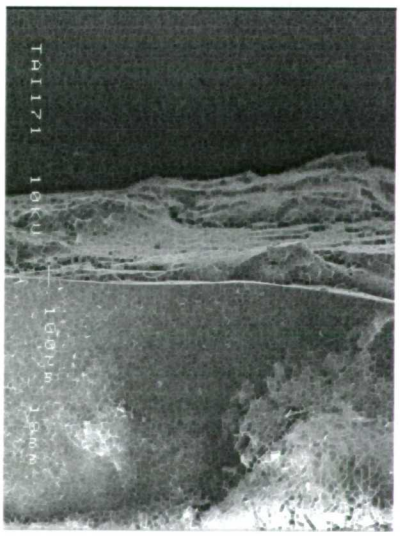

(c)

Figure 5-30 Micrographs of NR0, PS=0%.

Top views **Profile views**

log*T*=2.5 $\left(\log(dc/dn)=-7.5\right)$

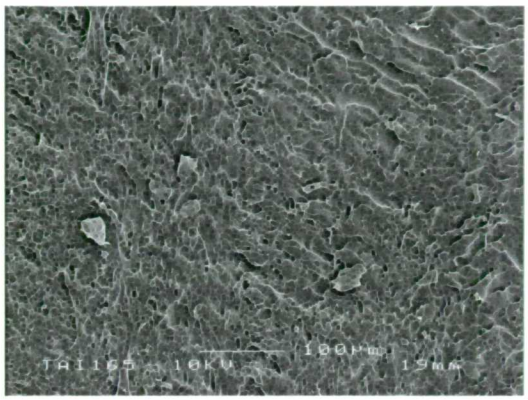

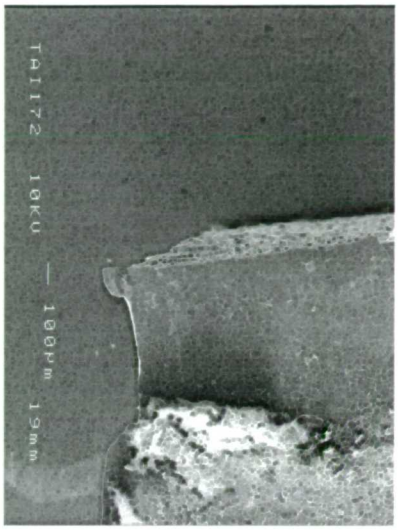

(a)

log*T*=2.7 $\left(\log(dc/dn)=-7\right)$

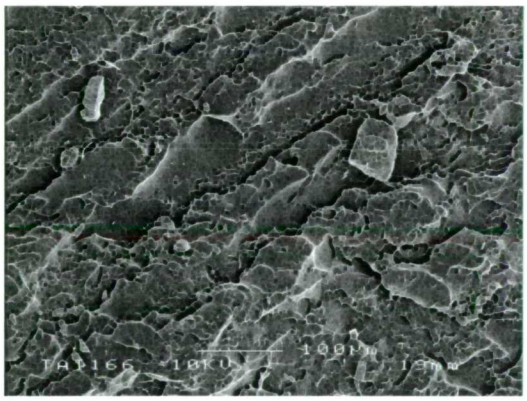

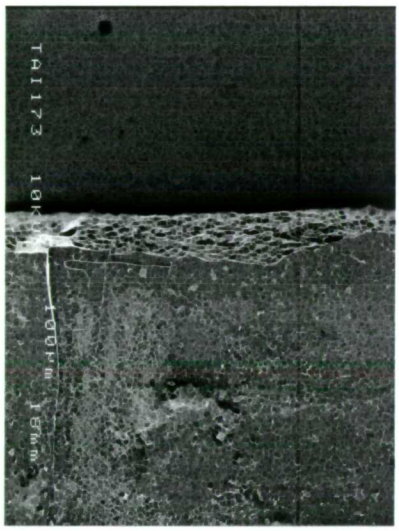

(b)

log*T*=3.1 $\left(\log(dc/dn)=-6.4\right)$

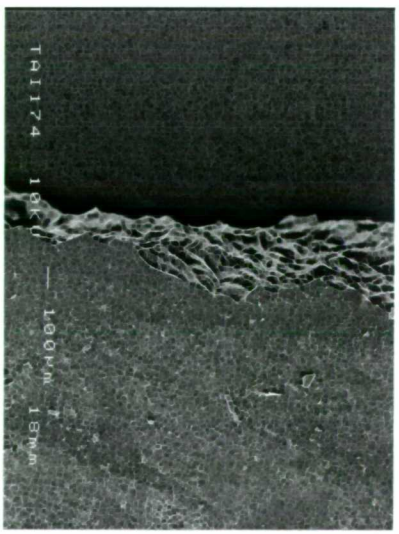

(c)

Figure 5-31 Micrographs of NR0, PS=200%.

Top views

Profile views

log*T*=2.5 (log(d*c*/d*n*)=-8.4)

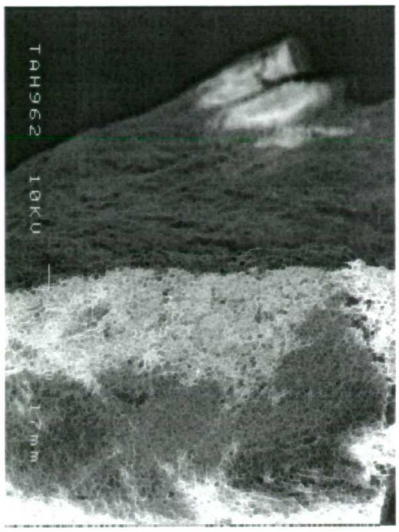

(a)

log*T*=3 (log(d*c*/d*n*)=-7.9)

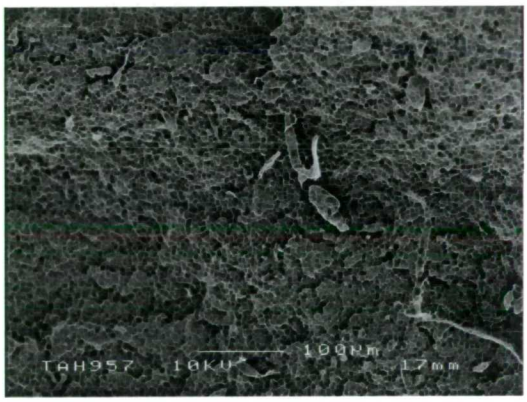

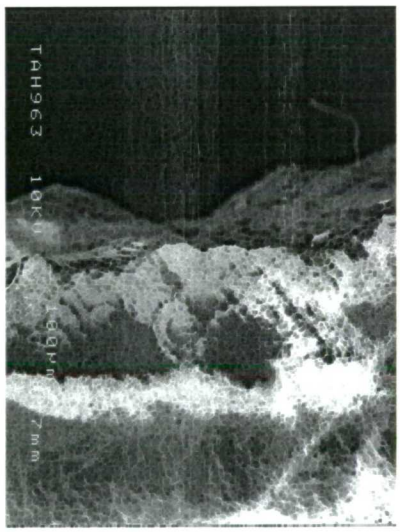

(b)

log*T*=3.3 (log(d*c*/d*n*)=-6.7)

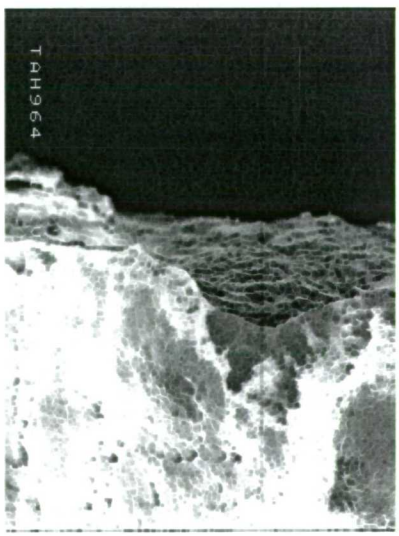

(c)

Figure 5-32 Micrographs of NR21, PS=0%.

Top views **Profile views**

log*T*=2.3 (log(d*c*/d*n*)=-8.4)

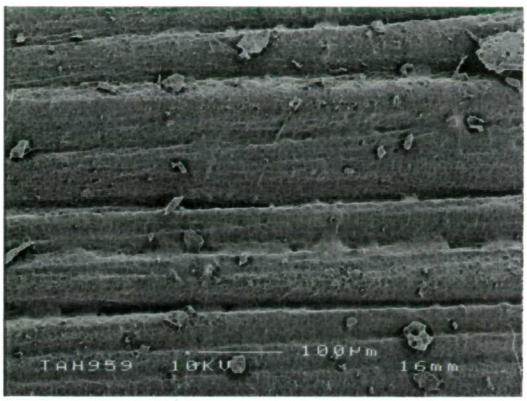

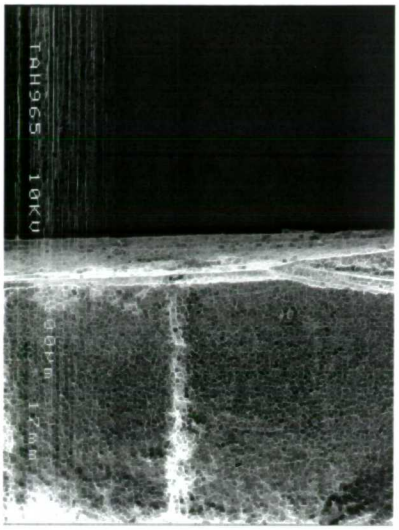

(a)

log*T*=2.9 (log(d*c*/d*n*)=-7.4)

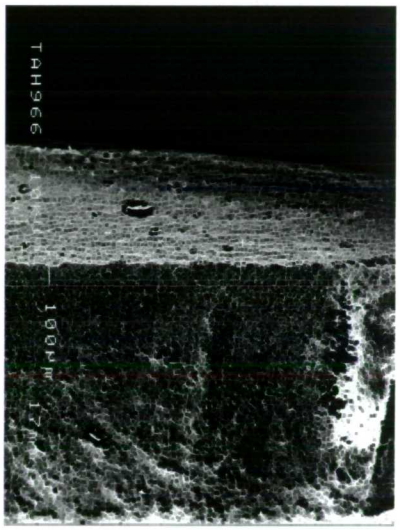

(b)

log*T*=3.2 (log(d*c*/d*n*)=-6.6)

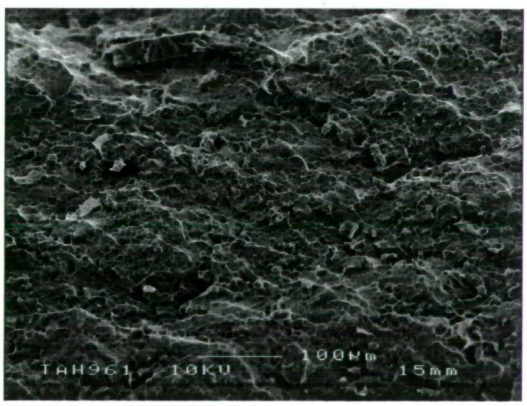

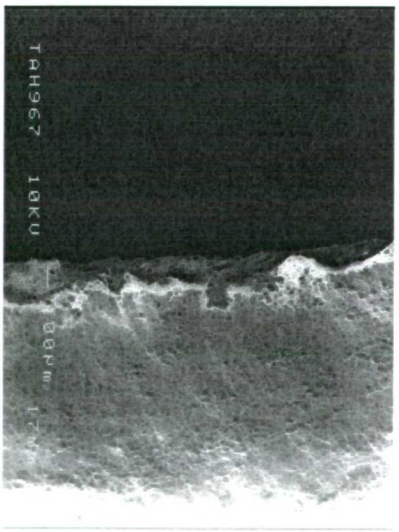

(c)

Figure 5-33 Micrographs of NR21, PS=50%.

Top views **Profile views**

log*T*=2.5 (log(d*c*/d*n*)=-7.7)

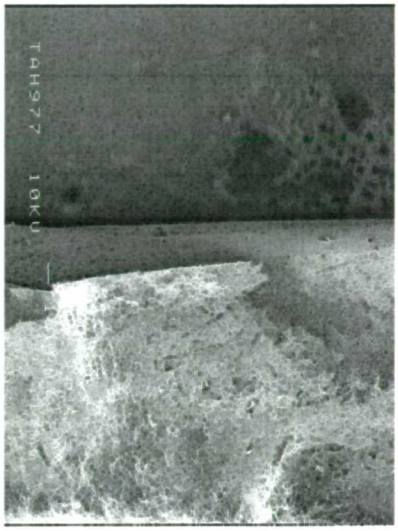

(a)

log*T*=3 (log(d*c*/d*n*)=-6.6)

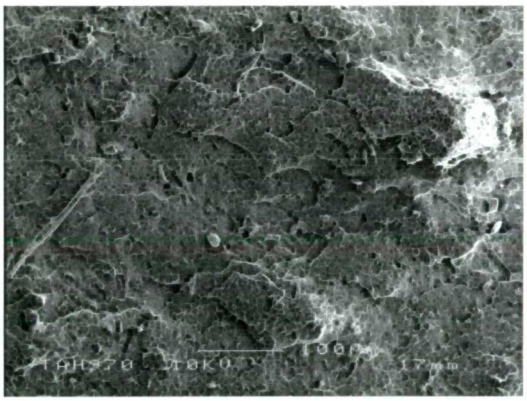

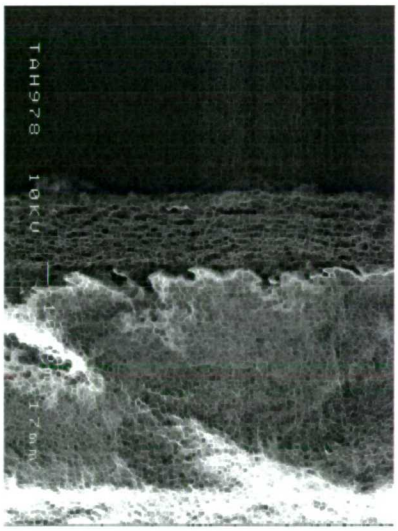

(b)

log*T*=3.2 (log(d*c*/d*n*)=-6.1)

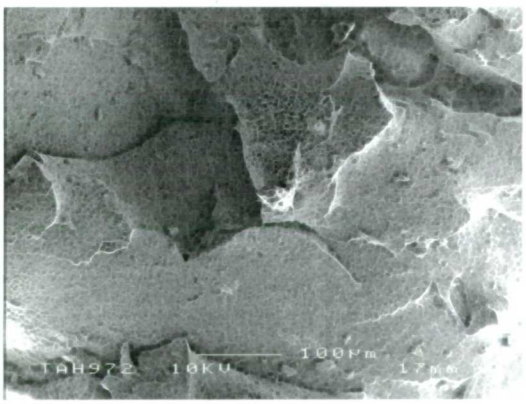

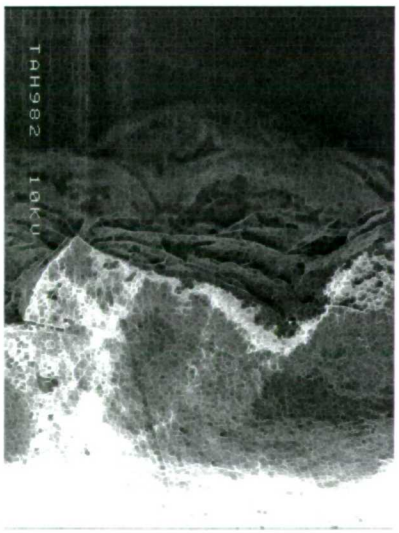

(c)

Figure 5-34 Micrographs of NR21, PS=100%.

Top views **Profile views**

log*T*=2.4 $\left(\log(dc/dn)=-7.6\right)$

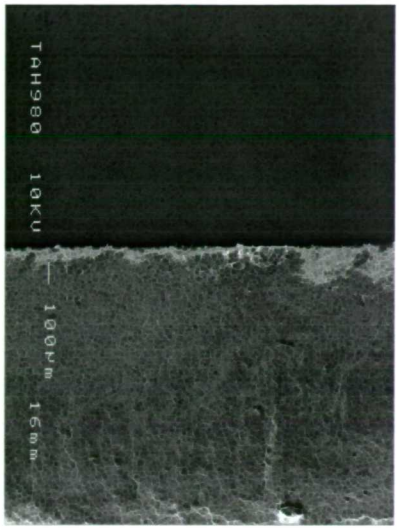

(a)

log*T*=3 $\left(\log(dc/dn)=-6.8\right)$

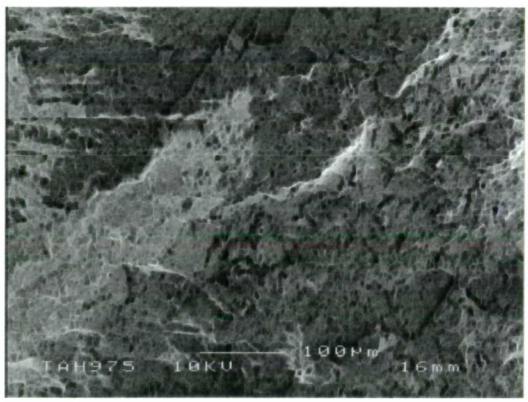

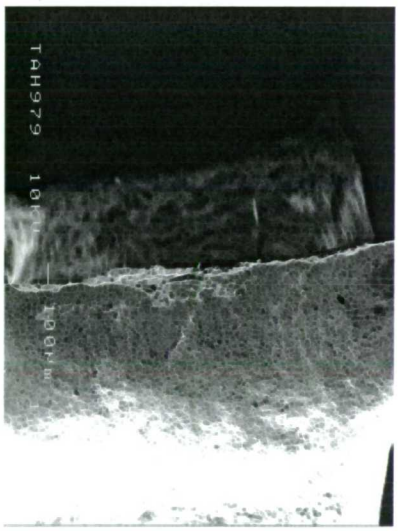

(b)

log*T*=3.1 $\left(\log(dc/dn)=-6.6\right)$

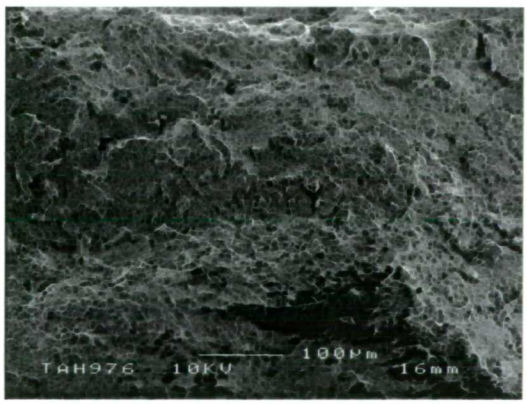

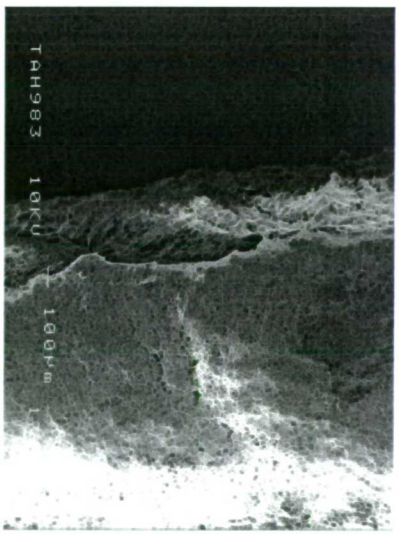

(c)

Figure 5-35 Micrographs of NR21, PS=150%.

Top views **Profile views**

log*T*=2.4 $\left(\log(dc/dn)=-9.7\right)$

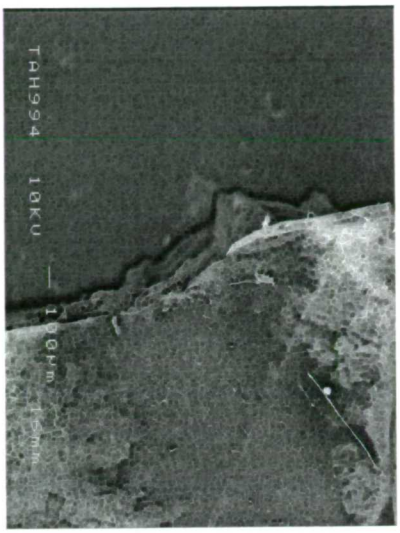

(a)

log*T*=3 $\left(\log(dc/dn)=-8.1\right)$

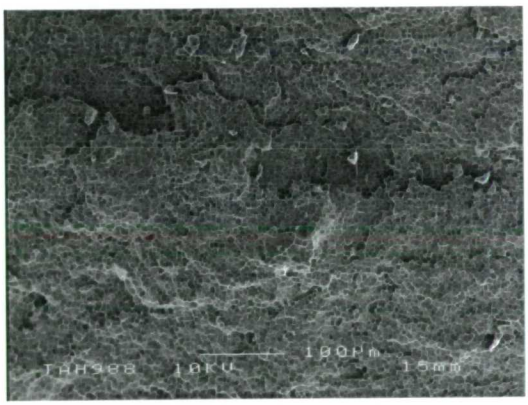

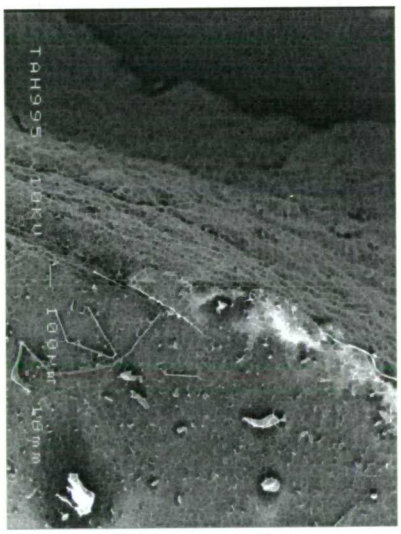

(b)

log*T*=3.5 $\left(\log(dc/dn)=-7.4\right)$

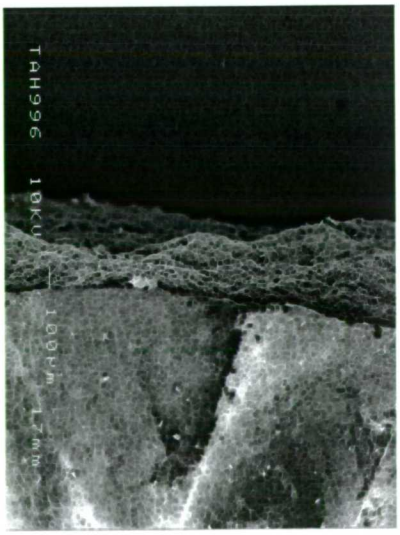

(c)

Figure 5-36 Micrographs of NR29, PS=0%.

Top views **Profile views**

log*T*=2.5 $\left(\log(dc/dn)=-8.2\right)$

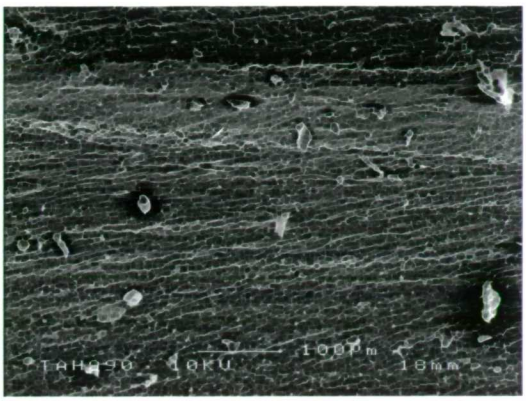

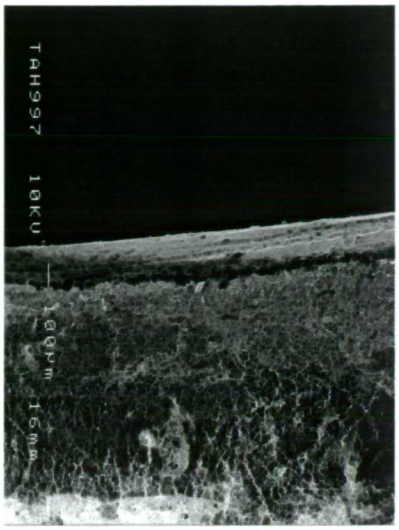

(a)

log*T*=3.1 $\left(\log(dc/dn)=-7.2\right)$

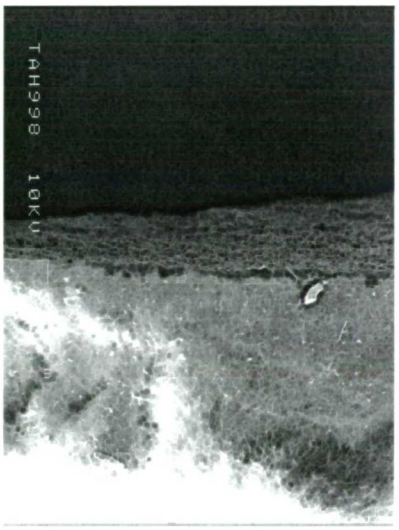

(b)

Figure 5-37 Micrographs of NR29, PS=25%.

Top views **Profile views**

log*T*=2.6 $\left(\log(dc/dn)=-7.6\right)$

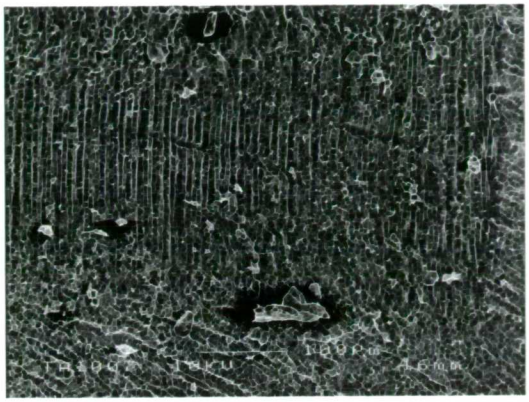

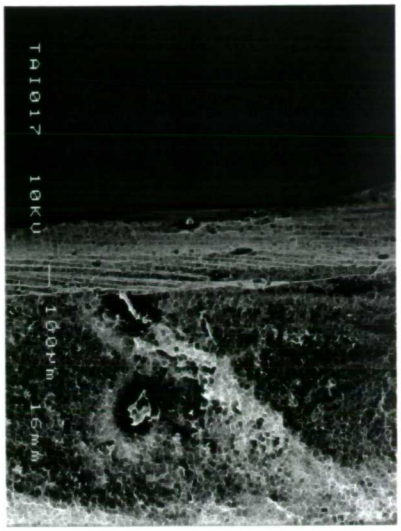

(a)

log*T*=3 $\left(\log(dc/dn)=-7.5\right)$

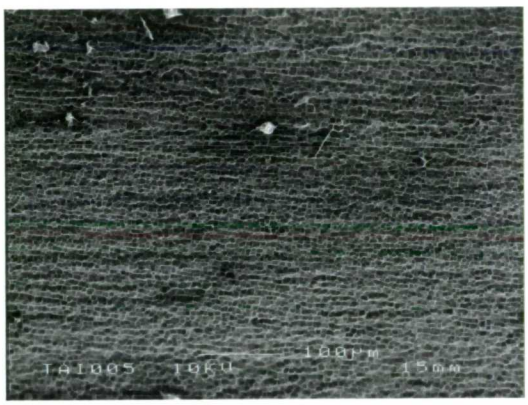

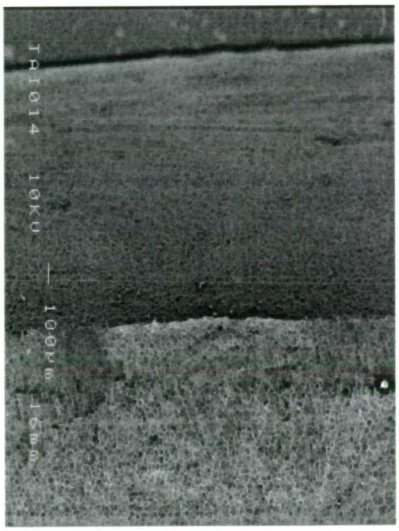

(b)

log*T*=3.4 $\left(\log(dc/dn)=-6.6\right)$

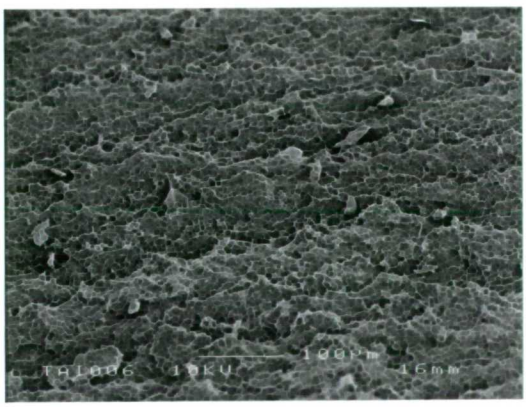

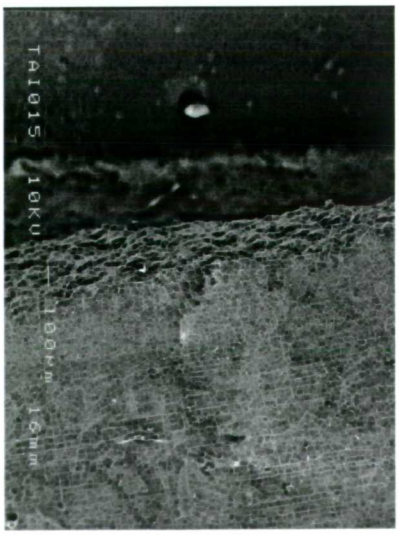

(c)

Figure 5-38 Micrographs of NR29, PS=50%.

Top views **Profile views**

log*T*=3 $\left(\log(dc/dn)=-7.5\right)$

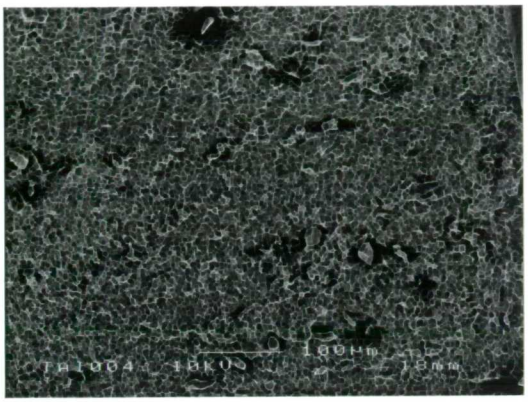

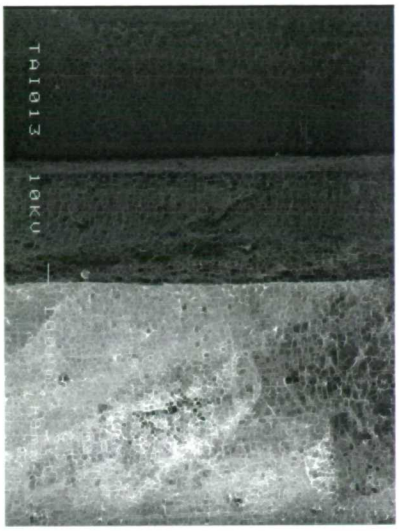

(a)

log*T*=3.5 $\left(\log(dc/dn)=-6.6\right)$

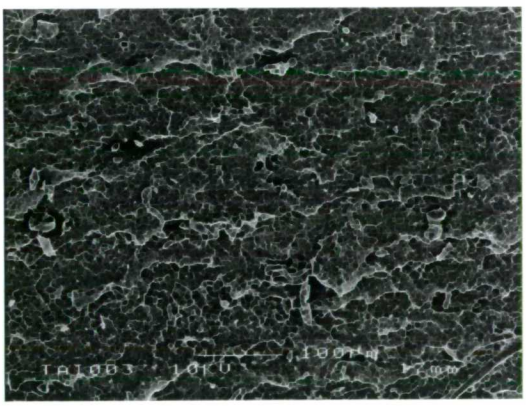

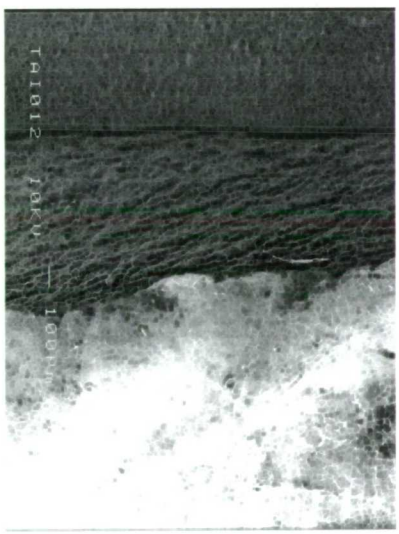

(b)

Figure 5-39 Micrographs of NR29, PS=75%.

Top views **Profile views**

log*T*=2.5 (log(d*c*/d*n*)=-7.7)

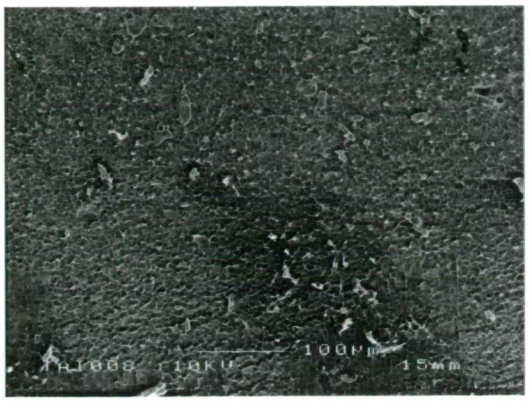

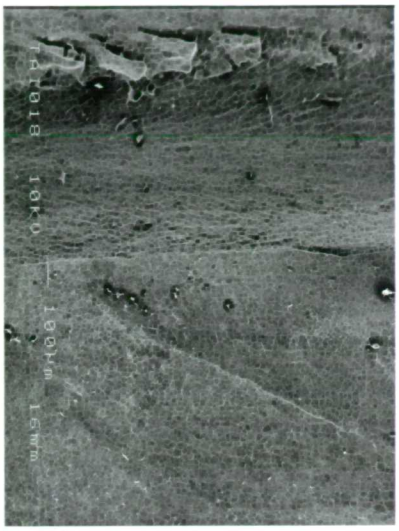

(a)

log*T*=2.9 (log(d*c*/d*n*)=-7.4)

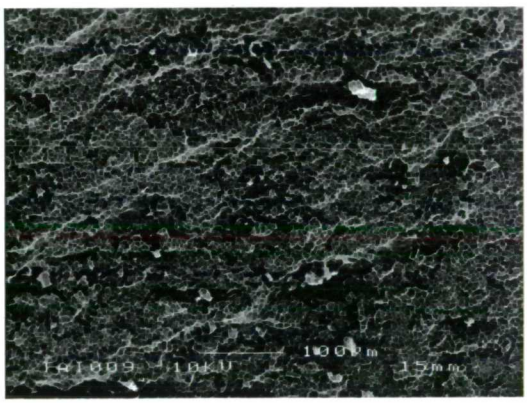

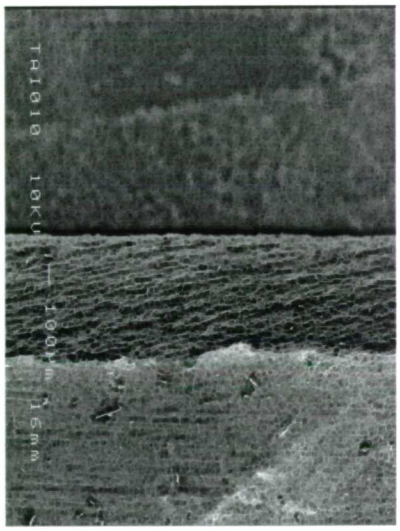

(b)

log*T*=3.4 (log(d*c*/d*n*)=-6.7)

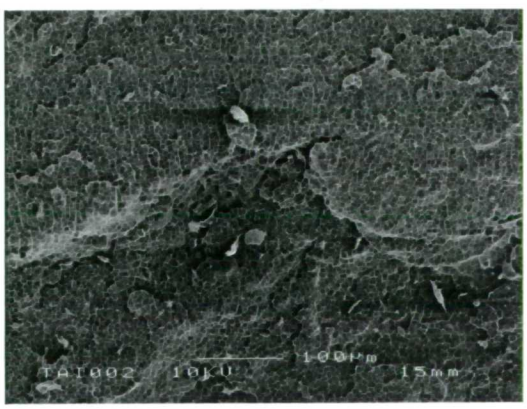

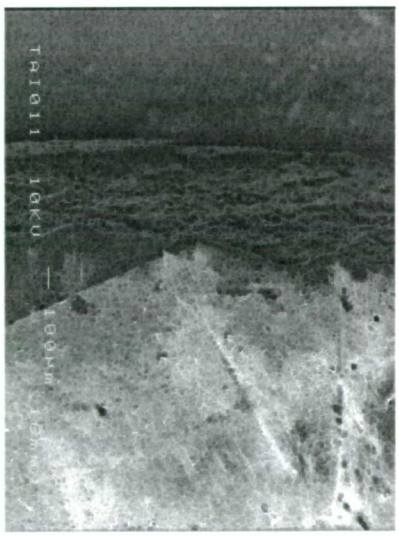

(c)

Figure 5-40 Micrographs of NR29, PS=100%.

Top views **Profile views**

log*T*=2.6 (log(d*c*/d*n*)=-7.7)

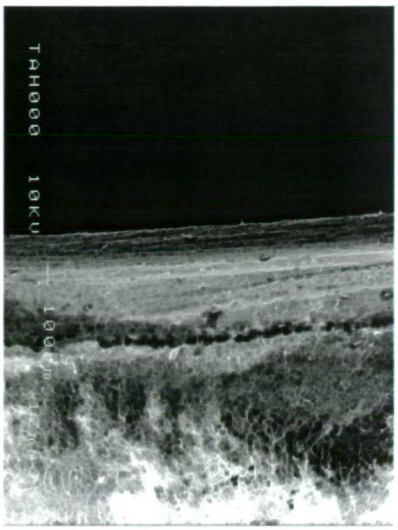

(a)

log*T*=3 (log(d*c*/d*n*)=-6.9)

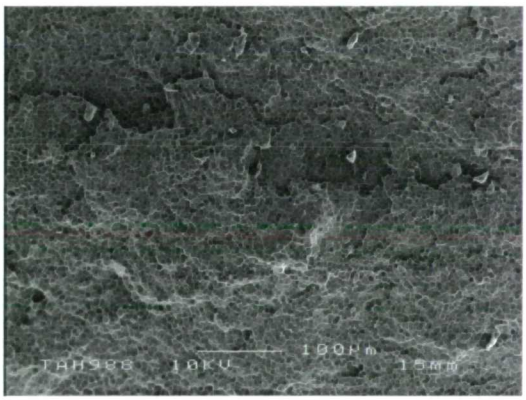

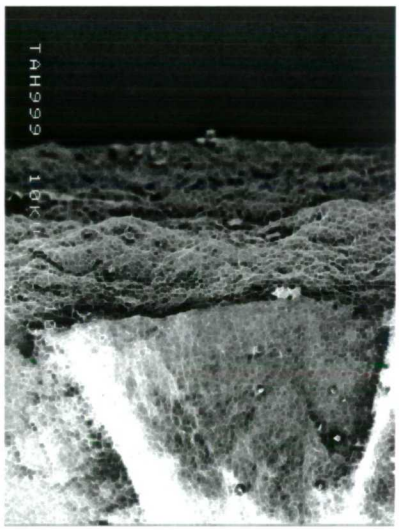

(b)

log*T*=3.4 (log(d*c*/d*n*)=-6.2)

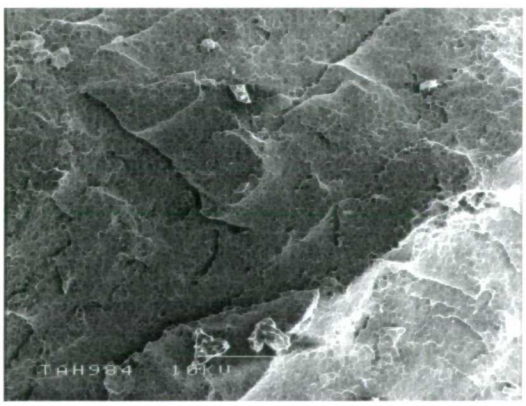

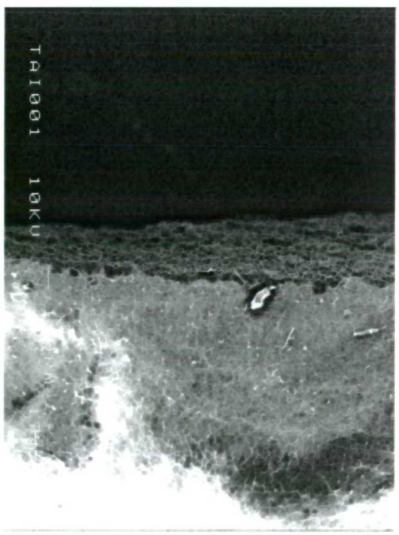

(c)

Figure 5-41 Micrographs of NR29, PS=150%.

Top views **Profile views**

log*T*=2.9 $\left(\log(dc/dn)=-8.7\right)$

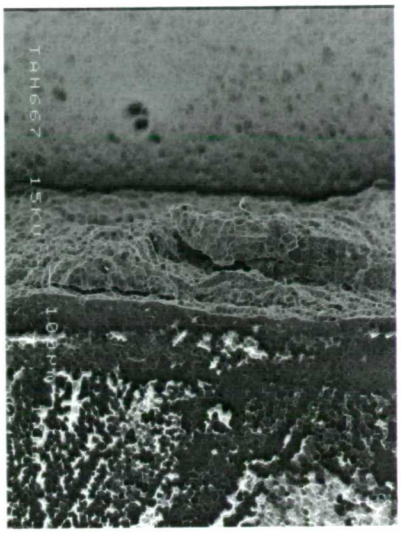

(a)

log*T*=3.5 $\left(\log(dc/dn)=-8\right)$

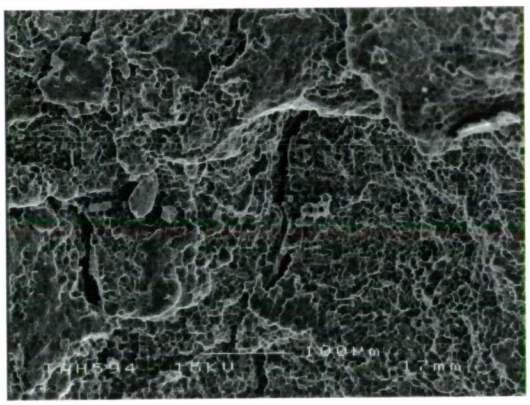

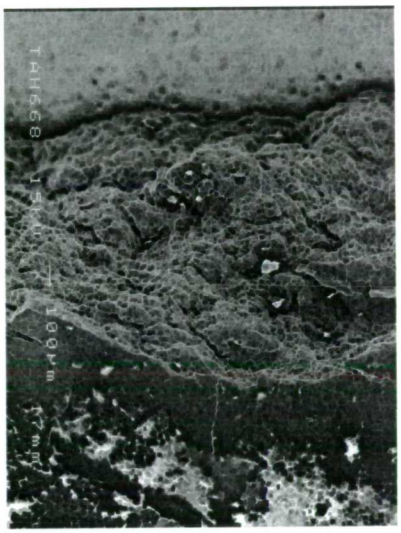

(b)

log*T*=3.7 $\left(\log(dc/dn)=-6.5\right)$

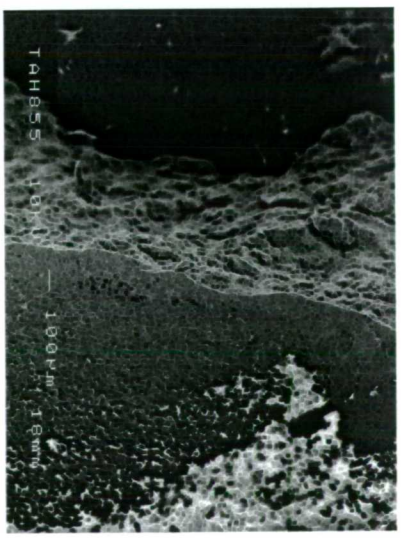

(c)

Figure 5-42 Micrographs of NR59, PS=0%.

Top views **Profile views**

log*T*=3 (log(d*c*/d*n*)=-8.3)

(a)

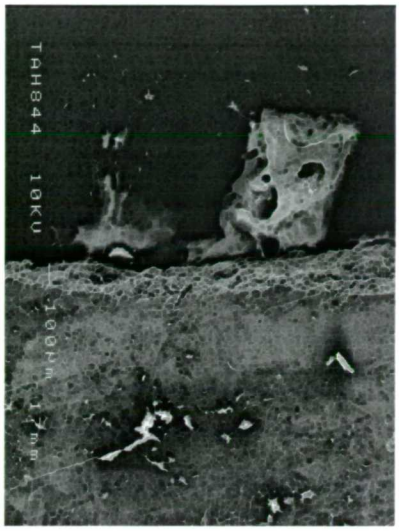

log*T*=3.5 (log(d*c*/d*n*)=-6.6)

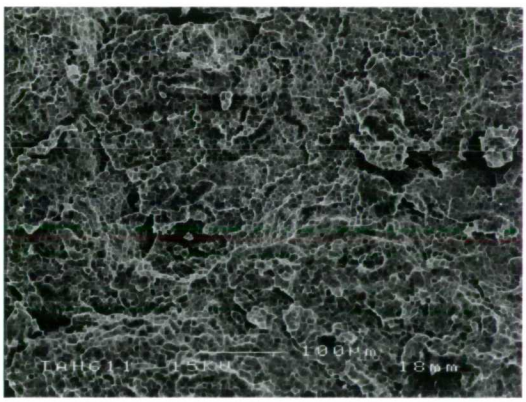

(b)

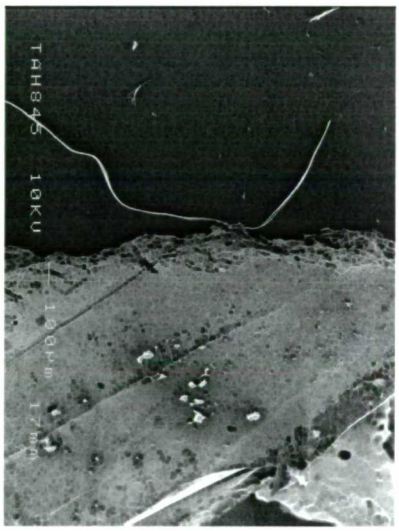

log*T*=4 (log(d*c*/d*n*)=-6)

(c)

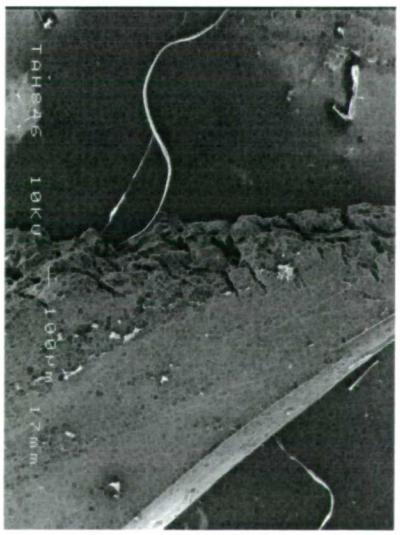

Figure 5-43 Micrographs of NR59, PS=25%.

Top views **Profile views**

log*T*=3 (log(d*c*/d*n*)=-8.2)

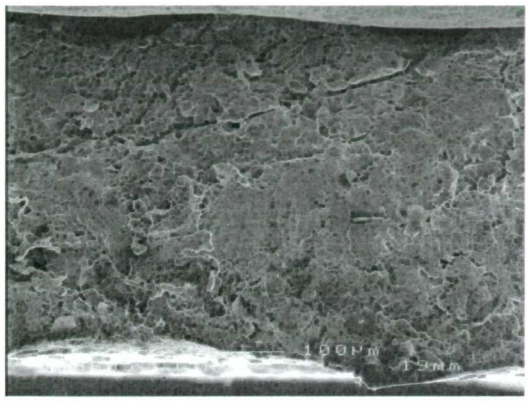

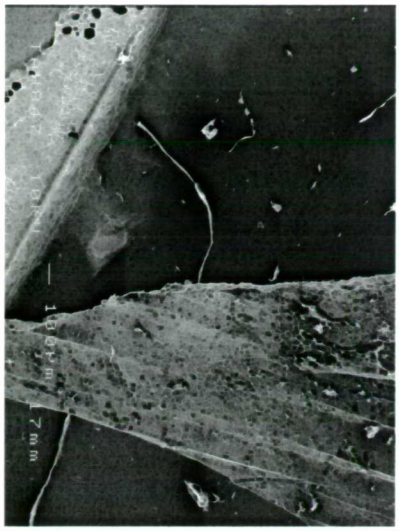

(a)

log*T*=3.6 (fast crack growth)

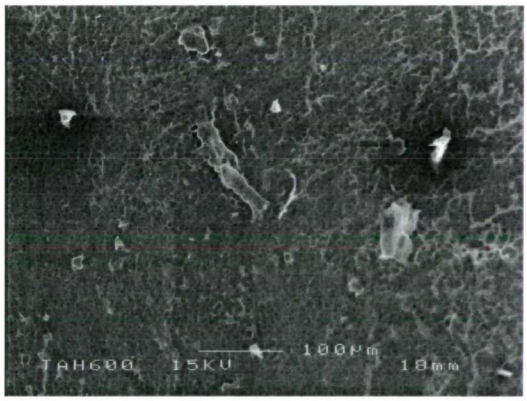

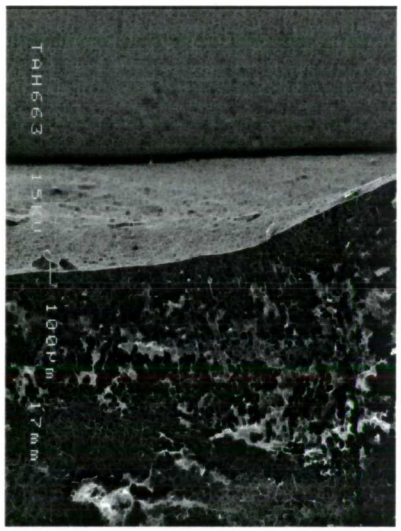

(b)

log*T*=3.6 (slow crack growth: log(d*c*/d*n*)=-6.2)

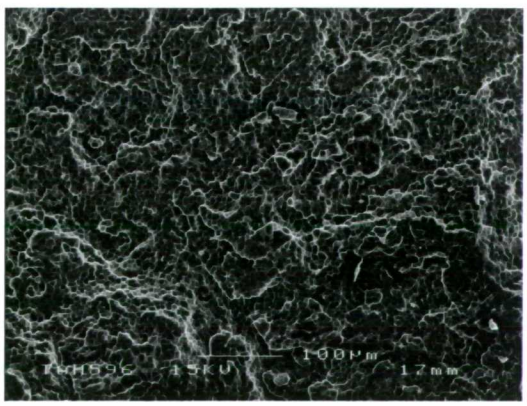

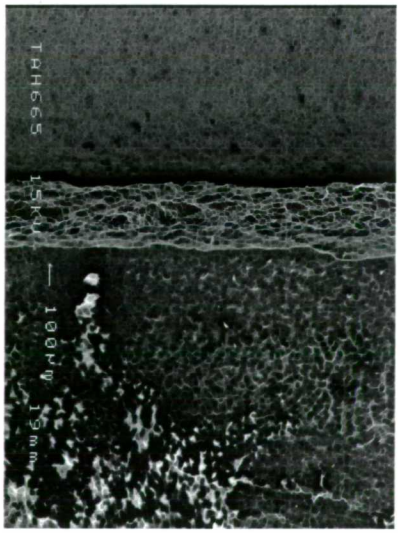

(c)

log*T*=3.8 $\left(\log(dc/dn)=-5.8\right)$

(d)

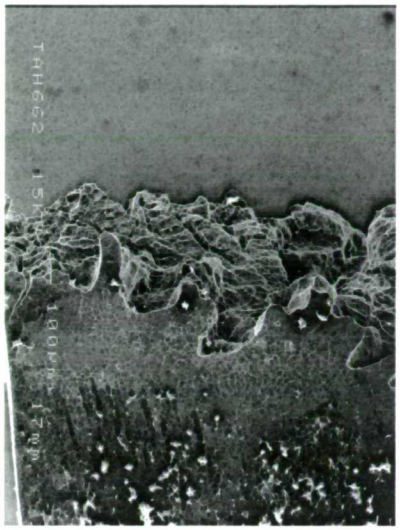

Figure 5-44 Micrographs of NR59, PS=50%.

Top views **Profile views**

log*T*=2.3 $\left(\log(dc/dn)=-8.7\right)$

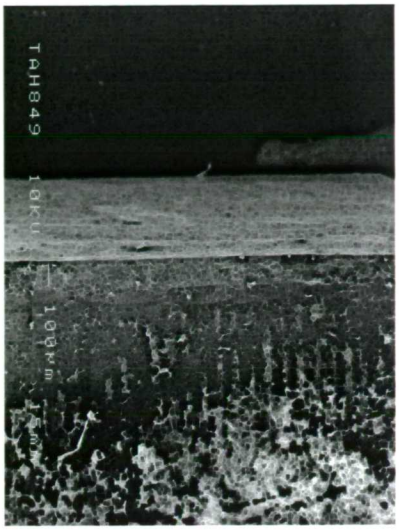

(a)

log*T*=3 $\left(\log(dc/dn)=-7.7\right)$

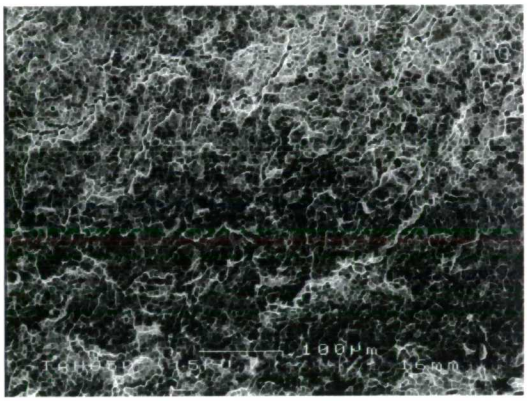

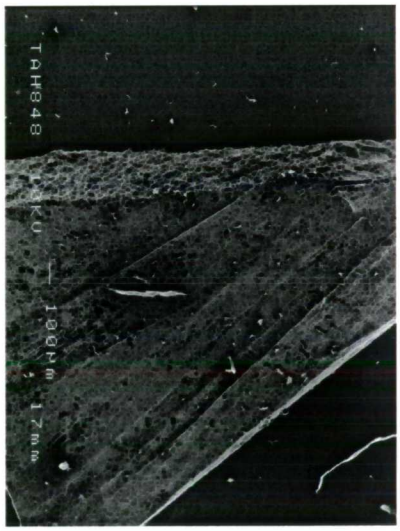

(b)

log*T*=3.2 $\left(\log(dc/dn)=-5.6\right)$

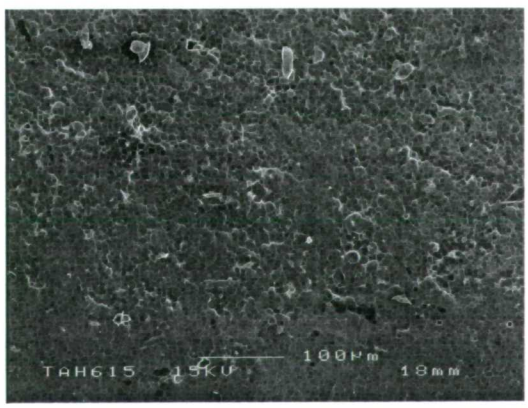

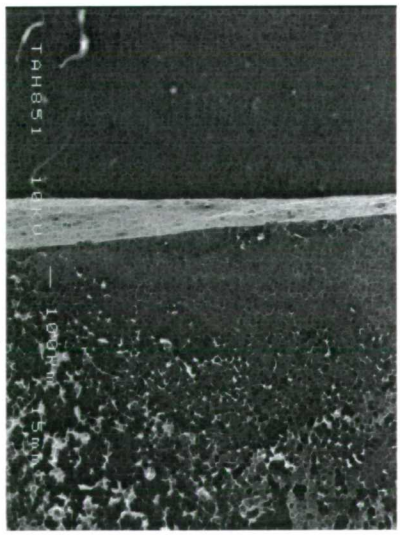

(c)

Figure 5-45 Micrographs of NR59, PS=75%.

Top views **Profile views**

log*T*=2.1 $\left(\log(dc/dn)=-8.4\right)$

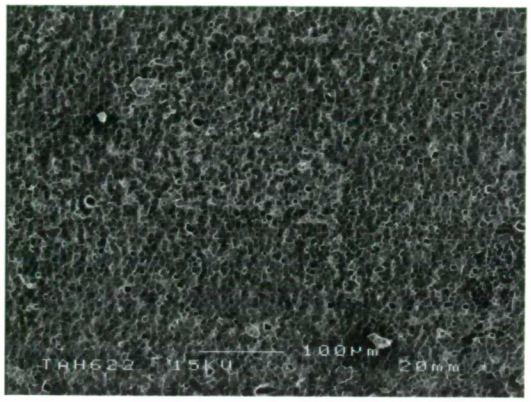

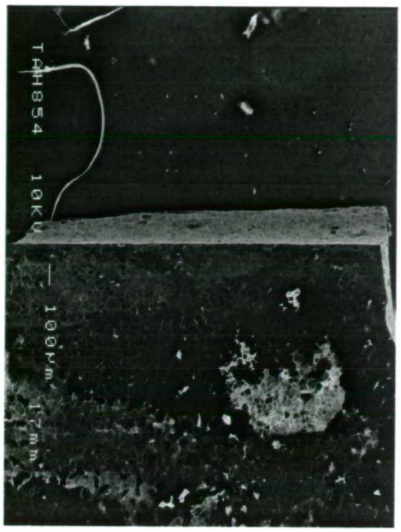

(a)

log*T*=2.5 $\left(\log(dc/dn)=-8.1\right)$

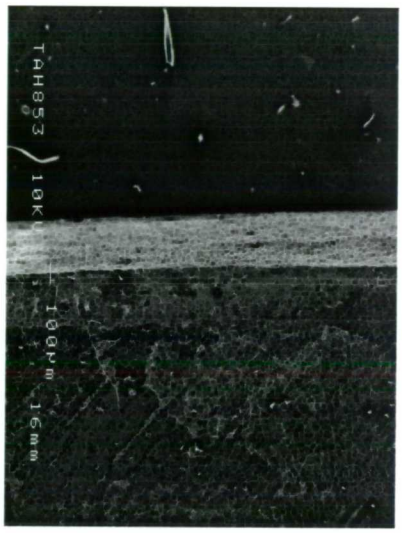

(b)

log*T*=2.9 $\left(\log(dc/dn)=-4.9\right)$

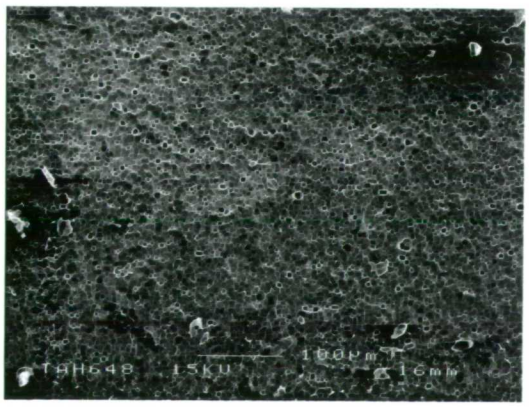

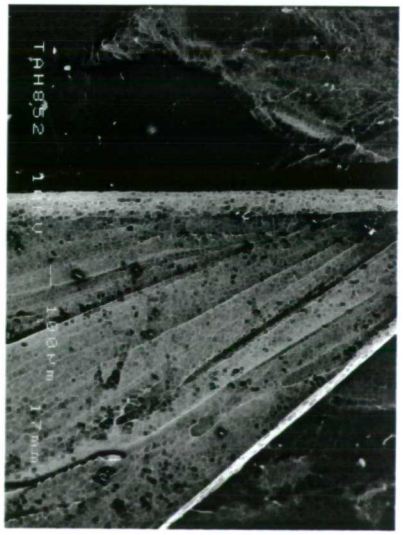

(c)

Figure 5-46 Micrographs of NR59, PS=100%.

Top views **Profile views**

log*T*=2.3 (log(d*c*/d*n*)=-8.4)

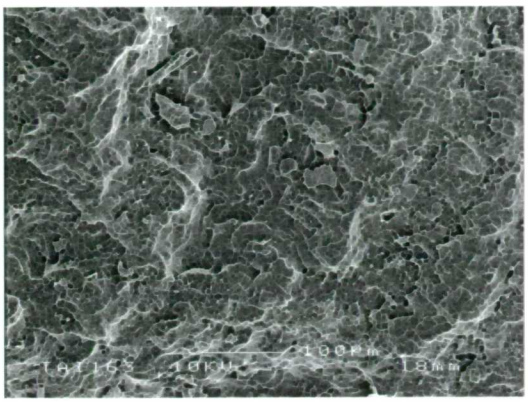

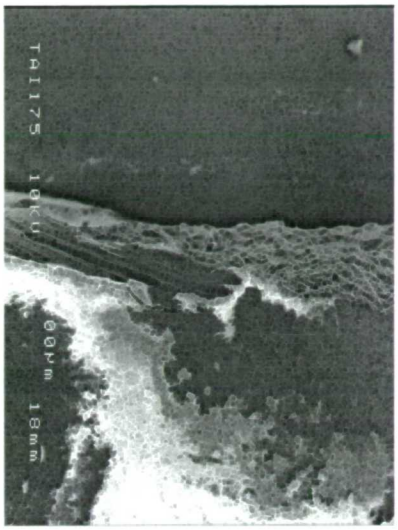

(a)

log*T*=2.6 (log(d*c*/d*n*)=-7.5)

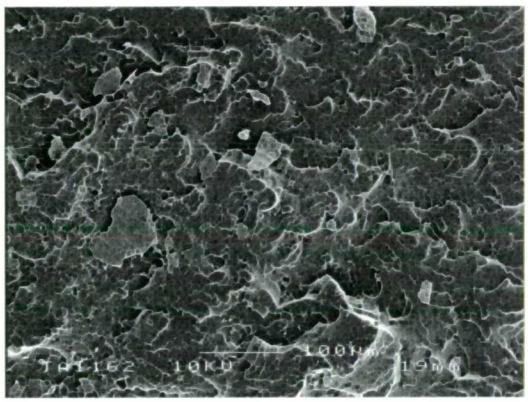

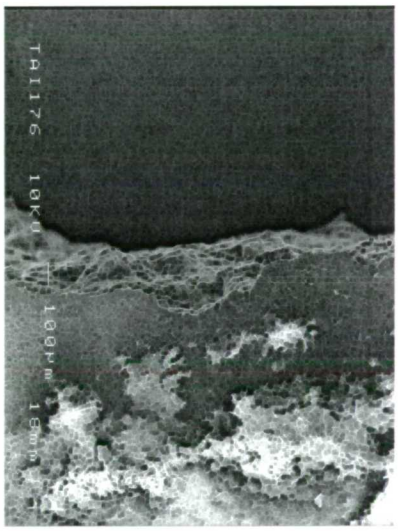

(b)

log*T*=3.1 (log(d*c*/d*n*)=-6.1)

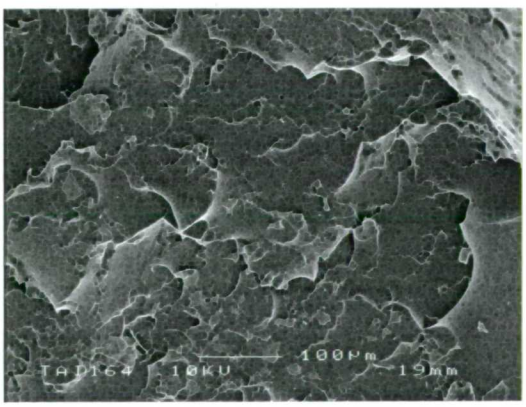

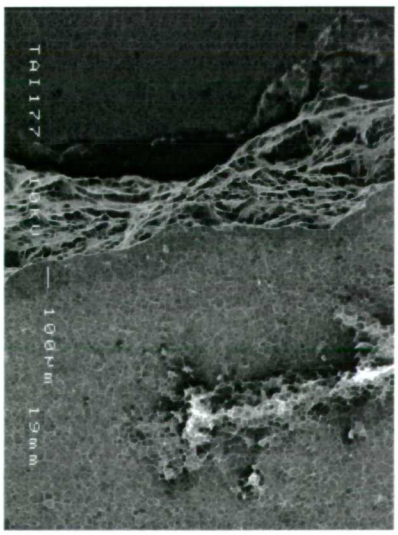

(c)

Figure 5-47 Micrographs of SBR0, PS=0%.

Top views **Profile views**

log*T*=1.8 (log(d*c*/d*n*)=-8.8)

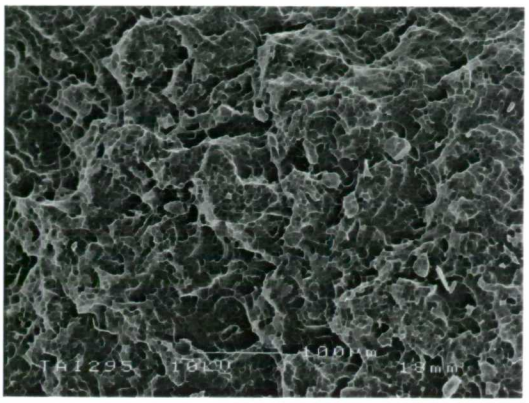

(a)

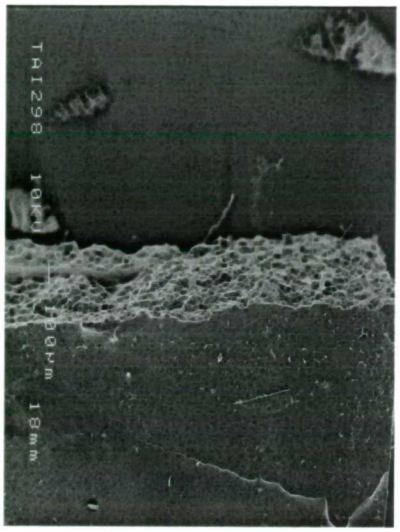

log*T*=2.2 (log(d*c*/d*n*)=-8.1)

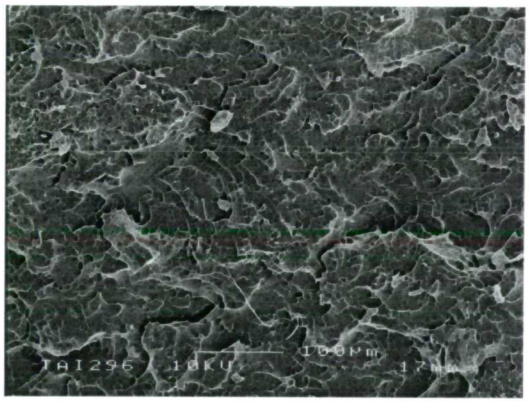

(b)

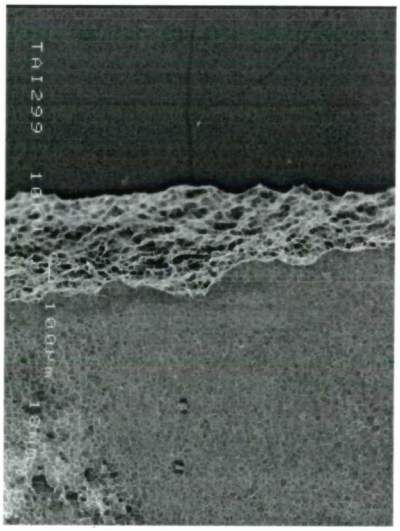

log*T*=2.5 (log(d*c*/d*n*)=-7.7)

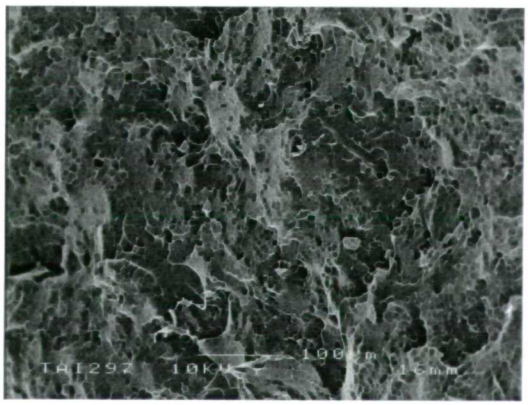

(c)

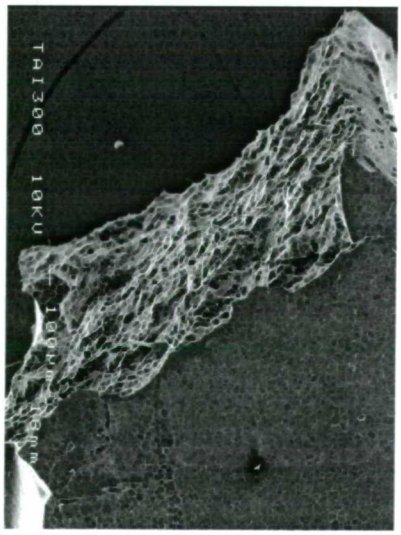

Figure 5-48 Micrographs of SBR0, PS=38%.

Top views **Profile views**

log*T*=2.6 $\left(\log(dc/dn)=-8.7\right)$

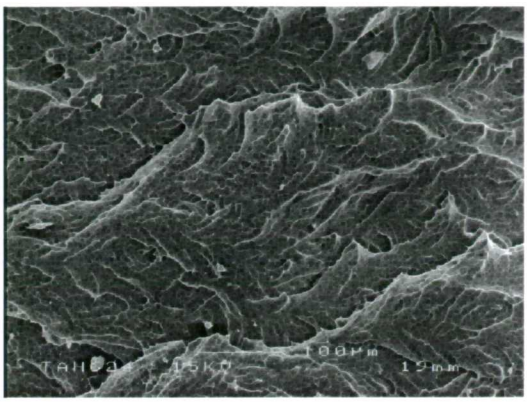

(a)

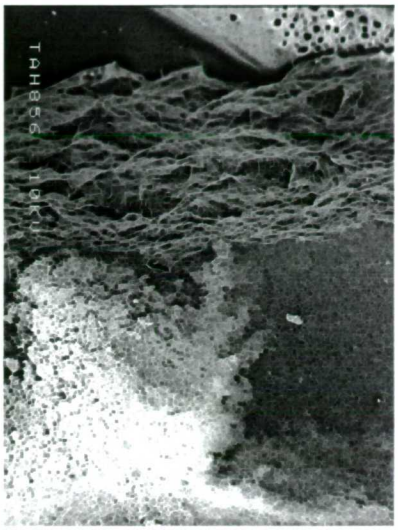

log*T*=3 $\left(\log(dc/dn)=-7.7\right)$

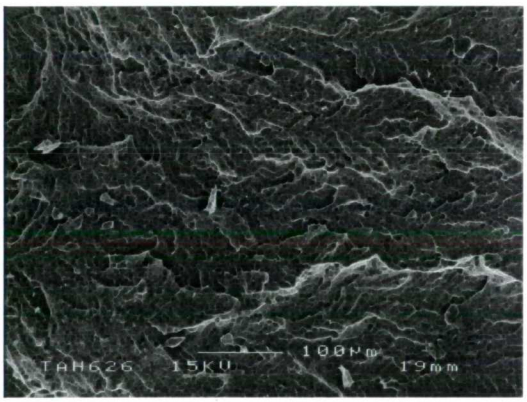

(b)

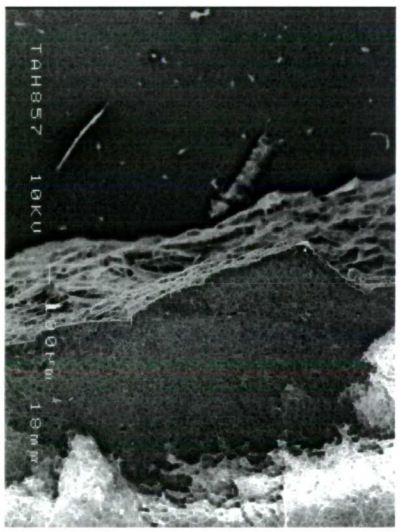

log*T*=3.3 $\left(\log(dc/dn)=-6.4\right)$

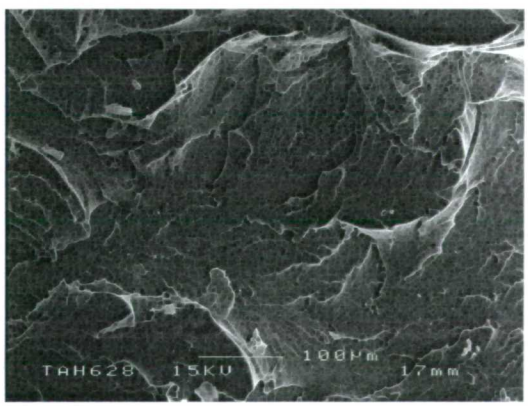

(c)

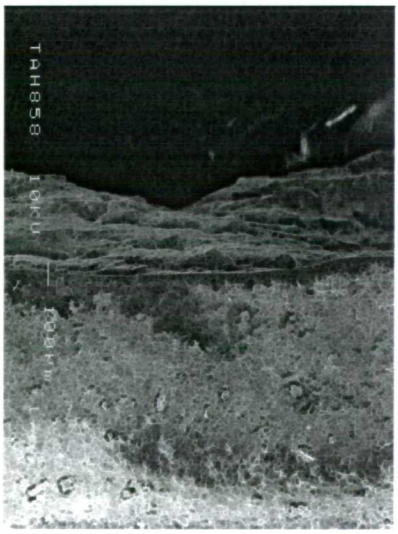

Figure 5-49 Micrographs of SBR30, PS=0%.

Top views **Profile views**

log*T*=2.5 $\left(\log(dc/dn)=-8.2\right)$

(a)

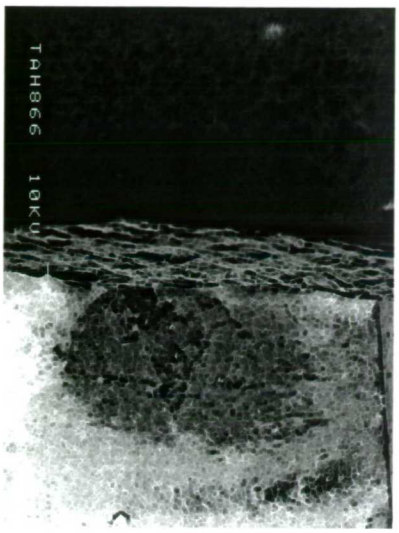

log*T*=3 $\left(\log(dc/dn)=-7.2\right)$

(b)

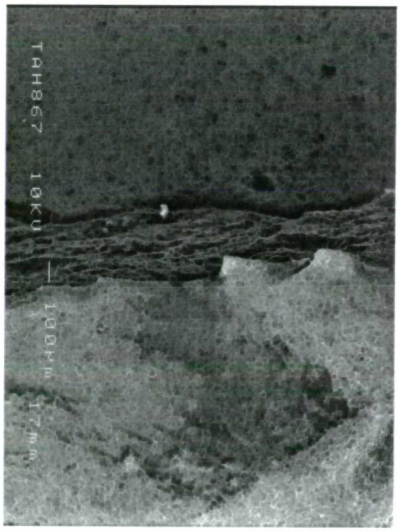

log*T*=3.4 $\left(\log(dc/dn)=-6.5\right)$

(c)

Figure 5-50 Micrographs of SBR30, PS=25%.

Top views **Profile views**

log*T*=2.5 (log(d*c*/d*n*)=-8)

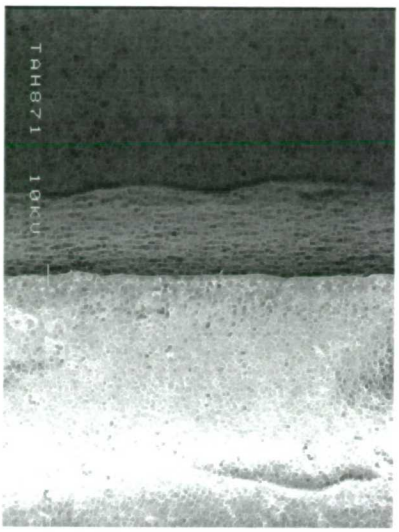

(a)

log*T*=2.9 (log(d*c*/d*n*)=-7.2)

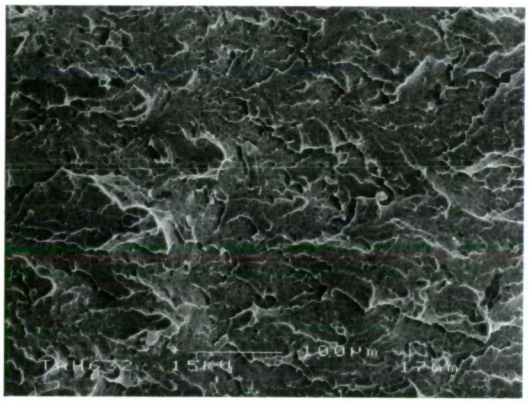

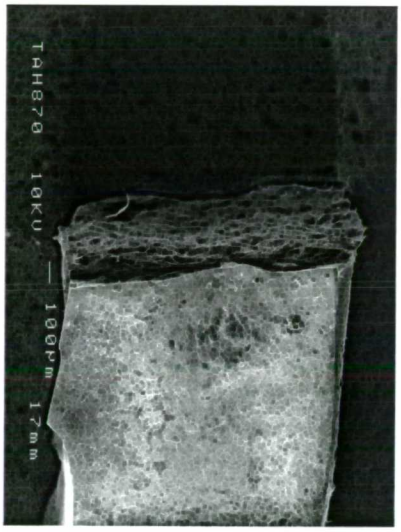

(b)

log*T*=3.3 (log(d*c*/d*n*)=-6.6)

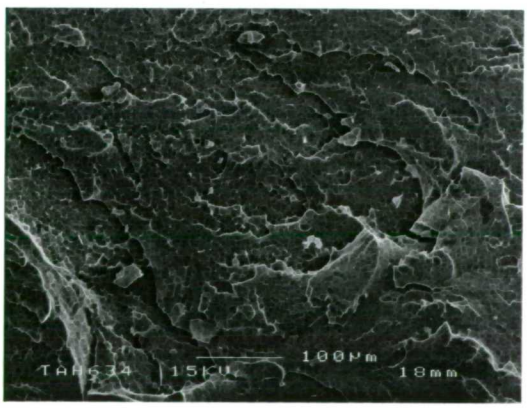

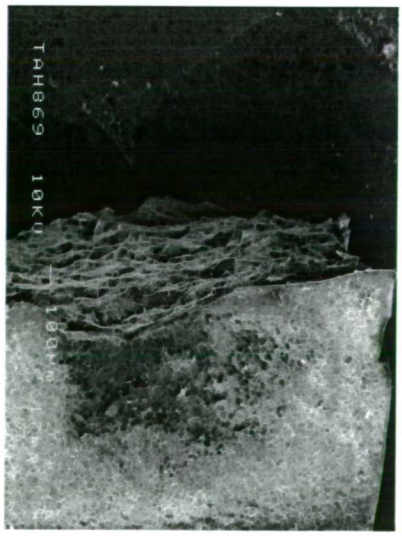

(c)

Figure 5-51 Micrographs of SBR30, PS=50%.

Top views **Profile views**

log*T*=2.2 $\left(\log(dc/dn)=-8.3\right)$

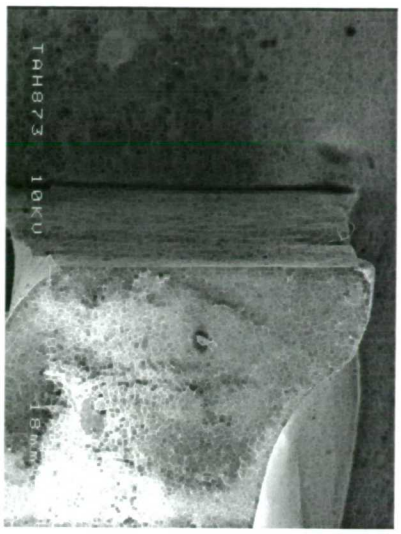

(a)

log*T*=2.5 $\left(\log(dc/dn)=-7.9\right)$

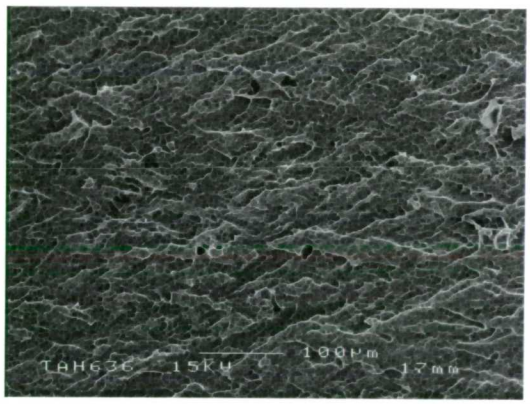

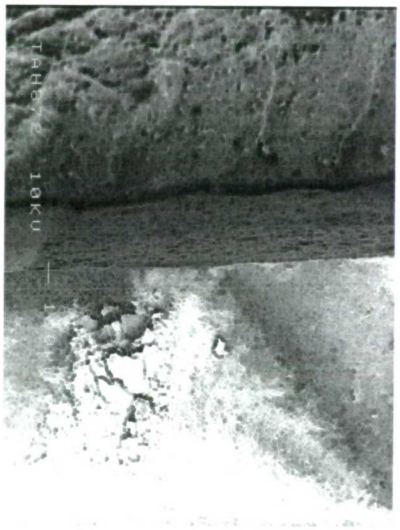

(b)

log*T*=2.8 $\left(\log(dc/dn)=-7.3\right)$

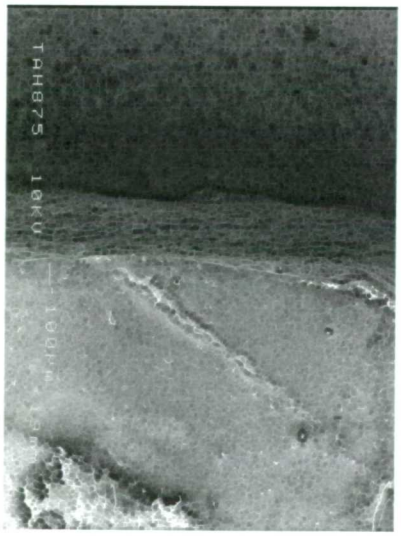

(c)

Figure 5-52 Micrographs of SBR30, PS=75%.

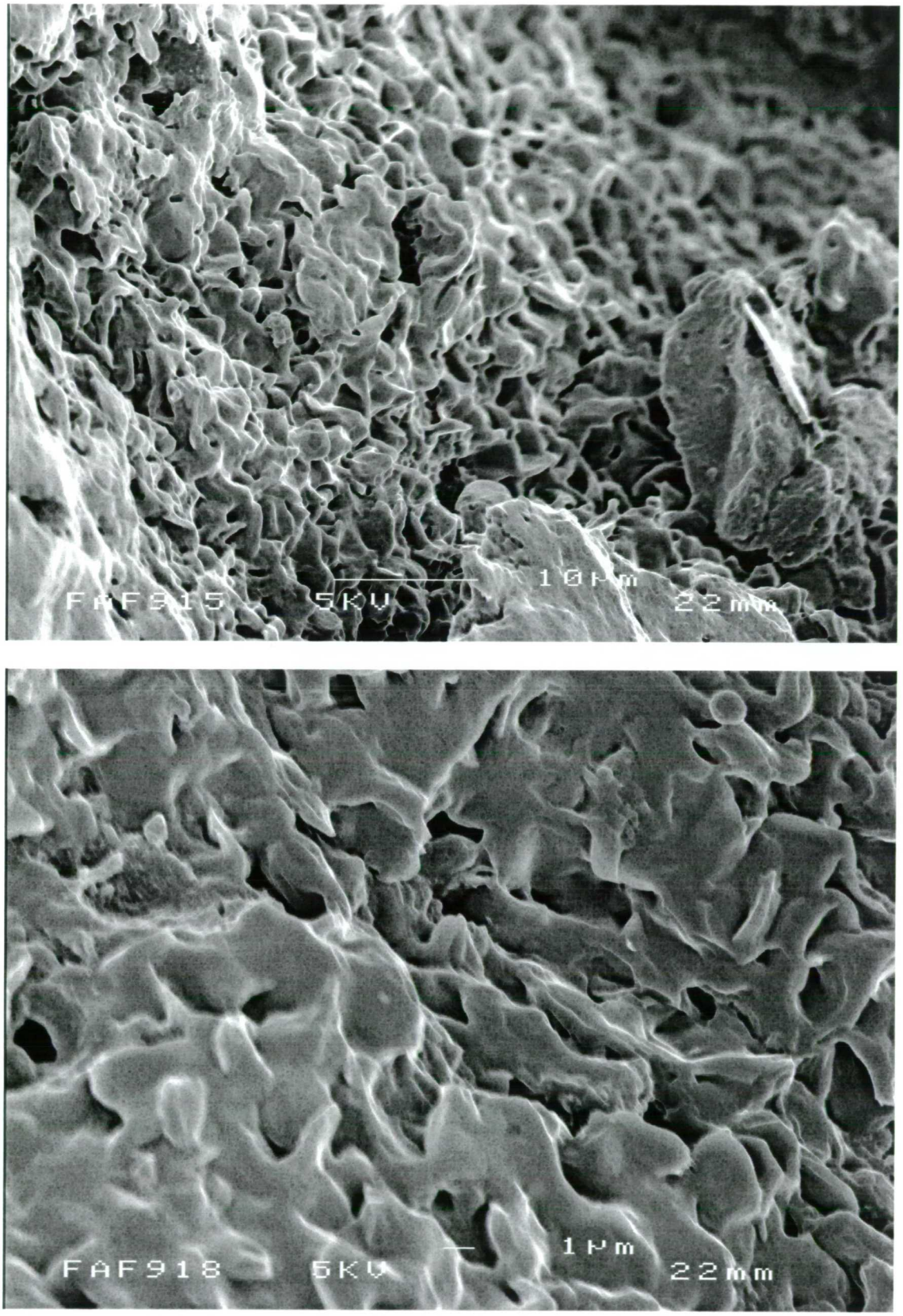

Figure 5-53 Micrographs of NR59, PS=0%, log$T$=3.6 showing smooth rounded features on the flanks of the crevasses.

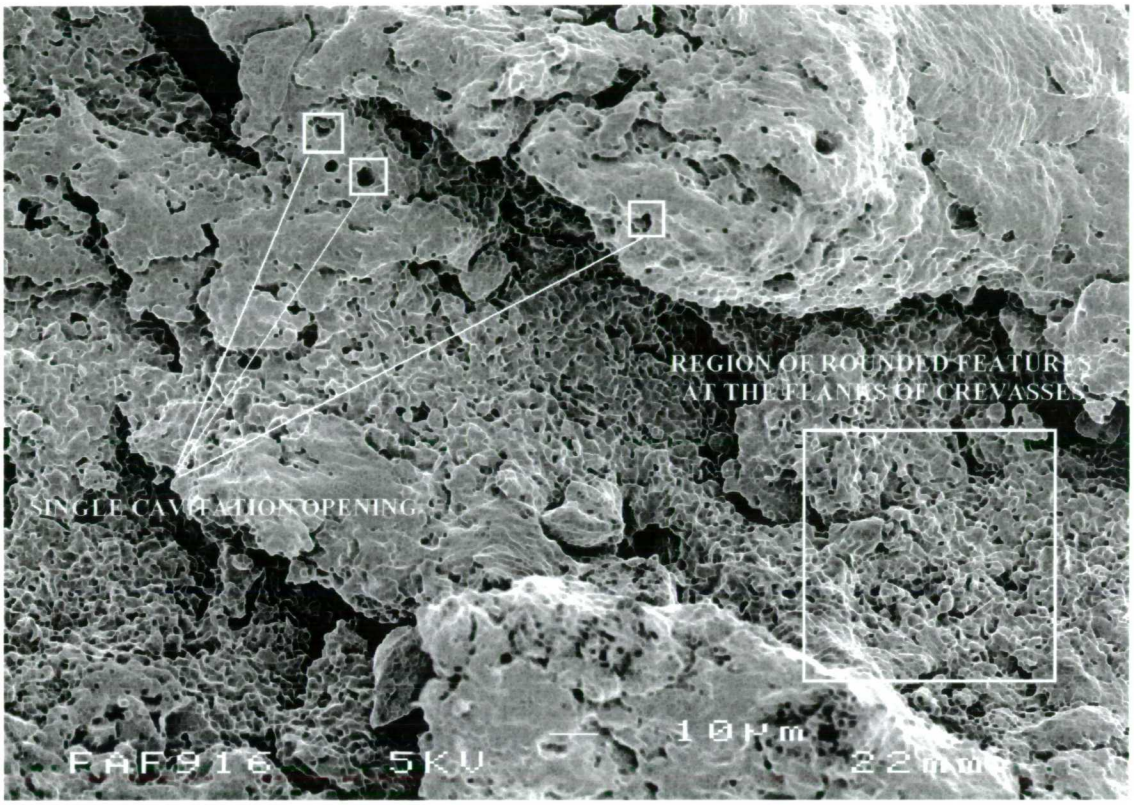

Figure 5-54 The rounded features observed on the flanks of the crevasses seem to have been formed from the same mechanism as the one responsible for the single cavities shown on the micrographs (NR59, PS=0%, log$T$=3.6) in Figure 5-53.

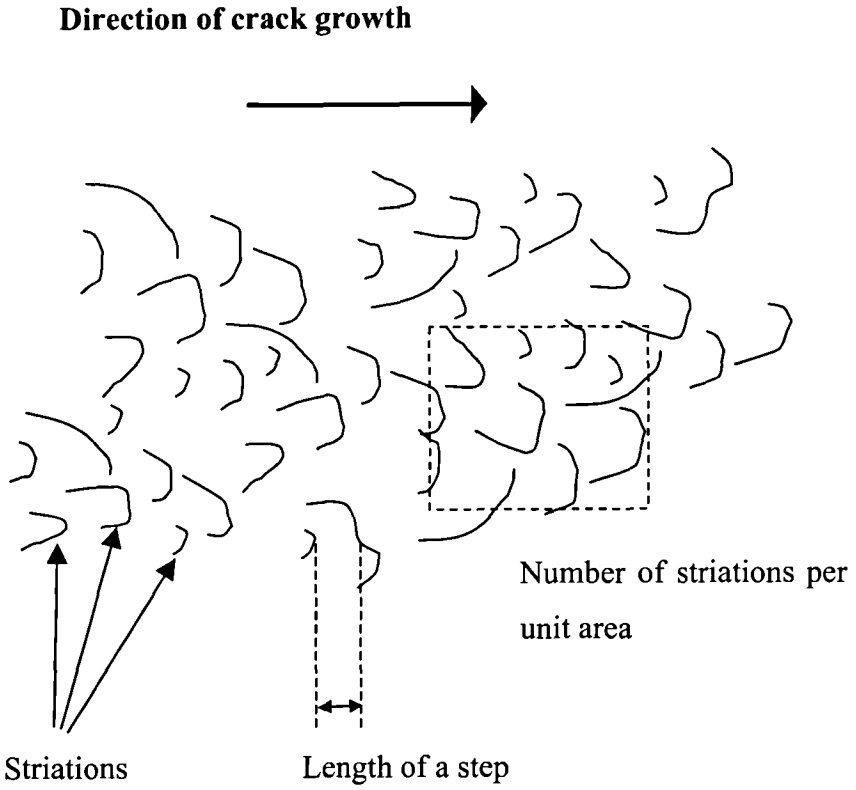

Figure 5-55 Schematic of the fracture surface morphology seen on the top view of a micrograph. This top view can be qualitatively described with either the number of striations per unit area or the length of a step.

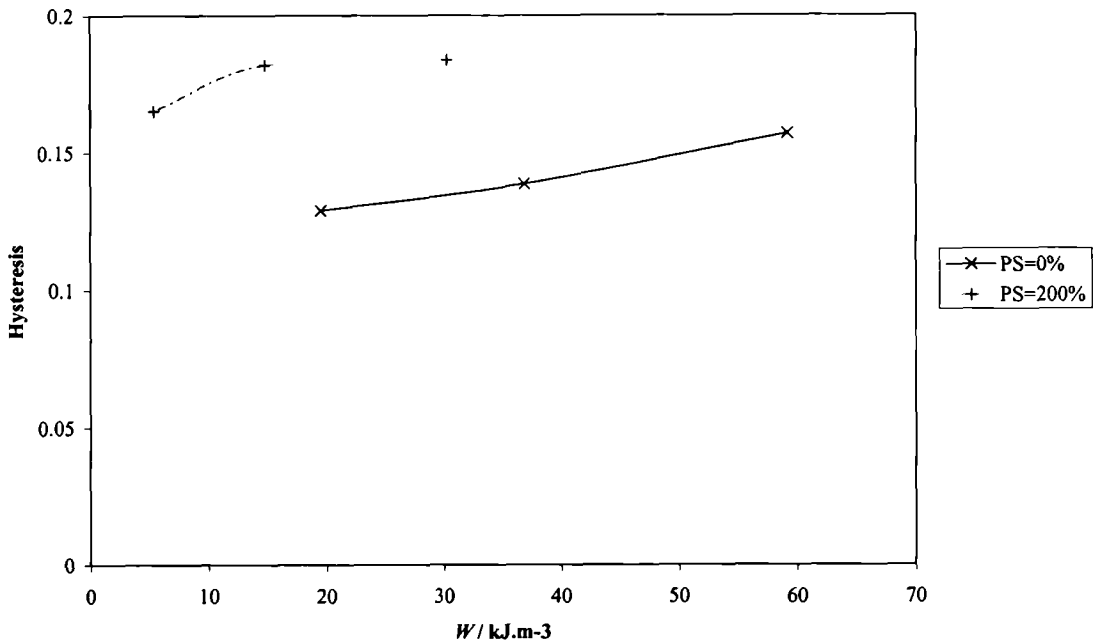

Figure 5-56 Increase of the hysteresis (energy lost/energy on loading) from pure shear (PS=0%) to PS=200% at small strains, for NR0.

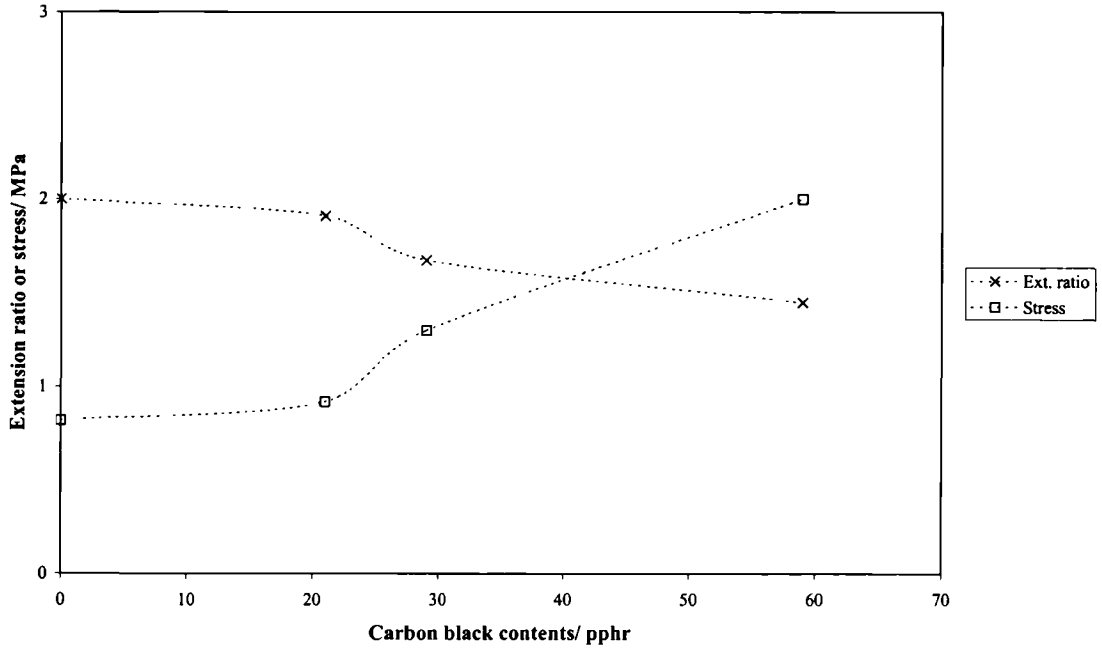

Figure 5-57 Evolution of the extension ratio and stress as a function of the carbon black content, for a constant elastic strain energy density, W=0.54 MPa (or T=10800 J.m^{-2})

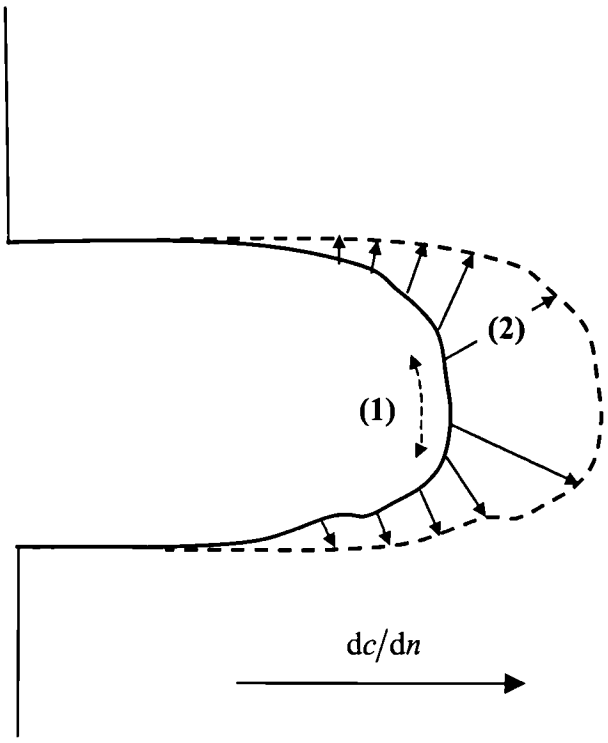

Figure 5-58 Region ahead of the crack tip going through a high strain cycle: **(1)** the loading of the material up to the breaking point; **(2)** relaxation of the material as the crack grows. The rate of loading in **(1)** is directly related to the crack growth rate dc/dn.

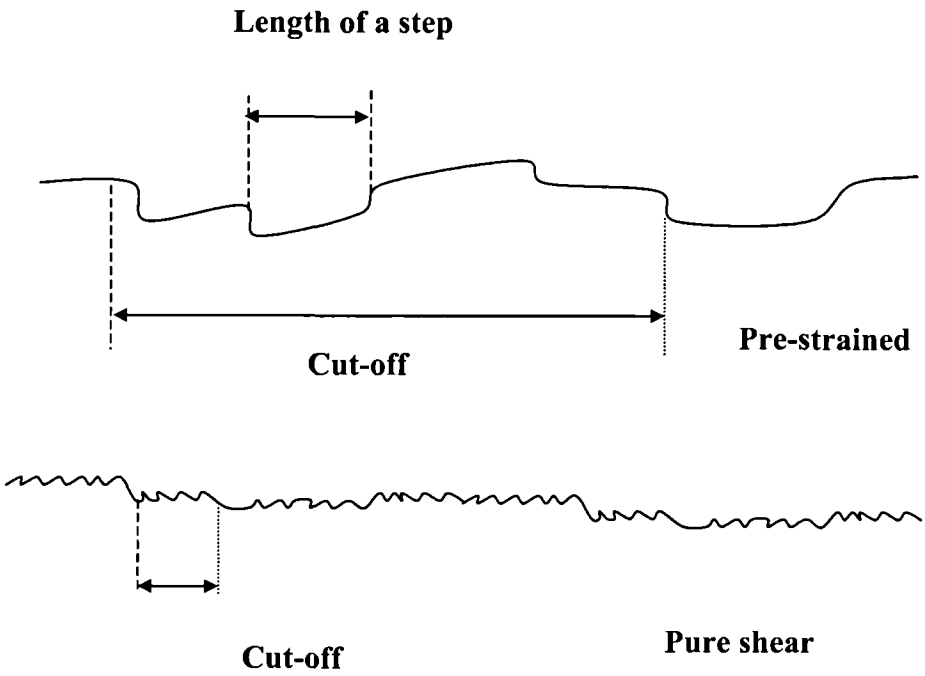

Figure 5-59 Illustrations showing the evolution of the profile fracture surfaces between a pre-strained and a pure shear (PS=0%) sample. The pre-strained samples exhibit smoother surfaces on a small scale (the length of a step) but coarser surfaces on a bigger scale (comparison of profile views). The cut-off wavelengths refer to the measurement of R_q described in 3.7.3.

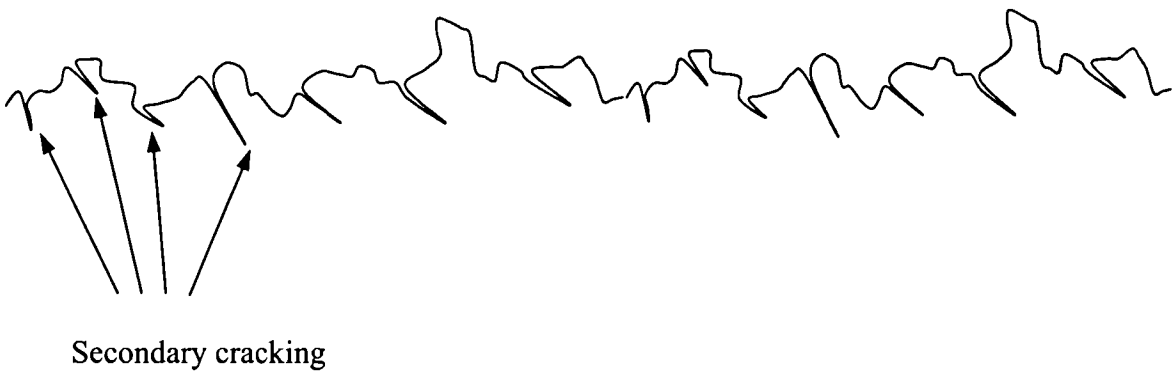

Figure 5-60 Illustrations showing the secondary cracking observed on the profile fracture surfaces of NR59, PS=0%, shown in Figure 5-42.

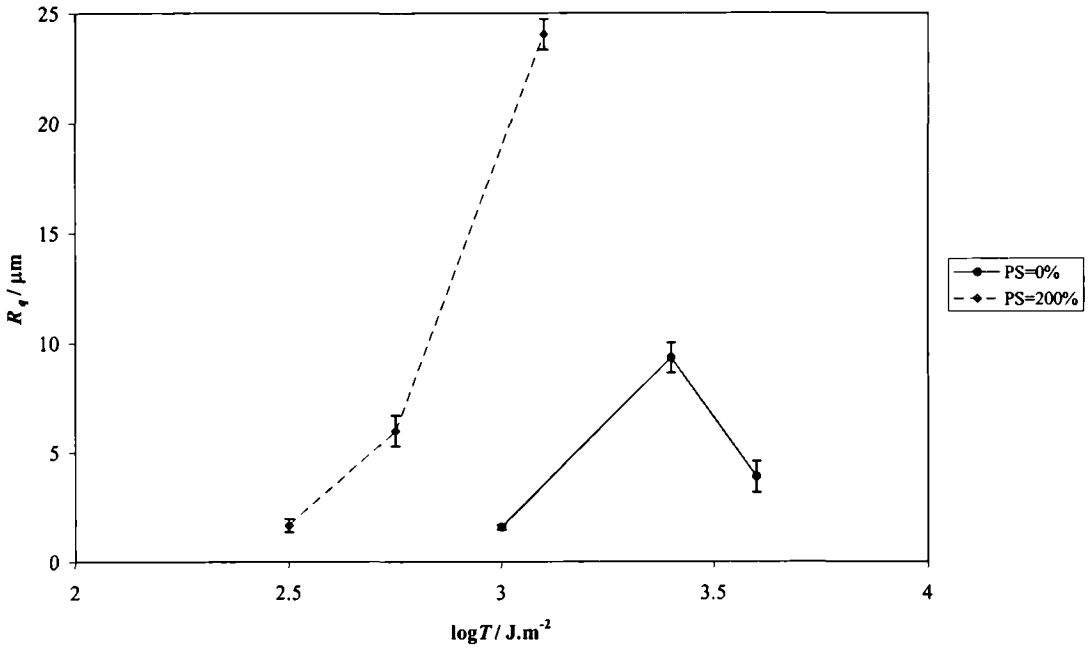

Figure 5-61 Roughness measurement (R_q) as a function of the tearing energy for a range of pre-strains (PS), for NR0.

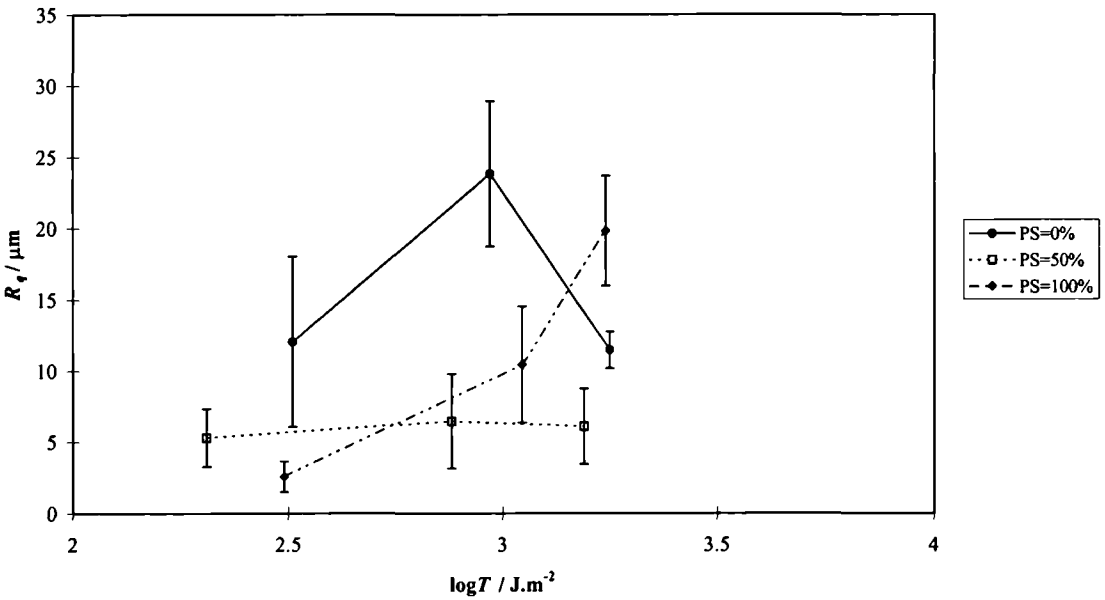

Figure 5-62 Roughness measurement (R_q) as a function of the tearing energy for a range of pre-strains (PS), for NR21.

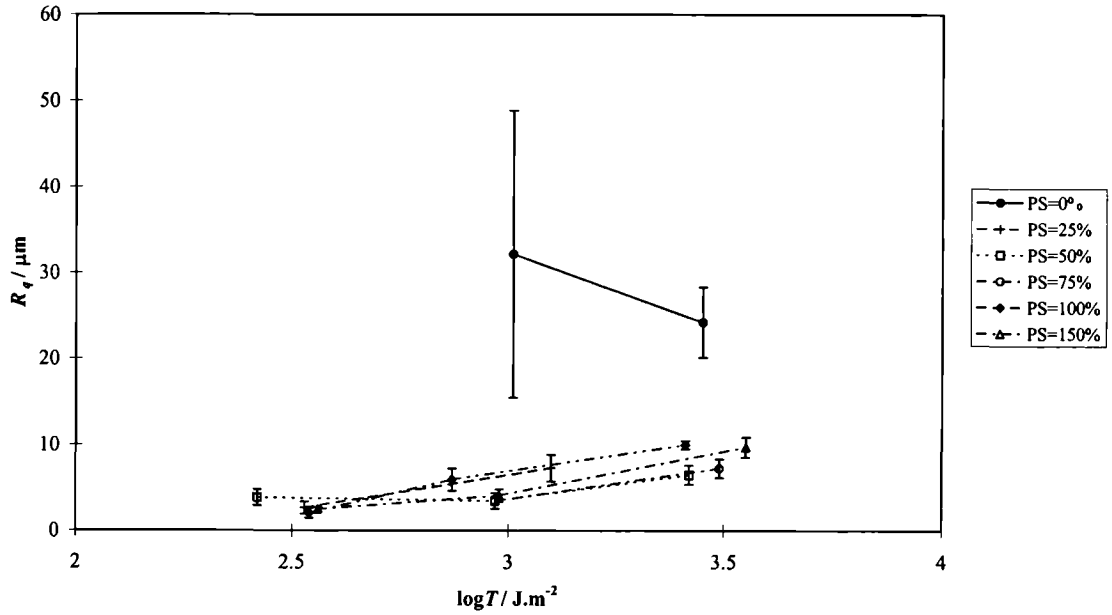

Figure 5-63 Roughness measurement (R_q) as a function of the tearing energy for a range of pre-strains (PS), for NR29.

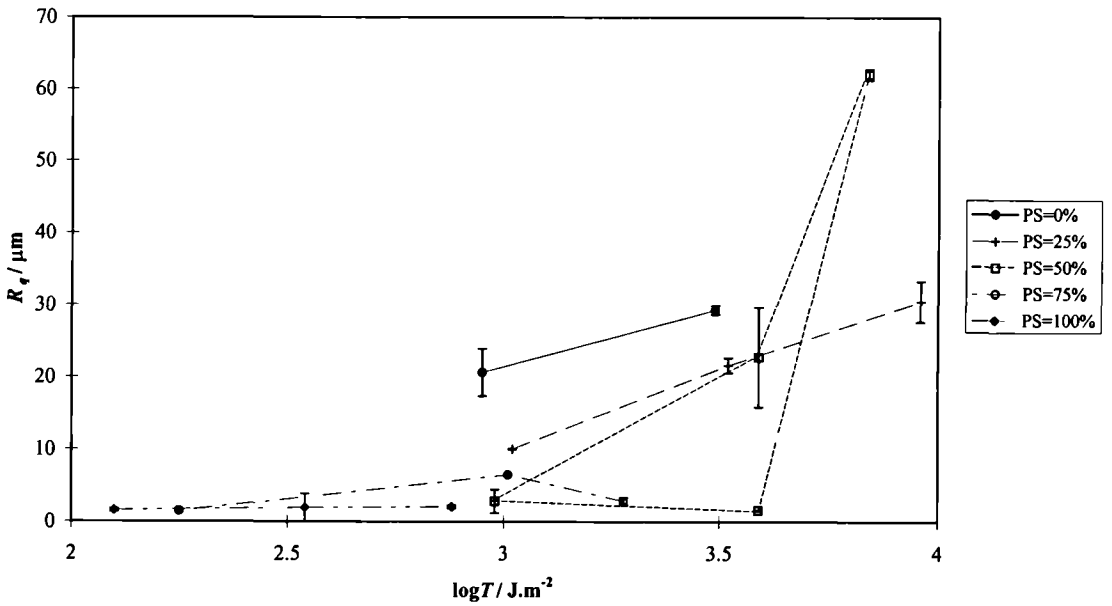

Figure 5-64 Roughness measurement (R_q) as a function of the tearing energy for a range of pre-strains (PS), for NR59.

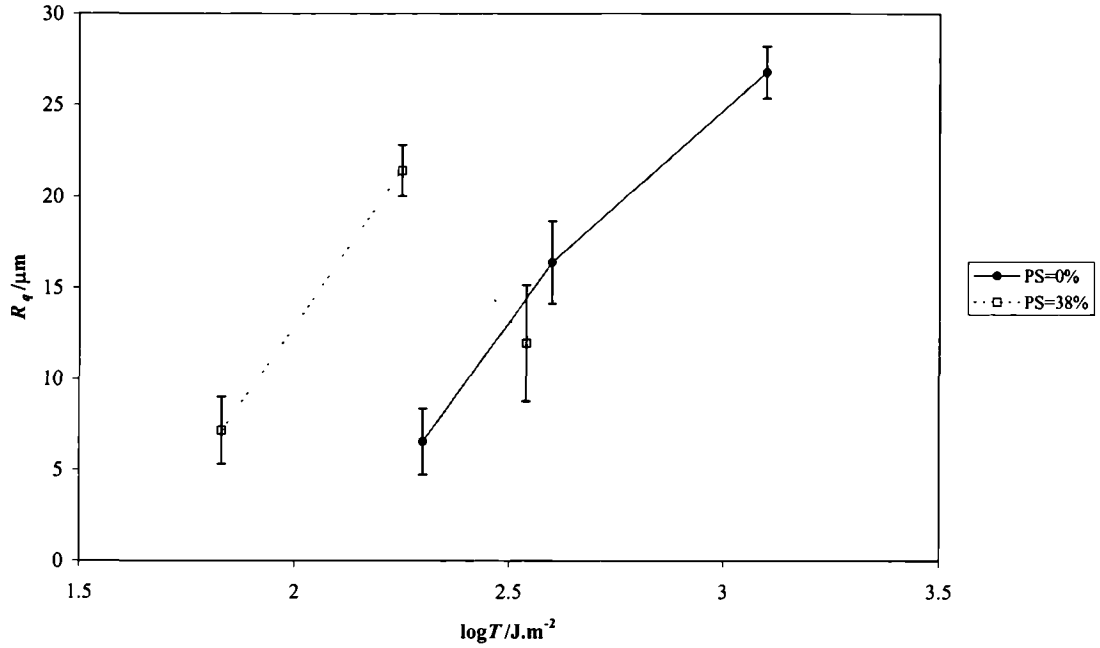

Figure 5-65 Roughness measurement (R_q) as a function of the tearing energy for a range of pre-strains (PS), for SBR0.

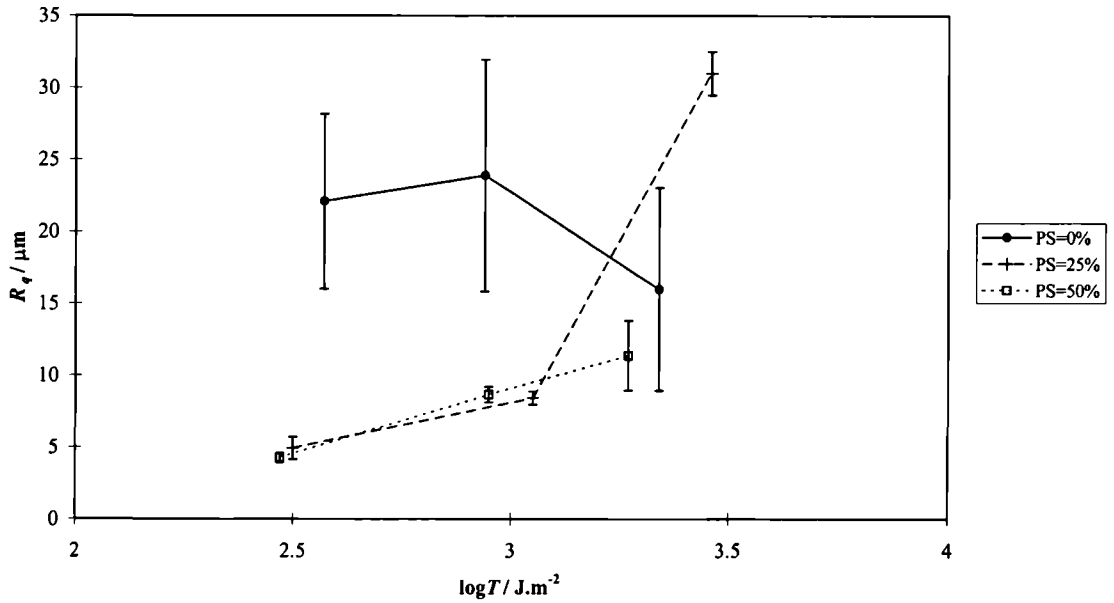

Figure 5-66 Roughness measurement (R_q) as a function of the tearing energy for a range of pre-strains (PS), for SBR30.

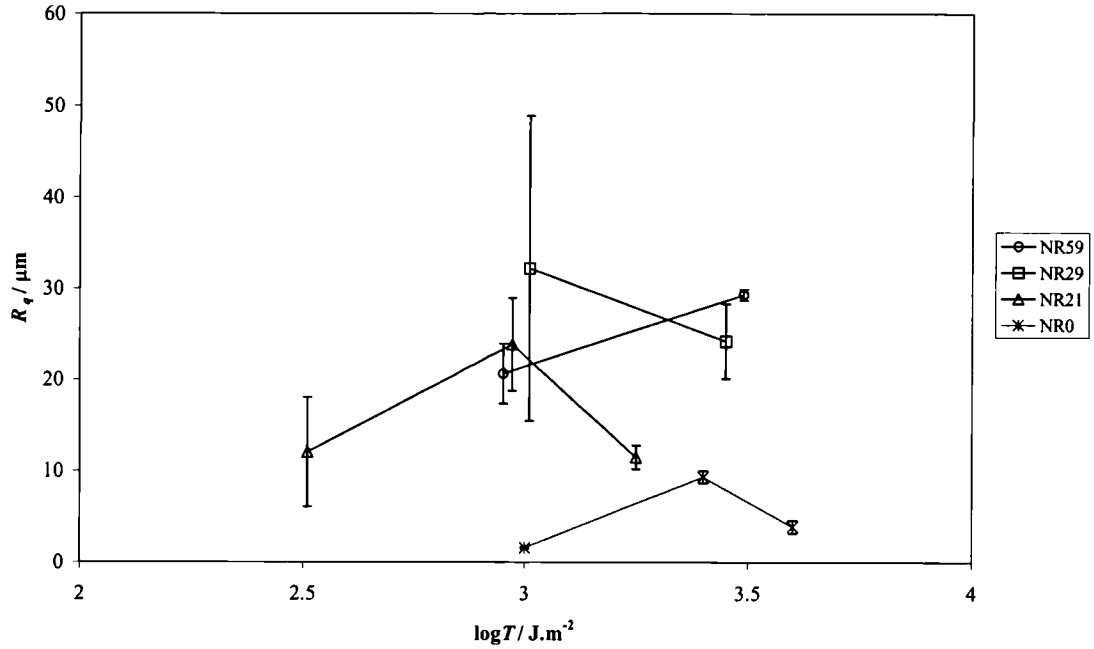

Figure 5-67 Roughness measurement (R_q) as a function of the tearing energy for a range of carbon black contents (NR21, NR29 and NR59).

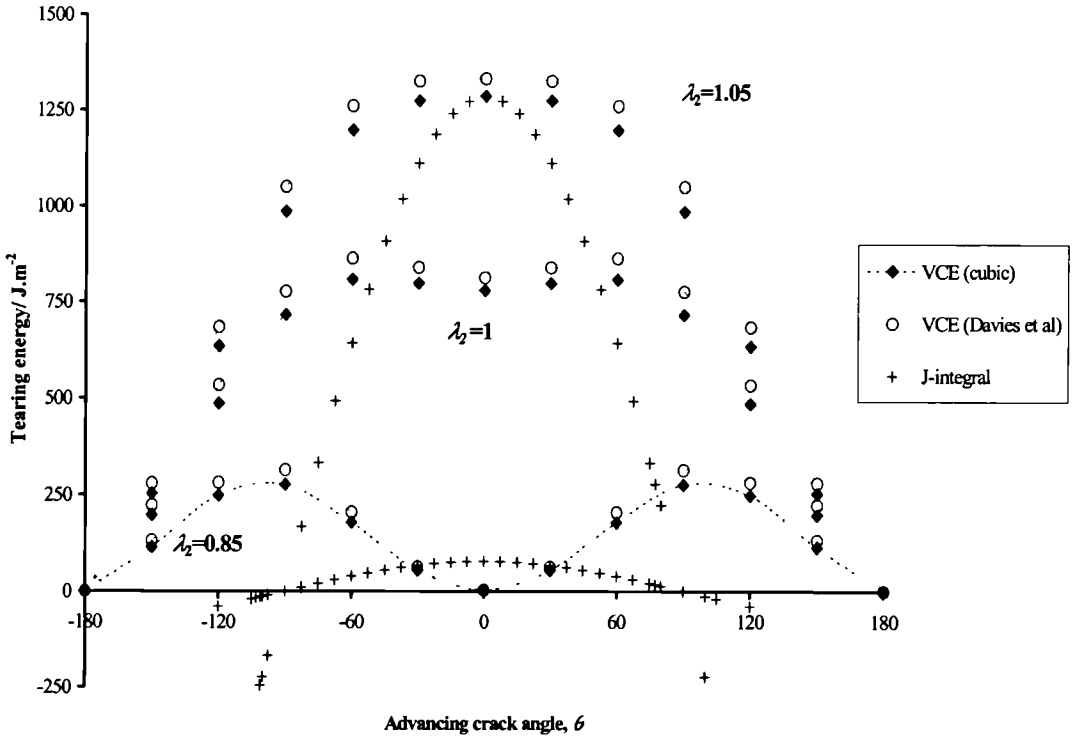

Figure 5-68 Tearing energy estimation for a pre-strained pure shear PS=50% with finite element analysis using the VCE (virtual crack extension) and the J-integral techniques. The J-integral predictions correspond to λ_2=1 and 1.05. The results of the J-integral for λ_2=0.85 are too small to be resolvable on this scale.

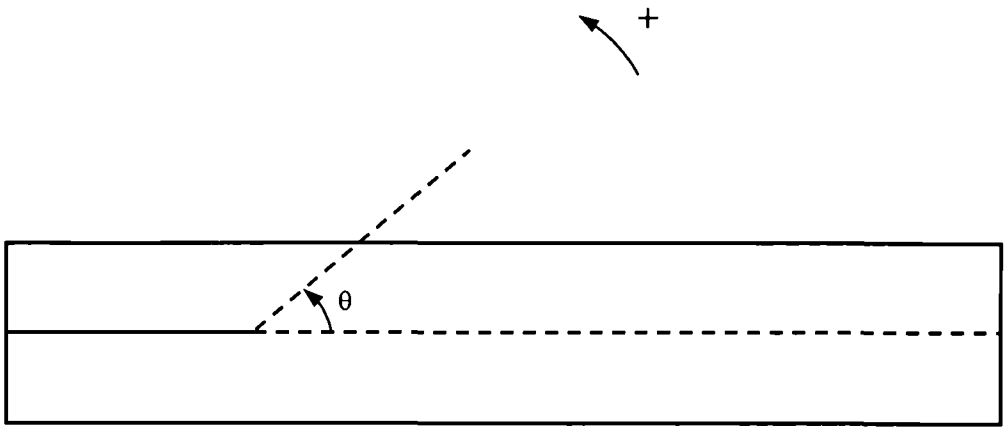

Figure 5-69 Definition of the advancing crack angle θ.

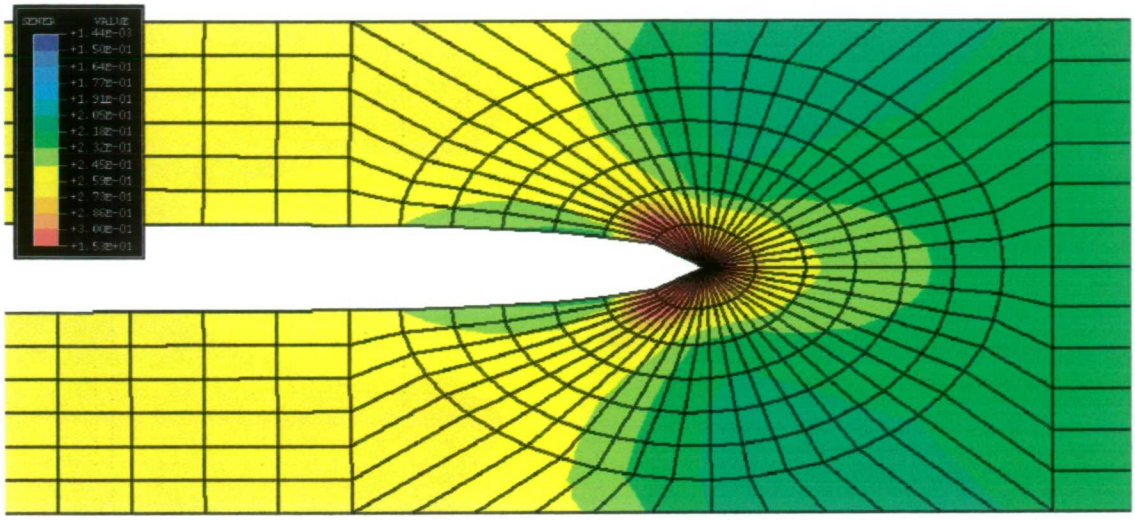

Figure 5-70 Elastic strain energy density contour plot from FEA (in $N.mm^{-2}$) around the crack tip region for a pre-strained specimen (PS=50%) and vertically deformed (λ_2=1) using the Davies *et al* elastic strain energy density function.

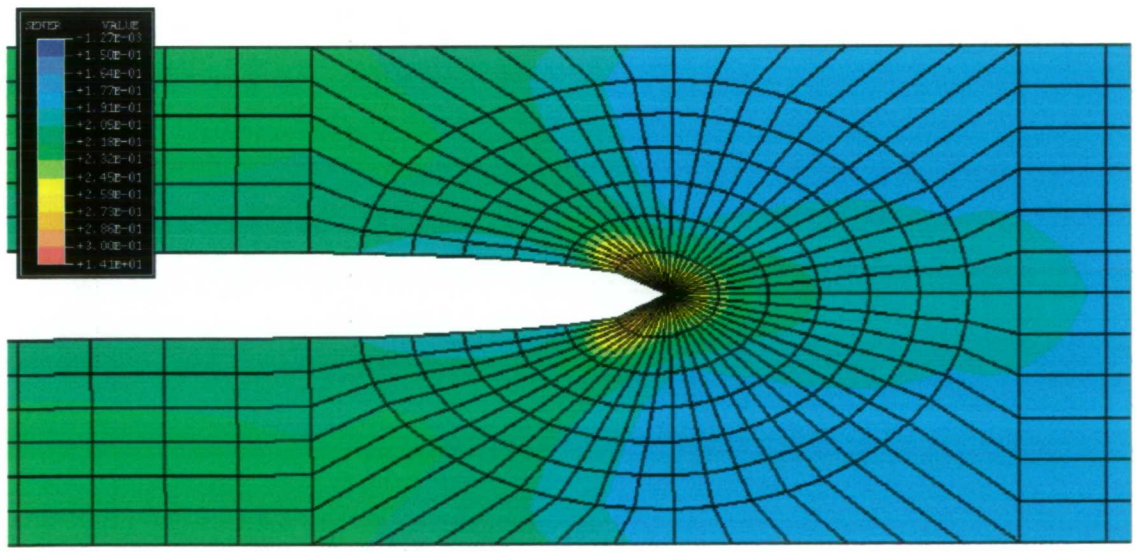

Figure 5-71 Similar contour plot as in Figure 5-55 using the cubic strain energy density function.

	PS=15%		PS=25%		PS=100%	
	T (J.m^{-2})	dc'/dN (m.cycle^{-1})	T (J.m^{-2})	dc'/dN (m.cycle^{-1})	T (J.m^{-2})	dc'/dN (m.cycle^{-1})
1st series	1200 (A)	**7.10^{-8}**	520	**2.10^{-8}**	370	**2.10^{-8}**
	Large cyclic strains (B)		Large cyclic strains (I)		Large cyclic strains (L)	
	1260 (C)	**4.10^{-8}**	340	**2.10^{-8}**	310	**2.10^{-8}**
2nd series	1310(D)	**7.10^{-8}**			310	**2.10^{-8}**
	Large cyclic strains (E)				Large cyclic strains (N)	
	1300(F)	**7.10^{-8}**			300	**2.10^{-8}**

Table 5-1 Crack growth rates before and after large amplitude cyclic strain tests were performed for various pre-strained samples, on NR29. The letters in parentheses correspond to the sequences of tests showed on Figures 5-8 to 5-10.

Pre-strain	**0%**	**25%**	**38%**	**50%**	**75%**	**100%**	**150%**	**200%**
NR0	3/-16.8	-	-	-	-	-	-	3.1/-15.6
NR23	2.3/-14.5	-	-	2/-13	-	1.9/-12.3	1.7/-11.7	-
NR29	2/-14.3	2/-11.3	-	2/-11.3	2/-11.3	2/-11.3	-	-
NR59	1.4/-12.4	1.3/-12.2	-	1.7/-13.1	1.7/-12.8	1.1/-10.9	-	-
SBR0	3.1/-15.6	-	1.7/-12	-	-	-	-	-
SBR30	1.7/-12.9	1.9/-13.1	-	1.9/-12.7	1.6/-12	-	-	-

Table 5-2 Table showing the slope values β (left) and the intercept to the y-axis b (right) in the crack growth behaviour relationship $(dc/dn) = \beta \log T + b_t$ for all materials and pre-strains.

REFERENCES

[1] Rivlin R. S. and Thomas A. G., *J. Polym Sci.*, **10**, 291 (1953).

[2] Gent A. N., Lindley P. B., and Thomas A. G., *J. Appl. Polymer Sci.*, **8**, 433 (1964).

[3] Lake G. J., and Lindley P. B., *Rubber J.*, **146,** Oct. 24 and Nov. 30 (1964).

[4] Rivlin R. S. and Thomas A. G., *J. Polym. Sci.*, **10**, 291 (1953).

[5] Pidaparti R. M. V., Yang T. Y. and Soedel W., *Int. J. Fracture,* **39**, 255 (1989).

[6] Claydon P. W., *Engng. Fracture Mech.*, **42**, 961 (1992).

[7] Hellen T. K., *Int. J. Numer. Meth. Engng* **9**, 187 (1975).

[8] Greensmith H. W., *J. Polymer Sci.*, **21**, 175, (1956).

[9] De D. and Gent A. N. *Rubber Chem. Technol.,* **69**, 834 (1996).

[10] Andrews E. H., *J. Mech. Phys. Solids*, **11**, 231 (1963).

[11] Medalia A. I., paper no 1 presented at a meeting of the Rubber Division, American Society, New-York, NY, April 8-11 (1986).

[12] Mullins L., *Rubber Chem. Technol.*, **42**, 339 (1969).

[13] De D. K., Ph.D. Thesis, University of London (1994).

[14] Yeoh O. H., *Rubber Chem. Tehnol.*, **63**, 792 (1990).

[15] Young D. G., *Rubber Chem. Technol.*, **59**, 809 (1986).

[16] Young D. G., *Rubber Chem. Technol.*, **63**, 567 (1989).

[17] Lake G. J. and Yeoh O. H., *J. Polym. Sci., Polym. Phys. Ed.*, **25**, 1157 (1987).

[18] Lake G. J. and Lindley P. B., *J. Appl. Polym. Sci.,* **8**, 707 (1964).

[19] Yeoh O. H., *Rubber Chem. Tehnol.*, **63**, 792 (1990).

[20] Davies C. K. L., De D. K. and Thomas A. G., *Rubber Chem. Technol.*, **67**, 716 (1994).

[21] Lake G. J., *Rubber Chem. Technol.*, **40**, 309 (1972).

[22] Clamroth R. and Eisele V., *Kautsch. Gummi Kunst.*, **28**, 433 (1975).

[23] Lake G. J. and Lindley P. B., *J. Appl. Polym. Sci.*, **8**, 707 (1964).

[24] Gent A. N. and Kim H. J., *Rubber Chem. Technol.*, **51**, 35 (1978).

[25] Treloar L. R. G., *Rubber Chem. Technol.*, **42**, 625 (1974).

[26] Smith K. J., Greene A. and Ciferri A., *Kolloid-Z*, **194**, 49 (1964).

[27] Gent A. N. and Pulford C. T. R., *J. Mater. Sci.*, **19**, 3612 (1984).

[28] Cho K., Jang W. J., Lee D., Chun H. and Chang Y-W., *Polymer*, **41**, 179 (2000).

[29] Brown P. S., Porter M. and Thomas A. G., *International Rubber Conference*, Kuala Lumpur, (1985).

[30] Thomas A. G., *J. Polym. Sci.*, **18**, 177 (1955).

[31] Lake G. J., Samsuri A., Teo S. C. and Vaja J., *Polymer*, **32**, 2963 (1991).

[32] Lake G. J., *Rubber Chem. Technol.*, **68**, 435 (1995).

[33] Samsuri A. B., Ph.D. thesis, University of North London (1989).

6

Fatigue crack growth under non-simple loading

6.1 Introduction

This chapter is the second part of the work on the study of the fatigue crack growth under non-simple loading. Here, the crack growth behaviour of pure shear specimens which undergo an initial pre-conditioning (applied and released longitudinal stretching before testing) and specimens loaded under simultaneous pure shear and simple shear are investigated.

6.2 Pre-conditioned specimens

The crack growth results for pre-strained specimens, where the pre-strain is retained during the application of a cyclic strain in an orthogonal direction, reported in Chapter 5, showed a significant weakening for all the compounds with an increase of the pre-strain. In the same perspective of investigating the importance of the strength anisotropy ahead of the crack tip, cyclic crack growth in pre-conditioned specimens (applied and released longitudinal stretching before testing) were performed here.

Previous work[1, 2, 3] performed on pre-conditioned materials (applied and then relaxed pre-strain) tested in static tear conditions using a trouser test-piece showed a drop in the tearing energy necessary to grow a crack at a given rate with an increase in the magnitude of applied and released pre-strain. No such work has been carried out on the effect of pre-conditioning on cyclic crack growth, which is investigated here.

An elastomer strip, 175 mm long was stretched rapidly and held for 5 minutes to a desired strain and then relaxed until the dimensions stabilised. NR29 and NR59 were the tested materials for which permanent sets measured after the application of

the pre-strain were never greater than 5%. The specimens were then loaded cyclically and the rate of crack growth measured using the test procedure described in section 3.6. The magnitude of pre-stretching applied before the test, expressed in percentage strain PC, to NR29 and NR59 was respectively PC=100-200% and PC=100%. The results are plotted on Figures 6-1 and 6-2 and compared here with the data for the corresponding pure shear virgin material (PC=0%).

No significant differences were observed in all conditions suggesting that pre-stretching had no effect of the subsequent cyclic behaviour. These results appear to contradict the previously reported tear measurements[1, 2, 3]. An explanation may be found in the type of vulcanising system used in this work. NR29 could be considered as an Efficient Vulcanising system and NR59 as a conventional system (section 3.2 and Table 3-1). An Efficient Vulcanising system has a higher accelerator to sulphur ratio producing more numerous monosulphidic cross-links than a conventional vulcanising system. According to Samsuri[2], the conventional vulcanising systems showed a greater sensitivity to pre-conditioning than the EV systems. This was attributed to the fact that conventional systems produce predominantly polysulphidic cross-links which can break and reform easily under strain in comparison with the monosulphidic cross-links present in EV systems. This effect was confirmed here as the permanent set due to the pre-conditioning was less for NR29 at 1% than NR59 at 5% both for PC=100%. Samsuri[2] explained that this induced anisotropy introduced by the pre-conditioning is retained after the pre-strain was removed causing the observed drop in tearing energy of the materials with a conventional vulcanising system. However, in the present work, for either NR29 or NR59, no effect due to the pre-conditioning on the cyclic crack growth behaviour was observed here.

A possible explanation could be the essential difference between the experiments conducted by Samsuri[2] (tear measurements under constant loading) and the present work (crack growth under cyclic loading). The cyclic loading could to some extent reduce or even erase the anisotropy of strength in the direction of the crack. According to Gent and Kim[4], the pre-conditioning caused the formation of an oriented region in the direction of the crack free of carbon black. This is due to segregation of elastomer and carbon black when the elastomer strain crystallises under the pre-conditioning. One can reasonably say that the cyclic loading in the

vertical direction would somehow produce the same effect and would probably re-establish an isotropy of strength, in a state close to the virgin state.

6.3 The 30° inclined pure shear test piece

6.3.1 FEA investigations

As discussed in section 3.5, if a pure shear test piece is inclined at a certain angle to the horizontal and pulled in the vertical direction (Figure 6-3), the test-piece is under a combination of a pure shear and a simple shear deformation. The fatigue crack growth behaviour of such a test-piece inclined at 30°, is studied here as described in section 3.6 by introducing a 40 mm long razor blade pre-crack normal to the short edge of the test-piece and parallel to its long axis. Because no analytical expression exists to calculate the tearing energy in this geometry, FEA will be used according to the method described in section 3.8, using the model shown in Figure 3-20. Both the VCE and the *J*-integral methods were used to estimate the magnitudes of the tearing energy. FEA was also used to estimate the direction of crack propagation as it is not readily known for this situation. This direction was assumed to correspond to the direction which released the greatest elastic strain energy, or expressed another way as the direction with the biggest tearing energy. The materials mechanical characteristics were represented in the FEA programme using the cubic strain energy function proposed by Yeoh[5] in which the constants were derived using the pure shear test data of NR29, as described in section 4.2.2. The ABAQUS input file using the *J*-integral method is shown in Appendix 6.

A first step in the FEA investigations consisted of checking the direction of crack propagation as indicated by the maximum tearing energy T_{max} was constant when vertical displacements of increasing magnitude d=1, 3 and 5 mm were applied to the test-piece. The predicted crack growth direction is defined by the angle θ between the crack and the horizontal direction (Figure 6-3). Hence a crack growth at $\theta = 60°$ is propagating at an angle of 90 degrees to the initial crack direction and at $\theta = -30°$ is growing in the direction of the initial crack. Figure 6-4 shows that the VCE method predicts T_{max} to occur at approximately $\theta_0 = -15°$. Because the form of

the curve is very shallow, a variation in angle θ of $\pm 15°$ centred on θ_0 (*i.e.* from $\theta = -30°$ to $\theta = 0°$) for example would correspond to 6% change in tearing energy with respect to T_{max}. It would then be expected experimentally to observe crack directions to cover quite a wide range of crack growth direction range.

The contour plot of the elastic strain energy density for d=5 mm is shown in Figure 6-5. The direction of the largest gradient of the elastic strain energy density (the largest energy release rate or tearing energy), corresponds to the bottom of the hump formed by the contour plots (Figure 6-5) at $\theta = -15°$, which is in agreement with the results shown in Figure 6-4.

On Figure 6-6, the VCE results are compared with the *J*-integral results for a test piece with a vertical displacement $d = 1$ mm. Both give a maximum tearing energy at the same angle, approximately $\theta = -15°$. But the rate of fall in the tearing energy magnitude outside the region of its maximum is much steeper for the *J*-integral method (Figure 6-6). In a similar manner as for the FEA results for the pre-strained pure shear geometry, the *J*-integral data produced negative values for the tearing energy for directions of crack growth which could be considered as backwards with respect to the initial crack growth. These results are erroneous and the developer of the software confirmed that the *J*-integral estimations were not reliable in directions other than for the straight-ahead or for the expected crack growth direction. Because these errors are similar to the ones observed in the literature review, section 2.5.2 on the VCE methods[6, 7, 8], it is believed that a common source of analytical errors exists.

6.3.2 Experimental investigations

Tear tests under a static loading, on the inclined test piece geometry were performed on SBR0 (unfilled) to check the validity of the expected crack propagation direction as predicted using FEA. SBR0 was chosen because it exhibits time-dependent crack propagation and it would also avoid any complications such as crack tip deviation due to the carbon black. The range of the angles of propagation θ lay between $\theta = -9°$ to $\theta = -2°$. This is broadly in line with the FEA prediction and any

slight difference can be attributed to the broad peak of the tearing energy versus crack growth direction curve shown in Figure 6-4.

Next fatigue crack growth experiments were performed on NR29, one of the engineering carbon black filled materials which had previously been tested in pure shear (section 5.3).

If it is assumed that the crack propagates in the direction of the initial pre-crack $\theta = -30°$ in the inclined geometry, the derivation of the tearing energy in pure shear described section 5.2.1 can also be applicable to estimate the tearing energy in the inclined geometry. Equation 5-3 is reapplied to measure the tearing energy with u being the elastic stored energy measured in the inclined specimen during the test, c the crack length in the direction $\theta = -30°$ and x being 30% of L_0, the unstrained height of the geometry (or distance between the grips) in the direction $\theta = 60°$. Due to the broad shape of the curve in Figure 6-4, it was thought that only small errors were introduced if this pure shear expression for the tearing energy was also used for crack propagating away from the direction $\theta = -30°$.

In Figure 6-7, the crack growth behaviour measured using pure shear test piece is compared with the results measured using the inclined geometry. A third set of data is shown where the value of the tearing energy was recalculated to account for the actual direction of crack growth using FEA results. The 3 sets of data fall reasonably well onto the same curve. As anticipated, similar crack growth results are found when similar geometries like the pure shear and the inclined pure shear are compared.

The angles of crack propagation lay between $\theta = -30°$ to $\theta = 11°$. According to the FEA results Figure 6-4, $\theta = 11°$ would correspond to less than a 10% drop in tearing energy with respect to T_{max}. Any small local flaw or inhomogeneity may become significant and thus quite a large scatter in the crack growth direction is not unreasonable. The fact that this range of angles is larger than the one obtained in tear tests on SBR0 could be explained by the extent of crack deviations in the cyclic crack growth experiment on NR29 attributable to a more pronounced strength anisotropy and higher degree of molecular orientations due either to the presence of the carbon black filler, the occurrence of crystallisation or to the cyclic deformations.

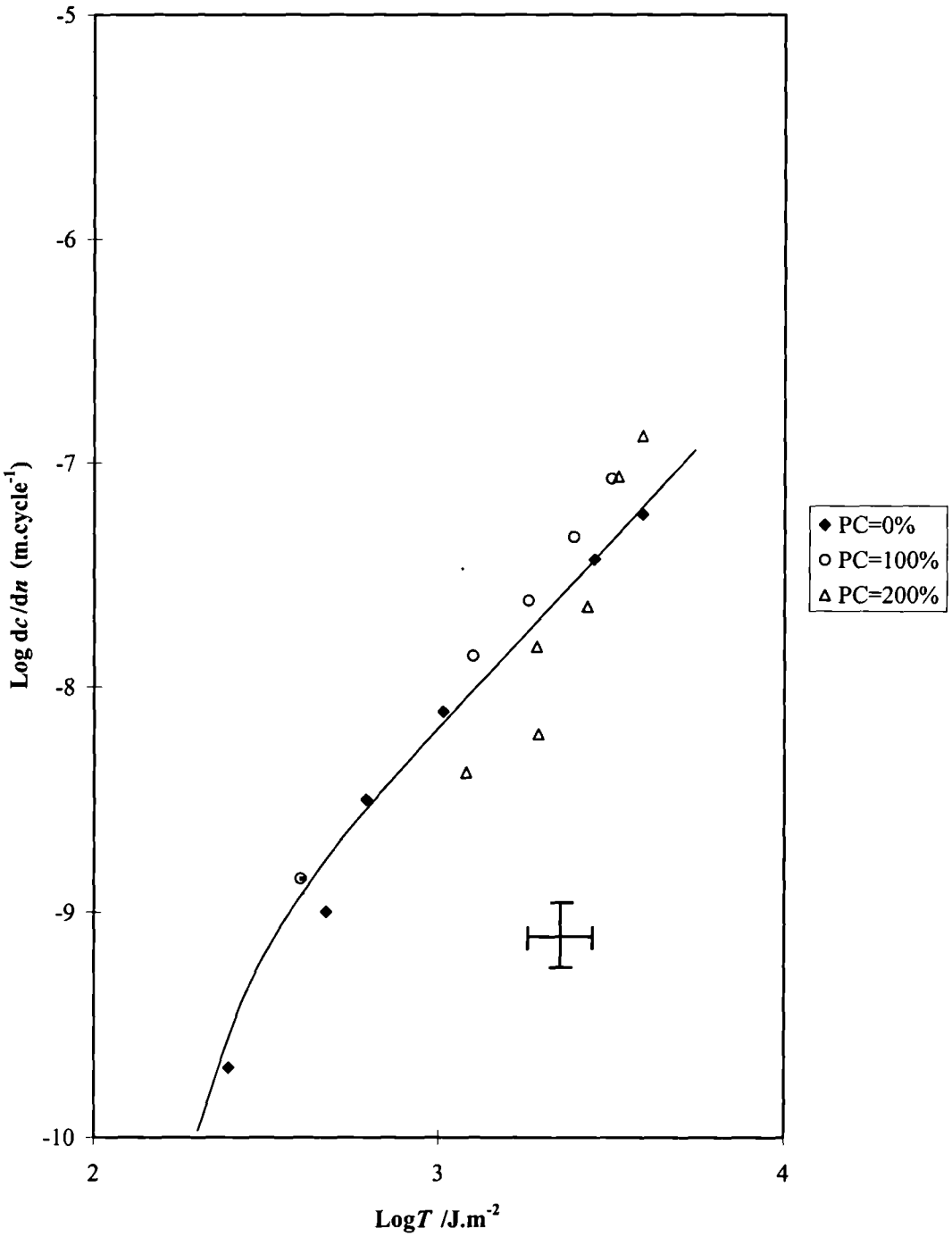

Figure 6-1 Crack growth per cycle (dc/dn) versus the tearing energy T on NR29, pre-conditioned to PC=100% and 200% (magnitude of pre-stretching before test, expressed in percentage strain).

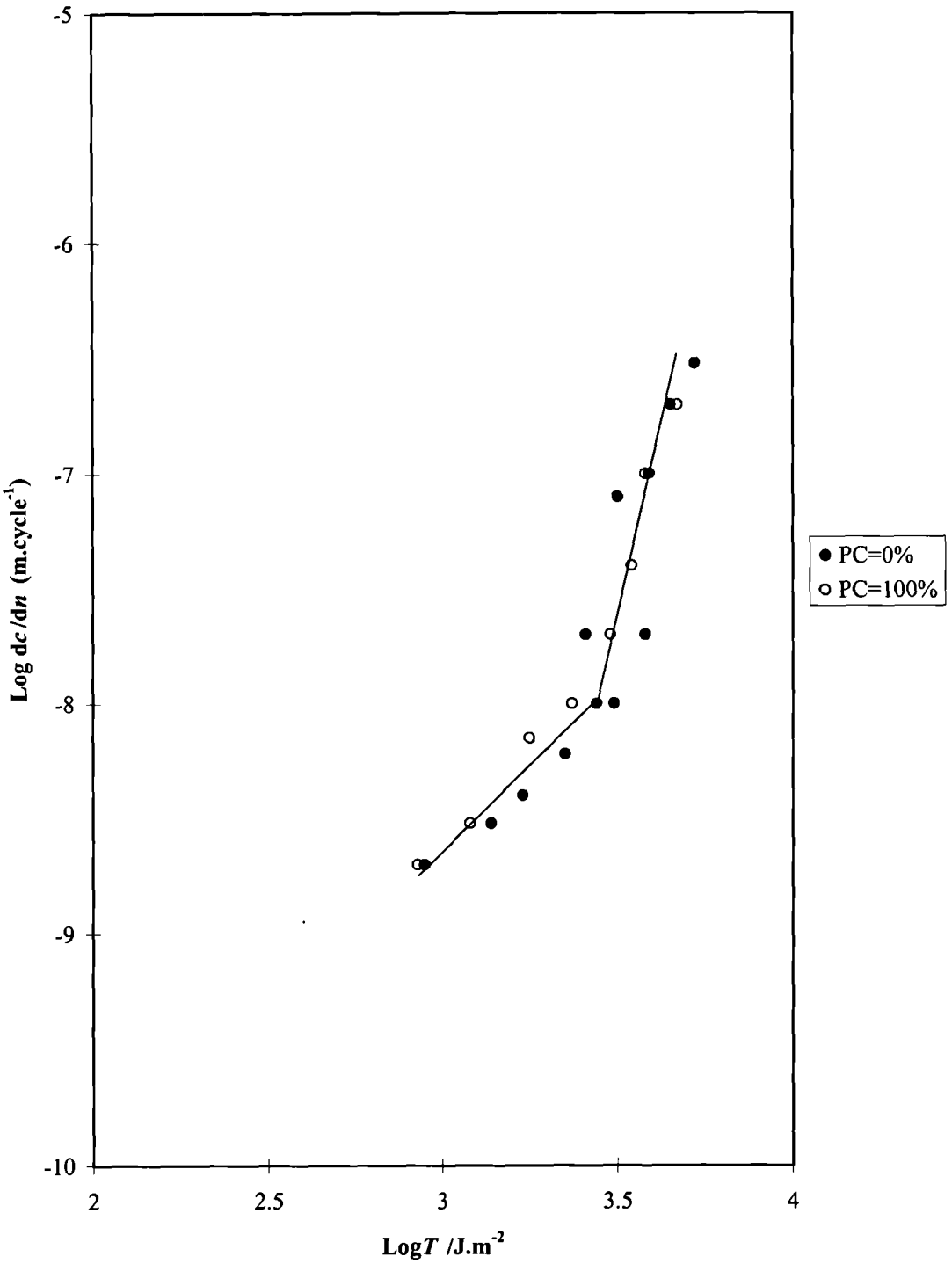

Figure 6-2 Crack growth per cycle (dc/dn) versus the tearing energy T on NR59, pre-conditioned to PC=100% (magnitude of pre-stretching before test, expressed in percentage strain).

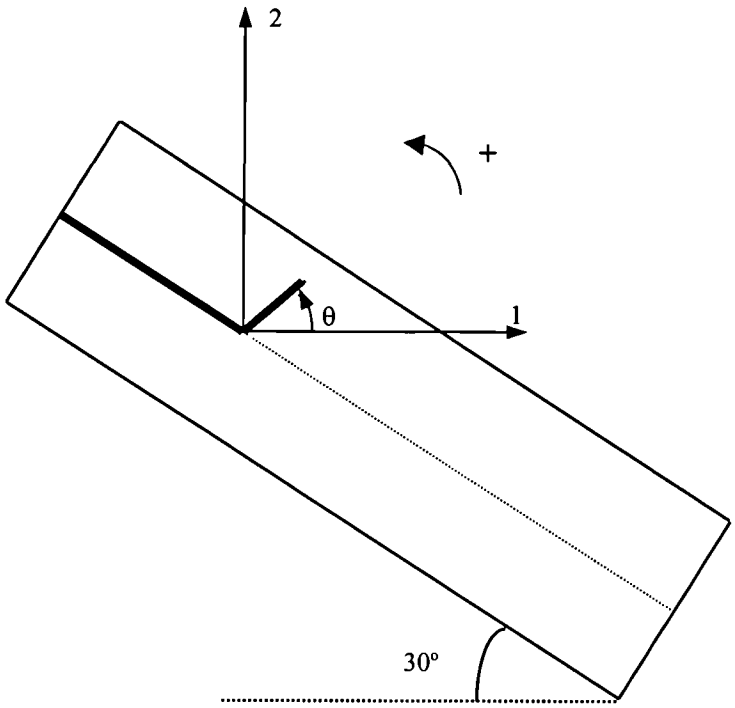

Figure 6-3 The 30° inclined pure shear test piece.

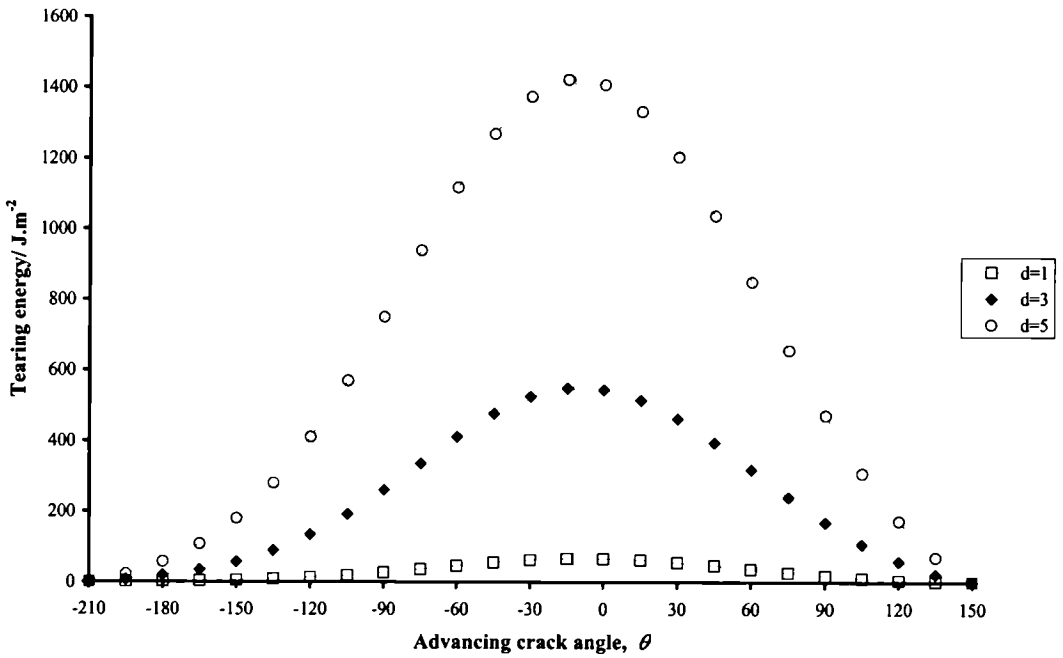

Figure 6-4 The tearing energy distribution as a function of the advancing crack angle θ using the VCE method for 3 different vertical displacements, d=1, 3 and 5 mm.

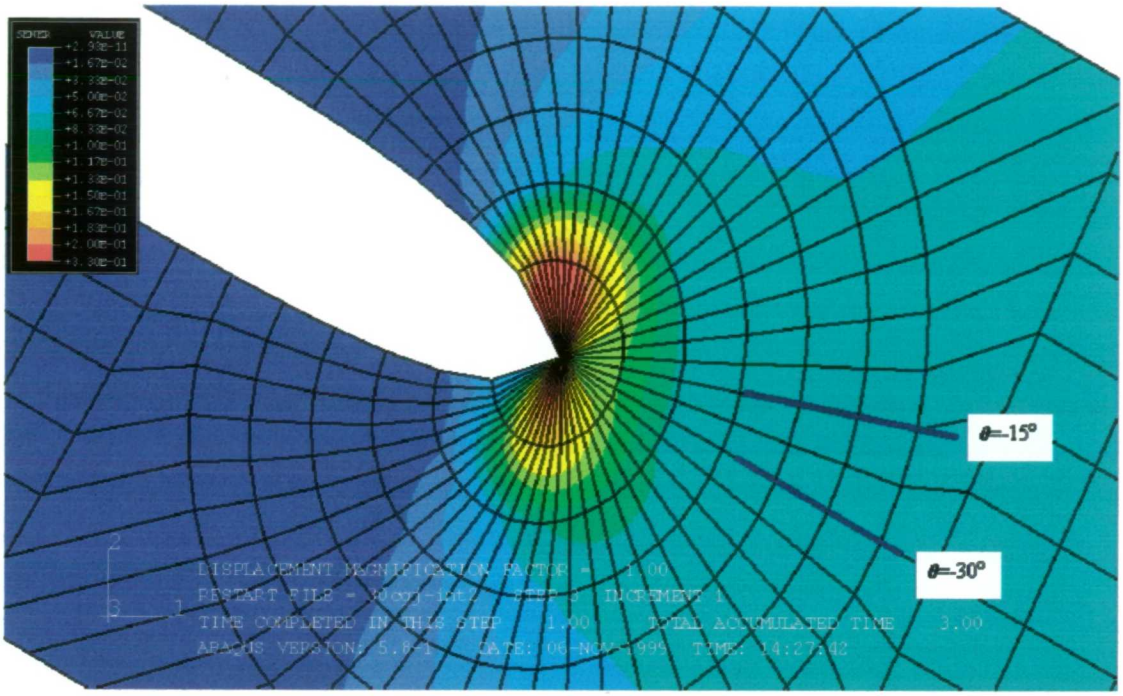

Figure 6-5 Elastic strain energy density contour plot from FEA (in N.mm^{-2}) around the crack tip region for the inclined geometry, vertically displaced to d=5 mm determined using the cubic elastic strain energy density function.

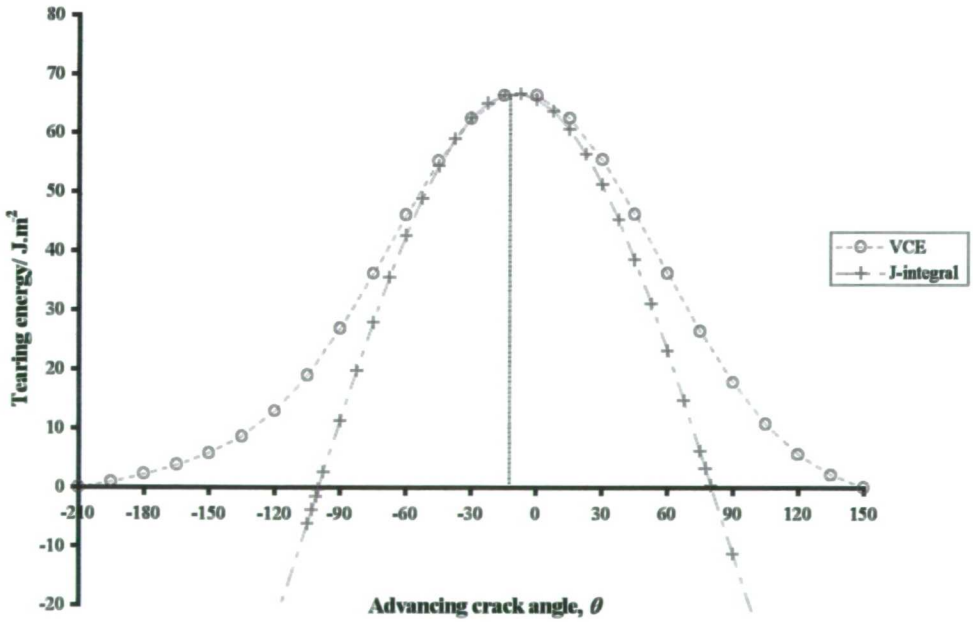

Figure 6-6 Comparison of the tearing energy distribution as a function of the advancing crack angle θ using the VCE and the J-integral methods for a vertical displacement d=1 mm.

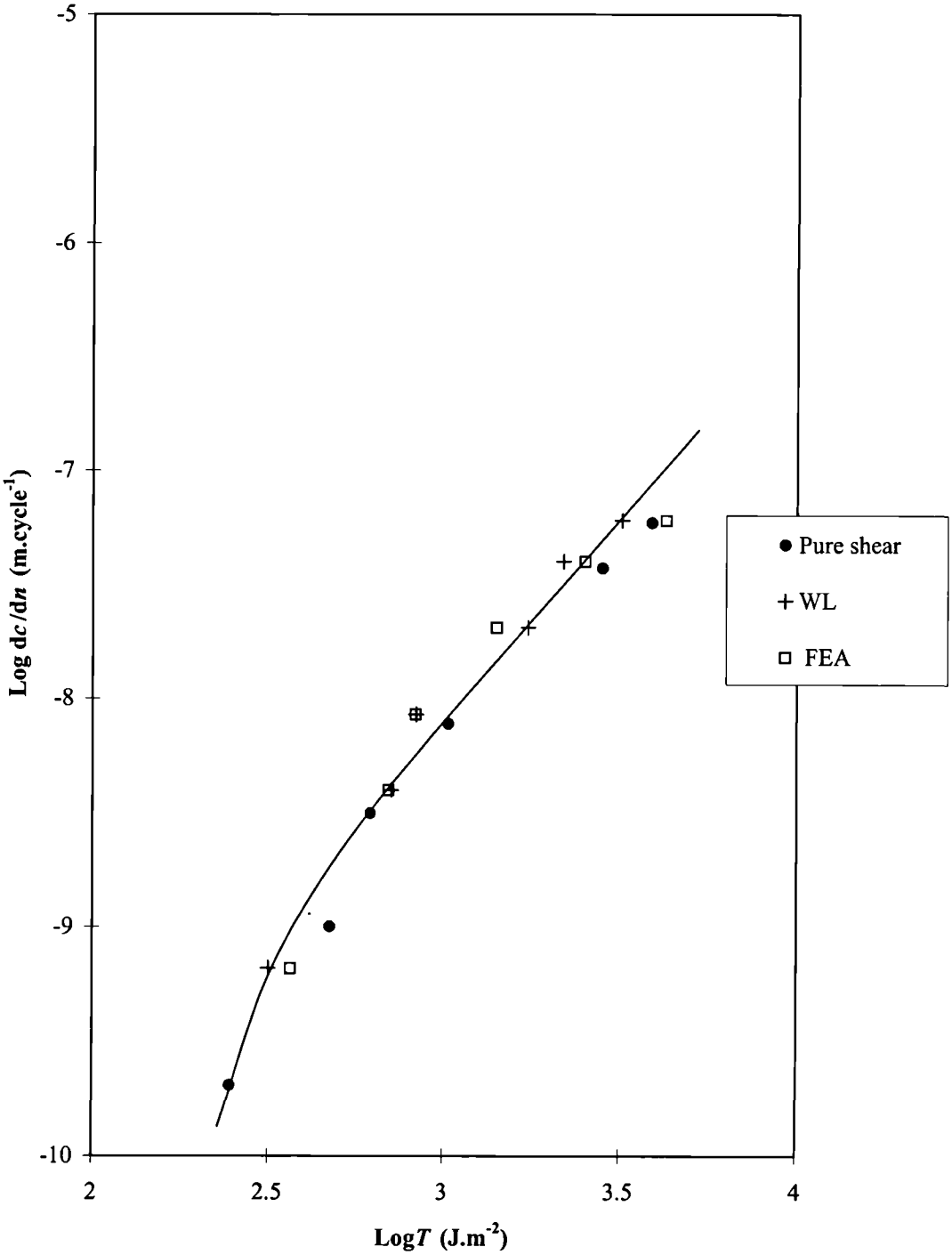

Figure 6-7 Comparison of the crack growth per cycle (dc/dn) versus the tearing energy T for NR29 on the inclined geometry (with the tearing energy either calculated from FEA (FEA) or using the pure shear expression (WL)) and data measured using the pure shear geometry.

REFERENCES

[1] Gent A. N. and Kim H. J., *Rubber Chem. Technol.*, **51**, 35 (1978).

[2] Samsuri A. B., Ph.D. thesis, University of North London (1989).

[3] Janssen H. J. J., *Proceedings of the Third Rubber Technology Conference,* London, W.Heffer and sons, Cambridge, England, 351 (1954).

[4] Gent A. N. and Kim H. J., *Rubber Chem. Technol.*, **51**, 35 (1978).

[5] Yeoh O. H., *Rubber Chem. Technol.*, **63**, 792 (1990).

[6] Pidaparti R. M. V., Yang T. Y. and Soedel W., *Int. J. Fracture* **39**, 255 (1989).

[7] Claydon P. W., *Engng. Fracture Mech.* **42**, 961 (1992).

[8] Hellen T. K., *Int. J. Numer. Meth. Engng.*, **9**, 187 (1975).

7

Summary and suggestions for future work

The focus of this thesis was the investigation of the cyclic crack growth behaviour of systems of gradually increasing complexity in an attempt to derive general rules which would eventually describe crack growth in complex engineering components. The non-simple loading investigated in this work were a longitudinally pre-strained pure shear test-piece and a 30° inclined pure shear test-piece pulled vertically inducing simultaneously pure shear and simple shear deformation modes. An energetic/fracture mechanics approach was adopted where the work to drive a crack growth is supplied by the release of elastic stored energy (tearing energy) in loaded component as a crack grows. It was then necessary to derive an elastic strain energy function which accurately describe the stress-strain behaviour of filled elastomers at the large strains encountered in this work. This was the focus of the first part of the thesis.

From the literature review in Chapter 2 (section 2.2.2), the statistical-thermodynamic theory and the use of phenomenological models are the two possible approaches to describe the stress-strain behaviour of elastomers. The statistical-thermodynamic theory derives the configurational entropy for a given extension first for a molecular chain and then for a molecular network. This first approach is restricted in its application by the assumptions made on the chain behaviour to have mathematically tractable solutions. The phenomenological approach, which does not bear any reference to the molecular structure, received its more general treatment from Rivlin[1]. The only assumptions were an elastic behaviour, incompressibility and isotropy in the unstrained state. From symmetry considerations and using the above assumptions, the elastic strain energy density could be expressed as a function of the two strain invariants I_1 and I_2.

It arose that for filled elastomers, the elastic strain energy density W is not a significant function of the second strain invariant I_2. That is $\partial W/\partial I_2$ is small when compared to $\partial W/\partial I_1$ where I_1 is the first strain invariant (section 2.2.3). Taking into account that simplification, two elastic strain energy density functions were used in the present study. The first elastic strain energy density (*e.s.e.d.*) function had been proposed by Yeoh[2]. It was a third degree polynomial in $I_1 - 3$, also called cubic function and it appeared easy to derive, simple to implement in a FEA programme and was known to have a good ability at predicting general bi-axial extension mechanical behaviour[3]. Conceptually, this function is a material model with a shear modulus varying as a second-degree polynomial in $I_1 - 3$, which is in agreement with the variation of the shear modulus for filled materials. This function was used in conjunction with an elastic strain energy function derived by Davies *et al*[4], this function being used as a benchmark because it has proved in the past reliable with similar filled materials as the ones used in the present work.

For both functions, it was confirmed that assuming a unique dependence on the first invariant I_1 was a reasonable assumption as the pure shear and the tensile experimental data compared reasonably well for the all range of materials on the reduced stress (or chord shear modulus) versus $I_1 - 3$ plot (section 4.3). It was also possible to attribute with a good confidence the small observed discrepancies to a non-negligible dependence of the elastic strain energy density function to I_2. This dependence on I_2, for unexplained reasons, was more pronounced for the filled SBR than for the filled NR materials. The dependence of the elastic strain energy density function to I_2, $\partial W/\partial I_2$, has been ascribed in the literature to the non-elastic behaviour of the molecular network caused by chain entanglements and other irreversible effects. Further investigations need to be pursued to confirm and explain the reasons why SBR materials would exhibit more notable non-elastic deviations from the molecular network point of view.

The ability of these 2 functions to predict mechanical behaviour of non-simply loaded filled elastomers was further investigated in performing tests on a pre-strained pure shear test geometry inducing a bi-axial stress field and a 30° inclined pure shear test geometry inducing simultaneously both a pure shear and a simple shear

deformation mode. In the first of these 2 geometries, a consistent increase of the reduced stress (or chord shear modulus) was observed with an increasing extent of the pre-strain for all the materials, with respect to the pure shear data. An attempt to relate this apparent stiffening effect to a contribution of $\partial W/\partial I_2$ was not conclusive. Because the longitudinal pre-strain had induced significant stiffness anisotropy, a description of the stress-strain behaviour in terms of elastic strain energy density function is no longer appropriate and produces an underestimation which could be as great as 40%. This stiffening effect was attributed to breaking and reformation of the carbon black and molecular network and also to restrictions of the molecular motion in the orthogonal direction of the pre-strain. An extension of this work would be to measure $\partial W/\partial I_2$ experimentally in the pre-strained test geometry, to attribute $\partial W/\partial I_2$ a functional form and attempt to predict the stiffening effect with increasing pre-strain observed in this thesis. $\partial W/\partial I_2$ could be estimated with a set-up capable of measuring the stresses generated in the direction of the pre-strain (the other principal stress). From the elastic strain energy function point of view, this phenomenological/continuum mechanics approach has shown its limit. A model taking into account the anisotropy induced upon deformation needs to be formulated. The work of Rivlin, for example, which included some solutions on the non-linear elastic deformation for anisotropic materials[5, 6, 7] would need to be revisited.

On the 30° inclined test geometry, the derivation of the vertical force necessary to strain the sample as a function of $\partial W/\partial I_1$, $\partial W/\partial I_2$ and the parameters of the geometry was resolved in section 4.4. This derivation used Rivlin's analytical solution[8], giving the forces to produce simultaneous extension, inflation and torsion of a cylindrical tube. The prediction of the force-displacement curves of filled materials using the cubic and Davies *et al* functions derived from pure shear experimental data showed good agreement with the experimental data. As far as the present author is aware, such verification of this particular analytical solution[8] has not been realised before using filled materials. And this result was important for the application of a finite element based fracture mechanics to predict the direction of crack growth in the 30° inclined test geometry in Chapter 6.

The work on the fatigue crack growth under non-simple loading was subdivided into chapters 5 and 6. Chapter 5 investigated the crack growth behaviour

of the pre-strained pure shear test-piece. Preliminary experiments were performed to estimate the extent of the edge effects in the pre-strain geometry, evaluate the correction factor x present in the tearing energy expression and the effect of strain history on the crack growth rate (sections 5.2.2 to 5.2.4). The fatigue crack growth tests in pre-strained conditions were supplemented with fracture surface analysis (microscopic observations and roughness measurements) and finite element investigations. Calling PS the extent of pre-strain expressed in percentage strain, it was observed that as the pre-strain increases, the crack growth data were shifted upwards on the $\log(\mathrm{d}c/\mathrm{d}n) = f(\log T)$ plots. It meant that all materials become weaker as T decreases at a given $\mathrm{d}c/\mathrm{d}n$ or $\mathrm{d}c/\mathrm{d}n$ increases at a given T. These changes varied from a factor 2 to a factor 25. Several hypotheses were advanced. As this weakening effect occurred for all combinations of filled/unfilled and strain-crystallising/non-strain crystallising materials, it would appear not to be intrinsically related to either carbon black or crystallisation effects.

For all materials and for "moderate" pre-strains/tearing energies on NR59, because the data, shifted upwards, and remaining parallel to the pure shear data (PS=0%) on the $\log(\mathrm{d}c/\mathrm{d}n) = f(\log T)$ plots, the pre-strain was attributed to a decrease in T_0 due to the reduction of the number of molecules to be broken per unit fracture surface area. This reduction in the number of molecules intersecting the plane of fracture was assumed to be mainly a function of the degree of molecular orientation in the bulk of the material due to the pre-strain. Because of the strain amplification effect due to the carbon black, the strain measured in the bulk of the material did not represent the local strain borne by the elastomer molecules. However the magnitude of the stresses generated by the pre-strain could give a reasonable measure of the molecular orientation as it measures the local stress borne by the elastomer molecules. Expressing the reduction in tearing energy as a function of the generated stress (due to the pre-strain), for a given $\mathrm{d}c/\mathrm{d}n$, produced very similar trends for all materials (filled/unfilled, strain-crystallising/non-strain crystallising). It consequently confirmed that the molecular orientation in the bulk of the material intrinsically governed the observed weakening. These findings were also corroborated by the fracture surface analysis. Although roughness measurements have no well-established and commonly accepted procedures, it was generally observed in this

work that the fracture surfaces became smoother with increasing pre-strain for all the materials. These results were confirmed with the microscopic observations of the fracture surfaces.

From the microscopic investigation point of view, it was also observed that the observed steps tended to be more widely spaced as the tearing energy/crack growth rate increased, at a given pre-strain. The mechanisms leading to the formation of these steps are unclear.

For the largest pre-strains or tearing energies for NR59, the picture is somehow different. For the largest pre-strains (PS=75% and 100%), for a large enough tearing energy, the crack growth rates zoomed up significantly. In similar conditions of pre-strains, time-dependent crack growth was observed under static loading (tear test). Probably because of experimental difficulties, it was not possible to attribute the region of high crack growth rates to a major contribution of the time-dependent component of crack growth. But it is probable that strain-crystallisation ceased in this high crack growth region because the bulk of the material was highly oriented/partially crystallised with crystals formed in the direction of crack growth (or direction of the pre-strain) making it easier for a crack to grow in the same direction.

For the largest tearing energies ($T \geq 2000\ \text{J.m}^{-2}$), for PS=25% and 50%, on NR59, very rough fracture surfaces were observed with roughness values approaching the ones of the non-prestrained samples. The observations that the fracture surfaces exhibited crevasses (extensive cracks deviating sideways from the main crack) which were believed to prevent catastrophic tearing at these high magnitudes of the tearing energy. A detailed observation of the flanks of these crevasses showed rounded features which forms could be clearly seen as resulting from the cavitation processes. Also observed on the fracture surfaces of the non-prestrained samples NR59 (PS=0%), these rounded features could be directly related to the presence of these crevasses and probably bear some relation with the occurrence of knotty-tearing in tear tests. These findings need to be investigated further with an emphasis on the possible role of cavitation in crack deviation.

From the more general point of view of the mechanisms involved in the fracture of elastomers, this thesis has highlighted the major influence of the formation of an anisotropic structure ahead of the crack tip. It was shown that the induced strength anisotropy was directly related to the molecular orientation. But the way this

molecular orientation is related to the other factors closely related to the fracture of elastomers, namely the high strain hysteresis and the cavitation formation, would need to be investigated.

In Chapter 6, a variant test-piece from the pre-strained pure shear test geometry was tested in fatigue crack growth. It consisted in pre-conditioning a pure shear specimen by applying and releasing a longitudinal stretching before testing. Neither for NR29 nor for NR59 which was more likely to retain an anisotropy after the stretch because of its labile polysulphidic cross-links, showed any effect of the pre-conditioning on the crack growth behaviour. It could be that even though some cross-links are broken and reformed during the pre-conditioning (more likely on NR59), the cyclic loading re-establishes a molecular orientation at the crack tip similar to the one present in the virgin state.

Also in Chapter 6, the finite element based fracture mechanics was successfully applied to the crack growth behaviour of the 30° inclined pure shear test-piece, using the elastic strain energy density function derived from pure shear data. The direction of the crack growth along with magnitude of tearing energies were reasonably well predicted by the virtual crack extension technique. Nevertheless, the *J*-integral calculation, done directly by the finite element software, produced erroneous results for crack directions other than the expected direction of crack growth. For these crack growth directions, negative values of the tearing energy were computed, results which have no physical meanings.

REFERENCES

[1] Rivlin R.S., Rheology vol 1, Eirich, F.R. Ed, Academic Press, New-York, **10,** 351 (1956).

[2] Yeoh O. H., *Rubber Chem. Tehnol.*, **63**, 792 (1990).

[3] James A. G. and Green A., *J. Appl. Polym. Sci.*, **19**, 2319 (1975).

[4] Davies C. K. L., De D. K. and Thomas A. G., *Rubber Chem. Technol.*, **67**, 716 (1994).

[5] Ericksen J. L. and Rivlin R. S., *Journal of Rational Mechanics and Analysis*, **3**, 281 (1954).

[6] Smith G. F. and Rivlin R. S., *Trans. Am. Mathematical Soc.*, **88**, 175 (1958).

[7] Smith G. F. and Rivlin R. S, *Journal of Rational Mechanics and Analysis*, **1**, 107 (1957).

[8] Rivlin R. S., *Phil. Trans Roy. Soc.* A, **242**, 173 (1949).

APPENDIX 1: Simultaneous extension, inflation and torsion of a cylindrical annulus

The forces required to maintain simultaneous extension, inflation and torsion in a uniform circular cylindrical tube were calculated by Rivlin[1]. The deformation to which a uniform circular cylindrical tube is subjected is defined by the following three successive deformations: (1) a uniform simple extension of extension ratio λ, (2) a uniform inflation of the tube in which its length remains constant and its external and internal radii change from their values of a_1 and a_2 respectively in the undeformed tube to $\mu_1 a_1$ and $\mu_2 a_2$ respectively, (3) a uniform torsion in which planes perpendicular to the axis of the tube are rotated in their own plane through an angle proportional to the distance of the plane considered from one end, the constant of proportionality being ς. In this deformation a point of the tube which is initially at a radial distance r from its axis moves to a radial distance μr, where μ is given by:

$$\lambda\mu^2 r^2 = r^2 + K \text{ and } K = a_1^2(\lambda\mu_1^2 - 1) = a_2^2(\lambda\mu_2^2 - 1).$$

It has been shown that this deformation can be maintained by the application of torsional couples M and tensile forces F_t to the ends of the tube together with a force R_v per unit area, measured in the deformed state, acting normally on the inner curved surface of the tube (Figure A1-(1)). M, F_t, and R_v are given by:

$$M = 4\pi\varsigma\int_{a_2}^{a_1}\mu r^3\left(\lambda\mu\frac{\partial W}{\partial I_1} + \frac{1}{\lambda\mu}\frac{\partial W}{\partial I_2}\right)\mathrm{d}r$$

$$F_t = \pi\int_{a_2}^{a_1} 2r\left[\begin{array}{l}\dfrac{2}{\lambda}\left(\lambda^2 - \dfrac{1}{\lambda^2\mu^2}\right)\left(\dfrac{\partial W}{\partial I_1} + \mu^2\dfrac{\partial W}{\partial I_2}\right) + \dfrac{1}{\lambda^2\mu^2}\left(\dfrac{1}{\lambda^2\mu^2} - \mu^2\right)\left(\dfrac{\partial W}{\partial I_1} + \lambda^2\dfrac{\partial W}{\partial I_2}\right)\left(1 - \dfrac{a_2^2}{r^2}\right) + \\ \varsigma^2\dfrac{\partial W}{\partial I_1}(a_2^2 - r^2) - 2\dfrac{\varsigma^2}{\lambda}r^2\dfrac{\partial W}{\partial I_2}\end{array}\right]\mathrm{d}r$$

$$R_v = 2\int_{a_2}^{a_1}\frac{1}{\lambda\mu^2}\left(\frac{1}{\lambda^2\mu^2} - \mu^2\right)\left(\frac{\partial W}{\partial I_1} + \lambda^2\frac{\partial W}{\partial I_2}\right)\mathrm{d}r - 2\varsigma^2\lambda\int_{a_2}^{a_1} r\frac{\partial W}{\partial I_1}\mathrm{d}r$$

The deformation considered is a sheet extended by an extension ratio α_2 in say the x-direction then deformed to α_1 in the y-direction and then subjected to a shear deformation parallel to the x direction (Figure A1-(2)). The angle of shear γ and the amount of shear are related by the following relation:

$$\tan\phi = \gamma .$$

The solution can be found from the results given by Gent and Rivlin[2] on the torsion, inflation and extension of a tube. Their results can be specified to a thin walled tube of wall thickness t and radius a. We have, writing α_1 for λ and α_2 for μ in their relations[2]:

$$\gamma = a\alpha_2\varsigma$$

and the following stresses, referred to the deformed dimensions:

Shear stress $\tau = \dfrac{M\alpha_1}{2\pi\alpha_2 a^2 t}$

Stress in α_1 direction (y-direction) $t_1 = \dfrac{F_t\alpha_1}{2\pi a t}$

Stress in α_2 direction (x-direction) $t_2 = -\dfrac{R_v a\alpha_1\alpha_2^2}{t}$

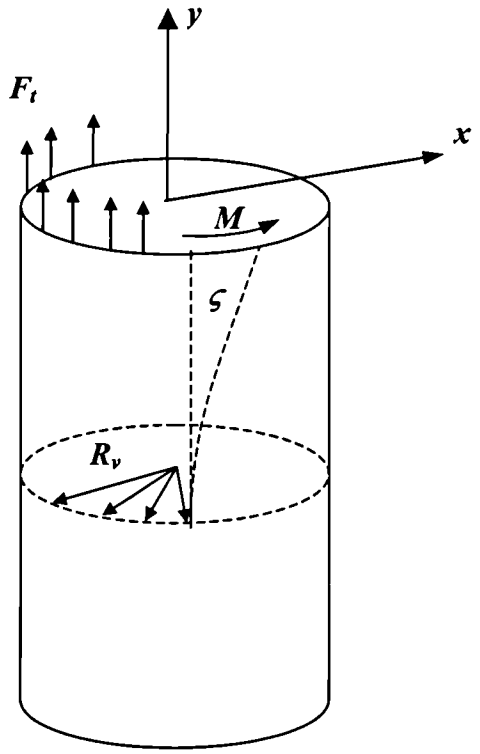

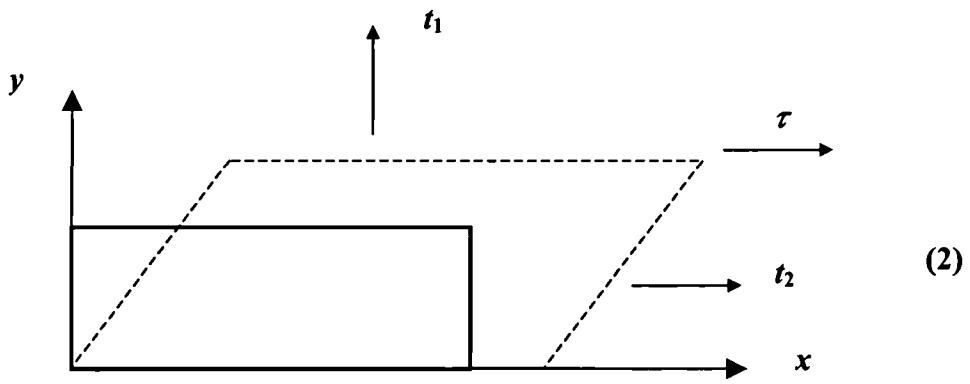

Figure A1

REFERENCES

[1] Rivlin R. S., *Phil. Trans. Roy. Soc. London* A, **242**, 173 (1949).

[2] Gent A. N. and Rivlin R. S., *Proc. Phys. Soc. London* B, **65**, 487 (1952).

APPENDIX 2: User subroutine to input the Davies et al elastic strain energy function

```
*USER SUBROUTINES
      SUBROUTINE UHYPER(BI1,BI2,AJ,U,UI1,UI2,UI3,TEMP,
     1NOEL,CMNAME)
C
      INCLUDE 'ABA_PARAM.INC'
C
C     SMOD=A,SMTC=C,ALPHA=n,THETA=K
      CHARACTER*8 CMNAME
      DIMENSION UI1(3),UI2(6),UI3(6)
      UI1(2)=0
      UI1(3)=0
      UI2(2)=0
      UI2(3)=0
      UI2(4)=0
      UI2(5)=0
      UI2(6)=0
      UI3(2)=0
      UI3(3)=0
      UI3(4)=0
      UI3(5)=0
      UI3(6)=0
      AJ=1.0
      SMOD=0.72
      ALPHA=0.3
      SMSTC=0.03
      THETA=0.04
      ETA=(1.0-(ALPHA/2.0))
      DELTA=((SMSTC**2.0)-3.0)
      OMEGA=SMOD/(2.0*(ETA))
      U=OMEGA*((BI1+DELTA)**ETA)+THETA*(BI1-3)**2.0
      UI1(1)=OMEGA*ETA*((BI1+DELTA)**(ETA-1.0))+2.0*THETA*(BI1-3)
      UI2(1)=OMEGA*ETA*(ETA-1.0)*((BI1+DELTA)**(ETA-2.0))+2.0*THETA
C     WRITE(6,*) AJ,NOEL,DELTA,OMEGA,ETA,ALPHA,SMSTC,SMOD
      RETURN
      END
```

APPENDIX 3: Calculation of the experimental errors on the tearing energy and the crack growth rate

(a) Calculation of the experimental errors on the tearing energy

The expression of the tearing energy in case of a pre-strained pure shear sample is given by the following expression:

$$T = \frac{u_S \lambda_1}{t(w' - c' + x'_p)} \qquad \text{(A5.1-1)}$$

where u_S is the elastic strain energy stored in the pre-strain sample, λ_1 the magnitude of the extension ratio due to the pre-strain, t' the thickness in the undeformed (non-pre-strained) and w', c', x'_p are respectively the width, the crack length and the correction factor, all referred to the deformed state. If the logarithm of Equation (A5.1-1) is taken then,

$$\log T = \log u_S + \log \lambda_1 - \log t - \log(w' - c' + x') \qquad \text{(A5.1-2)}$$

Differentiating Equation (A5.1-2) gives:

$$\frac{dT}{T} = \frac{du_S}{u_S} + \frac{d\lambda_1}{\lambda_1} - \frac{dt}{t} - \frac{dw' - dc' + dx'}{w' - c' + x'} \qquad \text{(A5.1-3)}$$

Converting the differentials into absolute errors gives:

$$\frac{\Delta T}{T} = \frac{\Delta u_S}{u_S} + \frac{\Delta \lambda_1}{\lambda_1} + \frac{\Delta t}{t} + \frac{\Delta w' + \Delta c' + \Delta x'}{w' - c' + x'} \qquad \text{(A5.1-4)}$$

The error on the width, referred to the deformed state, $\Delta w'$ incorporates the errors in the measurement of the width in the undeformed state, w and the extension ratio of the pre-strain λ_1 and we have $w' = w\lambda_1$. Then:

$$\log w' = \log w - \log \lambda_1 \qquad \text{(A5.1-5)}$$

Consequently:

$$\frac{\Delta w'}{w'} = \frac{\Delta w}{w} + \frac{\Delta \lambda_1}{\lambda_1} \qquad \text{(A5.1-6)}$$

Estimating Δw, the error on a length measurement using a ruler to be equal to 1 mm and the average width to be equal to 180 mm, we have $\Delta w/w = 0.5\%$. As the relative error on the extension ratio $\Delta\lambda_1/\lambda_1$ comes from errors in length and dimension measurements, it could be assumed as also equal to 0.5%. We have then $\Delta w'/w' = 1\%$.

The error on u_S, the elastic strain energy of the specimen can be approximated as the summation of the errors on paper weighing (u_S is measured by weighing the graph paper cut under the force-deflection curve), on the force and the deflection. The first one is estimated to be equal to 0.1% (the average mass of paper weighed is one gram and the balance precision is 0.001 gram) and the two others were estimated as both being equal to 2% (the errors on the force and deflection measurements are principally due to the Instron machine). We finally have $\Delta u_S/u_S = 4\%$.

Having the thickness measured using a dial gauge, we estimate $\Delta t = 0.02$ mm for a typical measured thickness of 2 mm. Consequently we have $\Delta t/t = 1\%$.

The crack length measured using a eight-time magnifying video camera produce an estimated error $\Delta c' = 0.2$ mm.

According to section 5.2.2.2 in Chapter 5:

$$x' = A\lambda_1 L_0 \qquad \text{(A5.1-7)}$$

where A is a constant and L_0 is the unstrained height. This gives:

$$\frac{\Delta x'}{x'} = \frac{\Delta \lambda_1}{\lambda_1} + \frac{\Delta L_0}{L_0} \qquad \text{(A5.1-8)}$$

$\Delta L_0 / L_0$ =2.5% as L_0 is measured with a Vernier and the estimated absolute error being $\Delta L_0 = 0.5$ mm with typical values of L_0 equal to 20 mm. With $\Delta \lambda_1 / \lambda_1$ =0.5%, $\Delta x'/x'$ is consequently equal to 3%.

Having as typical values of w', c' and x' respectively 180, 80 and 6 mm, we obtain $\Delta w' = 1.8$ mm, $\Delta c' = 0.2$ mm and $\Delta x' = 0.09$ mm and the last term of expression A5.1-4 is estimated as being equal to 2 %.

Consequently, the relative error on the tearing energy measurement can be estimated as being of the order of 10%.

(b) Calculation of the experimental errors on the crack growth rate $\mathbf{dc/dn}$

To estimate the error on the crack growth rate, the later should be expressed as follows:

$$\frac{dc}{dn} = \frac{c_2 - c_1}{n_2 - n_1} \qquad \text{(A5.1-9)}$$

where c_i is the crack length for a number of cycles n_i. Taking the logarithm of equation (A5.1-9) and differentiate the resulting expression, we obtain:

$$d\log\left(\frac{c_2 - c_1}{n_2 - n_1}\right) = d[\log(c_2 - c_1) - \log(n_2 - n_1)] = \frac{d(c_2 - c_1)}{c_2 - c_1} - \frac{d(n_2 - n_1)}{n_2 - n_1} \qquad \text{(A5.1-10)}$$

The error on the crack growth rate, the maximum value of expression A5.1-11 is:

$$\Delta\left[\log\left(\frac{c_2 - c_1}{n_2 - n_1}\right)\right] = \frac{2\Delta c}{c_2 - c_1} + \frac{2\Delta n}{n_2 - n_1} \qquad \text{(A5.1-11)}$$

where Δc and Δn are respectively the errors on the measurements of the crack length and the number of cycles. They are respectively estimated as being equal to 0.2 mm and 200 cycles. Average measured crack length and number of cycles are respectively 1 mm and 10 000 cycles. The relative error on the cyclic crack growth is then of the order of 7%.

APPENDIX 4: ABAQUS input file for the analysis of the pre-strained pure shear geometry using a user defined material behaviour (the Davies et al elastic strain energy density function)

```
*HEADING
*PREPRINT,ECHO=NO,HISTORY=NO,MODEL=NO
*RESTART,WRITE
*NODE,NSET=LOAD
9999,0,0,0
9998,0,0,0
*NODE, SYSTEM=R
     2, 40.000000000000, 0.0000000000000
     3, 40.000000000000, 20.000000000000
...
   1329, 30.000000000000, 6.6666666666666
   1330, 30.000000000000, 5.0000000000000
   1331, 30.000000000000, 3.3333333333333
   1332, 30.000000000000, 1.6666666666666
*NODE,NSET=TIP
 1312, 40.000000000000, 10.000000000000, 0.0000000000000
2241, 40.000000000000, 10.000000000000, 0.0000000000000
...
2286, 40.000000000000, 10.000000000000, 0.0000000000000
2287, 40.000000000000, 10.000000000000, 0.0000000000000
2288, 40.000000000000, 10.000000000000, 0.0000000000000
*ELEMENT,TYPE=CPS3,ELSET=rubber
   241,  1312,   16,   246
   242,  1312,   246,   244

   287,  1312,   252,   250
   288,  1312,   250,   16
*ELEMENT,TYPE=CPS4,ELSET=rubber
     1,    10,   226,    28,   216
     2,   216,    28,    29,   217

  1266,  1183,  1184,  1206,  1205
  1267,  1184,  1185,  1207,  1206
  1268,  1185,  1186,  1208,  1207
  1269,  1186,  1187,  1209,  1208
  1270,  1187,  1309,  1311,  1209
**
**Material definition- Defines the width of the model.
*SOLID SECTION, ELSET=RUBBER, MATERIAL=NR29
1
*MATERIAL,NAME=RUBBER
** A user defined material behaviour is called (Davies et al elastic strain energy
**density function)
*HYPERELASTIC,USER
```

```
*NSET, NSET=    top
     3,   372,   373,   374,   375,   376,   386,   387,
   388,   389,   390,   506,   508,   510,   512,   514,
...
1285,  1287,  1289,  1291,  1293,  1295,  1297,  1299,
  1301,  1303,  1305,  1307,  1309,  1311
*NSET, NSET= bottom
     2,   400,   401,   402,   403,   404,   407,   408,
   409,   410,   411,   618,   620,   622,   624,   626,
...
  1286,  1288,  1290,  1292,  1294,  1296,  1298,  1300,
  1302,  1304,  1306,  1308,  1310,  1313
**FIRST STEP TO DO THE PRESTRAIN
*STEP, NLGEOM
Linear Static Analysis
**
**
*STATIC
**The nodes 618 and 506 are displaced 87.5 mm to produce a 50% pre-strain
*BOUNDARY, OP=NEW
bottom,2,2
618,1,1,-87.5
618,6,6,0
1210,1,1,0
1210,6,6,0
506,1,1,-87.5
506,6,6,0
1211,1,1,0
1211,6,6,0
bottom,6,6
top,6,6
top,2,2
*EL PRINT,FREQ=0
*NODE PRINT, FREQUENCY=1
*EL FILE,FREQUENCY=0
*ENERGY FILE
*ENERGY PRINT
*END STEP
**SECOND STEP TO DO THE VERTICAL PULL
**The top node set is displaced 1 mm to produce the vertical pull
*STEP, NLGEOM
Linear Static Analysis
**
**
*STATIC
**
*BOUNDARY, OP=NEW
bottom,2,2
618,1,1,-87.5
```

```
1210,1,1,0
506,1,1,-87.5
1211,1,1,0
bottom,6,6
top,6,6
top,2,2,1
*EL PRINT,FREQ=0
*NODE PRINT, FREQUENCY=1
*EL FILE,FREQUENCY=0
*ENERGY FILE
*ENERGY PRINT
*END STEP
```

APPENDIX 5: Calculation of the contribution of the time dependent component of the crack growth to the total cyclic crack growth.

It is first of all necessary to determine the static crack growth characteristics (tearing test) for the particular pre-strain conditions and these data can be expressed with the following expression:

$$dc/dt = K_S T^{\beta} \qquad \text{(A5.2-1)}$$

The results of these experiments on NR59 at PS=75% and PS=100% are the following ones:

PS=75%	$K_S = 10^{-30}$ S.I.units	$\beta = 6.8$
PS=100%	$K_S = 10^{-14}$ S.I.units	$\beta = 2.5$

The contribution of the time dependent crack growth to the total is then as follow:

$$(dc/dn)_S = K_S \int_0^{t_c} T_t^{\beta} dt \qquad \text{(A5.2-2)}$$

where t_C is the duration of one cycle and T_t is the tearing energy at time t. Because the cyclic deformation is a sinusoidal deformation, Expression A5.2-2 can be written as follow:

$$(dc/dn)_S = K_S T_{max}^{\beta} \int_0^{t_c} [\sin \pi \upsilon t]^{\beta} dt \qquad \text{(A5.2-3)}$$

where T_{max} is the maximum tearing energy during the cycle and υ is the frequency of the cyclic deformation. The integral in the expression A5.2-3 was estimated using numerical integration techniques. The estimated values are respectively 0.06 and 0.09

for PS=75% and PS=100%. It is then possible to determine the functions $(\mathrm{d}c/\mathrm{d}n)_S$ as function of T_{max} for both pre-strains and these are compared with the crack growth data of NR59 in Figure 5-20.

APPENDIX 6: ABAQUS input file for the analysis of the 30° inclined pure shear geometry using the J-integral method

```
*HEADING
**30-DEGREE INCLINED PURE SHEAR GEOMETRY
** ABAQUS Input Deck Generated by HyperMesh Version2.1
*PREPRINT,ECHO=NO,HISTORY=NO,CONTACT=YES,MODEL=NO
*RESTART,WRITE,OVERLAY
*NODE,NSET=LOAD
9999,0,0,0
9998,0,0,0
*NODE, SYSTEM=R
...
*NODE,NSET=TIP
...
**
**The focussed mesh at the crack tip have a triangular form but are plane stress
**collapsed quadratic elements, the fourth node of the element being taken from
**NSET=TIP. The plane stress analysis is defined by the choice of the element type.
**
*ELEMENT,TYPE=CPS4,ELSET=rubber
...
**Material definition- Defines the width of the model.
*SOLID SECTION, ELSET=RUBBER, MATERIAL=NR29
1
*MATERIAL,NAME=NR29
**
**The cubic elastic strain energy density function with the material constants of
**NR29 was used in this analysis.
*HYPERELASTIC,N=3,POLYNOMIAL
0.4,0,0.021,0,0,0.00083,0,0
0,0,0,0,0
**
*NSET, NSET=CRACK
1312
*NSET, NSET=    top
...
*NSET, NSET=  bottom
...
**Boundary conditions-The MPC focuses the behaviour of the nodes of the top and
**bottom node set to single nodes at the origin, respectively 9999 and 9998. The
**nodes of the node set tip are tied together to the node 1312.
*MPC
BEAM,TOP,9999
BEAM,BOTTOM,9998
TIE,TIP,1312
*STEP, NLGEOM,INC=99
*STATIC
```

```
**The node 9999 is displaced 1 mm upwards.
*BOUNDARY
9998,1,2
9998,6,6
9999,1,1
9999,6,6
9999,2,2,1
**The J-integral is estimated in different directions by specifying cosine and the sine
**of the corresponding angle.
**120deg
*CONTOUR INTEGRAL,FREQUENCY=1,CONTOURS=5,OUTPUT=BOTH
CRACK,-0.5,0.86602,0
**105deg
*CONTOUR INTEGRAL,FREQUENCY=1,CONTOURS=5,OUTPUT=BOTH
CRACK,-0.2588180451,0.9659258263,0
**100deg
*CONTOUR INTEGRAL,FREQUENCY=1,CONTOURS=6,OUTPUT=BOTH
CRACK,-0.1736481777,0.984807753,0
**90deg
*CONTOUR INTEGRAL,FREQUENCY=1,CONTOURS=6,OUTPUT=BOTH
CRACK,0,1,0
*EL PRINT,FREQ=0
*NODE PRINT, FREQUENCY=1,NSET=LOAD
*EL FILE,FREQUENCY=0
*ENERGY FILE
*ENERGY PRINT
*END STEP
```

APPENDIX 7: Refereed journal papers published by the author as part of this research

Title: Crack growth and strain induced anisotropy in carbon black filled natural rubber

Authors: J.J.C. Busfield, C.H.H. Ratsimba and A.G. Thomas
Department of Materials, Queen Mary & Westfield College, London E1 4NS.
Journal: Journal of Natural Rubber Research, (1997) Vol. 12, p. 131-141.

Abstract: The work discussed outlines the development of a technique to predict failure of rubber components under repeated complex stressing. A fracture mechanics approach is adopted, which has been shown to work with simple plane stress type geometry in the past. Real components with three dimensional loading and geometry can be examined with the use of finite element analysis techniques. These now permit the investigation of real fracture type problems to large strain deformations.

To predict fatigue behaviour in components it is necessary to derive the energy release rate for that particular component, which in general involves FEA techniques. Also it is important to know the crack growth characteristics of the material. This is usually expressed in terms of the rate of crack growth as a function of the tearing energy (energy release rate). Conventional tearing energy, crack growth rate tests are performed in relatively simple deformation modes, using for example edge crack or pure shear test pieces. In practice components used in engineering undergo more complicated strain histories. In order to study these potential complexities in the crack growth characteristics, the effect of pre-strain on cyclic crack growth behaviour using a predominantly pure shear test piece with an applied pre-strain have been studied. For the filled compounds studied so far there do appear to be complications and the observed crack growth rates may be substantially increased by these pre-strains. Some of these results are presented and their consequences discussed.

Title: Crack growth and predicting failure under complex loading in filled elastomers

Authors: J.J.C. Busfield, C.H.H. Ratsimba and A.G. Thomas
Department of Materials, Queen Mary & Westfield College, London E1 4NS.
Journal: Finite Element Analysis of Elastomers (1999) Professional Engineering Publishing Ltd., Bury St. Edmunds, p. 235-250.

Abstract: The work discussed outlines the development of a technique to predict fatigue failure of rubber components under repeated complex stressing. A fracture mechanics approach is adopted, which has been shown to work with simple plane stress type geometries in the past. Real components with three dimensional loading and geometry can be examined with the use of finite element analysis techniques. This allows an estimate of the tearing energy or energy release rate to be made. With knowledge of the material's crack growth characteristics it should be possible to predict the rate of crack propagation and estimate the components fatigue life. This now allows us to investigate real fracture type problems to large strain deformations.